

University of Alberta
Department of Civil Engineering



Structural Engineering Report No.174

Bond Model for Strength of Slab-Column Joints

by
S.D.B. Alexander
and
S.H. Simmonds

February, 1991

Bond Model for Strength of Slab-Column Joints

by

S.D.B. Alexander

and

S.H. Simmonds

Structural Engineering Report 174

Department of Civil Engineering

University of Alberta

Edmonton, Alberta

February 1991

Abstract

This thesis presents the results of concentric punching tests performed on twelve reinforced flat plate specimens. On the basis of these tests, a model for the ultimate strength of flat plate-column connections is proposed.

Isolated, interior column-plate connection specimens were tested. Rotational restraint was provided at the plate boundaries. Specimens were 155 mm thick and 2750 mm square in plan. Four of the specimens were reinforced with steel fibers. The major variables were fiber content, position of steel reinforcement, density of steel reinforcement passing through the column and degree of edge restraint. These tests were designed to test the validity of the truss model, as proposed by Alexander and Simmonds.

The straight-line truss model is found to be an inadequate description of the behavior of a slab-column connection. A new model that provides a more accurate description of the behavior of the test specimens is developed in a manner consistent with a lower bound solution for punching failure. This model, called the bond model, is successfully applied to 116 tests in the literature.

The bond model describes an interior column-plate connection as the intersection of four radial strips that are parallel to the reinforcement. The punching load is a function of both the flexural strength of these strips and the ability of the adjacent plate to deliver load to the strips.

According to the bond model, punching failure results from the limited ability of a plate to generate force gradient in flexural reinforcement close to a column support. Particular attention is given to the importance of bond in limiting force gradient.

The bond model is compared to existing code approaches for estimating punching strength. There is some discussion as to how the bond model may be incorporated in a complete description of the shear-moment interaction of an edge or corner column-plate connection.

Table of Contents

1 Introduction	1
1.1 Description of Problem	1
1.2 Scope of Study	2
2 Background	4
2.1 Description of Punching Failure	4
2.1.1 Flexural Failure	5
2.1.2 Shear Failure	6
2.2 Methods of Testing	8
2.3 Observed Behavior	10
2.4 Existing Approaches for Estimating Punching Capacity	12
2.4.1 Concrete Rupture Models	12
2.4.2 Flexural Models	14
2.4.3 Truss Model	15
2.5 Objectives of Testing	17
3 Specimens, Apparatus and Procedure	20
3.1 Description of Test Specimens	20
3.1.1 Reinforcement	21
3.1.2 Concrete	22
3.1.3 Casting, Stripping and Storing of Specimens	24
3.2 Test Apparatus	25
3.3 Instrumentation	26
3.3.1 Strain Measurements	26
3.3.2 Linear Variable-Differential Transformers (LVDT's)	28
3.3.3 Load Cells	29
3.4 Test Procedure	29

4 Observations and Evaluation	41
4.1 Flexural Behavior	41
4.2 Strain Gauge Measurements	43
4.2.1 Bar Force Profiles	45
4.2.2 Force Gradients	45
4.2.3 Anchorage Failure	48
4.2.4 Bottom Mat Strain Gauges	49
4.3 Miscellaneous Observations	50
4.3.1 Cracking	50
4.3.2 Demec Data	51
4.3.3 Overall Expansion	52
4.4 Effects of Test Variables	52
4.4.1 Effect of Steel Placement	52
4.4.2 Effect of Fibers	54
4.4.3 Effect of Boundary Restraint	55
4.5 Evaluation of Straight-Line Truss Model	57
5 Development of the Bond Model	75
5.1 Background	75
5.2 Elements of Bond Model	78
5.2.1 Radial Strips	78
5.2.2 Loading of Radial Strip	79
5.2.2.1 Primary Shear	81
5.2.2.2 Torsional Shear	83
5.3 Equilibrium of Radial Strip	85
5.3.1 Actual Loading of Radial Strip	85
5.3.2 Simplified Loading of Radial Strip	86

5.4 Bond Model Capacities	88
5.4.1 Flexural Capacity of Radial Strip	88
5.4.2 Primary Shear Loading	90
5.4.2.1 Bond Strength	90
5.4.2.2 Nominal Shear Stress	91
5.4.3 Ultimate Strength of Slab-Column Connection	92
5.4.4 Limits of Bond Model	93
6 Application of Bond Model	101
6.1 Assessment of Bond Model Mechanism	101
6.1.1 Measured Force Gradients	101
6.1.2 Boundary Effects	105
6.1.3 Correlation of Ultimate Load and Measured Force Gradient	107
6.1.3.1 Specimens Without Fiber Reinforcement	108
6.1.3.2 Specimens With Fiber Reinforcement	112
6.2 Ultimate Strength Predictions Based on the Bond Model	113
6.2.1 Test Results from the Literature	114
6.2.2 One-Way Shear, Two-Way Shear and Bond	116
6.2.3 Beam Action Shear and Bond	122
6.3 Comparison of Bond Model with Code Methods	124
6.3.1 Critical Sections	124
6.3.2 Effect of Aspect Ratio	126
6.4 Further Discussion of Bond Model	127
6.4.1 Causes of Punching Failure	127
6.4.2 Edge Column-Slab Connections	129
6.4.3 Relationship Between Other Models and the Bond Model	130
6.4.4 Future Work	130

7 Conclusions	144
References	146
Reinforcement Details	150
Load and Deformation Measurements	153
Strain Gauge Data	177
Demec Data	208
Tests in the Literature	214

List of Tables

Table 3.1	Test Descriptions	32
Table 3.2	Concrete Test Results	33
Table 3.3	Concrete Toughness Test Results	33
Table 4.1	Selected Load-Deflection Data	60
Table 4.2	Geometry of Straight-Line Truss Model	60
Table 6.1	Measured Force Gradients	132
Table 6.2	Primary Shear Loads Based on Measured Gradients	132
Table 6.3	Summary of Bond Model Results for Tests in Literature (116 Tests)	133
Table 6.4	Measured and Predicted Values of w	133
Table C-1	Description of Force Gradient Intervals	177
Table E-1	Description of Test Specimens: Moe (1961)	214
Table E-2	Description of Test Specimens: Elstner and Hognestad (1956)	214
Table E-3	Description of Test Specimens: Kinnunen and Nylander (1960)	215
Table E-4	Description of Test Specimens: Regan, Walker and Zakaria (1979)	215
Table E-5	Description of Test Specimens: Rankin and Long (1987)	216
Table E-6	Description of Test Specimens: Gardner (1990)	217
Table E-7	Description of Test Specimens: Shilling and Vanderbilt (1970)	218
Table E-8	Description of Test Specimens: Lunt (1988)	219
Table E-9	Calculated Results: Moe (1961)	220
Table E-10	Calculated Results: Elstner and Hognestad (1956)	221
Table E-11	Calculated Results: Kinnunen and Nylander (1960)	222

Table E-12	Calculated Results: Regan, Walker and Zakaria (1979)	223
Table E-13	Calculated Results: Rankin and Long (1987)	224
Table E-14	Calculated Results: Gardner (1990)	226
Table E-15	Calculated Results: Shilling and Vanderbilt (1970)	227
Table E-16	Calculated Results: Lunt (1988)	228

List of Figures

Figure 2.1	Typical Punching Failure	19
Figure 2.2	Straight-Line Idealization of Compression Fan	19
Figure 3.1	Basic Reinforcement Layout	34
Figure 3.2	Typical Load vs. Strain for Steel Coupon Test	35
Figure 3.3	Photo of Steel Fiber	35
Figure 3.4	Load-Deflection of Fiber Reinforced Beams	36
Figure 3.5	Notched Beam and Cylinder Test Set-Ups	36
Figure 3.6	Standard Test Set-Up	37
Figure 3.7	Plan View of P19RC	37
Figure 3.8	Plan View of P19RB	38
Figure 3.9	Top Demec Pattern	39
Figure 3.10	Bottom Demec Pattern	39
Figure 3.11	Edge Rotation and Expansion Measurements	40
Figure 3.12	View of Test in Progress	40
Figure 4.1	Load-Deflection: Variable Clear Cover	61
Figure 4.2	Load-Deflection: Variable Spacing	61
Figure 4.3	Load-Deflection: Clear Cover of 11 mm	62
Figure 4.4	Load-Deflection: Clear Cover of 38 mm	62
Figure 4.5	Load-Deflection: Variable Edge Restraint	63
Figure 4.6	Idealized Folding Pattern of Plate	63
Figure 4.7	Diagram of Half Plate	64
Figure 4.8	Flexural Performance	64
Figure 4.9	Bar Force Profile: P11F0	65
Figure 4.10	Bar Force Profile: P19RB	65
Figure 4.11	Column Bar Force Gradients: P11F0	66

Figure 4.12	Column Bar Forces: P11F0	66
Figure 4.13	Perimeter Bar Force Gradients: P11F0	67
Figure 4.14	Perimeter Bar Forces: P11F0	67
Figure 4.15	Column Bar Force Gradients: P19S50	68
Figure 4.16	Column Bar Forces: P19S50	68
Figure 4.17	Bottom Mat Bar Forces at Face of Column	69
Figure 4.18	Bond Cracking	69
Figure 4.19	Top Crack Pattern: P19RE	70
Figure 4.20	Top Crack Pattern: P19RC	70
Figure 4.21	Bottom Crack Pattern: P19RE	71
Figure 4.22	Bottom Crack Pattern: P19RC	71
Figure 4.23	Shear Crack: P19RE	72
Figure 4.24	Summary of Bottom Demec Strains	72
Figure 4.25	Compression Side of Plate at Column: P19RE	73
Figure 4.26	Compression Side of Plate at Column: P11F66	73
Figure 4.27	Geometry of Straight-line Compression Strut	74
Figure 5.1	Radial Arch	97
Figure 5.2	Layout of Radial Strips	97
Figure 5.3	Isolated Radial Half-Strip	98
Figure 5.4	Derivation of Kirchhoff Shear	98
Figure 5.5	Equivalent Loading of Radial Half-Strip	99
Figure 5.6	Optimized Loading of Radial Half-Strip	99
Figure 5.7	Assumed Rupture Surfaces for Morita and Fujii Bond Estimate	100
Figure 5.8	Practical Loading of Radial Half-Strip	100
Figure 6.1	Geometry for Determining Effectiveness of Bottom Reinforcement	134

Figure 6.2	Effect of Reinforcement Ratio on One-Way Shear Strength	134
Figure 6.3	Bond Model Predictions Using ACI Code One-Way Shear Stress	135
Figure 6.4	Bond Model Predictions Using BS 8110 Code One-Way Shear Stress	136
Figure 6.5	Bond Model Predictions Using Morita and Fujii Estimate of Bond Strength	137
Figure 6.6	ACI Code Predictions	138
Figure 6.7	BS 8110 Code Predictions	139
Figure 6.1	Critical Sections Defined by Codes	140
Figure 6.2	Equivalent of Critical Section for Bond Model	140
Figure 6.3	Comparison of Bond Model and ACI Code	141
Figure 6.4	Comparison of Bond Model and BS 8110 Code	142
Figure 6.5	Effect of Column Rectangularity	143
Figure A-1	Top Mats with Reinforcement Spaced at 150 mm	150
Figure A-2	Top Mats for Specimens P19S75 and P19S50	151
Figure A-3	Bottom Mat and Positions of Reinforcement	152
Figure B-1	Load-Deflection Diagrams: P11F0	154
Figure B-2	Ratio of Edge Restraint to Average Load in Tie Rods: P11F0	154
Figure B-3	Data from LVDT's Measuring Plate Expansion: P11F0	155
Figure B-4	In-Plane Expansion of Plate Near Center-Line: P11F0	155
Figure B-5	Load-Deflection Diagrams: P11F31	156
Figure B-6	Ratio of Edge Restraint to Average Load in Tie Rods: P11F31	156
Figure B-7	Data from LVDT's Measuring Plate Expansion: P11F31	157
Figure B-8	In-Plane Expansion of Plate Near Center-Line: P11F31	157

Figure B-9	Load-Deflection Diagrams: P11F66	158
Figure B-10	Ratio of Edge Restraint to Average Load in Tie Rods: P11F66	158
Figure B-11	Data from LVDT's Measuring Plate Expansion: P11F66	159
Figure B-12	In-Plane Expansion of Plate Near Center-Line: P11F66	159
Figure B-13	Load-Deflection Diagrams: P38F0	160
Figure B-14	Ratio of Edge Restraint to Average Load in Tie Rods: P38F0	160
Figure B-15	Data from LVDT's Measuring Plate Expansion: P38F0	161
Figure B-16	In-Plane Expansion of Plate Near Center-Line: P38F0	161
Figure B-17	Load-Deflection Diagrams: P38F34	162
Figure B-18	Ratio of Edge Restraint to Average Load in Tie Rods: P38F34	162
Figure B-19	Data from LVDT's Measuring Plate Expansion: P38F34	163
Figure B-20	In-Plane Expansion of Plate Near Center-Line: P38F34	163
Figure B-21	Load-Deflection Diagrams: P38F69	164
Figure B-22	Ratio of Edge Restraint to Average Load in Tie Rods: P38F69	164
Figure B-23	Data from LVDT's Measuring Plate Expansion: P38F69	165
Figure B-24	In-Plane Expansion of Plate Near Center-Line: P38F69	165
Figure B-25	Load-Deflection Diagrams: P19S150	166
Figure B-26	Ratio of Edge Restraint to Average Load in Tie Rods: P19S150	166
Figure B-27	Data from LVDT's Measuring Plate Expansion: P19S150	167

Figure B-28	In-Plane Expansion of Plate Near Center-Line: P19S150	167
Figure B-29	Load-Deflection Diagrams: P19S75	168
Figure B-30	Ratio of Edge Restraint to Average Load in Tie Rods: P19S75	168
Figure B-31	Data from LVDT's Measuring Plate Expansion: P19S75	169
Figure B-32	In-Plane Expansion of Plate Near Center-Line: P19S75	169
Figure B-33	Load-Deflection Diagrams: P19S50	170
Figure B-34	Ratio of Edge Restraint to Average Load in Tie Rods: P19S50	170
Figure B-35	Data from LVDT's Measuring Plate Expansion: P19S50	171
Figure B-36	In-Plane Expansion of Plate Near Center-Line: P19S50	171
Figure B-37	Load-Deflection Diagrams: P19RE	172
Figure B-38	Ratio of Edge Restraint to Average Load in Tie Rods: P19RE	172
Figure B-39	Load-Deflection Diagrams: P19RC	173
Figure B-40	Ratio of Edge Restraint to Average Load in Tie Rods: P19RC	173
Figure B-41	Data from LVDT's Measuring Plate Expansion: P19RC	174
Figure B-42	In-Plane Expansion of Plate Near Center-Line: P19RC	174
Figure B-43	Load-Deflection Diagrams: P19RB	175
Figure B-44	Ratio of Edge Restraint to Average Load in Tie Rods: P19RB	175
Figure B-45	Data from LVDT's Measuring Plate Expansion: P19RB	176
Figure B-46	In-Plane Expansion of Plate Near Center-Line: P19RB	176
Figure C-1	Bar Force Profiles: P11F0	178

Figure C-2	Bar Force Profiles: P38F0	178
Figure C-3	Bar Force Profiles: P11F31	179
Figure C-4	Bar Force Profiles: P38F34	179
Figure C-5	Bar Force Profiles: P11F66	180
Figure C-6	Bar Force Profiles: P38F69	180
Figure C-7	Bar Force Profiles: P19S150	181
Figure C-8	Bar Force Profiles: P19S75	181
Figure C-9	Bar Force Profiles: P19S50	182
Figure C-10	Bar Force Profiles: P19RE	182
Figure C-11	Bar Force Profiles: P19RC	183
Figure C-12	Bar Force Profiles: P19RB	183
Figure C-13	Column Bar Force Gradients: P11F0	184
Figure C-14	Column Bar Forces: P11F0	184
Figure C-15	Perimeter Bar Force Gradients: P11F0	185
Figure C-16	Perimeter Bar Forces: P11F0	185
Figure C-17	Column Bar Force Gradients: P11F31	186
Figure C-18	Column Bar Forces: P11F31	186
Figure C-19	Perimeter Bar Force Gradients: P11F31	187
Figure C-20	Perimeter Bar Forces: P11F31	187
Figure C-21	Column Bar Force Gradients: P11F66	188
Figure C-22	Column Bar Forces: P11F66	188
Figure C-23	Perimeter Bar Force Gradients: P11F66	189
Figure C-24	Perimeter Bar Forces: P11F66	189
Figure C-25	Column Bar Force Gradients: P38F0	190
Figure C-26	Column Bar Forces: P38F0	190
Figure C-27	Perimeter Bar Force Gradients: P38F0	191
Figure C-28	Perimeter Bar Forces: P38F0	191

Figure C-29	Column Bar Force Gradients: P38F34	192
Figure C-30	Column Bar Forces: P38F34	192
Figure C-31	Perimeter Bar Force Gradients: P38F34	193
Figure C-32	Perimeter Bar Forces: P38F34	193
Figure C-33	Column Bar Force Gradients: P38F69	194
Figure C-34	Column Bar Forces: P38F69	194
Figure C-35	Perimeter Bar Force Gradients: P38F69	195
Figure C-36	Perimeter Bar Forces: P38F69	195
Figure C-37	Column Bar Force Gradients: P19S150	196
Figure C-38	Column Bar Forces: P19S150	196
Figure C-39	Perimeter Bar Force Gradients: P19S150	197
Figure C-40	Perimeter Bar Forces: P19S150	197
Figure C-41	Column Bar Force Gradients: P19S75	198
Figure C-42	Column Bar Forces: P19S75	198
Figure C-43	Perimeter Bar Force Gradients: P19S75	199
Figure C-44	Perimeter Bar Forces: P19S75	199
Figure C-45	Column Bar Force Gradients: P19S50	200
Figure C-46	Column Bar Forces: P19S50	200
Figure C-47	Perimeter Bar Force Gradients: P19S50	201
Figure C-48	Perimeter Bar Forces: P19S50	201
Figure C-49	Column Bar Force Gradients: P19RE	202
Figure C-50	Column Bar Forces: P19RE	202
Figure C-51	Perimeter Bar Force Gradients: P19RE	203
Figure C-52	Perimeter Bar Forces: P19RE	203
Figure C-53	Column Bar Force Gradients: P19RC	204
Figure C-54	Column Bar Forces: P19RC	204
Figure C-55	Perimeter Bar Force Gradients: P19RC	205

Figure C-56	Perimeter Bar Forces: P19RC	205
Figure C-57	Column Bar Force Gradients: P19RB	206
Figure C-58	Column Bar Forces: P19RB	206
Figure C-59	Perimeter Bar Force Gradients: P19RB	207
Figure C-60	Perimeter Bar Forces: P19RB	207
Figure D-1	Bar Force Profiles from Demec Measurements: P11F0	209
Figure D-2	Bar Force Profiles from Demec Measurements: P38F0	209
Figure D-3	Bar Force Profiles from Demec Measurements: P11F31	210
Figure D-4	Bar Force Profiles from Demec Measurements: P38F34	210
Figure D-5	Bar Force Profiles from Demec Measurements: P11F66	211
Figure D-6	Bar Force Profiles from Demec Measurements: P38F69	211
Figure D-7	Bar Force Profiles from Demec Measurements: P19S150	212
Figure D-8	Bar Force Profiles from Demec Measurements: P19S75	212
Figure D-9	Bar Force Profiles from Demec Measurements: P19S50	213
Figure D-10	Bar Force Profiles from Demec Measurements: P19RC	213

Notation

b	width of plate strip for definition of ρ^+ and ρ^-
$b_i; b_{si}; b_w$	non-dimensional terms characterizing rupture surface for Morita and Fujii procedure for estimating bond strength
b_w	width of beam
$c; c_1; c_2$	dimension of column face
d	effective depth of reinforcing mat measured from center of mat to far side of slab
d_b	diameter of reinforcing bar
d'	cover of reinforcing mat measured from center of mat to near side of plate
f_y	yield stress of steel
f_c'	cylinder strength of concrete
f_r'	concrete modulus of rupture
f_t'	concrete tensile strength from split cylinder test
j	ratio of internal flexural moment arm to d
k_r	restraint factor
k	ratio of ER to TR
l	loaded length of radial strip
m_n	distributed bending moment on side face of radial strip
m_t	distributed torsional moment on side face of radial strip
q	distributed load applied directly to radial strip, including self-weight
\bar{q}	line load on radial half-strip resulting from q
r_e, r_i, r_o	dimensions describing geometry of compression strut
s	spacing of reinforcement
s_{eff}	effective spacing of reinforcement (truss model)
v	distributed shear in plate
\bar{v}	line load on radial half-strip resulting from Kirchhoff shear

$w; w_l$	bond model loading term from one adjacent quadrant of plate
$w_{ACI}; w_{BRT}; w_{M&F}$	bond model loading term based on ACI code beam shear; BS 8110 code beam shear; Morita and Fujii procedure for estimating bond strength
A_b	area of single reinforcing bar
A_s	total area of flexural reinforcement for a beam
A_{st}	total area of strut steel (truss model)
A_{sT}	top steel reinforcing radial strip
A_{sB}	bottom steel reinforcing radial strip
CR	corner restraint load
E_c	concrete modulus of elasticity
E_s	steel modulus of elasticity
ER	edge restraint load
F_b	force in reinforcing bar
F_b'	force gradient in reinforcing bar
G_f	fracture energy of concrete
K	non-dimensional parameter used to estimate $\tan \alpha$ in truss model
L	total length of radial strip
M_s	flexural capacity of radial strip
M^+, M^-	positive and negative moment capacities of radial strip
P	column load
P_{calc}	summation of loads carried by all radial strips framing into column
P_{flex}	yield-line flexural capacity of plate assuming undeformed geometry
P_s	load carried by single radial strip
P_{truss}	ultimate load predicted by truss model
P_{ult}, P_y	test value of ultimate load; load at first yield
TR	average load in tie rods

V_c	shear force acting on beam cross-section
α	angle of concrete compression strut relative to horizontal (truss model)
$\delta; \delta_y; \delta_{ult}$	center deflection of plate; at yield; at ultimate load
ϵ	strain of reinforcement
ϵ'	strain gradient of reinforcement
ρ^+	density of bottom reinforcement in radial strip
ρ^-	density of top reinforcement in radial strip
τ	horizontal shear stress required by beam action shear
τ_{co}	bond shear on reinforcing bar according to Morita and Fujii procedure

Chapter 1

Introduction

1.1 Description of Problem

Flat plate structures consist of reinforced concrete slabs supported on columns without drop panels or column capitals. They are an economical form of high-rise construction because the absence of projecting beams, drop panels and capitals simplifies formwork and allows the application of interior finishes directly to the soffit of the slab.

The design of flat plate structures is generally governed by serviceability limits on deflection or by the ultimate strength of the column-plate connections. Failure of the column-plate connection, usually called punching failure, is of particular concern because of its catastrophic consequences.

Existing building code design procedures for the punching strength of column-plate connections are largely empirical. There is justifiable concern that, as building techniques and materials change, these procedures may not ensure safe structures. It is widely held that a mechanical model which explains the transfer of load between plate and column would form a more reliable basis for design procedures.

The development of a general model is complicated by two features of column-plate connections. First, the failure is concealed by the surrounding plate, making direct observation of the events leading to failure impossible. Second, column-plate connections may be loaded under any combination of vertical load and moment, making it difficult to develop a general model which can handle all load cases. It is not surprising that, despite considerable research, a simple but general mechanical model for the transfer of load between plate and column has yet to be developed.

1.2 Scope of Study

The truss model, as proposed by Alexander and Simmonds (1986), appears to have the potential of providing a general solution to the problem of estimating the strength of a slab-column connection. It handles a wide variety of loading combinations on edge column-slab connections with considerable accuracy, as well as concentrically loaded interior column-slab connections.

The truss model assumes that a slab-column connection may be adequately described as a space truss composed of straight-line concrete compression struts and steel tension ties. For a slab-column connection under concentric load, the main parameter which must be estimated in applying the truss model is the effective angle, α , between the compression struts and the plane of the slab. This is accomplished by means of an empirical expression based on tests reported in the literature.

Tests of twelve flat plate-column specimens are reported in this thesis. The principal goal of this testing was to check the validity of the truss model. If the model proved satisfactory, then it was believed that a less empirical approach to determining the effective angle, α , could be developed on the basis of extensive measurements of steel reinforcement strains in the vicinity of the column. If the truss model was shown to be inadequate, then it was hoped that these same measurements would suggest an alternative.

Based on the observations recorded in these tests and those in the literature, a revised model for the transfer of shear between a flat plate and a column is proposed. This new model, called the bond model, is a modification of the truss model, in which straight-line compression struts are replaced by curved compression arches. Bond of reinforcement plays a central role in determining the geometry of the arches.

The scope of this study is limited to connections with concentrically loaded, square or circular columns. In Chapter 6, however, the application of the bond model to the case of an edge or corner column-slab connection under combined shear and moment is discussed, as well as other implications of the model.

Chapter 2

Background

2.1 Description of Punching Failure

The term punching failure describes the localized failure of a reinforced concrete flat plate-column connection wherein the column and an attached portion of the plate push through the surrounding plate. The failure surface is usually described as a truncated cone or pyramid, with the fracture surface inclined at an angle of about 25 to 35 degrees with the horizontal. A section sawn through a typical punching failure is shown in Figure 2.1.

Almost all flat plate-column connections appear to fail by punching. However, punching failures may occur before or after the development of the full flexural capacity of the plate, as calculated by yield-line methods. As a result, there is considerable debate as to when a punching failure constitutes a shear failure. Clyde and Carmichael (1974) suggest that the two terms are synonymous. This view, however, is not universally shared.

Gesund (1975) states that many tests, reported in the literature as punching failures, were actually local flexural failures. He proposes three categories of column-plate connection failure: flexural punching, shear-tension punching and shear-compression punching. A semi-empirical parameter is used to predict the governing type of failure for any particular connection.

In a similar vein, advocates of plasticity approaches to punching, as presented by Regan and Braestrup (1985), contend that a "proper" punching failure is related only to rupture of the concrete and is not enhanced by flexural reinforcement. Dependence on flexural reinforcement is seen as evidence that the failure is not punching.

Criswell (1974) discusses a gradual transition between flexural and shear failures of slab-column connections. He tries to separate shear and flexural failures on the basis of how much ductility is evident prior to fracture and whether or not the flexural capacity of the plate is reached.

Punching failures are considered analogous to shear failures in beams. There are presumed to be two-way plate equivalents to the shear and flexural failures observed in beams. As will be shown, however, there is no clear definition of a flexural failure in a two-way plate. The assumption of two distinct categories of punching failure, namely flexural and shear, inevitably leads to a third transitional category.

2.1.1 Flexural Failure

In a reinforced concrete beam, flexural failure is defined by crushing of the concrete compression block. This may occur before (over-reinforced) or after (under-reinforced) yielding of the flexural reinforcement. In either case, the concrete compression force is an essential component of the resisting moment at a cross-section. Its loss directly affects the flexural capacity of the cross-section.

An under-reinforced concrete beam undergoes an abrupt change in structural stiffness upon yielding of its flexural reinforcement. Yielding is concentrated over a short length of the beam. The total load carried by the beam is relatively constant while deformations increase greatly, making the flexural capacity of the beam a well-defined upper limit on its carrying capacity.

Most would agree that if a beam reaches its flexural capacity, it does not fail in shear. If this is true, then it is also true that if a beam fails in shear, it does not reach its flexural capacity. For beams, because the flexural capacity is such a well-defined quantity, this indirect definition of shear failure is very useful. Assuming adequate anchorage

of the reinforcement so that the bars cannot pull out, any flexurally under-reinforced beam without shear reinforcement that fails prior to yielding may be termed a shear failure. The definition of a shear failure need not be based on the observed failure of a particular component within the beam that is essential to shear transfer. Instead, shear failures in beams are indirectly defined as those failures that are not flexural.

For two-way plates, flexural capacities are usually based on yield-line analyses. However, for most tests, reaching this calculated flexural capacity does not correlate well with the onset of ductile behavior. Test results on simply supported plates routinely exceed these upper bound estimates by as much as 30 per cent. Explanations for this excess flexural strength include membrane forces, boundary restraints and second order effects which allow the slab to act as a folded plate. In any case, it seems clear that the yield-line capacity of a plate does not provide a convincing definition of a flexural failure. Therefore, the calculated flexural capacity is an unattractive criterion for the definition of the upper limit of shear failure.

2.1.2 Shear Failure

The definition of flexural failure in beams is related to observed failure of internal components that can be shown to play a role in carrying moment. In order to define shear failure of a plate-column connection, more attention must be given to the behavior of those internal components that are necessary for shear.

Shear is related to moment gradient by the equations of statics. In reinforced concrete, assuming that all flexural tensions are carried by steel, moment gradient can be achieved either by arching action, which requires a changing internal flexural moment arm, or by beam action, which requires a force gradient in the reinforcement.

For a member to fail in shear, it must reach some limiting factor for beam or arching action. Beam action is governed by those factors which limit force gradient, namely bond and yield of the reinforcement. In the absence of shear reinforcement, arching action is controlled mainly by the proximity of the applied loads to the supports.

The question of whether a specimen fails in flexure or shear should be replaced with the question of whether the failure was concerned with the mechanism of moment capacity or moment gradient. Consider a lightly reinforced plate which exceeds its calculated yield-line capacity. With increases in deflection, yielding spreads away from the column and the average force gradient in the reinforcement close to the column is reduced. By the equations of statics, the loss of force gradient close to the column should reduce the shear capacity. Additional spreading of yield further compromises shear strength, raising the possibility that failure is reached when the declining shear strength reaches the flexural capacity.

Force gradient in the reinforcement may also be controlled by the bond strength at the reinforcement to concrete interface. A limiting bond strength would certainly provide a bound for the force gradient in the reinforcement. The nature of this limit, however, would be quite different than the one imposed by yielding of the steel. Bond failure would introduce a brittle quality to the failure mechanism.

One concludes that punching failure may always be explained in terms of a shear failure. Shear failures are the result of a failure of the slab to generate required moment gradient. They may occur before or after the development of a yield-line mechanism within the plate. This is consistent with the observation that almost all column-plate connections ultimately have a punching failure. The reason that all the failure surfaces look about the same, whether or not a folding mechanism has developed, is that they are all shear failures.

For the most part, it is felt that punching failures reported in the literature as flexural failures were really ductile shear failures brought about by the spread of yielding. Those punching failures which are considered "proper" are either over-reinforced flexural failures or brittle shear failures which resulted from bond failure of the reinforcement.

The distinction between a flexural failure and a shear failure which is caused by extensive yielding is perhaps only of academic interest. For the purposes of design, only the brittle punching shear failure is of interest. This suggests that a model for the punching strength of column-slab connections should begin with an understanding of reinforcement bond.

2.2 Methods of Testing

By far the greatest number of tests on concentrically loaded interior column-slab connections have been performed on isolated column-slab connection specimens with rotationally unrestrained edges. The plates are either circular or square in plan, with their size determined by the approximate position of radial contraflexure of a prototype structure. Plate loads are applied on the perimeter at either discrete point or line supports. In the case of square plates on line supports, corners are generally free to lift.

The overall flexural behavior of a simply supported, single column-slab connection test is affected by the gross geometry of the plate and loading arrangement. Round plates supported around the perimeter by a ring or by tie rods at evenly spaced positions have fairly uniform radial crack patterns, suggesting polar-symmetric behavior. Tests of this type were done by Kinnunen and Nylander (1960) and Gardner (1990).

For square plates on square supports with plate corners free to lift, such as those tested by Elstner and Hognestad (1956), Moe (1961), Regan et al (1979) and Rankin and Long (1987), load tends to concentrate on the central region of each edge of the plate.

This rearrangement of load effectively prevents the opening of radial cracks which are parallel to the reinforcement. Cracking that is associated with the yield-line mechanism of the plate is constrained to be at some angle to the reinforcement.

Isolated column-slab connection tests have been criticized for failing to model such features as moment redistribution and in-plane restraint. Nevertheless, this type of test remains popular owing to its simplicity.

Tests reported by Shilling and Vanderbilt (1970) and Lunt (1988) have more realistic boundary conditions. In these tests, some form of rotational restraint was provided on the plate edges.

For the tests of Shilling and Vanderbilt, the torsional stiffness of an edge beam cast integrally with the plate provided rotational restraint. Each specimen was vertically supported at four corners and the central column stub. Load was applied by means of an air bag. The rotational restraint provided by the edge beam was internal to the overall specimen and could not be measured directly.

The specimens tested by Lunt extended to the center span of the plate in all directions. Sixteen equal vertical loads were applied to the plate. Vertical extension arms attached around the perimeter of the plate permitted vertical displacement but restrained rotation. Although it would have been possible to measure directly the amount of rotational restraint provided by the extension arms, these loads were not reported.

Long and Masterson (1974) report a series of comparative tests between rotationally restrained and simply supported plates. Specimens were tested under combined shear and unbalanced moment. The restrained specimens were larger in plan and failed at higher loads than their simply supported counterparts. Masterson and Long attributed the increased strength to increased membrane forces generated by the surrounding plate acting as a tension ring.

2.3 Observed Behavior

Masterson and Long (1974) describe four stages in the punching failure at an interior column.

- (1) Vertical flexural cracks open at the face of column.
- (2) Slab tension steel close to the column yields.
- (3) Flexural and shear cracks extend into what was the compression zone of the slab.
- (4) Failure occurs before extensive yielding. Masterson and Long assume that failure is caused by rupture of the reduced compression zone.

Kinnunen and Nylander (1960) report that, at positions close to the column on the slab soffit, radial compressive strains decreased or even became tensile prior to failure. Under load, the specimens took on the shape of a cone, with the portion of slab outside the shear crack rotating as a rigid body in the radial plane with increasing curvatures in the circumferential direction. They conclude that any model of a slab-column connection must have the equivalent of arching action in the radial direction in order to be consistent with concrete strain measurements.

Measurements of internal concrete strains by Shehata, reported by Regan and Braestrup (1985), suggest that at a position within d of the column face, the distribution of circumferential strain is very nearly radial, with the maximum compressive strain at the slab soffit. This is in agreement with the observation by Kinnunen and Nylander of a conical deflected shape for their test specimens. Furthermore, the linear distribution of strain shows that behavior in the circumferential direction is analogous to a slender beam. In the radial direction, Shehata reports a non-linear strain distribution, with the maximum compressive strain located in the interior of the plate, closer to the tension steel. These measurements, like those of Kinnunen and Nylander, suggest arching action in the radial direction.

The appearance of a punching failure suggests that diagonal tension may be important in limiting shear strength. However, the diagonal crack typically forms at loads less than 70 per cent of ultimate (Broms, 1990). Regan and Braestrup state, that prior to punching failure, the inclined crack surface has already formed. Furthermore, the connection is stable in this cracked condition and may be repeatedly loaded and unloaded. These observations are supported by tests by Kinnunen and Nylander. Test specimens which were fabricated with pre-formed conical punching surfaces which completely surrounded the column showed at most only about a 25 per cent reduction in capacity.

Measurements of vertical concrete surface strains on the column support by Shilling and Vanderbilt (1970) show that load tends to concentrate at the corners of square columns. No strain concentrations were observed for specimens with round columns.

There appears to be an interaction between flexural strength and shear strength. Many empirical approaches for estimating punching strength, such as those developed by Elstner and Hognestad (1956) and Moe (1961), have a dependency on flexural strength. In particular, the shear strength is reduced as the ratio of shear strength to flexural strength increases.

Bottom reinforcement improves both the ultimate capacity and ductility of a connection. Clyde and Carmichael (1974) report three tests in which the primary variable was the amount of bottom reinforcement. Top reinforcement for all plates was at 0.84 per cent. The ultimate deflection doubled and load increased 25 percent as bottom steel content went from 0 to 100 per cent of the top mat.

There appears to be some scale effect in punching strength. Tests by Kinnunen, Nylander and Tolf (reported by Broms, 1990) show that for double scale specimens, the strength increases by a factor of about 3 rather than the factor of 4 which would be expected in the absence of scale effects. The British code accounts for scale effects in its expression for a limiting nominal shear stress.

2.4 Summary of Significant Methods for Estimating Punching Capacity

Most existing approaches describe punching in one of three ways. Concrete rupture models assume that something akin to diagonal tension failure in beams governs punching failure in plates. Most code models as well as plasticity approaches may be considered to be concrete rupture models. Flexural models describe an overall folding mechanism for the plate and assess the limits on ductility for this mechanism. Invariably, the final limit to ductility is found to be some critical stress or strain in the concrete compression block near the column. The truss model is most like a flexural model, except that it assumes failure to be governed by conditions where a concrete strut meets its steel tie and not where the strut meets the column.

2.4.1 Concrete Rupture Models

Upper bound plasticity approaches assume concrete to be a rigid-plastic material. Concrete fracture is described by some yield criterion for concrete, the most popular being the modified Coulomb failure criterion. The plasticity approach assumes a fracture surface of a particular form and derives an energy expression which describes rupture along this surface. This expression is then minimized by employing variational calculus.

In his development of a plastic punching model, Bortolotti (1990) states that the punching mechanism assumed in the plasticity approach is applicable only when the slab

is sufficiently rigid, either because of boundary restraint or level of reinforcement. This agrees with the statement by Regan and Braestrup (1985) that plasticity approaches were concerned with "proper" punching only. Regan and Braestrup also note that the plasticity approach predicts that a critical vertical shear stress on a critical section should be a good parameter for describing punching failure.

Most building codes assume that the capacity of a slab-column connection can be estimated on the basis of a nominal vertical shear stress acting on a critical section. The rationale for this approach rests largely in a presumed equivalence between diagonal cracking in beams and punching failure of plates. The position of the critical surface varies from code to code. In the case of the ACI code, it is located at $0.5d$ from the column face while in the British standard, it is located at $1.5d$ from the column face.

It is not clear how concrete rupture models can be reconciled with the test observation that diagonal cracking does not lead to punching. The most commonly held opinion is that the nominal shear stress should be considered an index of the severity of the loading. As stated by Criswell and Hawkins (1974) a nominal shear stress "is indicative of neither the actual shear stresses nor their distribution."

Code equations do not assume critical sections to be at the face of column. Furthermore, no attempt is made to calculate the true area of concrete in shear, which should be limited by the depth of the compression block at the face of the column. Experience has shown that better results are obtained with a critical section at some distance from the face of the column. The flexural depth of the plate, and not the depth of the compression block, is used as a measure for the depth of the shearing section.

The fact that code equations should work at all is evidence that something akin to beam action is at work within the plate. The concept of a critical, nominal shear stress is easily justified if the ultimate load is governed by the horizontal shear stresses resulting from bond.

2.4.2 Flexural Models

Flexural punching models for plate-column connections assume a fan-like mechanism of wedge-shaped sections of slab. The failure criterion may be based on a yield-line analysis, as in Gesund (1975) or a critical condition in the concrete compression block, as in Kinnunen and Nylander.

The yield-line approach is criticized by Long (1975) as not being consistent with the observed behavior of plate-column connections.

The mechanical model developed by Kinnunen and Nylander is widely considered to be the best description of the behavior of polar symmetric, interior column-plate connections. It assumes that the fan-like mechanism in the plate deforms until some critical tangential strain is reached in the compression block near the column face. This is roughly equivalent to assuming that punching failure is a flexural failure, with rupture of the compression block being the governing feature.

The limiting strains proposed by Kinnunen and Nylander have been criticized as not being realistic. Broms (1990) addresses some of these concerns. He uses a variation of the Kinnunen and Nylander model incorporating failure criteria for the concrete which are more justifiable. The model, however, remains essentially a flexural mechanism which is controlled by rupture of the compression block near the face of column.

Very little attention has been given to the location where the failure surface intercepts the tension reinforcement of the plate. Since average shear stresses are reduced with increasing perimeter, it has been assumed that this location cannot be critical. This may not be a good assumption.

Tests indicate that there is something very much like truss action operating in the immediate vicinity of the column. If this is true, then in this region the average moment arm between the compression block and the reinforcing steel decreases as distance from the column increases. As the moment arm decreases, a force gradient in the reinforcement becomes less effective in shear transfer.

For isolated column test specimens, load is applied externally at the assumed line of contraflexure. This is compatible with direct arching action between applied load points and support. In a real slab, however, the shear at the line of contraflexure is internal to the system. At the boundary of truss-like action around a column, beam action must take over. The effectiveness of beam action in carrying shear is reduced if the internal flexural moment arm is reduced.

2.4.3 Truss Model

Alexander and Simmonds (1987) propose a method for estimating ultimate strength of a slab-column connection based on a truss model. The truss model assumes that a slab-column connection can be idealized as a space truss composed of steel tension ties and straight-line, inclined concrete compression struts. The horizontal components of the struts are equilibrated by steel tension tie forces. The vertical components of the compression struts transfer vertical load between the slab and column.

Three assumptions are required in order to estimate the capacity of a slab-column connection under concentric load using the truss model. First, the amount of steel which

can act as tension tie (strut steel or A_{st}) is limited on the basis of proximity to the column. Second, all strut steel is assumed to yield. Third, the angle of the compression strut, α , is empirically predicted on the basis of a dimensionless parameter, K , which relates the horizontal force in each strut to the strength of the concrete cover confining the strut.

$$K = \frac{s_{eff} \times d' \times \sqrt{f'_c}}{A_b \times f_y \times (c/d)^{0.25}} \quad [2.1]$$

$$\tan \alpha = 1.0 - e^{-2.25K} \quad [2.2]$$

As a result of the preceding equations, the ultimate capacity of a slab-column connection under concentric load was given as:

$$P_{truss} = \sum[A_{st} \times f_y \times \tan(\alpha)] \quad [2.3]$$

The rationale behind the truss model is that punching failure results from the failure of the plate to confine the out-of-plane component of a compression fan. The average effect of the fan can be represented by a straight-line compression strut, as shown in Figure 2.2. It is assumed that in order to satisfy horizontal equilibrium, each compression fan must converge on its attendant tension tie. At the points where compression fans and tension ties meet, only the confining strength of the concrete covering the reinforcement prevents the reinforcement from pushing out of the plane of the slab.

As discussed in Alexander and Simmonds (1988), the truss model appears to be the most promising model for the ultimate behavior of slab-column connections available. It can handle a wide variety of problems, including the shear-moment interaction of edge column-slab connections. To remove the empiricism from the estimate of $\tan \alpha$, a reexamination of the truss model approach was required.

The definition of the parameter K depends on many of the same quantities which would be used in estimating the anchorage length for a reinforcing bar. It follows that,

since this empirical approach seems to work, punching may be the result of bond failure of the strut steel. The parameter K may not relate directly to $\tan \alpha$ but rather to the length where the reinforcing bar is met by the compression fan, called the transfer length.

The significance of this revised interpretation of K is that the flexural depth of the slab imposes a geometric constraint on the average value of $\tan \alpha$. The minimum length over which the yield force of a bar can be developed is never zero. Therefore, there must be some minimum transfer length between a compression strut and a reinforcing bar. For a slab-column connection in which the transfer lengths are near minimum, a decrease in the flexural depth of the plate must result in a decrease in the effective value of $\tan \alpha$. This dependency of $\tan \alpha$ on the flexural depth of the plate is not accounted for in the empirical equation for K .

2.5 Objectives of Testing

The straight-line idealization of a compression fan predicts that an effective compression strut will act between the centroid of the compression block at the face of the column and a point at the level of the tension reinforcement at some distance from the face of the column. The location where the reinforcement and compression fan meet should be marked by a declining magnitude of the bar force as distance from the column increases.

The primary objective for the present investigation has two parts. The first is to establish the geometry of the compression struts by measuring strains in the reinforcement that passes through or in close proximity to the column. The second is to observe how this geometry responds to variations in different parameters.

Four parameters are examined. Three of these, namely clear cover of reinforcement, spacing of reinforcement and fiber reinforcement of the concrete are expected to

affect the geometry of the compression struts by affecting the bond strength of the central reinforcing steel. The fourth parameter, moment redistribution, is expected to affect strains in the reinforcement at some distance from the column. As steel through the column region begins to yield, increased loads can be carried as long as the effective angle of the compression strut increases. This requires reinforcement at some distance from the column to unload as the point of contraflexure moves in toward the column.

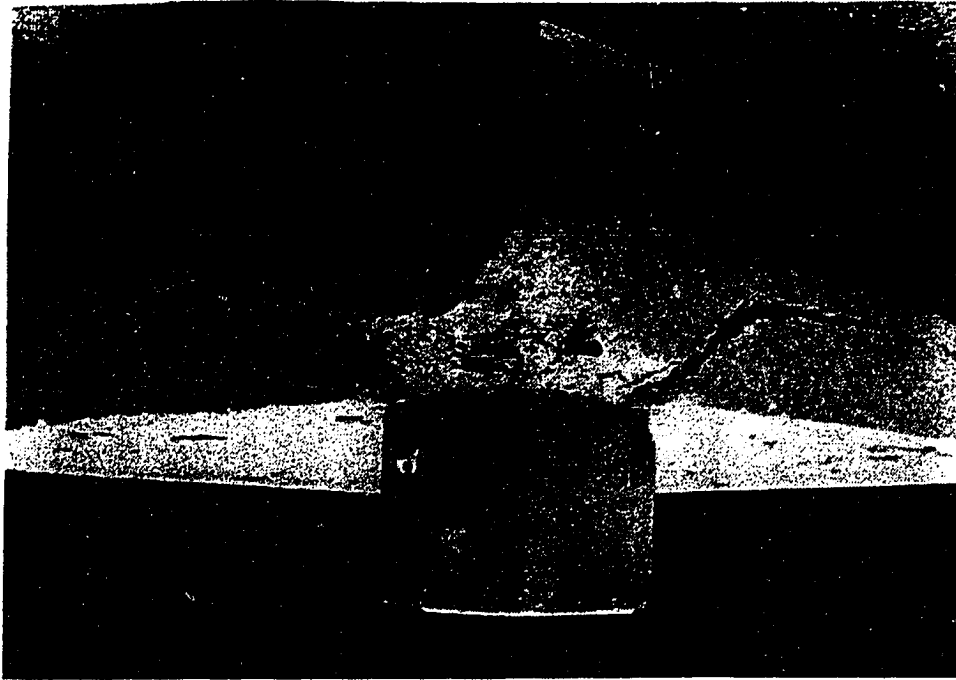


Figure 2.1 Typical Punching Failure

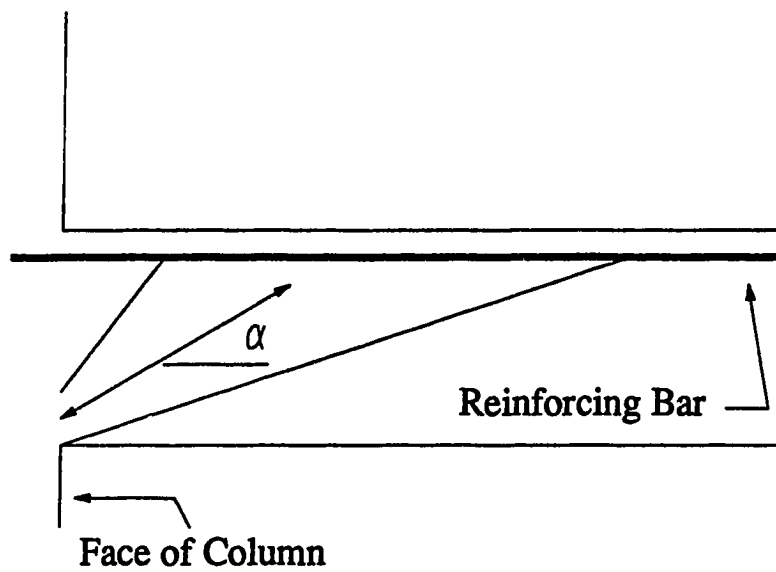


Figure 2.2 Straight-Line Idealization of Compression Fan

Chapter 3

Specimens, Apparatus and Procedure

3.1 Description of Test Specimens

The test program consisted of 12 isolated interior column-flat plate connections. The plates were 155 mm thick and 2750 mm square with 200 x 200 x 200 mm column stubs above and below the plate. Orientation of specimens for testing was as it would be in a real structure, with the column stub load acting vertically upwards and the top surface of the slab near the column in tension.

The plate edges were restrained against rotation for two reasons. First, rotational restraint provides a more realistic boundary condition by permitting internal redistribution of loads. Second, it is believed that punching strengths may be enhanced if plate loads are applied too close to the column. As a result, the specimens were somewhat larger in plan than comparable, simply supported specimens reported in the literature. Increased size leads to reduced flexural strength, creating the need for rotational restraint of the plate edges.

The effects of four variables are studied: clear cover of top mat, additional slab reinforcement through the column, steel fiber content and boundary restraint. Specimen designations provide abbreviated descriptions of each test, as outlined in Table 3.1. The variables of clear cover and fiber content were expected to affect punching capacities by changing bond behavior of the reinforcement. Increasing the amount of steel through the column was expected to increase the magnitude of the available tension tie. The boundary restraint series was not originally planned. After the first test (P11F0) had been completed, it was realized that a better understanding of the boundary restraints was needed.

The basic top mat reinforcement layout, shown in Figure 3.1, has twelve #10M bars at 150 mm spacing. Top mats for P19S50, P19S75 and the three specimens in the edge restraint series had additional bars. Specimen P19S75 had three additional bars each way, resulting in a reinforcement spacing of 75 mm over the middle 450 mm of the plate. In P19S50, six reinforcing bars were added each way, bringing the bar spacing in the central 450 mm of plate to 50 mm. For the specimens of the restraint series, the spacing of the top mat was maintained at 150 mm spacing each way but two additional bars each way were placed at the outer edge of the top mat, bringing the total number of bars to fourteen each way. All twelve specimens had the same bottom mat, shown in Figure 3.1. Additional reinforcing details are provided in Appendix A

The specimens were for the most part lightly reinforced in order to limit the amount of steel close to the column. The primary goal was to obtain a reasonably complete picture of the behavior of the reinforcing steel in the immediate vicinity of the column.

The specimens were not intended to be representative of some particular prototype slab. However, for the purposes of establishing reasonable bar cut-offs, columns were assumed to be spaced at about 4500 mm on center. According to the detailing requirements for slabs in CAN3-A23.3, the minimum distance from the face of column for bar cut-off of column strip steel would be about 900 mm.

3.1.1 Reinforcement

All specimens were reinforced with 10M deformed reinforcing bars with a nominal area of 100 mm^2 and a minimum specified yield of 400 MPa. Tension tests were performed on sample coupons. Although the steel used for the twelve specimens came from two separate shipments, there were no significant differences in the material properties.

A typical load-strain plot from a coupon test is given in Figure 3.2. The reinforcing steel had a well-defined yield plateau at 43.8 kN and an ultimate load of 72 kN. On the basis of the nominal area for the bar of 100 mm², the steel had a yield stress of 438 MPa and a modulus of elasticity of 183,000 MPa.

3.1.2 Concrete

Normal weight concrete for all twelve specimens was obtained from a local supplier. Four separate castings were required, at intervals of approximately five weeks, and the same concrete mix was ordered for each. The mix had 12mm aggregate, a specified slump of 75 mm and an estimated 28 day compressive strength of 25 MPa.

Xorex corrugated steel fibers, 50 mm in length, were added to the concrete in four specimens. A photograph of an individual fiber is shown in Figure 3.3. Fiber contents were determined by wash-out tests at casting time. In order to facilitate the addition of steel fibers, WRDA-19 plasticizer was added to the mix at a rate of 1.5 liters per cubic meter. Both plasticizer and fibers were added on site.

Compression and split cylinder tests were performed on all concrete mixes. Modulus of rupture tests, in accordance with ASTM Standard C 78, were also performed on some mixes. Cylinders were nominally 150 mm in diameter and 300 mm long. Beams were 152 x 152 x 914 mm. The results of these tests are summarized in Table 3.2. All cylinders and beams were air-cured alongside the test plate specimens.

A number of toughness tests were performed. These are summarized in Table 3.3.

Third point loading tests as described in ASTM Standard C 1018 were performed on four fiber reinforced beam specimens. The set-up of these tests is the same as that used in a modulus of rupture test. The results of these tests were not entirely satisfactory, owing to excessive flexibility in the test frame. Load-deflection curves for these tests are given in Figure 3.4.

The flexural toughness indices, I_5 , I_{10} and I_{30} , are ratios of areas under the load-deflection diagram of a third point loading beam test. The denominator is the enclosed area at first cracking. The numerators of I_5 , I_{10} and I_{30} are the enclosed areas at 3, 5.5 and 15.5 times the first-crack deflection respectively.

Toughness tests were made on six notched beam and cylinder specimens. Fracture energy measurement tests as described in the RILEM Draft Recommendation (1985), were done on notched beam specimens measuring 152 x 152 x 914 mm. In addition, sixteen fracture energy tests, based on the RILEM procedure, were performed on notched cylinders.¹ The test set-up and nominal specimen dimensions for the notched toughness tests are given in Figure 3.5.

The term fracture energy, G_f , is a measure of the energy per unit area required to cause tensile failure of concrete. For a notched beam test, G_f is the area under the entire load-deflection curve divided by the projected area of the fracture surface.

The notched toughness tests on beams are appealing because they may be used for both plain and fiber reinforced concrete. In addition, the notched beam test, unlike the third point loading test in ASTM Standard C 1018, has a modest requirement for testing machine stiffness (Hillerborg, 1985). Results for fracture energy based on notched beam tests clearly show the beneficial effects of steel fiber reinforcement.

¹ These tests were based on a suggestion by Dr. Arne Hillerborg.

The toughness tests on notched cylinders do not give results that are consistent with the larger span beam specimens for fiber reinforced concrete. There is, however, reasonable agreement in the case of the single, plain concrete mix that was tested both ways. There may be some value in exploring the possibilities of a notched cylinder alternative to the larger notched beam test, at least for plain concrete.

3.1.3 Casting, Stripping and Storing of Specimens

All plates were cast upside down for two reasons. First, the truss model emphasizes the importance of the concrete cover and it is easier to control the distance between the form and the steel rather than the distance between the steel and the screeded surface. Second, casting upside down allows both the extension lugs for demec measurements to be fitted into drilled holes in the form and the short strain gauge lead wires to exit the specimen through the bottom of the form, thereby keeping them out of the way during casting.

The set of specimens with a clear cover of 11 mm were cast first. To maintain workability of the mix, WRDA-19 plasticizer was added, at the rate of 1.5 l/m³, prior to the placing of any concrete. Specimen P11F0 was then cast. The amount of concrete remaining in the truck was estimated and the amount of steel fibers needed to provide a nominal weight density of 30 kg/m³ was then added. Specimen P11F31 was then cast, with the actual weight density of fibers determined by washout test. As before, the amount of concrete remaining in the truck was estimated and additional steel fibers were added to the mix, bringing the final nominal weight density to 60 kg/m³. Actual fiber content was again determined by washout test.

By the time the concrete for the first two specimens had been placed, workability of the concrete had begun to deteriorate. Therefore, additional plasticizer, at an estimated rate of 0.75 l/m^3 , accompanied the final dose of steel fibers. Casting of all three specimens took about 1.5 hours.

The second set of specimens to be cast were those with a clear cover of 38 mm. The procedure followed was the same as that used for the 11 cover specimens except that plasticizer was added to the concrete after casting the first specimen, P38F0. There were two reasons for this, based on the experience of casting the first set of specimens. For specimen P11F0, the plasticized concrete was so sloppy that there was some concern about the possibility of mix segregation. In addition to this, the plasticizer was effective for a limited time. By delaying the initial dose in casting the 38 mm cover specimens, re-dosing was not required. Casting of the second set of specimens took about 1 hour.

For the third and fourth castings, concrete was placed directly from the truck with no on-site modifications. It took slightly more than one half hour to place the concrete for each set of specimens.

After casting, specimens were covered with polythene and allowed to cure for 7 to 10 days. Sides of the forms were removed one or two days after casting. Two to three weeks after casting, the specimens were lifted clear of the form. Four steel lifting lugs and shackles, attached to the sides of the specimen by means of threaded, cast-in-place inserts, permitted the plates to be lifted in a horizontal position. The plates could be turned over by lifting on only one edge. Specimens were stored on edge awaiting testing.

3.2 Test Apparatus

Three different test set-ups are shown in Figures 3.6, 3.7 and 3.8. The primary load was applied by jacking with a manual pump between the laboratory strong floor and the

central column stub of the specimen. The specimen was tied down to the strong floor by eight 19 mm diameter steel tie rods. All specimens had some form of rotational restraint applied at the plate boundary.

For all specimens except P19RC and P19RB, edge rotational restraint consisted of positive edge moments which were applied by jacking up on structural steel extension arms on all four sides of the plate, as shown in Figure 3.6. The four edge restraint jacks plus a fifth jack that was used to monitor the load were linked to a common manifold and controlled by a separate manual pump.

For plate P19RC, shown in Figure 3.7, the upward jacking loads were applied at the corners of the specimen, thereby restraining the corner levers. As with the previously described edge restraint, the corner restraint jacks plus a fifth load monitoring jack were linked to a common manifold, separate from the central jack.

Specimen P19RB combined both methods of edge restraint. This required a total of three manual pumps: one for the central load jack, a second for the edge restraint jacks and a third for the corner jacks.

In order to minimize membrane forces in the plane of the slab caused by the supports, all edge and corner restraint jacks were mounted on roller bearings, placed to allow radial movement with respect to the central column stub.

3.3 Instrumentation

3.3.1 Strain Measurements

The primary goal of the testing program was to try to establish the geometry of a strut and tie mechanism within the slab-column connection. It was believed that the end-points of concrete compression struts could be established from strain distributions along

reinforcing bars close to the column.

In each test, strain measurements were made on a total of eight top-mat reinforcing bars. Four of these bars (two in each direction) passed through the column and are referred to as **column bars**. The remaining bars, 125 mm from the column face, are referred to as **perimeter bars**.

Forty electrical resistance foil strain gauges, with a nominal resistance of 120 ohms and a gauge length of 5 mm, were placed on the top mat of each specimen. A layout of the gauges is shown in Figure 3.1. Discounting any differences between inner and outer layers of steel, there are seven geometrically distinct locations of strain gauges on two geometrically distinct reinforcing bars. It was thought that this would provide sufficient duplication of data to ensure reliability.

At each gauge location, the deformations of the reinforcement were ground smooth. In an effort to minimize the impact of the gauges on the bond characteristics of the steel, single gauges were used at each location and grinding was restricted to the smallest area that would permit placement of the gauge.

Gauges within the column stub region were attached with an epoxy adhesive. The remaining gauges were attached with a cyano-acrylate adhesive. After lead wires were attached, all gauges were covered with a layer of flowable silicon to provide electrical insulation. This was followed by a thick patch of conventional silicon sealant. To lessen the effect on the steel-concrete bond, the patch was confined to the immediate area of the gauge and did not wrap around the bar.

On each of the three specimens in the R series, an additional eight strain gauges were placed on the bottom (compression) mat of steel at the face of the column. These were attached with epoxy adhesive.

Demountable mechanical extensometer (demec) measurements were made on the perimeter and column bars in each direction. Extension lugs were brazed onto the reinforcing bars at 50 mm intervals, following the layout given in Figure 3.9. Demec points were attached with sealing wax to the ends of the lugs. Prior to casting, each lug was sheathed with a short length of rubber tubing. The tubing and lug fit into drilled holes in the bottom of the form. The rubber tubing was removed before testing, leaving a space of approximately 5 mm between the lug and the surrounding concrete. On the compression side of the plate, concrete surface strains were measured using demec points at the positions shown in Figure 3.10.

All demec measurements were made with a prototype electronic extensometer, developed at the University of Alberta by S.J.Kennedy, R.Gitzel, D.Lathe and A.Dunbar. The device automatically records extensometer readings for later down-loading to a personal computer. The electronic extensometer permitted large numbers of readings to be made by only one person, and eliminated the problem of typing errors when transferring raw data into a computer for processing. Unfortunately, the extensometer results were disappointing. It is felt that localized cracking, awkwardness of some of the measurement locations, flexibility of the brazed on lugs and flexibility of the extensometer itself combined to reduce the accuracy of the measurements.

3.3.2 Linear Variable-Differential Transformers (LVDT's)

On most specimens, two 15 volt LVDT's were mounted in each direction on vertical extension arms, approximately 300 mm from the plate center-line, and wires were strung across to corresponding positions on extension arms on the opposite side of the plate. This arrangement is shown in Figure 3.11. From these readings, the average edge rotation and overall radial expansion of the plate could be estimated.

The center deflection of the plate was obtained by measuring the stroke of the central jack relative to the strong floor with a single 15 volt LVDT.

3.3.3 Load Cells

All vertical loads to the specimens were measured, thereby allowing a check on overall equilibrium. A full bridge arrangement of strain gauges was installed on each tie rod, allowing the tie rods to serve as load cells. The central load was monitored with a 1800 kN load cell. Five jacks of the same type and manufacture, connected to a common manifold, were used in providing either edge or corner restraint. Four of these jacks reacted against the test specimen; the fifth jack reacted against a 90 kN load cell. Because the jacks were geometrically similar and subjected to a common hydraulic pressure, it was assumed that the load in all five jacks was equal.

3.4 Test Procedure

Prior to testing, each specimen was checked for alignment within the testing apparatus. The apparatus, which allowed for minor adjustments, could also be used to move the specimen if larger adjustments were required. The edge restraint jacks were used to translate the plate. The specimen was rotated by supporting the plate on the central jack.

Owing to the length of time required to take sets of demec readings, most tests took between two and three days to complete. Specimens remained loaded for the duration of the test, except for those occasions when the correction of problems such as hydraulic leaks required the removal of load.

With one exception, tests were started by lifting the specimen clear of the blocking with either the edge or corner restraint jacks and measuring the combined self weight of the specimen and attached loading apparatus. The center jack was then brought to bear

on the specimen and the LVDT used to measure the stroke was adjusted and zeroed. All slack was removed from the tie rods and the end nuts were made finger tight. Load was then applied through the center jack, with adjustments to the restraint jacks made as required. Figure 3.12 shows a typical test in progress.

Specimen P11F66 was first lifted on the center jack. Tie rods were then tightened and the edge restraint jacks were brought to bear. The test continued with load applied to the center jack and adjustments made to the restraint jacks as required.

In addition to the LVDT, load cell and strain gauge output, the data acquisition system recorded the date and time that each set of data was taken. The system stores each set of readings as a separate load step. This provided a logging system for recording other observations made throughout the tests.

The position of radial contraflexure could be controlled by adjusting the ratio of edge restraint to average tie rod load. Throughout most tests, a maximum ratio of average tie rod (TR) to edge restraint load (ER) of about 1.6 was maintained by adjusting the edge restraint jacks. For the specimens with edge restraint only, this made the applied load statically equivalent to a ring load at a radius of approximately 910 mm from the center of the column. At large deflections, this ratio was allowed to increase as dictated by the specimen, thereby simulating the tightening of the ring of contraflexure with moment redistribution. During testing, the required magnitude of ER was determined from the center load (P) according to the following relationships.

$$TR = \frac{P + 4ER - \text{selfweight}}{8} = 1.6ER \quad [3.1]$$

$$1.6 = \frac{P + 4ER - \text{selfweight}}{8ER} = \frac{P - \text{selfweight}}{8ER} + 1/2 \quad [3.2]$$

$$ER = \frac{P - \text{selfweight}}{8.8} \quad [3.3]$$

Tests of specimens P19RC and P19RB were conducted somewhat differently. After the initial set-up, specimen P19RC was actively loaded through only the central jack until load step 66. Corner restraint loads were purely reactive with no set limits on the ratio of corner restraint to average tie rod load. At load step 66 (load and stroke approximately 270 kN and 42 mm respectively), additional load was placed on the corner restraints in order to check the sensitivity of the central load to increased corner restraint. There was almost no change in the load at the central jack as a result of this procedure.

As was the case for specimen P19RC, specimen P19RB was initially lifted on the corner restraints. The center and edge restraint jacks were then brought to bear. The edge restraint load was adjusted according to Equation 4.3. The corner restraint jack was not adjusted until load step 31 (load and stroke approximately 265 kN and 20 mm respectively). It appeared at this point that the structural stiffness of the specimen was declining significantly. Additional load was placed on the corner restraints. This resulted in an increase in the measured center load and a slight improvement in stiffness. At load step 41 (load and stroke approximately 295 kN and 25 mm respectively), the corner restraint load was again increased. At load step 42 an attempt was made to increase the edge restraint load. However, hydraulic leaks prevented the edge restraint jacks from accepting additional load. At this point, valves between the pumps and the edge and corner restraint jacks were closed. For the remainder of the test load was applied to the center jack only, with no active loading of the edge and corner restraint jacks.

Table 3.1 Test Descriptions

Mark	Type of Test	Clear Cover (mm)	Series and Relevant Quantity	Remark
P11F0	Plate	11	Fiber, 0 kg/m ³	Restraint, Edge 150 mm Spacing
P11F31	Plate	11	Fiber, 31 kg/m ³	Restraint, Edge 150 mm Spacing
P11F66	Plate	11	Fiber, 66 kg/m ³	Restraint, Edge 150 mm Spacing
P38F0	Plate	38	Fiber, 0 kg/m ³	Restraint, Edge 150 mm Spacing
P38F34	Plate	38	Fiber, 34 kg/m ³	Restraint, Edge 150 mm Spacing
P38F69	Plate	38	Fiber, 69 kg/m ³	Restraint, Edge 150 mm Spacing
P19S150	Plate	19	Spacing, 150 mm	Restraint, Edge No Fiber
P19S75	Plate	19	Spacing, 75 mm	Restraint, Edge No Fiber
P19S50	Plate	19	Spacing, 50 mm	Restraint, Edge No Fiber
P19RE	Plate	19	Restraint, Edge	150 mm Spacing No Fiber
P19RC	Plate	19	Restraint, Corner	150 mm Spacing No Fiber
P19RB	Plate	19	Restraint Both Edge and Corner	150 mm Spacing No Fiber

Table 3.2 Concrete Test Results

Plate	Lot	Fiber Content (kg/m ³)	f'_c (MPa)	f'_t (MPa)	E_c (MPa)	f'_r (MPa)
P11F0	1	0	33.2	2.46	NA	4.16
P11F31	1	30.8	35.8	2.84	23,500	4.25
P11F66	1	65.7	35.0	3.77	22,170	4.22
P38F0 (plast.)	2	0	35.6 (38.1)	2.68 (2.90)	NA (24,200)	4.54 (4.93)
P38F34	2	33.8	38.4	2.84	23,200	5.58
P38F69	2	69.0	38.5	3.52	24,400	5.30
P19S150 P19S75 P19S50	3	0	26.0	2.19	20,700	N/A
P19RE P19RC P19RB	4	0	35.3	3.22	29,000	N/A

Table 3.3 Concrete Toughness Test Results

Plate	Lot	Fiber Content (kg/m ³)	G_r (N/m) Cylinder	G_r (N/m) Beam	I_5	I_{10}	I_{30}
P11F0	1	0	N/A	172	N/A	N/A	N/A
P11F31	1	30.8	1966	1515	3.09	3.34	3.53
P11F66	1	65.7	1608	4607	4.02	5.57	6.73
P38F0 (plast.)	2	0	(203)	(183)	N/A	N/A	N/A
P38F34	2	33.8	1377	2550	3.44	4.00	4.36
P38F69	2	69.0	1471	5964	3.64	5.17	6.85
P19S150 P19S75 P19S50	3	0	246	N/A	N/A	N/A	N/A
P19RE P19RC P19RB	4	0	299	N/A	N/A	N/A	N/A

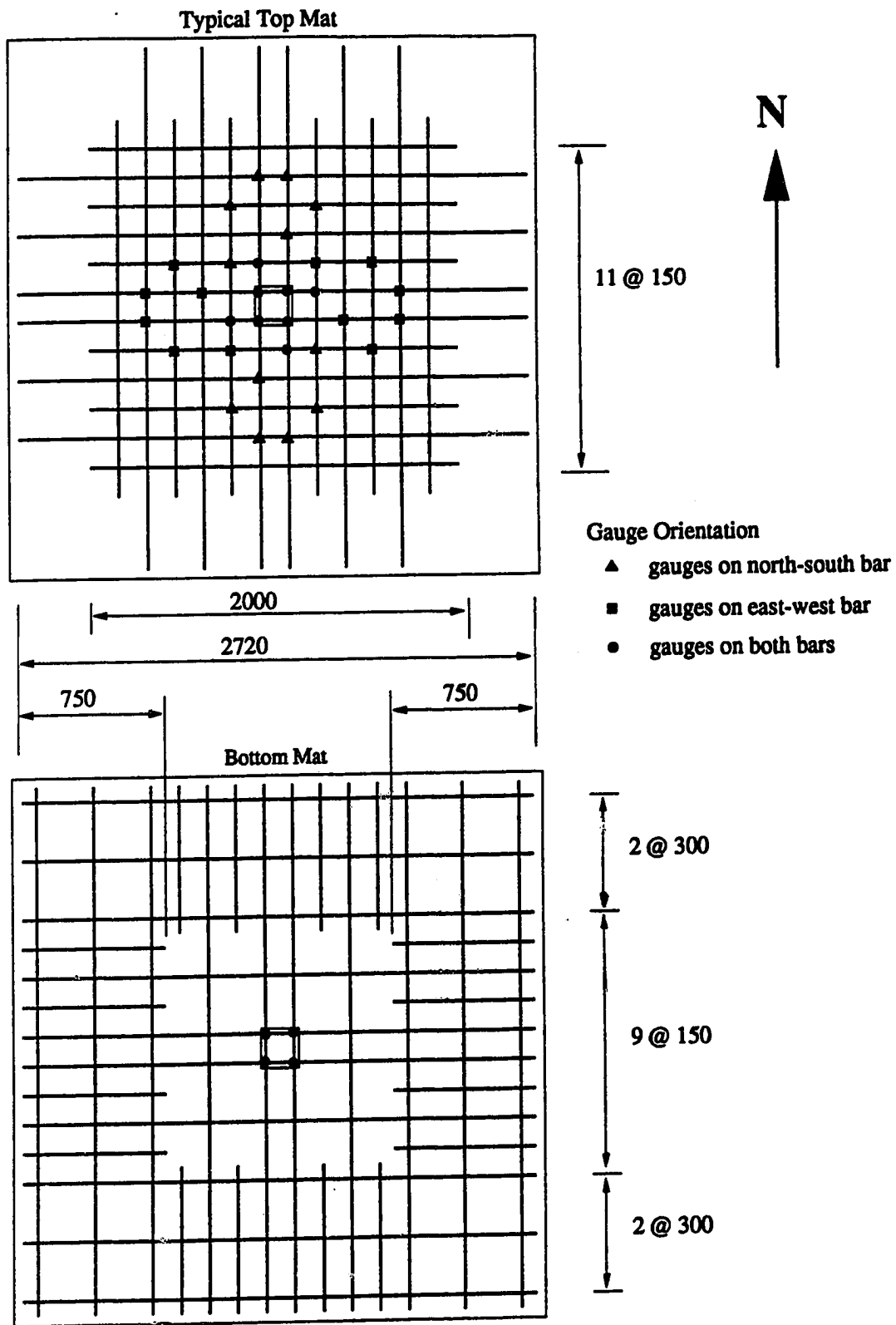


Figure 3.1 Basic Reinforcement Layout

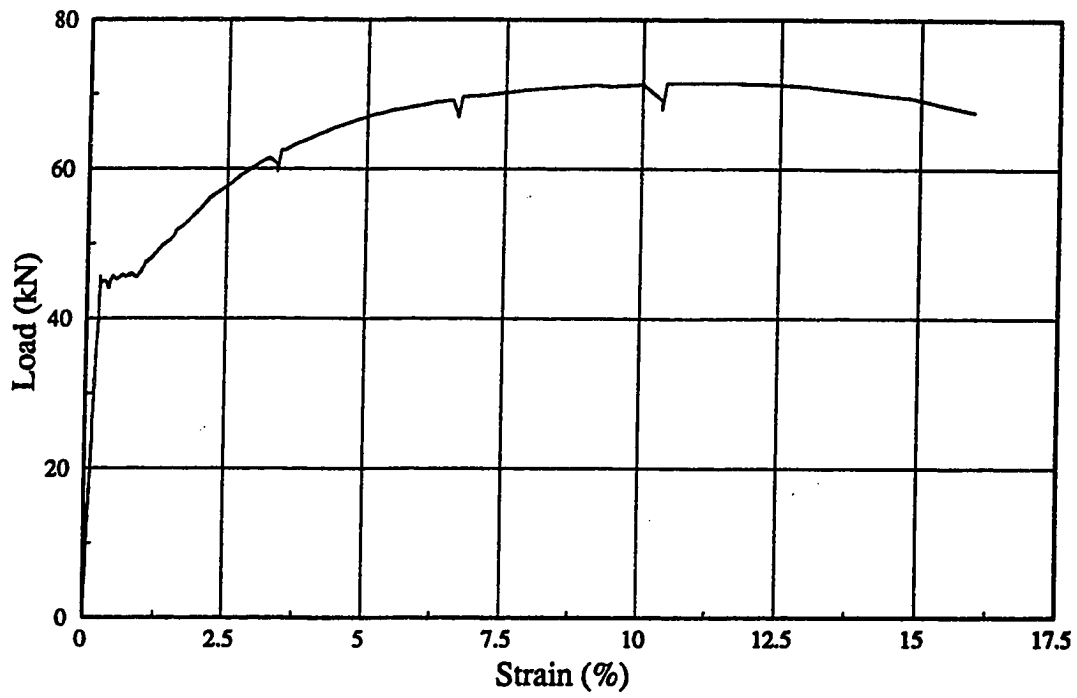


Figure 3.2 Typical Load vs. Strain for Steel Coupon Test

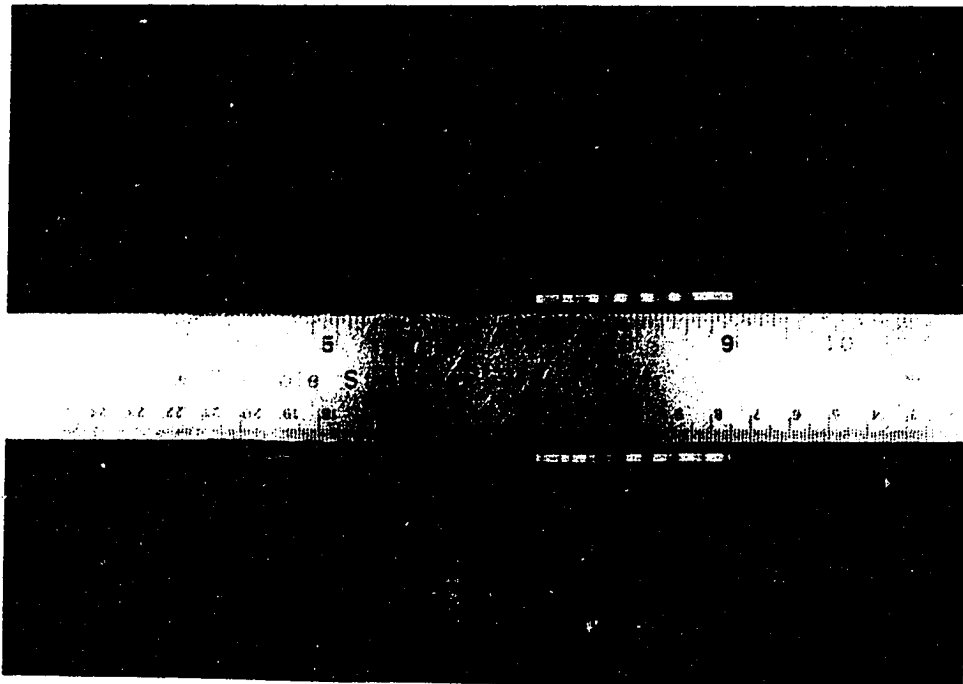


Figure 3.3 Photo of Steel Fiber

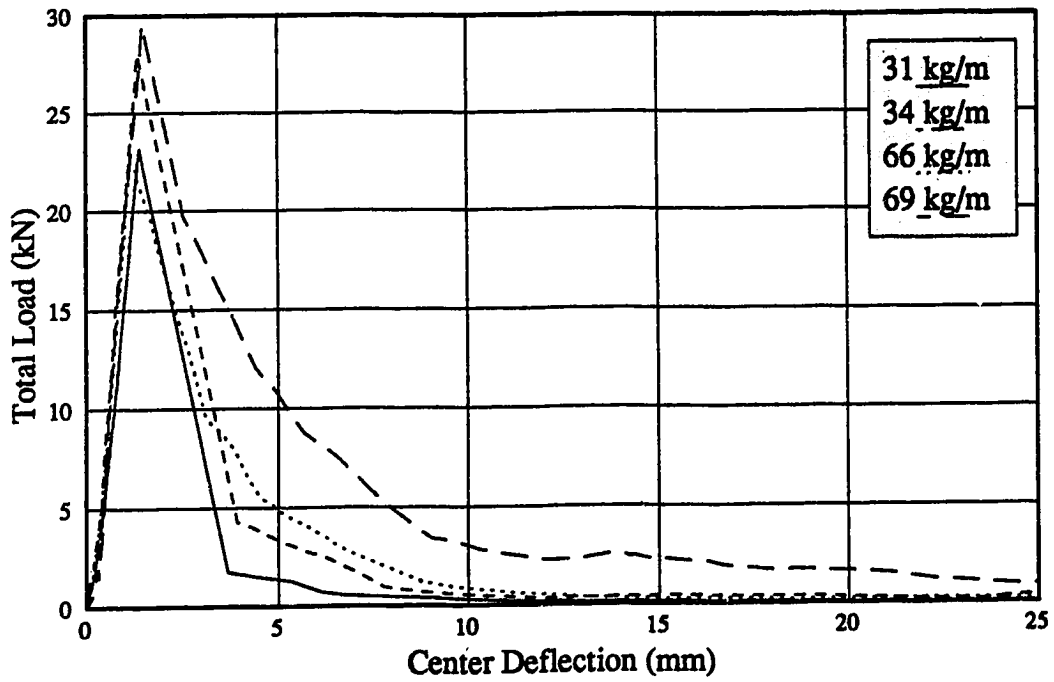
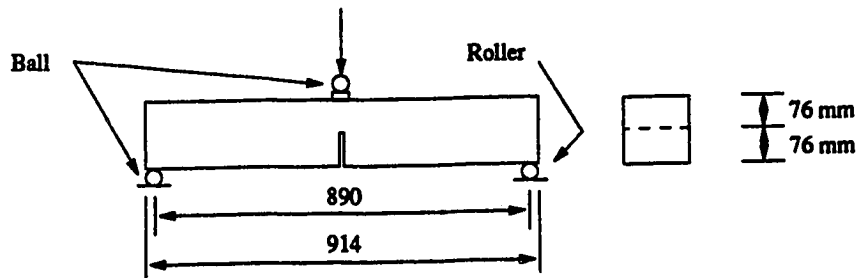
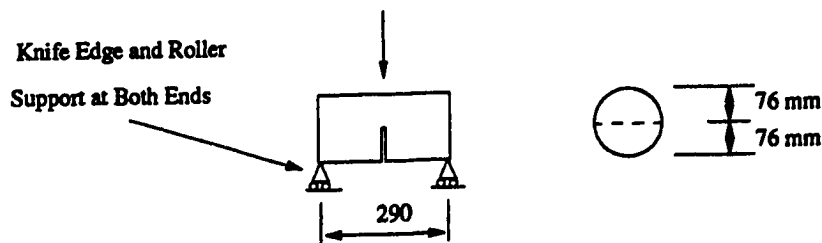


Figure 3.4 Load-Deflection of Fiber Reinforced Beams



Notched Beam Test



Notched Cylinder Test

Figure 3.5 Notched Beam and Cylinder Test Set-Ups

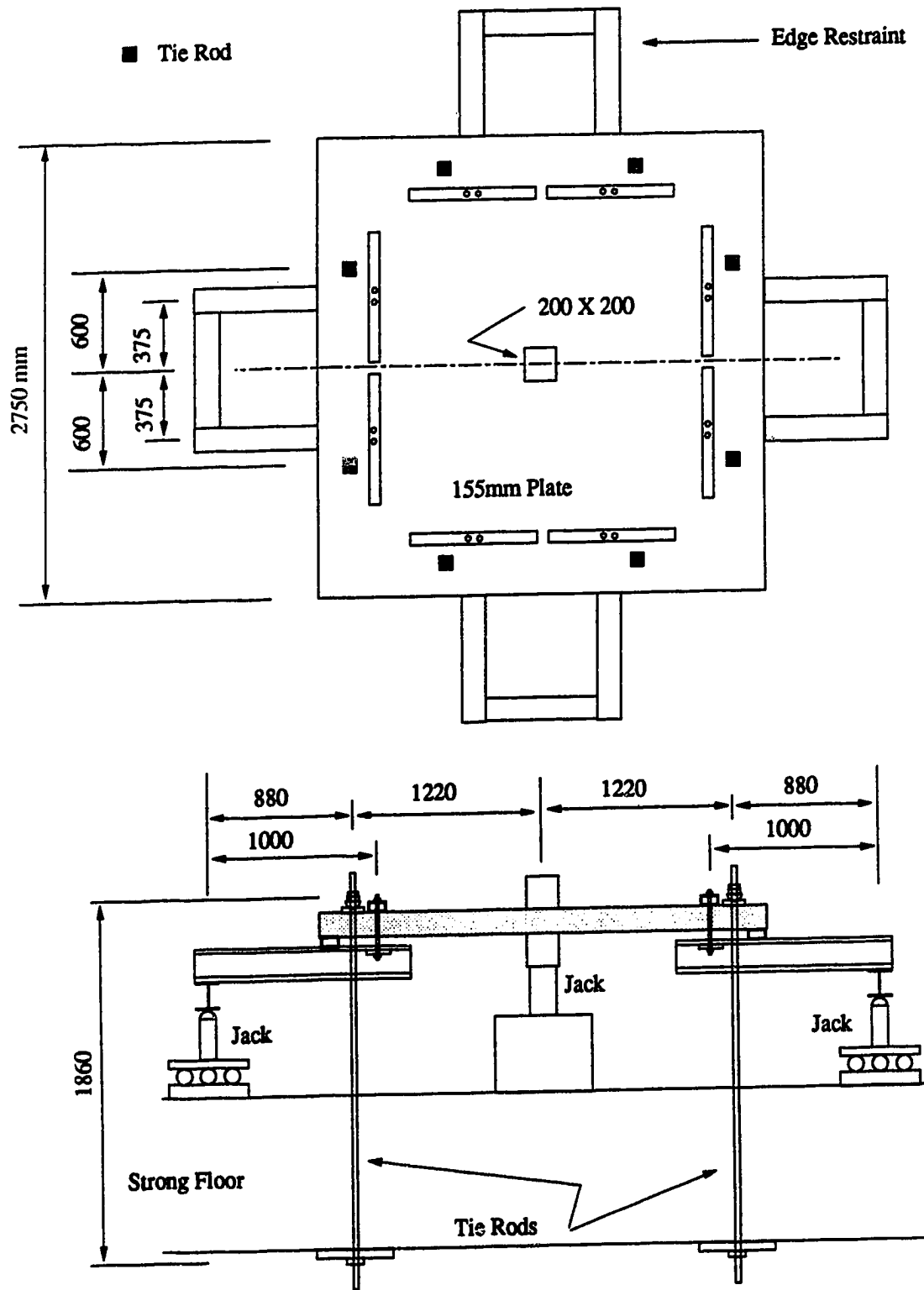


Figure 3.6 Standard Test Set-Up

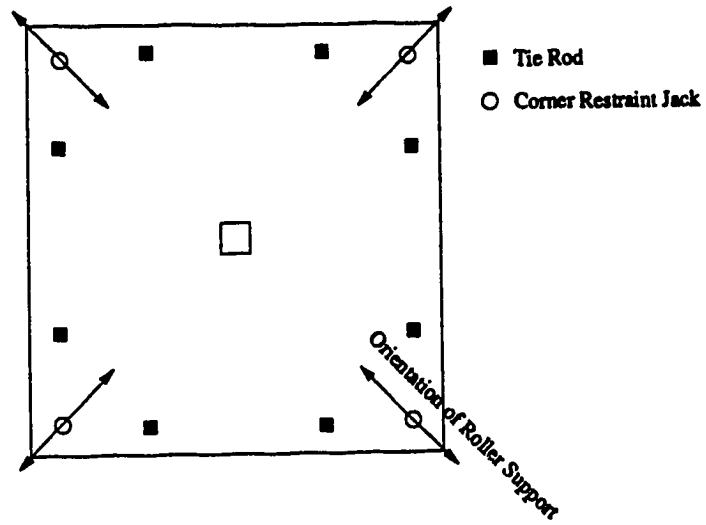


Figure 3.7 Plan View of P19RC

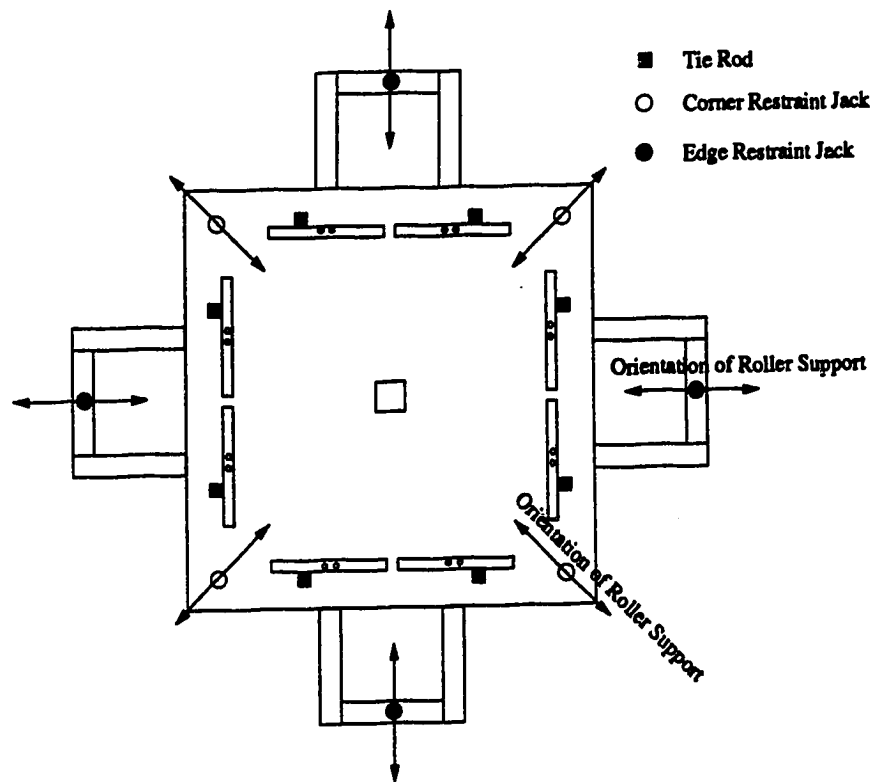


Figure 3.8 Plan View of P19RB

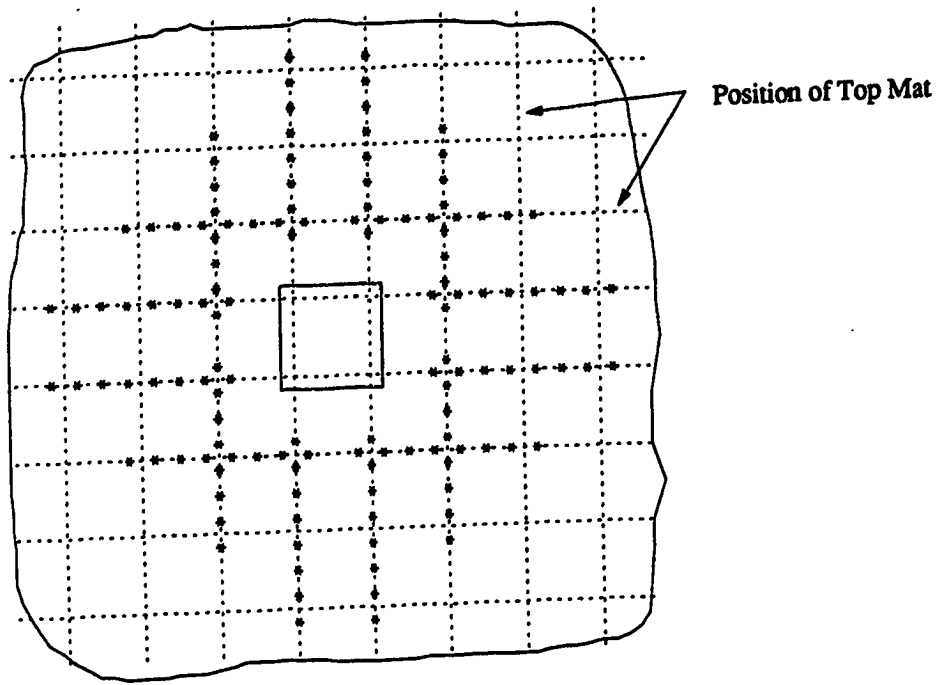


Figure 3.9 Top Demec Pattern

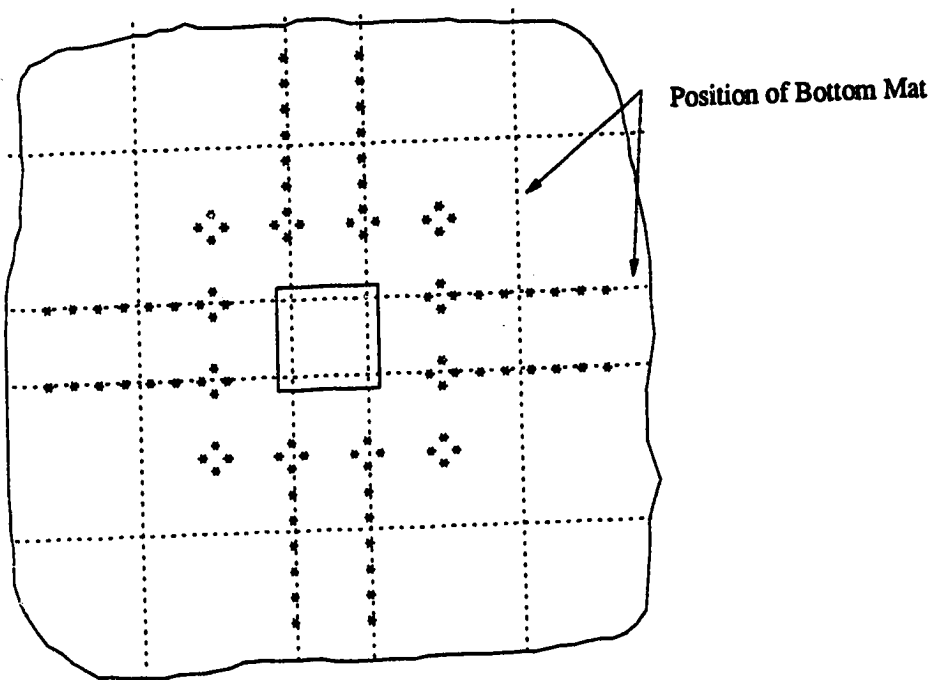


Figure 3.10 Bottom Demec Pattern

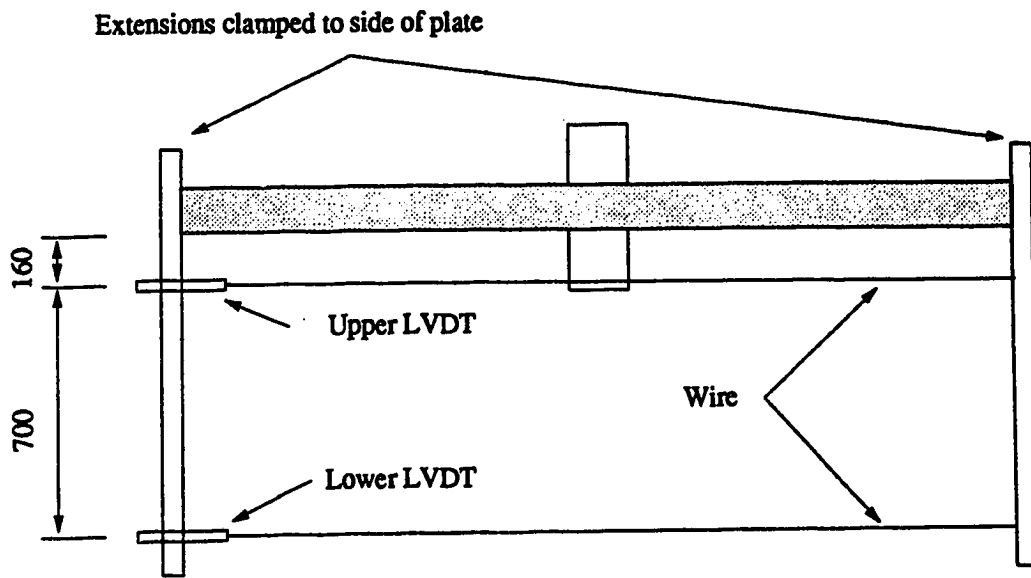


Figure 3.11 Edge Rotation and Expansion Measurements

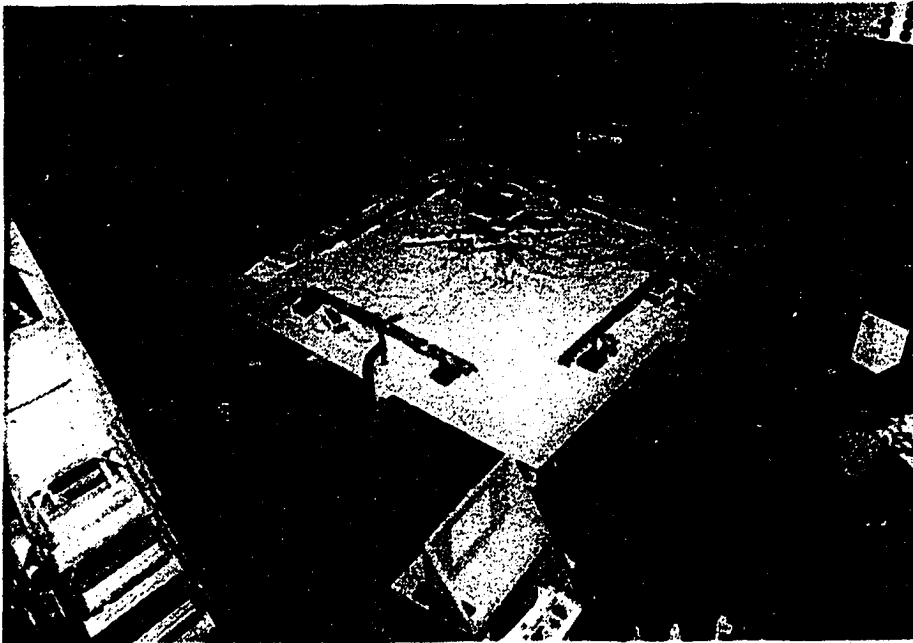


Figure 3.12 View of Test in Progress

Chapter 4

Observations and Evaluation

4.1 Flexural Behavior

The load-deflection diagram helps to identify changes in load carrying mechanisms within the specimens. Direct comparison with the load-deflection behavior of other tests in the literature is questionable because of differences in boundary conditions.

The load-deflection diagrams for all tests are given in Figures 4.1 to 4.5. For clarity, unloading and reloading sequences have been deleted from these plots. Complete load-deflection diagrams for each test are given in Appendix B. It should be noted that the deflection of the plates at the tie rod positions is not zero because of the elastic extension of the tie rods. This can be estimated based on the reported loads in Appendix B and the elastic stiffness of the rods. Values of the center load at first yielding of steel (P_y) and at ultimate (P_{ult}) are given in Table 4.1, as well as values of deflection corresponding to first yield and ultimate load.

Nearly all the tests exhibited three stages of behavior, marked by significant changes in the slope of the load-deflection curves. Stage I refers to uncracked behavior. Stage II initiates with cracking around the column perimeter and terminates with the formation of a folding mechanism within the plate. In stage III, the plate undergoes large plastic deformations as the yielded portion of each reinforcing bar lengthens. For these tests, the boundary between stage II and stage III was consistently at a deflection of about 20 mm. These stages are illustrated with the load-deflection diagrams shown in Figure 4.1.

The load-deflection behavior at the beginning of stage II is linear. At this point the specimen may be described as a cracked elastic plate. Toward the end of stage II, the slope of the load-deflection diagram decreases as the folding mechanism develops within the plate. Although this non-linear load-deflection behavior is mostly a result of yielding of the reinforcement, its onset does not always correlate well with first yielding of the reinforcement. For example, from Table 4.1, the deflection at first yield for specimen P19RE is 11.3 mm. However, the load-deflection behavior for this plate, shown in either Figure 4.1 or 4.5, does not show any significant loss of stiffness until a deflection of about 15 mm. In contrast to this, the deflection at first yield for specimen P19S50 is 18.9 mm while, from Figure 4.2, the apparent onset of non-linear load-deflection behavior in stage II is at about 17.5 mm. The inconsistent relationship between the beginning of non-linear load-deflection behavior in stage II and first yielding of the reinforcement is attributed partly to bond-slip of the reinforcement. This is discussed in Section 4.2.3.

The idealized folding pattern of the plates with standard edge restraint is illustrated in Figure 4.6. Although the extension arms were effective in restraining rotation about an axis parallel to the slab edge, any component of rotation about an axis perpendicular to the edge was comparatively unrestrained.

In Chapter 2 it is stated that the flexural capacity of a two-way plate as calculated by yield-line methods is routinely exceeded by test results. Membrane forces, boundary restraints and second order effects which allow the slab to act as a folded plate are most often cited as reasons for underestimating the flexural strength. In this investigation, little or no restraint was applied to the specimen in the plane of the slab by the loading apparatus. As a result, the significance of folded plate action in enhancing the flexural strength of each slab may be assessed.

Consider the diagram of one-half of a specimen, shown in Figure 4.7. At ultimate load axis A-A is at a negative yield-line, implying that all top steel crossing A-A is at yield. Assuming undeformed geometry, one can determine the flexural moment arm of the plate and hence calculate the total bending moment, M , distributed along axis A-A. The magnitude of the edge restraint load, ER , may be expressed as a factor, k , times the load on one tie rod, TR , with k determined from test measurements. Using the value of k at maximum load together with the previously computed value of M , a theoretical value for TR can be calculated by satisfying the rotational equilibrium of the half-plate about axis A-A. Using this value of TR and $ER = k \times TR$ the total load, P_{flex} , may be calculated.

$$P_{flex} = selfweight + \sum TR - \sum ER \quad [4.1]$$

At failure, all specimens carried load in excess of their calculated flexural capacities. In Figure 4.8, the ratio of the test load, P_{ult} , to the calculated load, P_{flex} is plotted against $(\delta + jd)/jd$, where δ is the center deflection and jd is the flexural moment arm of the plate. For specimens at ultimate load, not only does P_{ult}/P_{flex} vary linearly with $(\delta + jd)/jd$, but the constant of proportionality is very nearly unity.

The reason that P_{flex} consistently underestimates P_{ult} lies in the assumption of undeformed geometry in determining the flexural moment arm of the plate. In Figure 4.7, with two-way bending, if there is a plastic hinge along axis A-A, then there must also be a plastic hinge centered on axis B-B. The folding of the plate along axis B-B enhances the flexural moment arm for bending about axis A-A.

4.2 Strain Gauge Measurements

All top mat strain gauges were placed on either column bars or perimeter bars. The term **column bar** denotes any of the four reinforcing bars passing through the column at

a distance of 75 mm from the center-line of the plate. Perimeter bar refers to any of the four bars at 125 mm from the face of column (225 mm from plate center-line). There are seven geometrically distinct gauge locations on each top mat. On the column bar, gauges are located at 85 mm, 225 mm, 375 mm and 675 mm from the center-line of the plate. On the perimeter bar, gauges are located at 75 mm, 225 mm and 525 mm from the center-line of the plate. An additional eight strain gauges were installed on the bottom mat at the face of the column in the three specimens of the restraint series.

All data from strain gauges are presented as average bar forces. Measured strains were converted to bar forces on the basis of coupon tests of the reinforcing steel. After this conversion, values of bar force from geometrically similar gauge locations were averaged. Complete diagrams of average bar force data obtained from strain gauges are presented in Appendix C.

Some strain gauge circuits became non-functional during the course of every test. There are three main reasons for this. First, the strain at some gauge locations may exceed the limitations of the strain gauge adhesive. Second, the electrical leads may be sheared from the gauge as a result of slip of the reinforcing bar relative to the surrounding concrete. Third, cracking of the concrete may break the electrical leads. In order to exclude non-functioning gauges from averages, some judgement was required in deciding the load step at which any particular gauge ceased working. To assist in this, the output of a suspect gauge was compared to the output from gauges at geometrically similar locations within the same specimen.

The quality of strain gauge data varied between test series. Whereas almost all strain gauges in the S-series functioned up to failure of the specimen, with excellent agreement of readings between geometrically similar locations, the fiber reinforced specimens with 38 mm clear cover had a poor record of gauge survival and readings were more scattered. This is discussed further in Section 4.4.1.

4.2.1 Bar Force Profiles

A bar force profile is a diagram of the variation in force along the length of a reinforcing bar. Figures 4.9 and 4.10 show typical force profiles for the column bar and the perimeter bar at selected levels of load. The horizontal coordinate is the distance between the gauge and the center-line of the plate. For all diagrams, a bar force of zero is reported at distances from the center-line of 1000 mm for the perimeter bar and 1360 mm for the column bar. These locations correspond to the termination points of the bars.

Bar force profiles show the changes in the internal behavior of a specimen at various load levels. They are used to monitor the extent of yielding during a test and to determine where a bar is effectively anchored relative to the column. The slope of a force profile gives a measure of the intensity of average bond stresses along the reinforcement.

4.2.2 Force Gradients

As discussed in Chapter 2, a force gradient in the reinforcement is needed to carry shear by beam action. Therefore, the existence of a force gradient at a particular location may be viewed as at least affording the potential to carry shear by beam action. Similarly, the absence of a force gradient may be taken as definite proof that any shear at that location is the result of arching action.

Average force gradients in the perimeter and column bars are obtained by calculating the slope of the bar force profiles over the intervals between adjacent gauge locations. For each interval, the gauge locations closest to and farthest from the column are called respectively the upper and lower gauge locations. By including the termination points of the reinforcing bars as effective gauge locations (bar force = 0), four intervals for the column bar and three intervals for the perimeter bar may be defined. For each bar, the intervals are numbered, starting with the interval that is closest to the plate center-line, as shown in Figure 4.9. The value of the force gradient over each interval is plotted against the deflection at the center of the plate to produce a bar force gradient diagram. Bar force and force gradient diagrams for each test are provided in Figures C-13 to C-36. For reference, a load-deflection diagram is included in each figure.

The maximum value of force gradient recorded for a particular interval may be limited in one of three ways: (1) by yielding of the reinforcement at the upper gauge location, (2) by failure of the bond between the steel and the concrete or (3) by the internal mechanics of the plate. The first two limitations on force gradient result in the redistribution of load within the plate; the loss of one load carrying mechanism leads to the development of another. The third limitation is an outcome of load redistribution; the internal load carrying mechanism of a plate changes from one that requires a force gradient at a particular location to one which does not. All three limitations on force gradient are illustrated by the test results of specimen P11F0. Figures 4.11 and 4.13 show force gradient diagrams for the column and perimeter bars of specimen P11F0. Values of the bar force at the different gauge locations are plotted against deflection in Figures 4.12 and 4.14.

In Figure 4.13, the force gradient over the second interval of the perimeter bar reaches a maximum value of approximately 100 N/mm at a center deflection of about

22 mm. The upper and lower gauge locations for this interval are 225 mm and 525 mm from the center-line of the plate, respectively. Figure 4.17 shows that, for a deflection of about 22 mm, the bar force reaches yield (44 kN) at the upper gauge location, while at the lower gauge location, the bar force continues to increase. The gradient over this interval is limited by yielding of the reinforcing bar at the upper gauge location.

In Figure 4.11, the force gradient over the first interval of the column bar reaches a maximum value slightly greater than 100 N/mm at a deflection of about 12 mm. Between 12 mm and 16 mm of deflection, the force gradient drops off slightly. At about 16 mm of deflection, the force gradient begins to decline sharply. Figure 4.12 shows that at a center deflection of 12 mm, the average column bar force at a distance of 85 mm from the plate center-line is about 35 kN. The average bar force at this position does not reach yield until a deflection of about 18 mm, by which time the magnitude of the force gradient has dropped to about 75 N/mm. It is believed in this case that the force gradient is limited by bond of the reinforcement.

The force gradient over the second interval of the column bar, shown in Figure 4.11, is believed to illustrate the third type of limitation on force gradient. At a deflection of about 18 mm, the gradient peaks at a value of only 60 N/mm. This is well below the maximum value of 100 N/mm reached at other intervals on both the column and perimeter bars of specimen P11F0, suggesting that bond failure is probably not responsible for this comparatively low value of force gradient. However, a deflection of 18 mm corresponds with reaching first yield of the perimeter bar. The premature loss of force gradient in the column bar may have been caused by an increase in the amount of radial arching action, brought on by yielding of the perimeter bar.

4.2.3 Anchorage Failure

Anchorage failure can be viewed as a special case of bond failure. Bond strength imposes a limiting value to the maximum bar force gradient that can be sustained over any particular interval. An anchorage failure is the result of reaching the limiting value of force gradient at the end of the reinforcing bar. Therefore, the magnitudes of the bar force gradients over the third interval of the perimeter bar and the fourth interval of the column bar are compared to previously set maximum values in order to check for anchorage failure.

Consider the column bar force gradients for specimen P19S50, shown in Figure 4.15. The maximum value of force gradient over the third interval is approximately 47 N/mm, reached at a deflection of about 15 mm. The magnitude of force gradient over this interval is reasonably well maintained up to a center deflection of about 25 mm. This establishes a limiting bond capacity for the column bar. At ultimate load, the force gradient over the fourth interval reaches the limiting value established over the third interval, resulting in anchorage failure of the column bar.

It should be noted that for specimen P19S50, the bar located 125 mm from the plate center-line (50 mm adjacent to the column bar) was cut off at 1000 mm from the plate center-line. No strain measurements were made on this bar. However, if the strains measured on the column bar are reasonably close to the strains which might have been measured in the adjacent bar, then anchorage failure of this bar should be expected when the column bar force 675 mm from the plate center-line reaches about 15 kN.

Figure 4.16 shows that this occurs at a center deflection of about 20 mm, and that there is also a change in the slope of the load-deflection diagram at this point. It is considered that this reduction in the stiffness of the plate is due to partial anchorage failure of the reinforcement.

From the appearance of the bar force gradient diagrams, it would appear that anchorage failure may have played a part in determining the ultimate load of many of the specimens. In most cases, the cut-off perimeter bar is the most critical. Force gradients for the third interval of the perimeter bar of specimens P19S150, P11F31, P11F66 and P38F69, shown in Appendix C, appear to have reached previously established maximum values. In addition, values of force gradient suggest that anchorage failure was at least imminent in specimens P19RC and P19RE.

Specimen P19S75 is unique in that it is the only specimen with a reinforcing bar located on the line of symmetry of the plate, providing a crack initiator at the exact location of the fold line of the flexural mechanism. Observed cracking over this center-line bar appeared to be more severe than in other tests. It is felt that this cracking compromised the anchorage of the center-line bar, although this cannot be established by direct measurements because no strain gauges were mounted on this bar.

All specimens had what would be visually classified as punching failures, in that they had the classic, pyramid-shaped failure surface. None of the specimens gave any outward indication of anchorage failure in the form of a horizontal split which extended to the edge of the plate, or even to the end of the cut-off bars. This suggests that visual assessment after failure may not be a reliable way to detect anchorage failures.

4.2.4 Bottom Mat Strain Gauges

In the three specimens of the restraint series, P19RE, P19RC and P19RB, eight strain gauges were placed on the bottom mat of each specimen, just inside the column. The averaged output from these gauges, in the form of bar forces, is given in Figure 4.17, with negative sign indicating compression.

For each of the three specimens initially, the plate is uncracked and the bottom reinforcement at the column face is on the compression side of the neutral surface. The maximum compression force in the bottom reinforcement is reached at the first cracking load of the plate, about 100 kN. After cracking, the migration of the neutral surfaces downward results in tensile increments of strain. At an advanced stage, the bottom reinforcement lies above the neutral surface of the plate and is in tension. This stage corresponds to a load of about 250 kN in all three tests.

At this point, there is a divergence in behavior. Both specimens P19RC and P19RE show a marked reduction in bar force, which is particularly sudden in the case of P19RC. This probably signals extreme fiber crushing of the flexural compression block at the face of column.

In specimen P19RB, there was no evidence of concrete crushing. The gauges continued to read tension until failure, although the magnitude of that tension is significantly lower than was recorded in P19RE or P19RC. This is probably the result of the much reduced deflection of specimen P19RB.

4.3 Miscellaneous Observations

4.3.1 Cracking

V-shaped bond cracking, as shown in Figure 4.18, was observed in the specimens with an 11 mm clear cover. The appearance of these cracks coincided closely with reaching peak force gradients in the steel.

Photographs of specimen P19RE after testing (Figures 4.19 and 4.21) show typical crack patterns. The crack pattern on the top surface of the plate (Figure 4.19) clearly shows the dominant folding pattern of the specimen. The crack pattern on the slab soffit

(Figure 4.21) shows the effects of the edge restraint. Similar patterns were observed in all specimens except P19S75, P19S50 and P19RC. Figures 4.20 and 4.22 give the pattern of cracking for specimen P19RC. Specimens P19S75 and P19S50 did not have well developed crack patterns. As was noted in Section 4.2.3, while under load a relatively prominent crack opened on the center-line of specimen P19S75. After failure, this crack was not especially noticeable.

In some specimens, the inclined failure surface broke through the top surface of the plate in advance of failure. In the case of P19RE, upon the appearance of this crack (see Figure 4.23), all jacking was stopped. Over a period of 48 minutes, the center load fell gradually from its maximum value of 303 kN to 283 kN while the deflection was maintained.

4.3.2 Demec Data

Prior to taking a set of demec readings, all hydraulic valves were closed and the load was allowed to stabilize for a period of time between one or two hours. On some occasions, the specimen was left loaded overnight and demec readings were taken first thing in the morning. A full set of readings took about one hour to complete.

Results from demec readings are presented in the form of average bar force profiles at various levels of load (see Appendix D). Bar force peaks correspond very closely to the positions of crossing reinforcing bars, indicating that the transverse steel acts as a crack initiator. Dips in bar force between peaks are attributed to in-and-out bond.

The average results for concrete strains at eight positions close to the column on the compression side of the plate are summarized in Figure 4.24, which shows that the ratio of circumferential to radial strain generally increases as each test progresses. At ultimate, radial concrete compression strains were between 20 and 50 per cent of the circumferen-

tial strain at the same location. The increasing ratio of circumferential to radial compressive strain is consistent with increasing radial arching action in conjunction with circumferential beam action.

4.3.3 Overall Expansion

Results from edge mounted LVDT's are presented in Appendix B. All results confirm an overall radial expansion of the plate, which is consistent with the kinematic requirements for the formation of a punching failure surface. However, the expansion is consistently linear with center deflection, suggesting that the formation of a diagonal rupture surface within the plate is a gradual rather than sudden process.

In general, there is no significant expansion of the bottom surface. There is considerable expansion at the top surface, in the order of 4 mm of expansion across the full width of the plate for every 30 mm of deflection. Restraint of this expansion could result in significant increases in strength.

4.4 Effects of Test Variables

4.4.1 Effect of Steel Placement

From Figures 4.3 and 4.4, it can be seen that for any comparable level of fiber content, the specimen with a clear cover of 38 mm had a greater ultimate deflection. All specimens with a clear cover of 38 mm showed greater stage III strength gains than those with 11 mm clear cover. In the case of plate P38F0, the post-yielding strength gain was sufficient to overcome the difference in load at the beginning of stage III between plates P38F0 and P11F0. In stages I and II, the structural stiffness depends upon the flexural

depth of the plate. As a result, the specimens with a clear cover of 11 mm and a flexural depth of 132 mm carried higher loads at stage III than did the specimens with a clear cover of 38 mm and a flexural depth of 105 mm.

Figure 4.1 shows that the load-deflection diagrams for specimens P19S150 and P11F0 are virtually identical, despite the differences in flexural depth. Increased flexibility of the bond-slip relationship resulting from bond cracking, as discussed in Section 4.3.1, is considered responsible for reducing the stiffness of specimen P11F0 relative to specimen P19S150.

Specimen P38F0 failed at a load which was 3 per cent higher than specimen P11F0. The straight-line truss model predicts an increase in strength of 37 per cent, clearly indicating that the effect of flexural depth has not been adequately accounted for. However, it should be pointed out that the Canadian and American codes predict a drop in strength of 27 per cent.

For stages I and II, the load-deflection behavior of the specimens of the spacing series, shown in Figure 4.2, is similar to that of the other specimens. Both plates P19S75 and P19S50 show almost no stage III behavior. In contrast, plate P19S150 shows considerable ductility, with enough plastic strength gain to match the ultimate load of specimen P19S75.

As shown in Figures C-8 and C-9, the peak load of the perimeter bar in specimens P19S75 and P19S50 is consistently greater than the peak load in the column bar. This effect is particularly noticeable for specimen P19S50. Figure C-48 shows first yielding of the perimeter bar at a deflection of about 20 mm; Figure C-46 (also 4.16) shows first yielding of the column bar at a deflection of about 30 mm. A similar observation for slab-column specimens with concentrated reinforcement is made in Elstner and Hognestad (1956). As the concentration of reinforcement increases, the amount of con-

crete available to bond an individual bar decreases. The reduced straining of the column bars is believed to be the result of a reduced stiffness in the bonding of the reinforcement and may also be linked to the anchorage of the column bars, discussed in Section 4.2.3.

In general, the strain gauges for the fiber reinforced specimens with a clear cover of 38 mm did not perform as well as did those for the specimens with a clear cover of 11 mm. One reason for this may be that because a larger cover requires a greater length of lead wire to be embedded in the concrete, there is an increased probability that a crack will sever the electrical connection. A second plausible reason is that the specimens with a clear cover of 38 mm deformed in a way that was more likely to shear the electrical leads from the gauges. Bar force profiles for the 11 mm and 38 mm clear cover series, shown in Figures C-1 through C-6, show that, despite larger deflections, there is consistently less straining over the fourth interval of the column bar in the specimens with a clear cover of 38 mm than is the case in the comparable specimens with a clear cover of 11 mm. For the specimens with a clear cover of 11 mm, curvatures are spread throughout the plate while in the specimens with a clear cover of 38 mm, the curvatures are more concentrated in the vicinity of the column.

4.4.2 Effect of Fibers

In both stages I and II, structural stiffness increased with the fiber content. Evidence of increased stiffness can be seen in Figures 4.3 and 4.4. At the beginning of stage III, at about 20 mm of deflection, the fiber reinforced specimens carried from 20 to 30 per cent more load than the specimens without fiber reinforcement. The additional strength and stiffness at smaller deformations is attributed to the ability of the fiber reinforcement to bridge small cracks, effectively increasing the level of reinforcement.

Deflections at failure increased significantly with fiber content. This is attributed to the ability of the fiber reinforced specimens to sustain large rotations in the concrete compression blocks. Figure 4.8 shows that the increased ultimate deflection of the fiber reinforced specimens is sufficient to explain their higher failure loads. This suggests that at very large deflections, only the conventional reinforcement was able to bridge the cracks at the plastic hinges of the fiber reinforced plates. At ultimate load, the steel fibers did not contribute significantly to the moment capacity at a yield-line.

The nature of failure was changed with the addition of fibers. With the exception of specimen P38F69, the fiber reinforced specimens had reasonably stable unloading curves during failure. The specimens split apart gradually as the load fell off. Specimen P38F69 had a sudden failure, as is usually associated with punching.

Although most plates showed some evidence of spalling of concrete at the face of the column prior to punching failure, the failure surface of the specimens without fiber reinforcement closely followed the outline of the column, as shown in Figure 4.25. In contrast, the failure surface on the compression side of the slab of the fiber reinforced specimens did not follow the outline of the column, but broke through the soffit of the slab at some distance from the column following no particular pattern, as shown in Figure 4.26.

4.4.3 Effect of Boundary Restraint

Specimen P19RE was similar to specimen P19S150, providing some basis for comparing the results of the three restraint series tests with those of the other nine tests. Both specimens P19RE and P19S150 were tested under the same relative magnitudes of edge restraint and tie rod loads. The reinforcement spacing and flexural depth of the plates are

equal. Concrete properties differ because the specimens were cast from different batches. The major difference between the two plates was that specimen P19RE had an additional two reinforcing bars each way at the outer edge of the top mat.

As shown in Figure 4.1, although the load-deflection diagram for specimen P19RE is consistently higher than that for specimen P19S150, the main changes in the slope of the load-deflection diagrams occur at roughly the same value of deflection. In addition, the perimeter bar force gradient diagrams for these two tests, shown in Figures C-39 and C-51, are strikingly similar. Although the peak magnitudes of the gradients are slightly higher for specimen P19RE, both figures show that the peak values of gradient are reached at the same values of deflection.

There are a few differences between the column bar force gradient diagrams of specimens P19S150 and P19RE, shown in Figures C-37 and C-49. The gradient over the first interval of the column bar in specimen P19S150 reaches a smaller peak value at a smaller deflection than is the case for specimen P19RE. This suggests that a shift to radial arching action may have occurred earlier for specimen P19S150 than for specimen P19RE. From the bar force diagrams in Figures C-38 and C-50 it can be seen that yielding spread farther from the column in specimen P19S150 than in specimen P19RE. In particular, the column bar force at a distance of 675 mm from the plate center-line reaches yield in specimen P19S150 whereas it reaches about 75 per cent of yield in specimen P19RE. This additional yielding accounts for the observed differences between the two specimens in the gradients over the third and fourth intervals of the column bar. Both the earlier shift to arching action and the additional spread of yielding are attributed to a lower bond strength resulting from the lower concrete strength of specimen P19S150. Despite their differences, it is felt that the similarities between specimens P19S150 and P19RE demonstrate that the trends observed in the restraint series are generally appli-

cable to the other nine tests.

Although the boundary conditions for specimens P19RE and P19RC were quite different, their load-deflection diagrams are almost identical. Still, perimeter bar force gradient diagrams in Figures C-51 and C-55 suggest that there may be differences in the internal load carrying mechanisms. The gradient over the first interval of the perimeter bar appears to play a more prominent role in the behavior of specimen P19RC than specimen P19RE. Both gradients reach peak values at a deflection of about 6 mm. In the case of specimen P19RE, the magnitude of the gradient steadily declines from this point on. In the case of specimen P19RC, this first peak value is a local maximum only. A second peak value is reached at a deflection of about 14 mm. At a deflection of 20 mm, the magnitude of the gradient for specimen P19RE is only 20 N/mm whereas the value for specimen P19RC is still about 80 N/mm.

4.5 Evaluation of Straight-Line Truss Model

On the basis of the straight-line truss model, the length over which the force in the reinforcement decreases should correspond to the intersection of the compression strut with the reinforcement. Therefore, the force profile of a bar that passes through the column should reveal the position of one end of the compression strut.

The assumed geometry of a straight-line compression strut is shown in Figure 4.27. The strut acts as a straight-line compression member, with one end at the center of the flexural compression block at the face of the column and the other end at the level of the top mat reinforcement, a distance r_c from the face of the column. The distances r_i and r_o from the face of the column mark the length over which the bar force is expected to decline to zero.

Consistent with the assumptions of the truss model, test values of $\tan \alpha$ were calculated as the ratio of final central column load to the force of the strut steel, A_{st} , acting at yield. Based on this value of $\tan \alpha$, the dimension r_s is calculated.

$$r_s = d / \tan \alpha \quad [4.2]$$

The distances r_i and r_o are estimated on the basis of column bar force profiles.

Consider, for example, the bar force profiles for specimen P11F0, shown in Figure 4.10. At a load of 230 kN (90% of ultimate), yielding of the column bar has spread to at least 375 mm from the plate center-line, or 275 mm from the column face. This places a minimum value on r_i of 275 mm. The value of r_o is not as well defined as that of r_i . From Figure 4.10, it appears that the smallest distance between the center-line of the plate and the far end of the strut is about 1000 mm. This corresponds to a value of 900 mm for r_o .

Bar force profiles for all specimens are provided in Figures C-1 to C-12. Values of r_o , r_i and r_s are listed in Table 4.2. Values of r_o and r_i for specimen P38F34 are not given because too many strain gauges failed during the test.

The results listed in Table 4.2 do not support the straight-line truss model. Except for specimens P19S75 and P19S50, values of r_i are consistently greater than r_s , whereas the straight-line compression strut, as shown in Figure 4.10, requires that r_i be less than r_s .

The bar force profiles do not display the post-yielding behavior that was originally expected with the straight-line strut idealization. Figure 4.10 shows bar force profiles for specimen P19RB. Since this specimen was the most heavily restrained, it was expected to show most clearly the effects of redistribution. At a load of 267 kN (78% of ultimate), r_i and r_o are approximately 125 mm and 700 mm, respectively. As the load increases to 324 kN (94% of ultimate) the values of r_i and r_o increase to about 275 mm and 900 mm,

respectively. Under the assumptions of the straight-line truss model, an increase in both r_i and r_o must lead to a decrease in the strut angle, α . However, a decrease in α is not consistent with an increase in load.

Combining the corner and edge restraints increased both the stiffness and ultimate load of specimen P19RB. The straight-line truss model, however, predicts an increased load with increased boundary restraint only if the boundary restraint includes compression forces in the plane of the slab. The model predicts no beneficial effect for rotational restraint alone. Therefore, the increased strength of specimen P19RB is not in agreement with predicted behavior based on the straight-line truss model.

It is concluded on the basis of measured bar force profiles that the straight-line idealization of the concrete compression fan is not adequate. In Chapter 5, a modification of the truss model is proposed which is in better agreement with the test data of this investigation.

Table 4.1 Experimental Load-Deflection Data

Test	Self Weight (kN)	P_y (kN)	δ_y (mm)	P_{ult} (kN)	δ_{ult} (mm)
P11F0	35.7	165	13.5	257	48
P11F31	36.6	193	11.2	324	69
P11F66	37.4	210	13.0	345	75
P38F0	35.2	147	14.1	264	62
P38F34	36.8	174	14.5	308	85
P38F69	36.9	184	14.9	330	93
P19S150	35.7	155	12.5	258	49
P19S75	36.2	202	15.8	258	27
P19S50	35.0	268	18.9	319	29
P19RE	35.7	173	11.3	304	50
P19RC	27.3	177	11.9	282	44
P19RB	35.8	242	14.6	343	37

Table 4.2 Geometry of Straight-Line Truss Model

Test	N_{st}	A_{st} (mm ²)	P_{ult} (kN)	$\tan \alpha$	r_e (mm)	r_i (mm)	r_o (mm)
P11F0	8.6	860	257	0.682	198	275	900
P11F31	8.6	860	324	0.860	157	400	1275
P11F66	8.6	860	345	0.916	147	400	1275
P38F0	8	800	264	0.753	139	275	600
P38F34	8	800	308	0.879	119	125	575
P38F69	8	800	330	0.942	111	125	600
P19S150	8	800	258	0.736	170	400	1275
P19S75	16.8	1680	258	0.351	356	0	1275
P19S50	25.6	2560	319	0.283	442	0	1275
P19RE	8	800	304	0.878	142	275	1275
P19RC	8	800	282	0.804	155	275	1275
P19RB	8	800	343	0.979	128	275	900

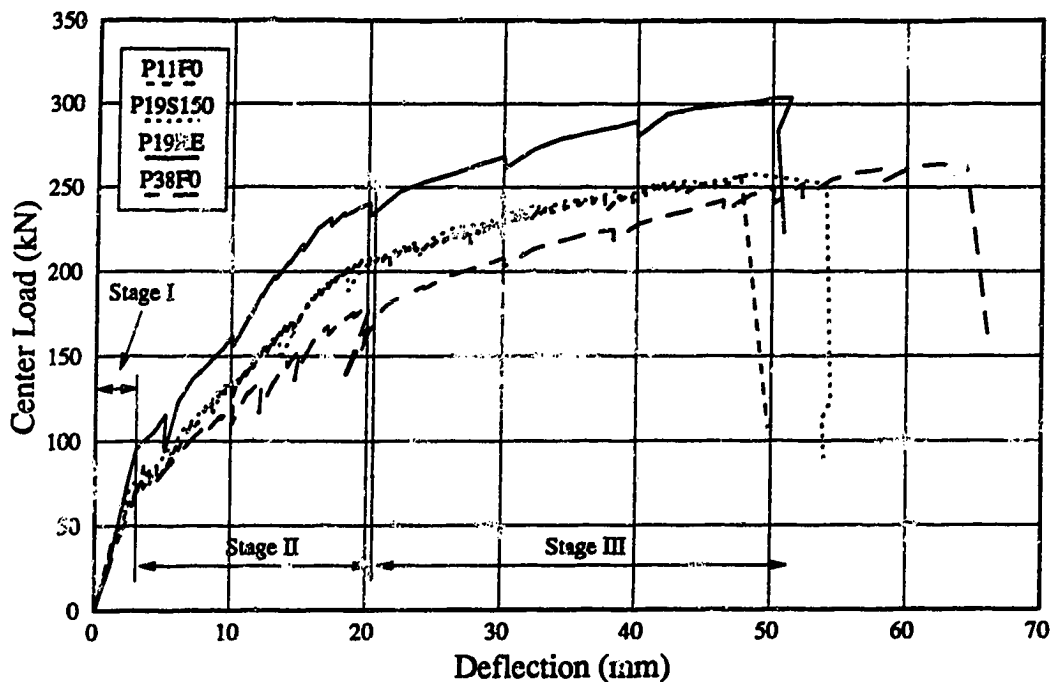


Figure 4.1 Load-Deflection: Variable Clear Cover

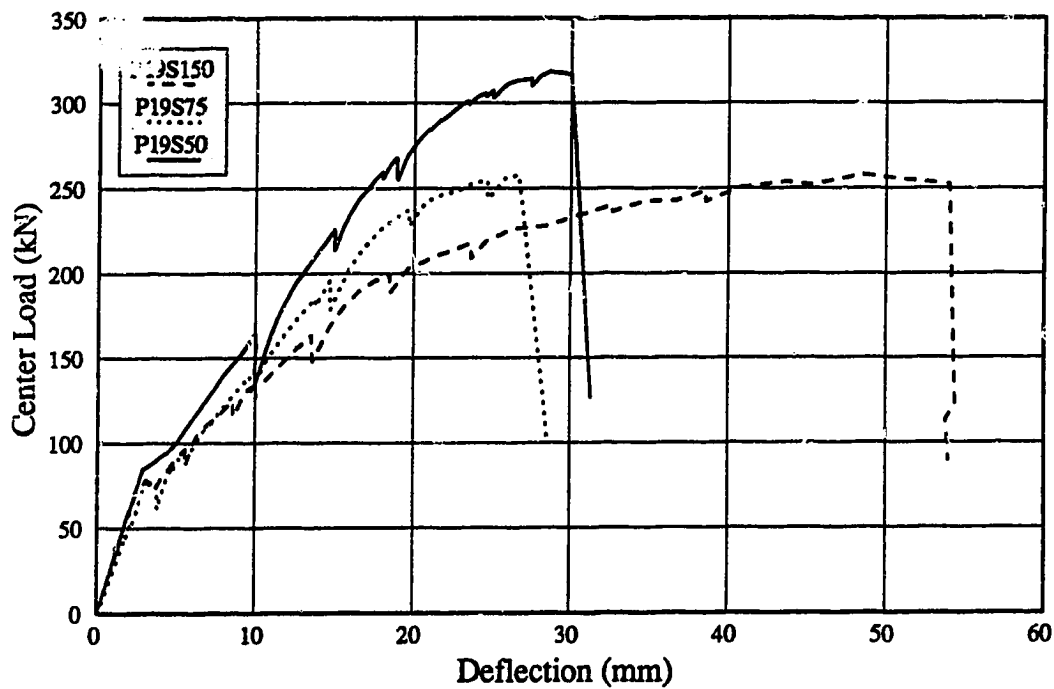


Figure 4.2 Load-Deflection: Variable Spacing

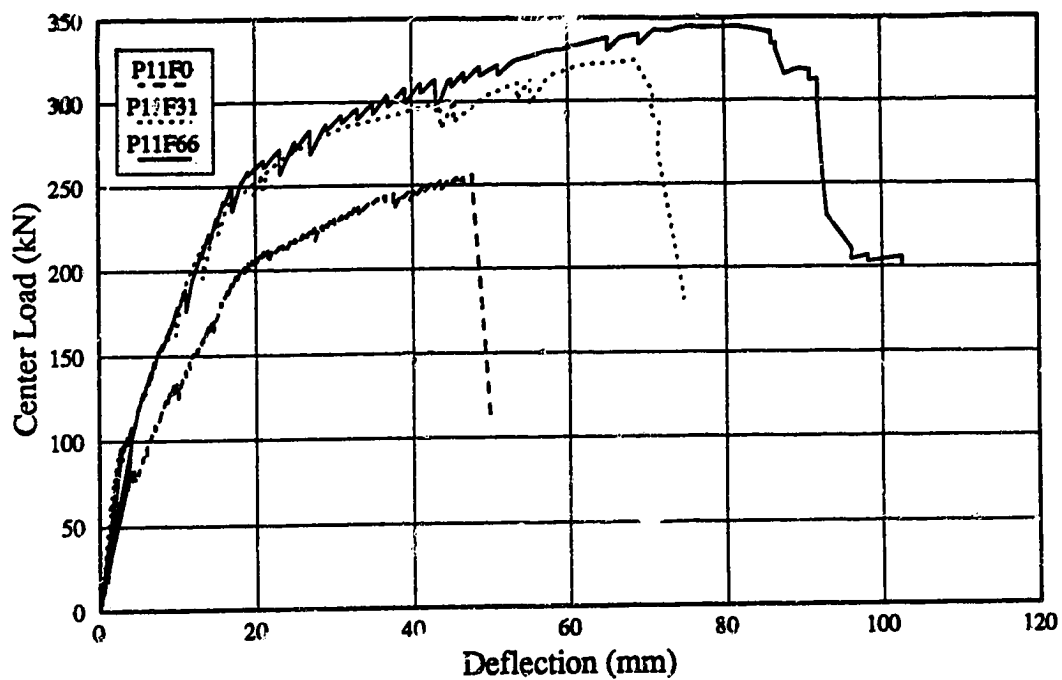


Figure 4.3 Load-Deflection: Specimens with 11 mm Clear Cover

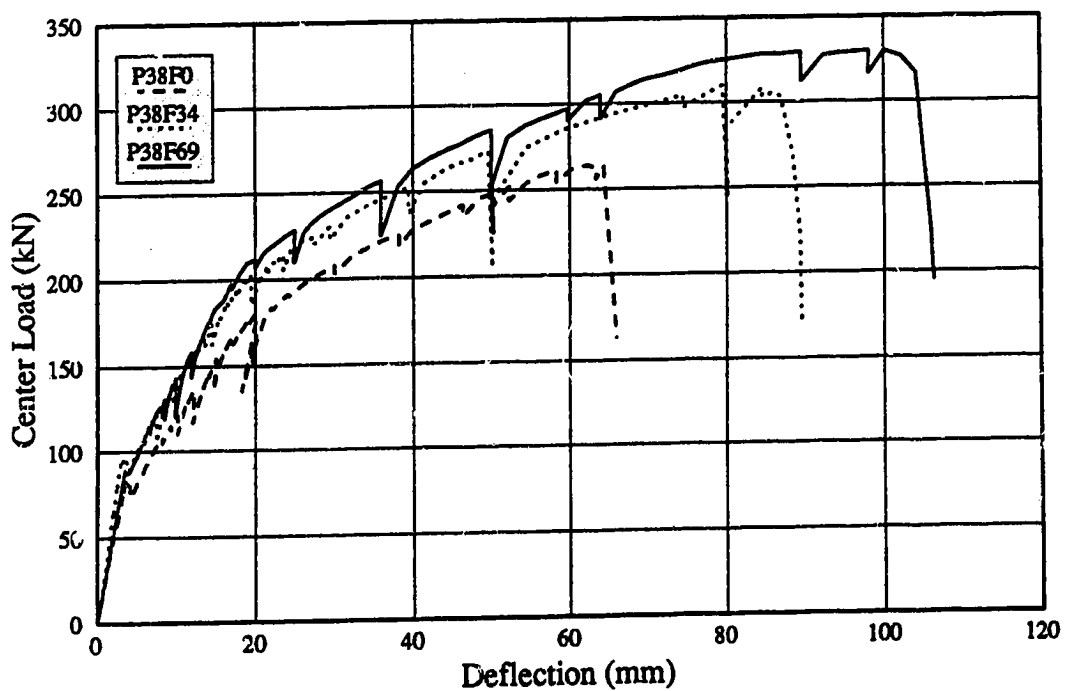


Figure 4.4 Load-Deflection: Specimens with 38 mm Clear Cover

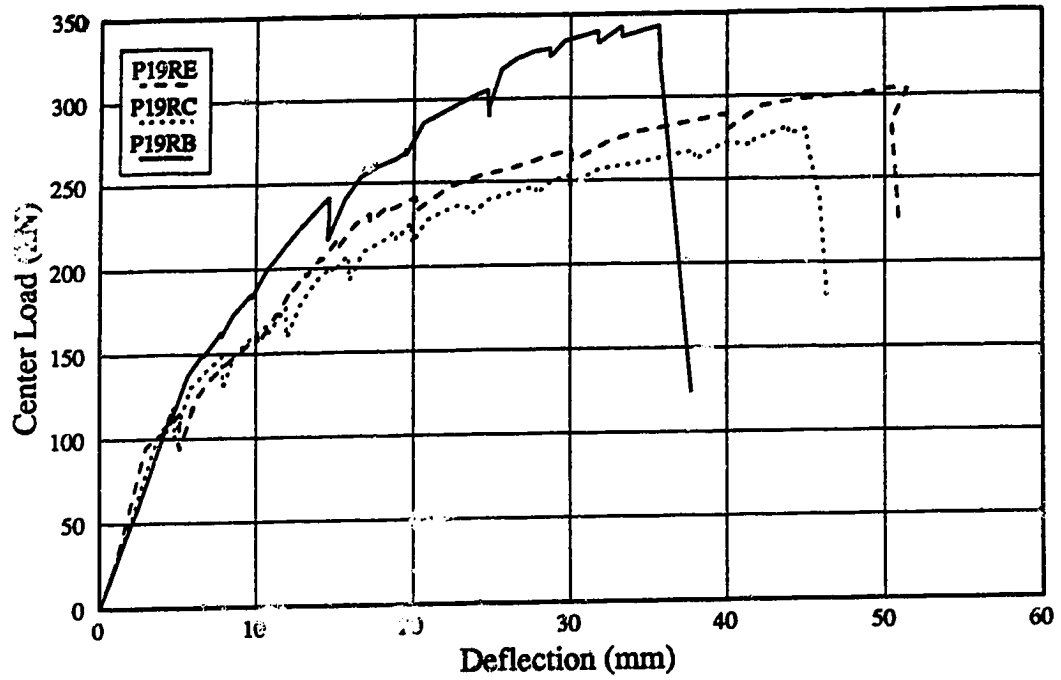


Figure 4.5 Load-Deflection: Variable Edge Restraint

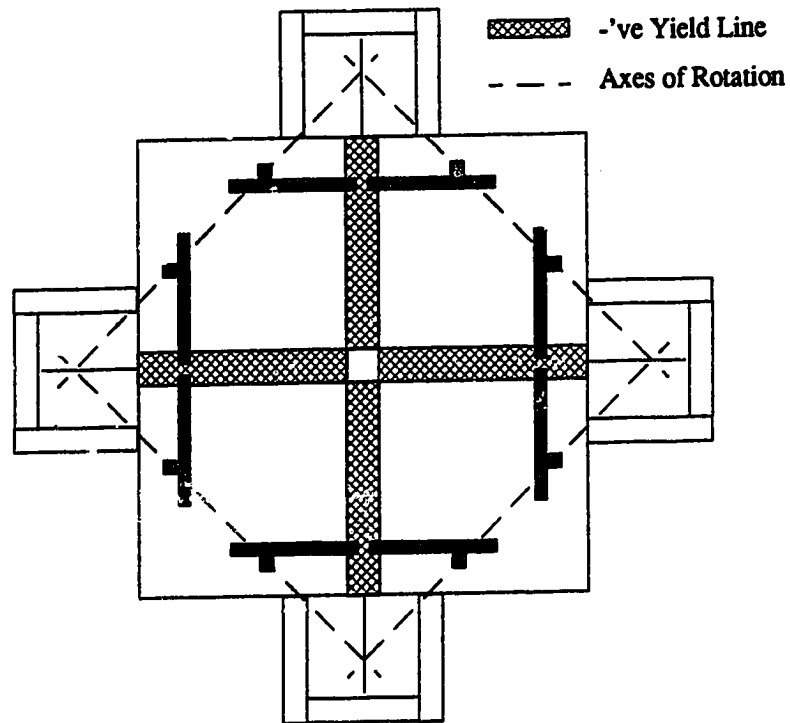


Figure 4.6 Idealized Folding Pattern of Plate

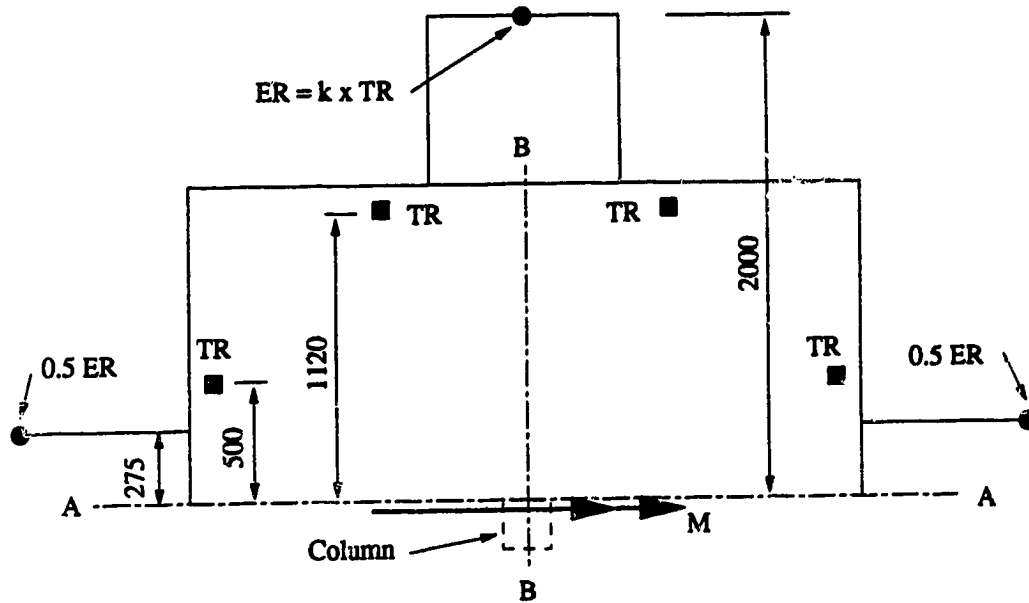


Figure 4.7 Diagram of Half Plate

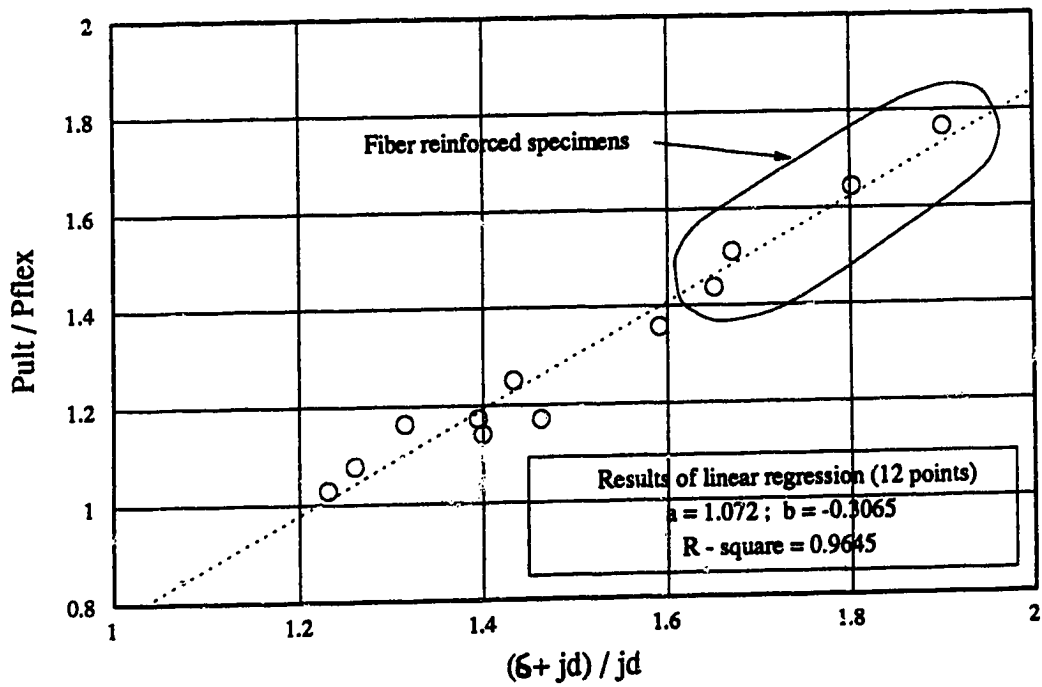


Figure 4.8 Flexural Performance

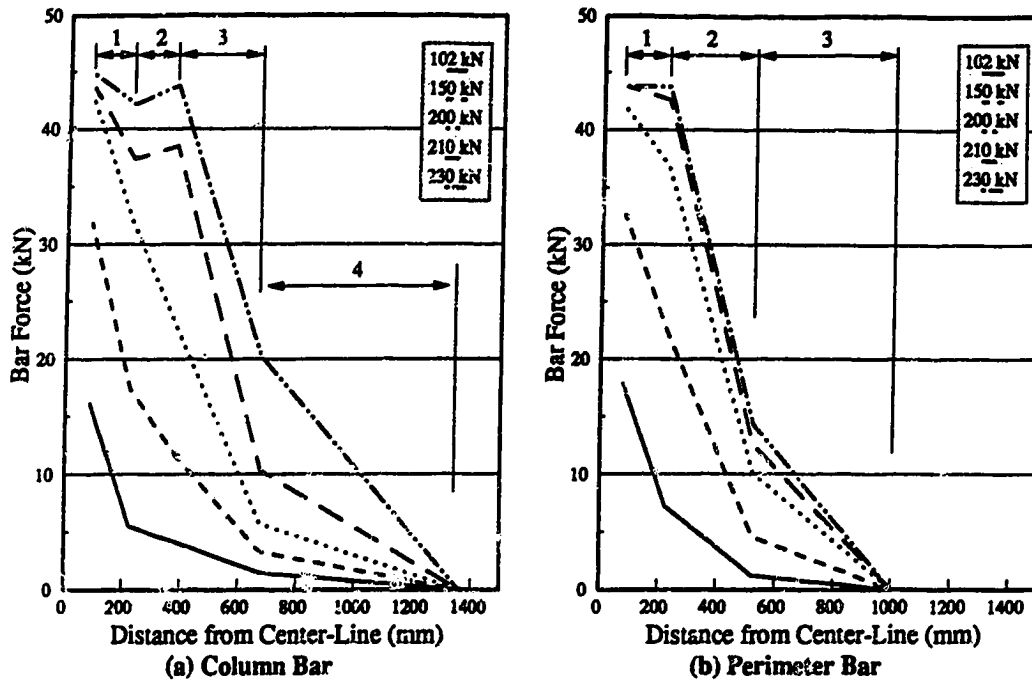


Figure 4.9 Bar Force Profile: P11F0

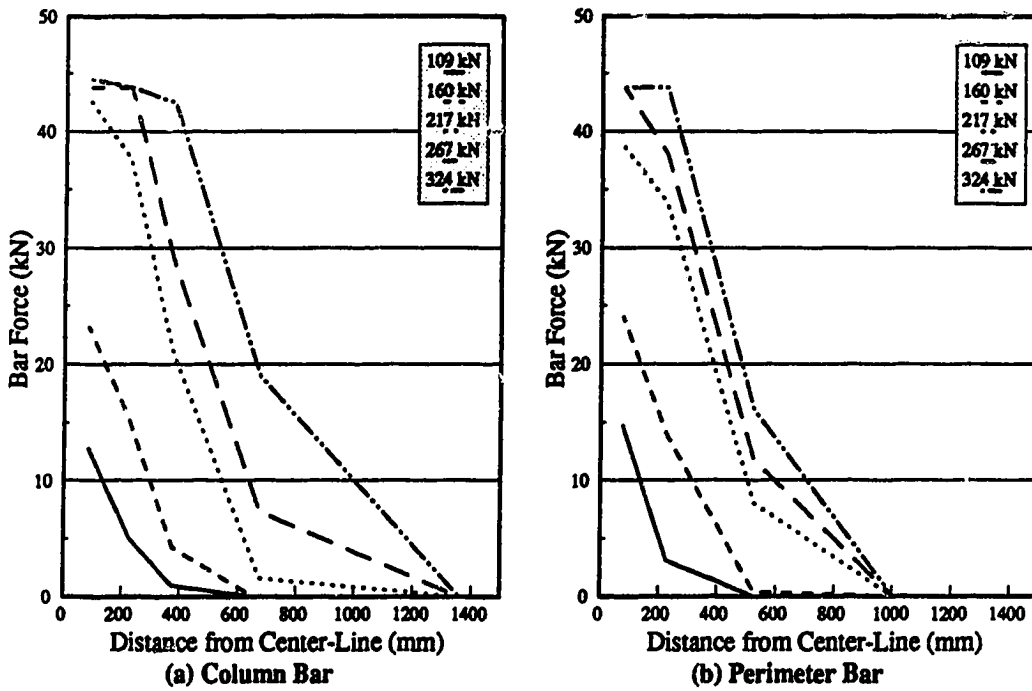


Figure 4.10 Bar Force Profile: P19RB

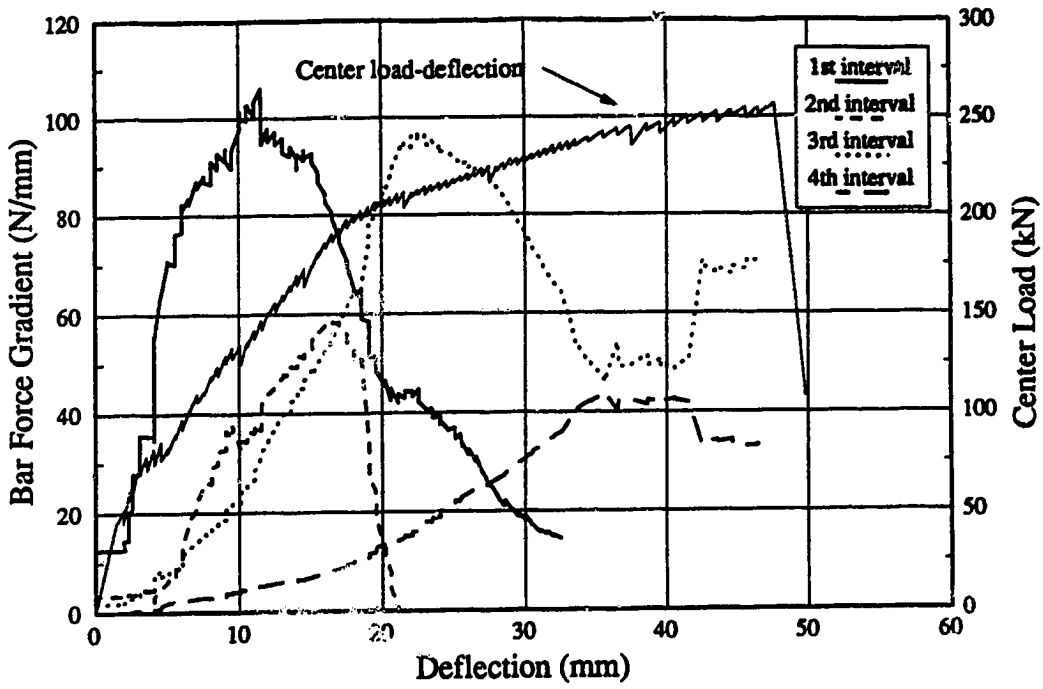


Figure 4.11 Column Bar Force Gradients: P11F0

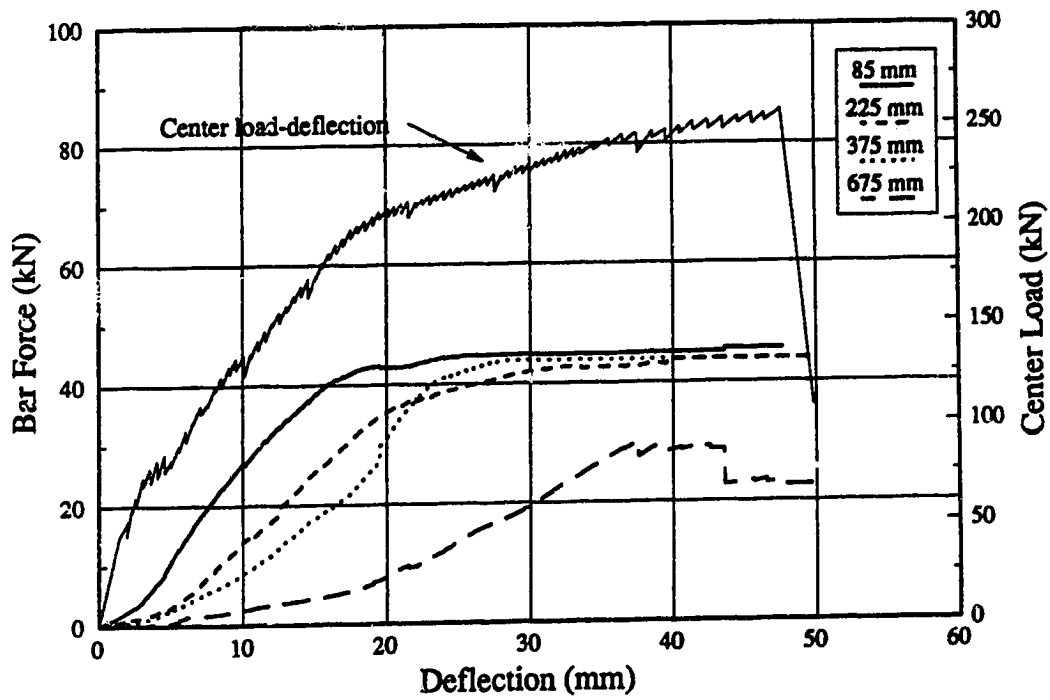


Figure 4.12 Column Bar Forces: P11F0

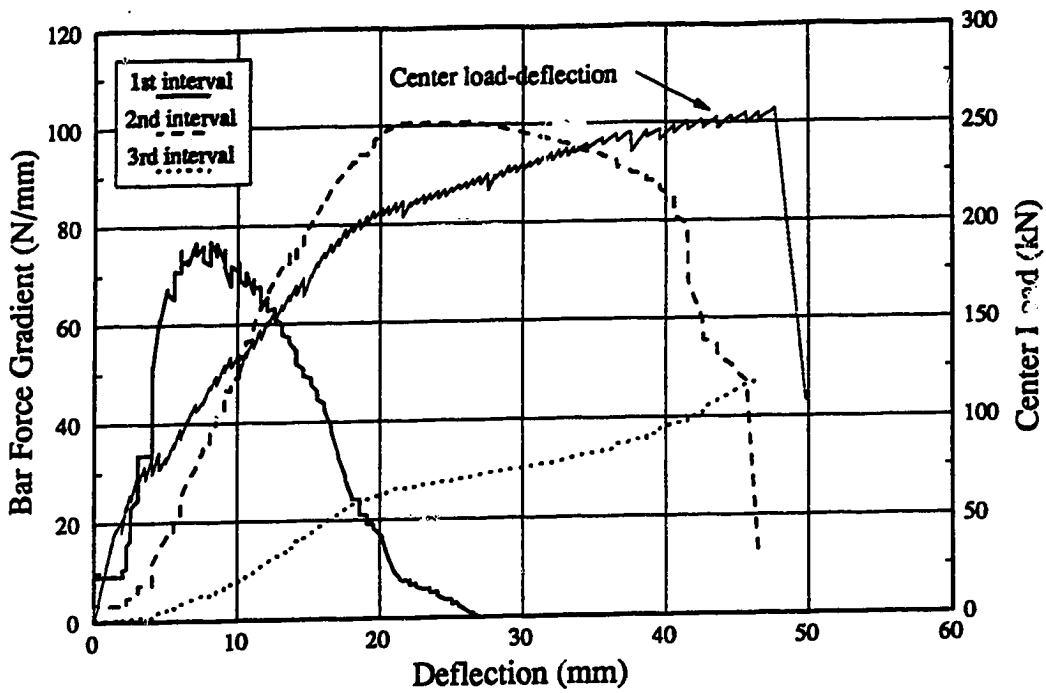


Figure 4.13 Perimeter Bar Force Gradients: P11F0

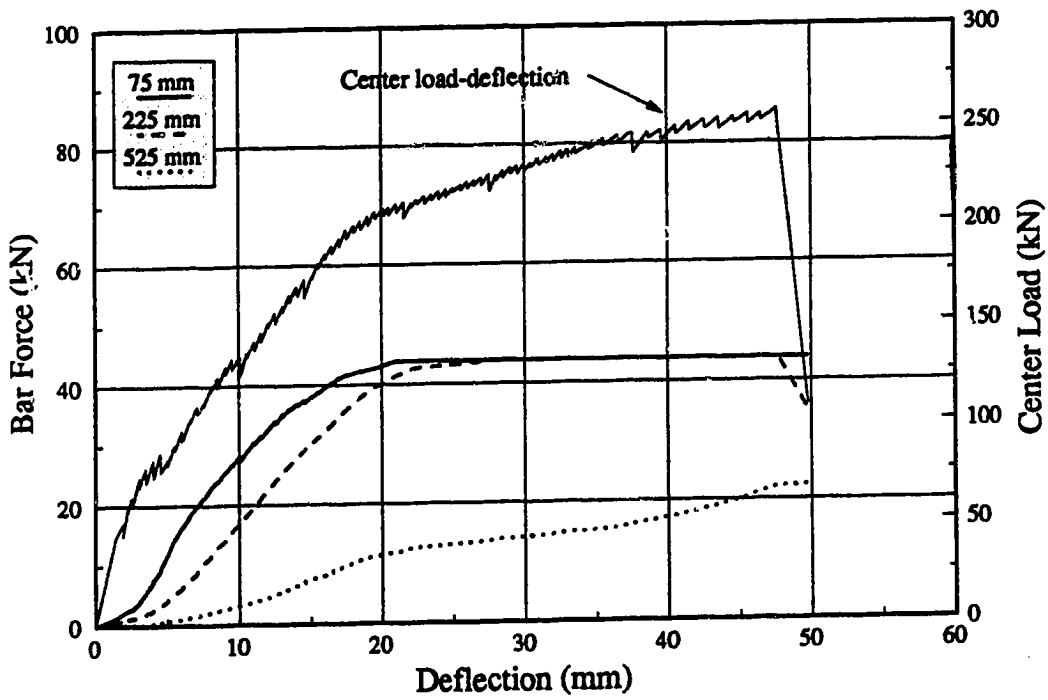


Figure 4.14 Perimeter Bar Forces: P11F0

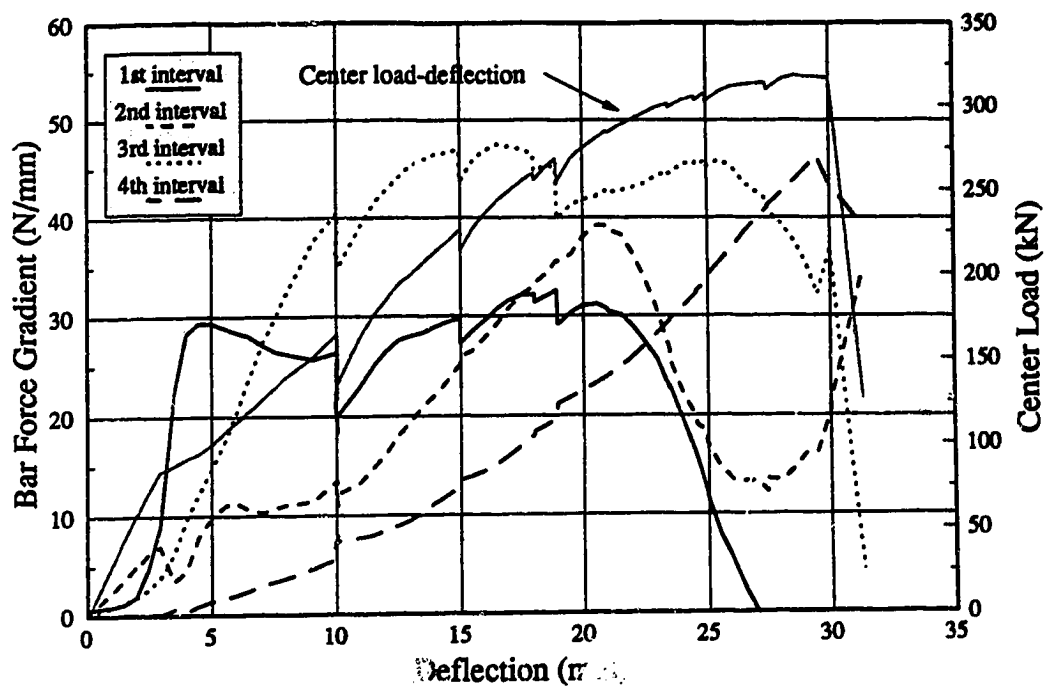


Figure 4.15 Column Bar Force Gradients: P19S50

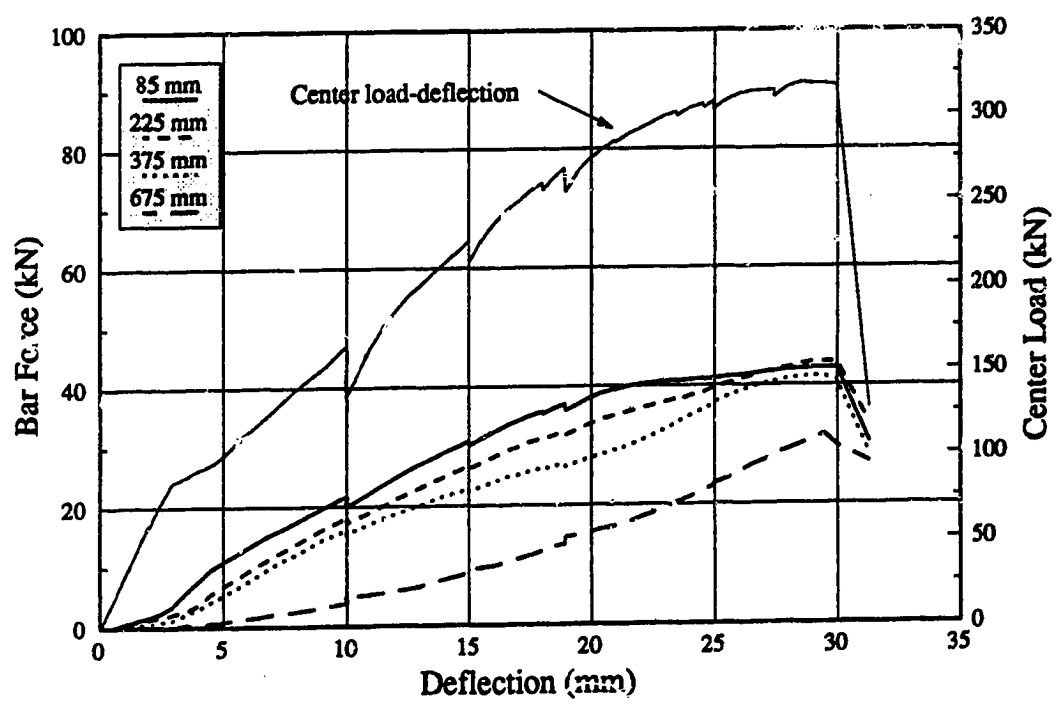


Figure 4.16 Column Bar Forces: P19S50

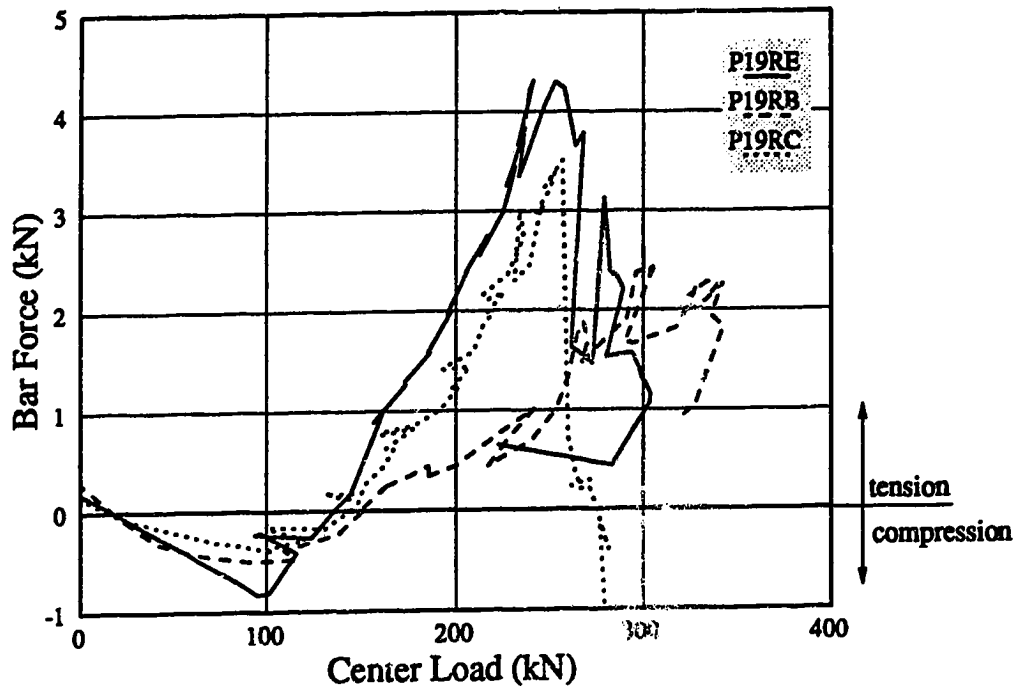


Figure 4.17 Bottom Mat Bar Forces at Face of Column

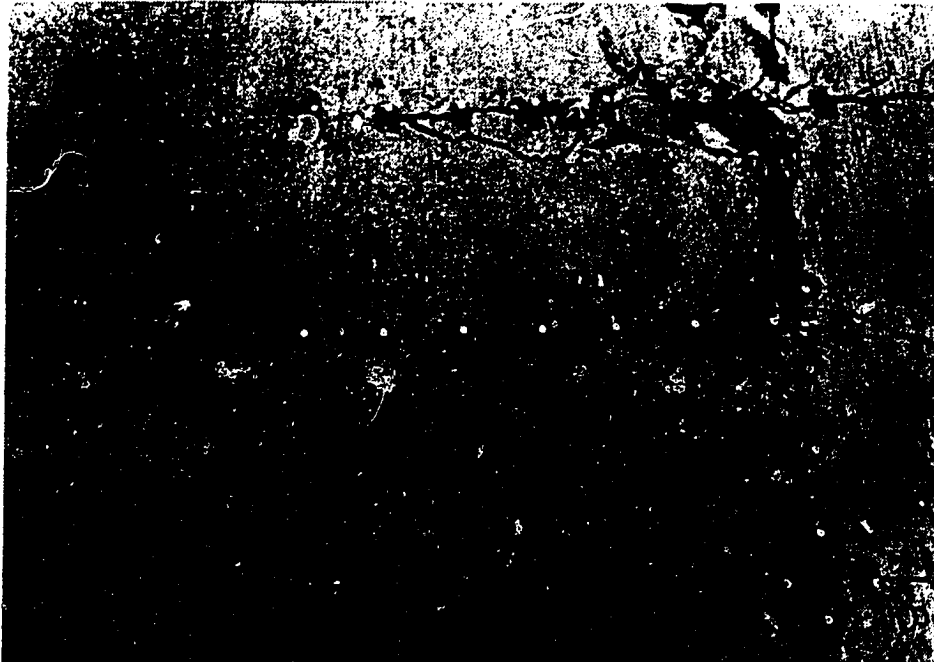


Figure 4.18 Bond Cracking



Figure 4.19 Top Crack Pattern: P19RE



Figure 4.20 Top Crack Pattern: P19RC

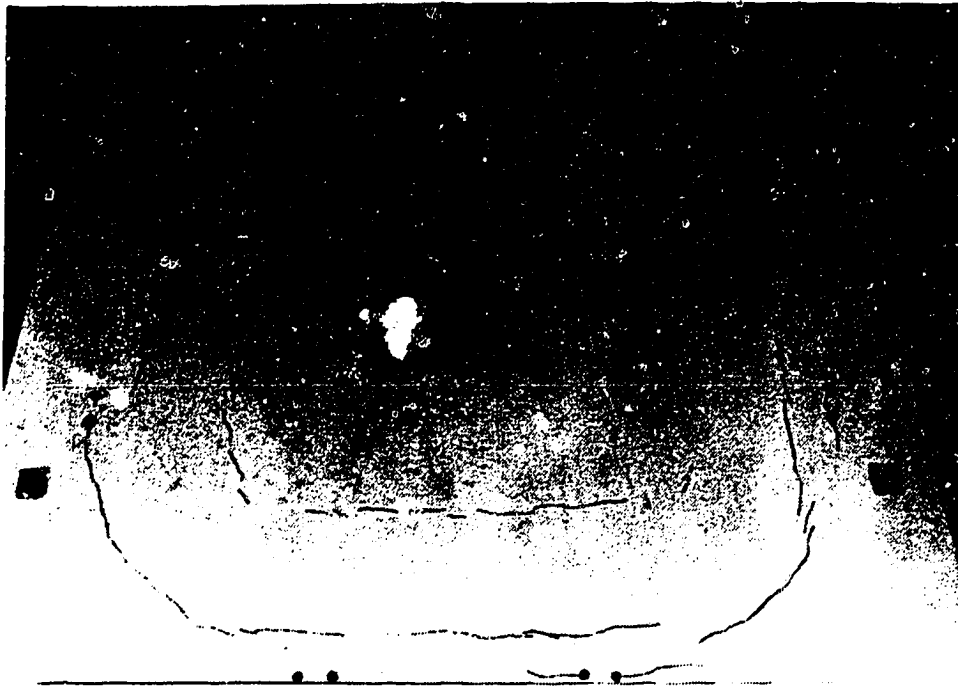


Figure 4.21 Bottom Crack Pattern: P19RE



Figure 4.22 Bottom Crack Pattern: P19RC

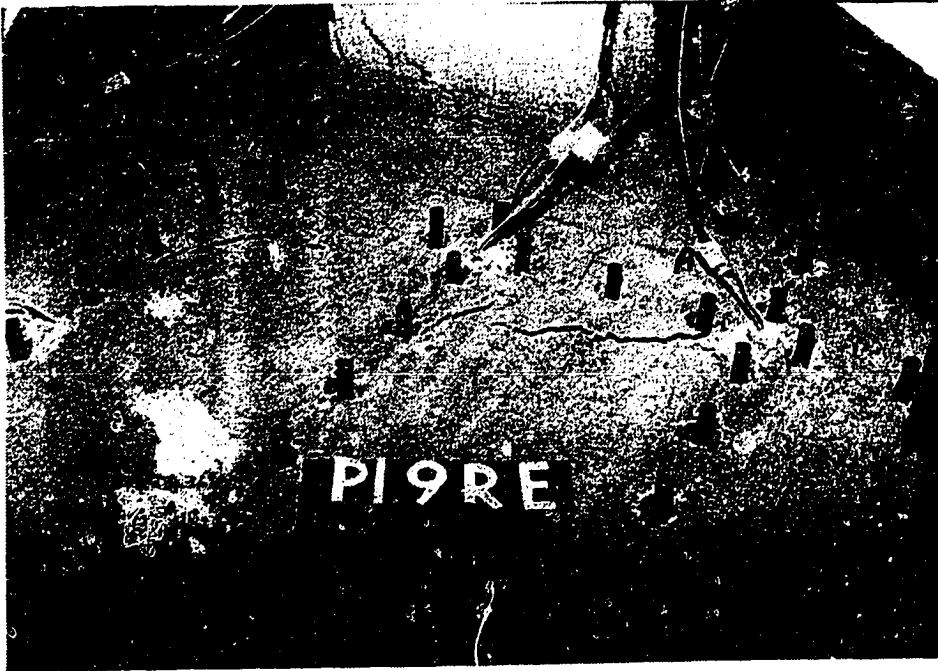


Figure 4.23 Shear Crack: P19RE

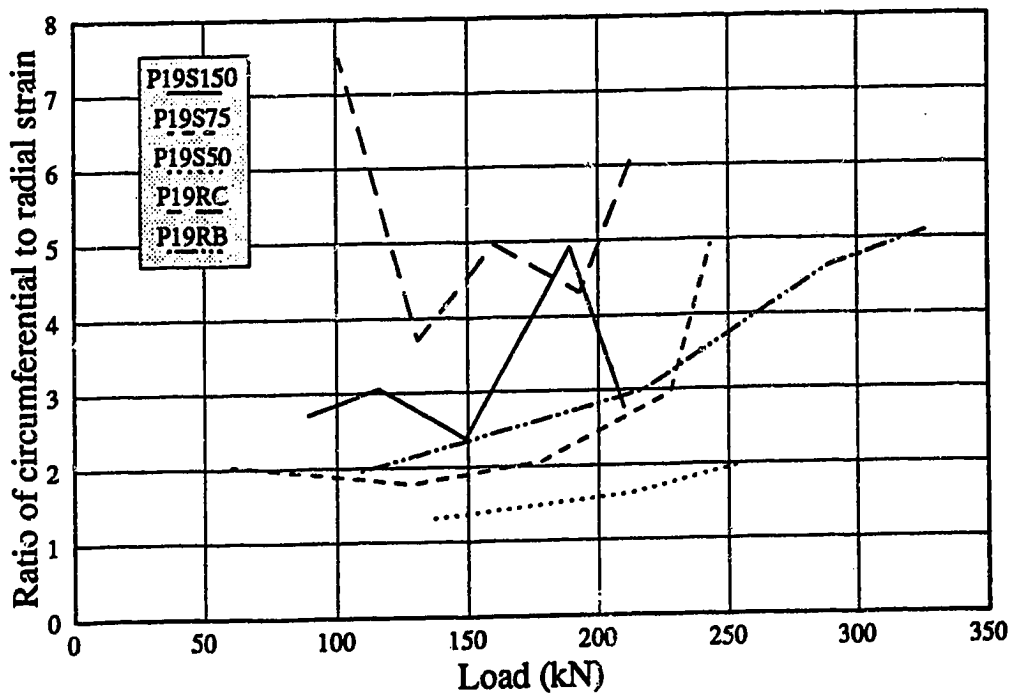


Figure 4.24 Summary of Bottom Demec Strains

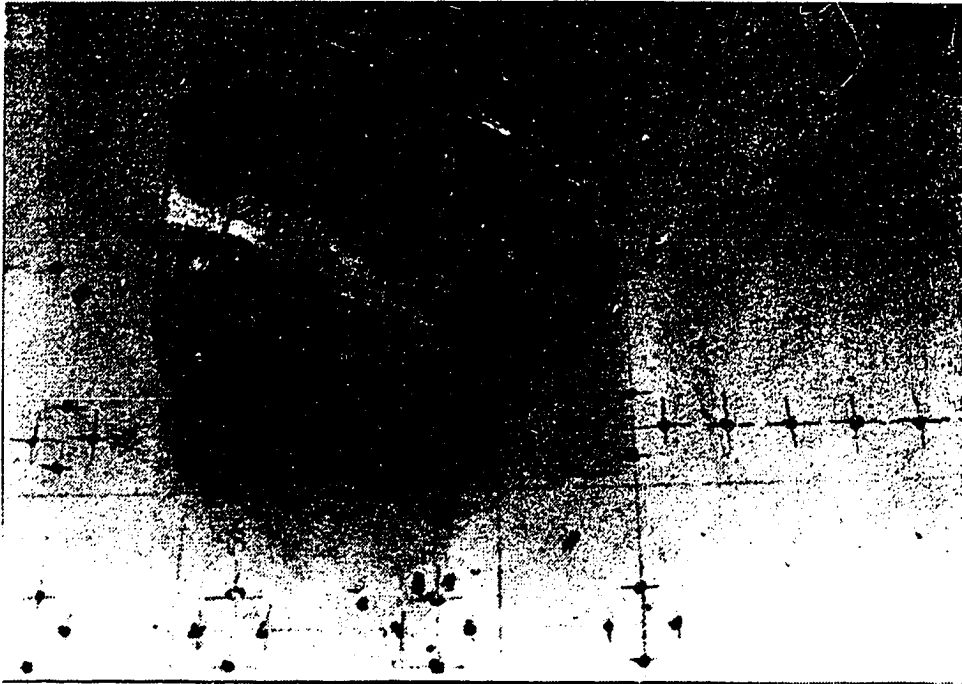


Figure 4.25 Compression Side of Plate at Column: P19RE



Figure 4.26 Compression Side of Plate at Column: P11F66

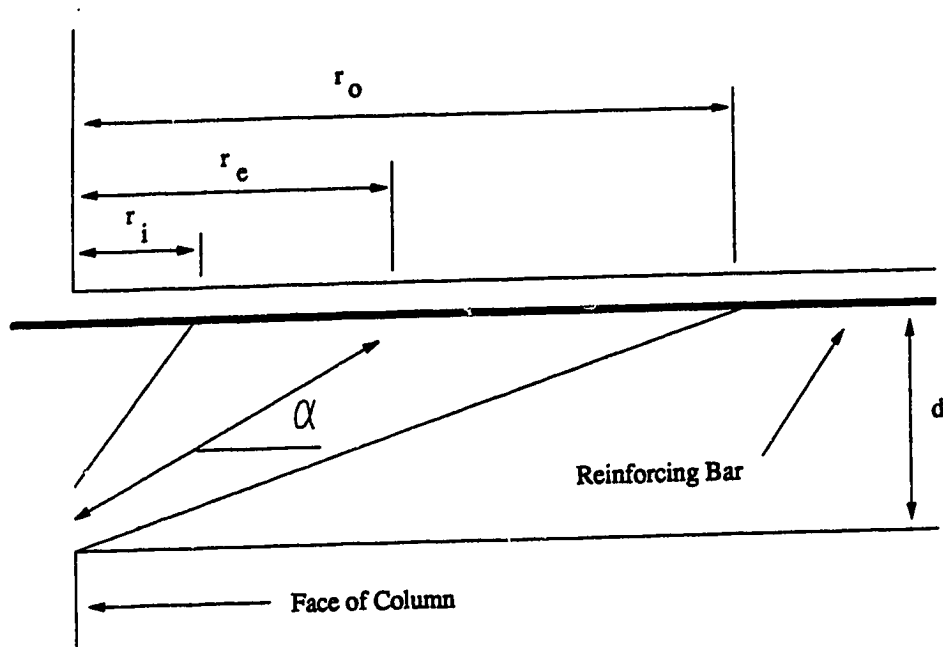


Figure 4.27 Geometry of Straight-line Compression Strut

Chapter 5

Development of the Bond Model

5.1 Background

The truss model describes a slab-column connection as a space truss composed of steel tension ties and straight-line concrete compression struts. Failure is assumed to initiate at the intersection between a compression strut and its attendant steel tie and is the result of the inability of the slab to confine the out-of-plane component of the compression strut.

Although the truss model provides an excellent qualitative description for much of the behavior of slab-column connections (Alexander and Simmonds, 1987), in Chapter 4 it is shown that the geometry of a straight-line compression strut does not agree with experimental measurements. In particular, the location of the intersection between the effective centroid of the strut and the top mat reinforcing steel, based on failure loads, does not agree with the position of the strut as determined from bar force profiles (ie. r_i is generally greater than r_c). A model that retains the desirable characteristics of the truss model and is consistent with experimental measurements is required.

As an alternative to the straight-line strut, consider the curved arch shown in Figure 5.1. A curved arch is more consistent with measured bar force profiles since r_i need not be less than r_c . In a plan view, the arch would be parallel to the reinforcement. As was the case in the truss model, the horizontal component of the arch is equilibrated by tension in the reinforcement. As long as the width of the arch is limited to the width of the column support, the arch may be considered a purely radial component within the plate. This approach also preserves the truss model concept of shear being carried radially by an inclined concrete compression strut. The geometry of the curved radial arch, however, cannot be determined from the bar force profile of the reinforcement tying the arch.

If the horizontal force component in the arch is assumed to be constant, then the shear carried by the arch varies, from a maximum at the face of the column where the slope of the arch is large, to a minimum, or perhaps zero, at the intersection of the arch and the reinforcing steel, where the slope of the arch is small. The shear that was carried by the arch at the face of the column must be dissipated in a direction perpendicular to the arch at some distance away from the column. The rate at which shear can be dissipated determines the curvature of the arch.

At this point, it is necessary to examine how shear may be carried in a reinforced concrete flexural member. In a R/C beam, moment is calculated as the product of the steel force, T , and an effective moment arm, jd . Moment gradient or shear results whenever the magnitude of the force or moment arm varies along the length of the member (x - axis).

$$V = \frac{d(Tjd)}{dx} = \frac{d(T)}{dx} jd + \frac{d(jd)}{dx} T \quad [5.1]$$

The shear carried by a beam may be divided into two separate components. Shear that is the result of a gradient in tensile force acting on a constant moment arm is said to be carried by **beam action**. Shear resulting from a constant tensile force acting on a varying moment arm is said to be carried by **arching action**. Whereas beam action at a particular cross-section requires bond forces at that cross-section, arching action requires only remote anchorage of the reinforcement. For any particular cross-section, the maximum beam action shear is limited by the force gradient that can be sustained in the reinforcement; the maximum shear that can be carried by arching action is limited by the proximity of the applied loads to the support.

Note that a distinction is made between bond and anchorage. **Bond** describes the transfer of force between a reinforcing bar and the surrounding concrete in a region which is not affected by the termination point of the bar. **Anchorage** describes the ability

to prevent the end point of the bar from slipping through the concrete. Although a bond failure limits the reinforcing bar force gradient, it does not limit the magnitude of the bar force provided there is adequate anchorage.

Returning now to the curved radial arch, it must be decided which of the two available mechanisms, beam action or arching action, can account for the dissipation of shear perpendicular to the arch. Several observations, discussed in Chapter 2, suggest that beam action is the only possible mechanism of shear transfer in what amounts to a circumferential direction. For example, Kinnunen and Nylander (1960), report that the deformed shape of test specimens under load is essentially conic, with little or no curvature in the radial direction. This would require a linear distribution of circumferential strain through the thickness of the plate, with maximum compressive strain at the slab soffit. Shehata (reported in Regan and Braestrup, 1985) confirmed this strain distribution by direct measurement. As long as the maximum circumferential compressive strain is constrained to be at the slab soffit, the centroid of the circumferential concrete compression block must remain close to the bottom of the slab. This means that the flexural depth, jd , in the circumferential direction is relatively constant, and any shear that is to be carried in the circumferential direction must be carried by the two-way plate equivalent of beam action.

According to the proposed model, the ability of a plate to carry shear by beam action plays a central role in determining the shear strength of a slab-column connection. Beam action shear requires a force gradient in the reinforcement. In Chapter 4, three potential limits of force gradient are proposed. Of these three, two are limits imposed by cross-sectional strength, namely yielding of the reinforcement and bond failure. Although almost all plate-column connections ultimately punch, as discussed in Chapter 2, only the punching failures that precede widespread yielding of the reinforce-

ment are of concern to designers. For those connections that fail prior to widespread yielding, bond strength is considered to be the most important limitation on force gradient.

The truss model assumes straight-line compression struts acting at a constant angle of inclination. The proposed model is really a modification of the truss model, and might be called a truss model with curved or variable angle struts. However, the geometry of the strut is not directly assessed in the proposed model. Instead, the punching capacity of a slab-column connection is found to be a function of the flexural capacity of the radial arches and the ability of the adjacent quadrants of two-way plate to generate beam action shear on the side faces of the arches. Owing to the preeminence of bond strength in limiting beam action shear, the model is called the **bond model** for punching shear failure.

5.2 Elements of Bond Model

5.2.1 Radial Strips

The orthogonally reinforced slab-column connection is modelled as a rectangular grillage, as shown in Figure 5.2. Four strips, parallel to the reinforcement, extend from the column. The width of each strip is defined by the column size. For a square or rectangular column, the width of the strip is equal to the side dimension of the column (c) perpendicular to the strip. For a round column, the width of the strip is equal to the diameter of the column. The end of the strip farthest from the column support will be called the remote end. The remote end of a strip is at either the edge of the specimen for a simply supported plate or at the center of span for a continuous plate. The total length of a strip is designated as L .

Within a strip, the directions parallel and perpendicular to the strip (r - axis and n - axis respectively) coincide with the radial and circumferential directions of the plate.

The strips themselves may be described as radial. Any load reaching the column must pass through one of these four strips. The strength of the connection is determined by assessing both the flexural strength of each radial strip and the ability of the adjacent quadrants of two-way plate to load each radial strip.

Treating the connection as a rectangular system of structural elements avoids the difficulties associated with modifying a polar-symmetric model to account for orthogonal reinforcement. It does, however, limit the proposed model to joints between columns and orthogonally reinforced concrete plates.

5.2.2 Loading of Radial Strip

Consider the free body diagram of one-half of a radial strip shown in Figure 5.3. The half-strip extends from the column to a position of zero shear. In the case of a simply supported plate with a single, central column, the zero shear position is at the edge of the specimen. For a continuous plate with multiple column supports, the location of maximum positive radial moment close to the center of span corresponds to the position of zero shear.

A radial strip must support the combined effect of any load applied directly to the strip (q), including the self-weight of the strip, and the internal shears and moments developed on the side faces of the strip by the adjacent quadrants of two-way plate.

In Figure 5.3, the near side face of the half-strip is loaded in shear (v), torsion (m_t) and bending (m_n) by the adjacent quadrant of two-way plate. The far side face lies on an axis of symmetry for the plate. Under concentric loading, both shear and torsion on this face are zero. The bending moment applied to the far side face of the half-strip is equal and opposite to the bending moment on the near side face.

The combination of shear and torsion on the side face of the radial half-strip is replaced by a statically equivalent line load, \bar{v} (Kirchhoff shear), acting on the strip. This

procedure is outlined below with reference to Figure 5.4. Note that the sketches in Figure 5.4 are not free body diagrams. Only those shears and moments that appear in the equation of rotational equilibrium for a plate element about the r -axis and for a radial half-strip element about the n -axis are included.

Rotational equilibrium about the r -axis of the plate element shown in Figure 5.4 gives the following relationship.

$$\Delta m_n \times \Delta r = v \times \Delta r \Delta n - \Delta m_t \times \Delta n \quad [5.2]$$

$$\frac{\partial m_n}{\partial n} = v - \frac{\partial m_t}{\partial r} \quad \text{or} \quad m_n' = v - m_t' \quad [5.3]$$

For the case of concentric punching, the radial strip center-lines are, by symmetry, lines of zero shear and torsion. Consider the forces on a small segment of radial half-strip, also shown in Figure 5.4. In order to satisfy rotational equilibrium about the n -axis, there must be a total shear force, Q , in the half radial strip.

$$Q \times \Delta r = m_t \times \Delta r \quad \text{or} \quad Q = m_t \quad [5.4]$$

The line load (\bar{v}) which is statically equivalent to the combined shear and torsion on the side face of the radial half-strip is sum of all vertical loads applied to the strip segment.

$$\bar{v} \times \Delta r = v \times \Delta r + \Delta Q \quad [5.5]$$

$$\bar{v} = v + \frac{\partial Q}{\partial r} = v + \frac{\partial m_t}{\partial r} \quad [5.6]$$

Combining Equations 5.3 and 5.6 gives:

$$\bar{v} = \frac{\partial m_n}{\partial n} + 2 \times \frac{\partial m_t}{\partial r} \quad \text{or} \quad \bar{v} = m_n' + 2 \times m_t' \quad [5.7]$$

The term \bar{v} is often referred to as the Kirchhoff shear. It has its origins in elastic plate theory as a way of satisfying equilibrium at a free or simply supported edge of a plate. Hillerborg (1975) discusses the applicability of this condition to an internal plate boundary.

The Kirchhoff shear is a line load which is statically equivalent to the combination of shear and torsion applied to a side face of a radial strip. Figure 5.5(a) shows the actual loading on a radial half-strip, excluding the bending moments about the n -axis. Figure 5.5(b) shows the same radial half-strip with the Kirchhoff shear replacing the torsions and shears.

The Kirchhoff shear has two components. The first is a shear resulting from the gradient in bending moment perpendicular to the radial strip. This is referred to as primary shear. The second is a shear resulting from twisting moment gradient along the side face of the radial strip, called torsional shear.

5.2.2.1 Primary Shear

Primary shear results from the gradient in bending moment perpendicular to the radial strip. As in a beam, bending moment gradient must be achieved through some combination of beam and arching action. It will be shown that primary shear is the ultimate source of all load entering the radial strip from the adjacent quadrants of two-way plate.

Bending moment gradient perpendicular to the radial strip must be the result of beam action alone. If F_b is the bar force, then, as with the beam action term of Equation 5.1, this bending moment gradient may be expressed as follows.

$$m_n' = (F_b jd/s)' = \frac{jd}{s} \times F_b' \quad [5.8]$$

In a region dominated by beam action, bending moment gradient and force gradient in the reinforcement are equivalent. Direct estimates of primary shear may be obtained by measuring strains in slab reinforcement at intervals perpendicular to the strip. Bar strains can be related to bar forces through steel coupon tests. Average force gradients in the reinforcement may be calculated as the difference in bar force between two positions on the same reinforcing bar divided by the distance between these two positions.

It is assumed that for any particular specimen, there is some limit to the force gradient which can be sustained at the boundary between steel and concrete. This would amount to a bond limitation on the quantity m_n' .

For very lightly reinforced plate-column connections, behavior near ultimate load is characterized by widespread yielding of the reinforcement at increasing distances from the column. Under such circumstances, the maximum force gradient at the edge of the radial strip may be limited by the spread of yielding, rather than bond.

Given that there is some upper limit on m_n' , primary shear has the potential to deliver a finite distributed load to any particular position along the side of the radial strip, equal to the maximum bending moment gradient perpendicular to the strip at that position.

The term F_b' is the force gradient in a single reinforcing bar. If this term is averaged over the spacing of the reinforcement, the resulting term is the horizontal shear stress required for moment gradient.

$$\tau = \frac{F_b'}{s} \quad [5.9]$$

Equation 5.8 may be rewritten as follows:

$$m_n' = \tau \times jd \quad [5.10]$$

From Equations 5.9 and 5.10 it can be seen that, in a region dominated by beam action, a limiting value of force gradient in the reinforcement is the equivalent of a limiting shear stress.

5.2.2.2 Torsional Shear

Torsional shear is the result of gradient in the torsional moment on the side face of the radial strip, in a direction parallel to the radial strip. The factors governing the magnitude of the torsional moment and the torsional moment gradient are not known, nor is it clear how these quantities might be measured in a test. Some of the problems associated with estimating torsional shear are outlined below.

- (1) Unless a slab-column connection is highly over-reinforced, the bending moment near the column perpendicular to the radial strip will be at or near the yield moment at failure. It is not clear how large the torsional moment at this location may be. The normal moment yield criterion (Marti and Kong, 1987) suggests that under these conditions the torsional moment should be zero. However, a combination of doweling action in the plane of the slab of the reinforcement perpendicular to the radial strip and horizontal shear stresses in the compression block may allow some non-zero torsional moment.
- (2) The factors which might control the torsional moment gradient near the column are not known. If a torsional moment on the side face of the radial strip can be maintained to the column support, then it produces a concentrated load at the support equal to twice the value of the torsional moment. If, however, the torsional moment begins to decline at some distance from the support, then it adds to the Kirchhoff shear and requires flexural support from the radial strip, necessitating an interaction between the primary and torsional shear mechanisms close to the column.

- (3) The deformations required to generate torsional shears may be so large as to require a loss of force gradient in the reinforcement close to the column, either through spread of reinforcement yielding or extensive damage to the confining concrete. Either of these would result in a trade-off between primary and torsional shear mechanisms.

Although it may not be possible to estimate directly the contribution of torsional shear to the overall capacity of a plate-column connection, it is possible to outline some of the effects of torsional shear on the basis of equilibrium conditions.

At the remote end of the radial strip, the magnitude of the torsional moment must be zero. In the case of a continuous plate, this statement is based on symmetry. In the case of a simply supported plate, zero torsional moment is a boundary condition. For a concentrically loaded column, the torsional moment must also approach zero at the column support as a result of symmetry.

A consequence of the requirement for zero torsion at the column end of the radial strip provides a criterion for minimum load capacity. For a concentrically loaded column, if there is a non-zero torsional moment at any point along the side face of a radial strip, then according to Equation 5.7, the total Kirchhoff shear between that point and the face of the column must be equal to at least 2 times the magnitude of the torsion. Since both faces of the radial strip are loaded in the same way, the minimum support reaction for the radial strip is equal to 4 times the magnitude of the torsional moment. Since there are four radial strips, the total minimum column reaction is 16 times the magnitude of the torsional moment.

Since the torsional moment is zero at both ends of the radial strip, the total contribution to Kirchhoff shear made by torsional moment gradient must be zero. Starting at the column end of the strip and moving outward, a positive increment in torsional shear must be accompanied by a positive (downward) increment in Kirchhoff shear, according to Equation 5.7. Near the remote end of the strip, the value of the torsional moment must

return to zero, resulting in negative (upward) increments to the Kirchhoff shear. The negative and positive increments in Kirchhoff shear resulting from torsional moment gradient must always sum to zero over the full length of the radial strip.

Torsional shear affects the distribution of Kirchhoff shear along the length of the radial strip. The root source of all shear load on the side face of the radial strip is primary shear. With regard to loading the radial strip, however, the effective point of application of this shear load may be moved much closer to the column by the action of torsional shear.

5.3 Equilibrium of Radial Strip

5.3.1 Actual Loading of Radial Strip

Consider the free body diagram in Figure 5.5(a) and (b), showing the net forces and moments acting on a radial half-strip. In Figure 5.5(a), the line load, \bar{q} , is the sum of the self-weight of the half-strip and any distributed loads applied directly to the half strip. In Figure 5.5(b), the Kirchhoff shear, \bar{v} , replaces the shears and torsional moments on the side face of the half-strip.

The radial strip supports all the loads shown in Figure 5.5(b) by acting as a cantilever beam. The maximum capacity of this system is obtained by optimizing the distribution of Kirchhoff shear, subject to certain constraints.

The total flexural strength of the cantilever is the sum of M^- and M^+ . Flexural equilibrium of the radial strip leads to Equation 5.11 and vertical equilibrium produces Equation 5.12. In each of these equations, the factor two accounts for the fact that both \bar{v} and \bar{q} were defined for a radial half-strip. The quantity P_s is the total load carried by one radial strip of an interior column-slab connection.

$$M^+ + M^- = M_s = 2 \times \int_0^L (\bar{v} + \bar{q}) r dr \quad [5.11]$$

$$P_s = 2 \times \int_0^L (\bar{v} + \bar{q}) dr \quad [5.12]$$

5.3.2 Simplified Loading of Radial Strip

The total line load at any point on a radial half-strip is the sum of the directly applied line load, \bar{q} , and the Kirchhoff shear, \bar{v} , the latter being composed of torsional shear and primary shear. In order to evaluate the integrals of Equations 5.11 and 5.12, three assumptions are made regarding the distribution of load along the length of the radial strip. These assumptions both simplify and optimize the loading of the radial strip.

- (1) All Kirchhoff shear is assumed to be the result of primary shear. The torsional shear contribution is considered negligible.
- (2) At a distance l from the column end of the radial strip, the Kirchhoff shear decreases from the maximum value permitted by primary shear (m_n') to a value of zero. The length l is referred to as the loaded length of the radial strip.
- (3) The direct load on the radial strip is assumed to be negligible ($\bar{q} = 0$).

Assumption (1) is conservative since it underestimates the intensity of Kirchhoff shear close to the column end of the radial strip. For the case of a punching failure occurring before significant deformation of the plate, it is justified because the behavior at ultimate load does not favour the development of large torsional moments on the side face of the radial strip. There are two reasons for this.

First, the side face of the radial strip is close to an axis of symmetry, where the torsional moment is constrained to be zero. A large torsional moment on the side face of the radial strip requires that the orientation of the principal moment axes be markedly different than the n and r axes of the strip. This is not consistent with small deformations of the plate.

Second, near ultimate load, the plate is cracked in flexure, reducing its torsional stiffness. In addition, the torsional moments are parallel to the reinforcement and require the development of dowel forces in the plane of the slab. With low torsional stiffness, large deformations would be necessary to generate significant torsional moments, but large deformations are not consistent with a brittle punching failure.

Assumption (2) optimizes the loading of the radial strip with regard to maximizing total load. It is not inherently conservative and almost certainly violates conditions of compatible deformations within the plate. It is however, consistent with the development of a lower bound estimate on punching capacity, which allows the violation of compatibility deformations within the plate provided that statics are satisfied at every point, the primary shear mechanism has enough ductility to allow redistribution and the torsional shear capacity is at least sufficient to offset any direct load on the strip.

If assumption (2) is accepted, then assumption (3) is conservative and justified for slab-column connections. For a prototype slab under uniformly distributed load, the area of slab supported by a single column is large compared to the plan area of the loaded length of the radial strips. For a typical slab-column connection test specimen, loads are applied outside the immediate vicinity of the column and only the dead weight of the radial half-strip contributes to \bar{q} . In either case, \bar{q} is small compared to primary shear and may be neglected. For a spread footing, the plan area of the radial strips accounts for a significant fraction of the entire footing area. The intensity of load applied directly to the

radial strip is much larger than in the case of a column-supported plate. As a result, it may be overly conservative to neglect \bar{q} in estimating the punching capacity of a footing-column connection.

The optimized loading of a radial half-strip is shown in Figure 5.6. The loading term w is defined as follows.

$$w = m_n'_{\max} = \frac{jd}{s} \times F_b'_{\max} = \tau_{\max} \times jd \quad [5.13]$$

Rather than define w as a line load on a radial half-strip, it is convenient to consider w as the simplified, optimized Kirchhoff shear load acting on one side of a radial strip by an adjacent quadrant of two-way plate. A radial strip of an interior column-slab connection has two adjacent quadrants of two-way plate. The total line load on a radial strip of an interior column-slab connection is $2w$. For an edge or corner column, however, there will be radial strips that are parallel to the free edge of the plate and have only one adjacent quadrant of two-way plate. In this case, the total line load is w .

5.4 Bond Model Capacities

In this section, an attempt will be made to quantify the elements of the bond model which will determine the ultimate strength of a slab-column connection. Estimates are needed for the flexural capacity of the radial strip and the magnitude of the primary shear.

5.4.1 Flexural Capacity of Radial Strip

The flexural strength of each radial strip can be estimated in the same way as any under-reinforced concrete beam. The assumption of yielding in the reinforcement, at least for those bars passing through the column, is consistent with observed behavior. Expressions for the negative moment capacity, M^- , at the column end of the strip and the

positive moment capacity, M^+ , at the remote end of the strip, are given in Equations 5.14 and 5.15. The factor, k_r , accounts for the degree of rotational restraint at the remote end of the radial strip.

$$M^- = \rho^- \times f_y j d^2 \times c_2 \quad [5.14]$$

$$M^+ = k_r \times \rho^+ \times f_y j d^2 \times c_2 \quad [5.15]$$

Equations 5.14 and 5.15 require definitions of the effective densities in the radial strip of the top and bottom reinforcement, ρ^- and ρ^+ . It would seem reasonable to assume that any steel which passes through the column contributes to M^- . There is, however, a problem in dealing with reinforcing bars which are close to the column. Furthermore, for uniformly spaced reinforcement, the values of ρ^- and ρ^+ should not depend on whether the mat is bar centered or space centered. The following definitions of ρ^- and ρ^+ satisfy these criteria.

$$\rho_c^- = \frac{A_{sT}}{b \times d} \quad [5.16]$$

$$\rho_c^+ = \frac{A_{sB}}{b \times d} \quad [5.17]$$

A_{sT} is the total cross-sectional area of top steel passing through the column plus one half the area of the first top bar on either side of the column. Similarly, A_{sB} refers to the total area of bottom mat steel passing through the column plus one-half of the first bottom bar on either side of the column. The quantity d is either the flexural depth of the top or bottom mat of reinforcement, as appropriate. The term b also depends upon which mat is being considered. It is the column dimension plus the distance to the first reinforcing bar on either side of the column.

The restraint factor, k_r , is zero for the typical, isolated slab-column connections with rotationally unrestrained edges. For prototype slabs or test specimens whose boundaries extend to the center of span and are fully restrained against rotation, k_r is equal to unity.

5.4.2 Primary Shear Loading

The maximum intensity of primary shear loading, w , on a radial half-strip is calculated by multiplying the limiting force gradient in the reinforcement perpendicular to the radial strip by its internal flexural moment arm and dividing by the spacing of the reinforcement (Equation 5.13). The reinforcement spacing and internal moment arm are either known or can be estimated accurately. Although the force gradient along a reinforcing bar may be limited by either yielding of the reinforcement or by bond failure, it is the limitation imposed by bond failure that results in a brittle punching shear failure. Therefore, one way of estimating the primary shear loading term w uses a direct estimate of bond strength.

According to Equation 5.9, in a region dominated by beam action, a limiting force gradient in the reinforcement is equivalent to a limiting shear stress. In Section 5.4.2.2 it is shown that this limiting shear stress is no different than that used to estimate the concrete contribution to the shear strength of slender beams. Values of critical nominal shear stress for one-way beams are well established in design codes. Primary shear may be estimated on the basis of code values for critical nominal shear stress. In this way, the bond model provides a link between code provisions for the design of one-way and two-way flexural members.

5.4.2.1 Bond Strength

The conditions which exist for the top steel in two-way plate near a column are not conducive to high values of bond stress. Lack of confinement perpendicular to the plane of the slab makes splitting failure likely. Two-way bending causes transverse tension which further reduces bond strengths.

Morita and Fujii (1982) present an empirically derived relationship for bond stress at splitting failure. The value of b_1 is the lesser of b_{s1} or b_{v1} . The terms b_{s1} and b_{v1} are non-

dimensional measures of the amount of concrete which must fracture in a splitting failure. Splitting in the plane of the reinforcement is accounted for by b_{si} , while a local wedge-shaped split around a single bar is accounted for by b_{vi} , as illustrated in Figure 5.7.

$$b_{si} = \frac{s}{d_b} - 1 \quad [5.18]$$

$$b_{vi} = \sqrt{3} \times \frac{2d'}{d_b} \quad [5.19]$$

$$\tau_{co} = \sqrt{f'c} \times (0.09614b_i + 0.1337) \quad [5.20]$$

The maximum value of primary shear load on a radial half-strip as limited by τ_{co} is:

$$w_{M\&F} = jd \times \left\{ \frac{\pi d_b}{s} \times \tau_{co} \right\} \quad [5.21]$$

5.4.2.2 Nominal Shear Stress

The term τ , defined in Equation 5.9, is equivalent in concept to a nominal shear stress in a slender one-way beam. For a beam of width s , the average shear on a horizontal section which separates the reinforcing steel from the rest of the beam is:

$$v_c = \frac{T'}{s} = \frac{V}{jd \times s} \quad [5.22]$$

where T' is the force gradient in the tension reinforcement. This nominal shear stress forms the basis of building code approaches for estimating the concrete contribution to shear strength. It is an attempt to estimate the capacity of the beam to develop the average bond requirements demanded by shear. Therefore, building code methods of estimating one-way shear strength should be directly applicable to two-way plates.

In the interests of simplicity, building codes usually assume $j = 1.0$ in Equation 5.22. Therefore, Equation 5.10 should be modified to reflect this approximation.

$$m_n' = \tau \times jd_s = v_c \times d \quad [5.23]$$

This should provide a reasonable estimate of maximum moment gradient.

Values of v_c according to the American and British standards are:

$$ACI \quad 318: \quad v_c = 0.166 \times \sqrt{f'_c} \quad [5.24]$$

$$BS \quad 8110: \quad v_c = 0.29 \times (\rho_{\%} \times f'_c)^{\frac{1}{3}} (400/d_s)^{\frac{1}{4}} \quad [5.25]$$

The corresponding values for primary shear loading applied to a radial half-strip, w , are:

$$ACI \quad 318: \quad w_{ACI} = d \times 0.166 \times \sqrt{f'_c} \quad [5.26]$$

$$BS \quad 8110: \quad w_{BRIT} = d \times 0.29 \times (\rho_{\%} \times f'_c)^{\frac{1}{3}} (400/d_s)^{\frac{1}{4}} \quad [5.27]$$

5.4.3 Ultimate Strength of Slab-Column Connection

In practice, the slab reinforcement of most slab-column connections is uniformly distributed, at least in the immediate vicinity of the column. So long as the reinforcement perpendicular to a radial strip is uniform, the value of w does not vary along the length of the radial strip. This is true whether w is based on an estimate of bond or a critical shear stress. Therefore, while the value of w may vary continuously, as shown in Figure 5.6, a typical plate with uniform distribution of reinforcement and a uniform thickness should have a uniform value of w , as shown in Figure 5.8(a). Equation 5.11 may be further simplified and solved for the loaded length, l .

$$M_s = 2 \times \int_0^L (w)r dr = 2 \times \int_0^l (w)r dr = 2 \times \frac{wl^2}{2} \quad [5.28]$$

$$l = \sqrt{M_s/w} \quad [5.29]$$

Combining Equations 5.12 and 5.29 yields:

$$P_s = 2 \times \int_0^L (w) dr = 2 \times \int_0^l (w) dr = 2 \times wl = 2 \times \sqrt{M_s \times w} \quad [5.30]$$

A change in the spacing of the reinforcement perpendicular to the radial strip or a change in the thickness of the plate, at a distance l_1 from the face of the column, can be accounted for by having a step in the loading diagram, as shown in Figure 5.8(b). For this type of loading, the solution of Equations 5.11 and 5.12 results in the following.

$$P_s = 2 \times [l_1 \times (w_1 - w) + l \times w] \quad [5.31]$$

$$= 2 \times \left[l_1 (w_1 - w) + \sqrt{[M_s - (w_1 - w)l_1^2]w} \right]$$

The punching capacity of a slab-column connection is obtained by summing the contribution of each radial strip.

$$P_{calc} = \sum P_s \quad [5.32]$$

5.4.4 Limits of Bond Model

The bond model assumes that radial strips projecting from the column are loaded on their side faces by shears resulting from the beam action of the adjacent quadrants of two-way plate. Under certain conditions, however, the calculated failure load of a slab-column connection will be greater if it is assumed that the radial strips themselves carry shear by one-way beam action. Assuming the mechanism of the bond model, with arching action in the radial strips, will result in a lower predicted ultimate load.

According to the bond model, a loaded length, l , may be calculated for each radial strip. For the typical case, where the loading term, w , is constant, l is given by Equation 5.29. The radial strip is loaded on both faces by what amounts to a one-way shear. Therefore, for a single radial strip, the total loaded length is $2l$. If the width of the radial strip is greater than $2l$, then more load can be carried to the column by beam action of the radial strip than by the mechanism proposed by the bond model.

Combining Equations 5.13, 5.14, 5.15 in 5.29 and assuming that the flexural depth of all the reinforcement is approximately equal and that any bottom reinforcement is fully effective, the width of the radial strip (or side length of the column), c , may be solved in terms of the loaded length.

$$l = \sqrt{\frac{(\rho^+ + \rho^-) \times c \times jd^2 \times f_y}{\tau_{\max} \times jd}} = \sqrt{\frac{\rho \times c \times d \times f_y}{\tau_{\max}}} \quad [5.33]$$

$$c = \frac{l^2 \times \tau_{\max}}{\rho \times f_y \times d} \quad [5.34]$$

Combining the above expression with the condition that the side length of the column be equal to twice the cantilever length gives a relationship between the critical ratio of column dimension to slab flexural depth.

$$c = \frac{(c/2)^2 \times \tau_{\max}}{\rho \times f_y \times d} \quad [5.35]$$

$$\frac{c}{d} = \frac{4\rho f_y}{\tau_{\max}} \quad [5.36]$$

Assuming a concrete strength of 30 MPa, a steel strength of 400 MPa, top and bottom reinforcing densities of 1 per cent and that the maximum shear stress, τ_{\max} , can be approximated by the ACI code value for one-way shear, the critical ratio of column size to flexural depth would be in the order of 35. If only the top reinforcement is contributes to the moment capacity of the radial strip, M_r , then the critical ratio is about 17.

The preceding approach assumes that a radial strip acts exclusively in either beam action or arching action. However, the transition between arching action and beam action as the column size increases relative to the depth of the plate may not be so sudden. Imagine a series of tests in which the column size increases incrementally. Each increment in side length may be used either to carry one-way shear directly to the column or to

increase M_c by an increment, ΔM_c . The change between one-way and two way behavior occurs when the increment of side length (dc) contributing to M_c is more than twice the resulting increment in loaded length (dl).

$$l \times dl \times 2d \times \tau_{\max} = \Delta M = \rho f_y j d^2 \times dc \quad [5.37]$$

$$\frac{dl}{dc} = \frac{\rho f_y j d}{2 \times \tau_{\max} \times l} = \frac{1}{2} \quad [5.38]$$

This relationship, when squared and combined with Equation 5.33, gives a critical value of c/d which divides pure arching action from mixed beam action and arching action within the radial strips.

$$\frac{c}{d} = \frac{\rho f_y \times j}{\tau_{\max}} \quad [5.39]$$

As before, assuming a concrete strength of 30 MPa, top and bottom reinforcement densities of 1 per cent and a steel yield stress of 400 MPa, this second method suggests that the change from radial arching action to radial beam action begins at values of c/d in the order of 7 for plates in which the bottom reinforcement is fully engaged and 3.5 for plates in which only the top reinforcement is effective.

It should be noted that if this effect of large columns is ignored, the bond model will err on the conservative side.

There is a second limitation of the bond model requires that the column dimension have a minimum size relative to the depth of the plate. For an extremely small column, it is possible that the capacity of the connection will be governed by a splitting failure of the radial strip. According to the mechanics of the bond model, each radial strip is loaded on both faces by the loading term, w . This is an internal load, however, and is distributed through the thickness of the slab. As a result, part of the load enters the radial strip above the center of the radial arch while the remainder enters below. That portion that enters below must be supported by vertical tensile stresses that effectively hang the load from the arch. These stresses should be maximum at the end of the loaded length, since at this

position virtually all of the loading term, w , enters the strip below the level of the arch. The critical value of c/d for this type of behavior can be estimated by calculating the vertical tensile stress at the end of the loaded length of a radial strip. This is done in Equation 5.40, using the loading term w_{ACI} and assuming a tensile strength of concrete of $0.5\sqrt{f'_c}$.

$$c \times 0.5\sqrt{f'_c} = 2 \times w_{ACI} = 2 \times d \times 0.166\sqrt{f'_c} \quad [5.40]$$

This procedure places the critical value of c/d at about 0.66. Most slabs will have values of c/d in excess of 1.5. As a result, this requirement for minimum column size is not considered to be a serious limitation of the bond model.

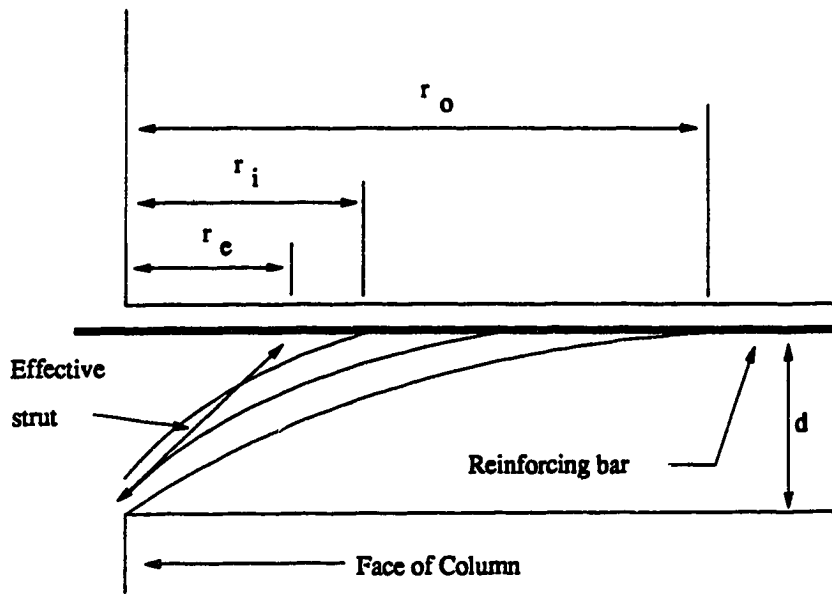


Figure 5.1 Radial Arch

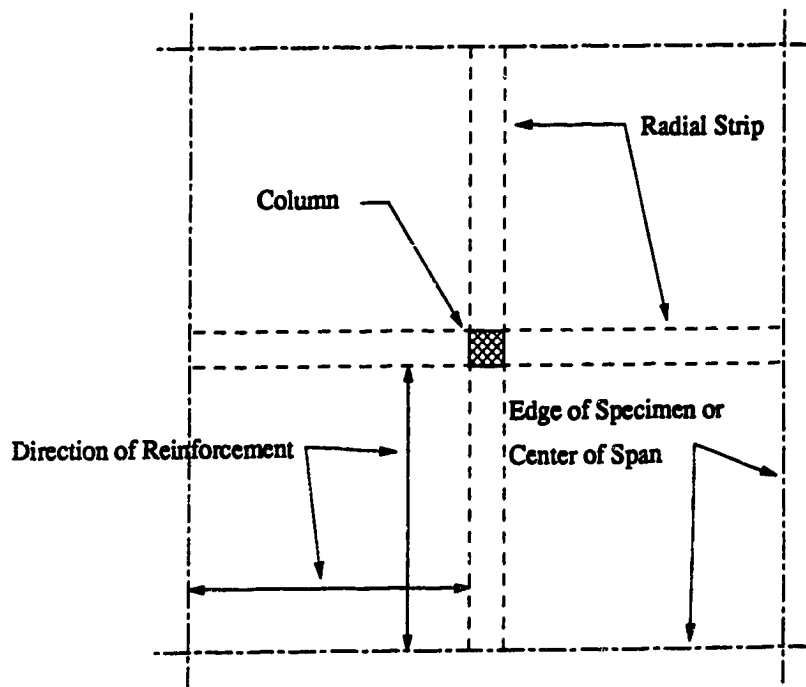


Figure 5.2 Layout of Radial Strips

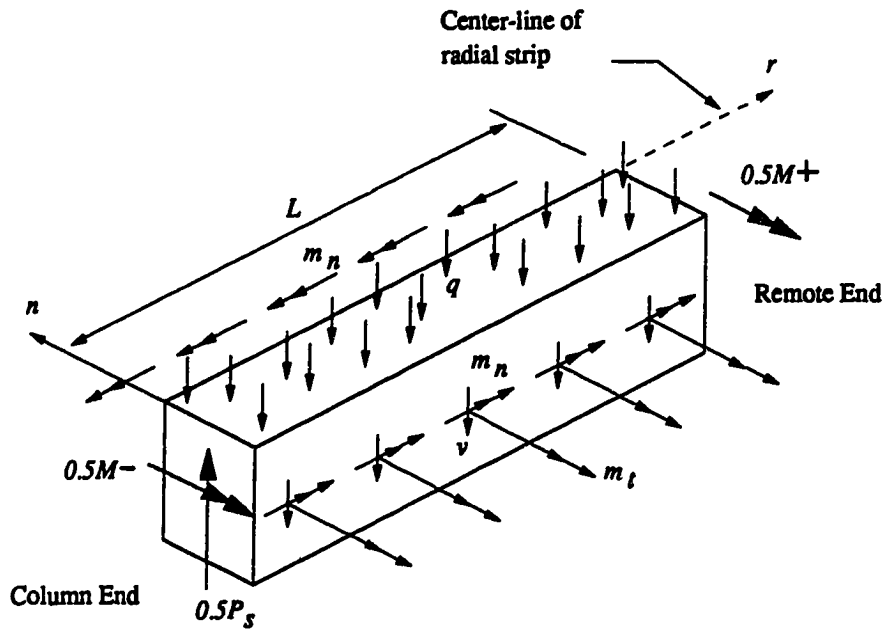


Figure 5.3 Isolated Radial Half-Strip

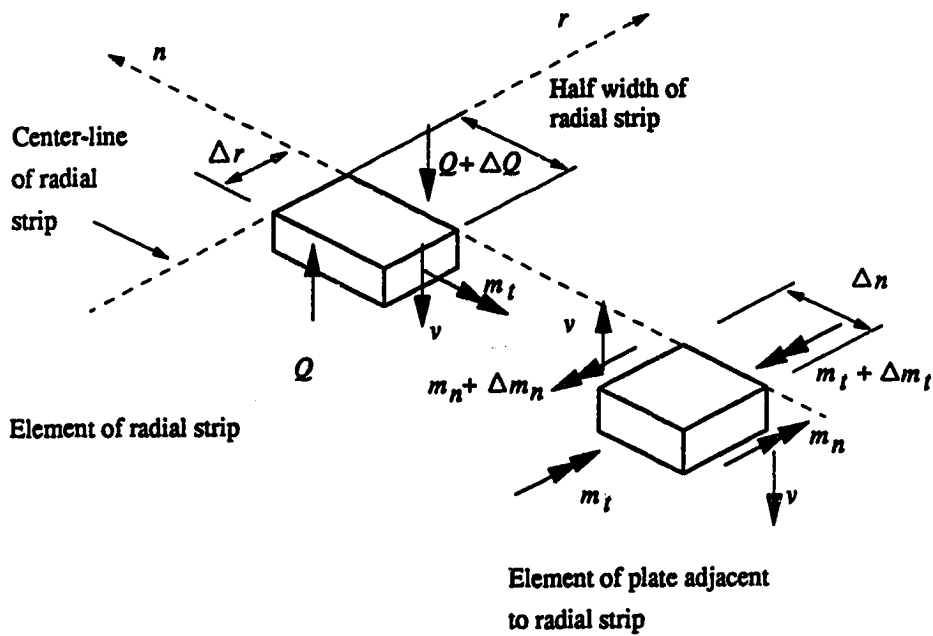


Figure 5.4 Derivation of Kirchhoff Shear

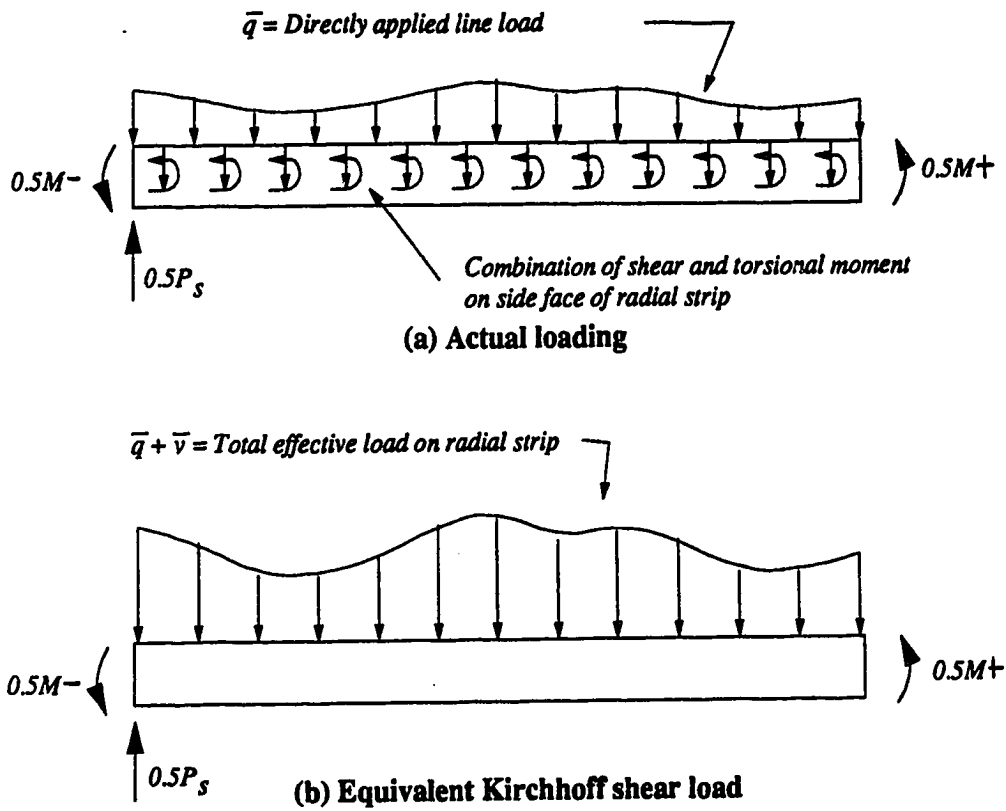


Figure 5.5 Equivalent Loading of Radial Half-Strip

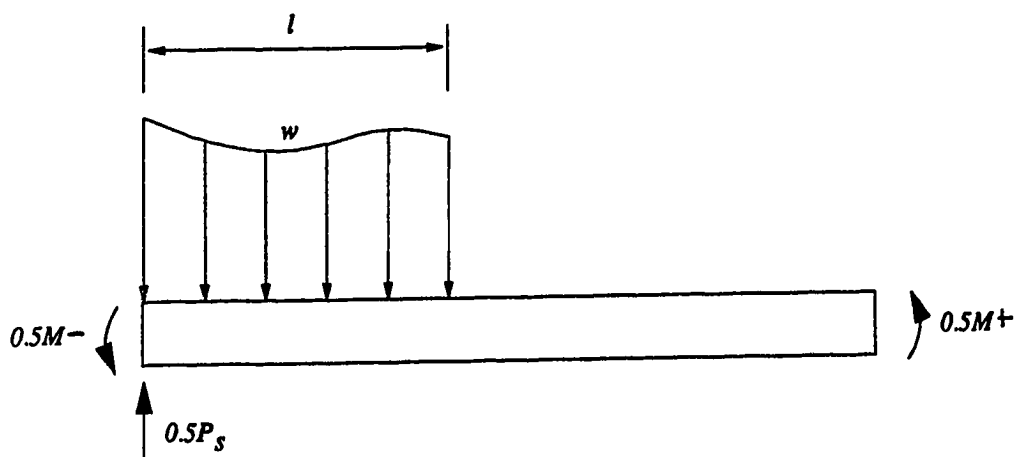


Figure 5.6 Optimized Loading of Radial Half-Strip

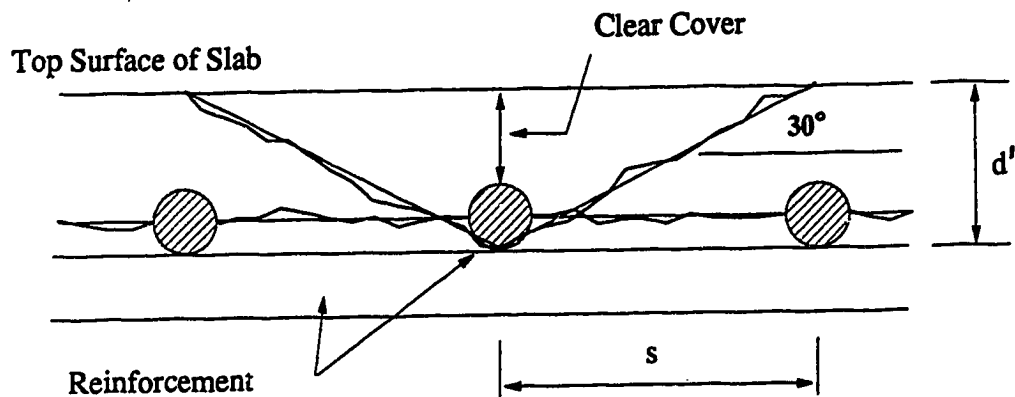


Figure 5.7 Assumed Rupture Surfaces for Morita and Fujii Bond Estimate

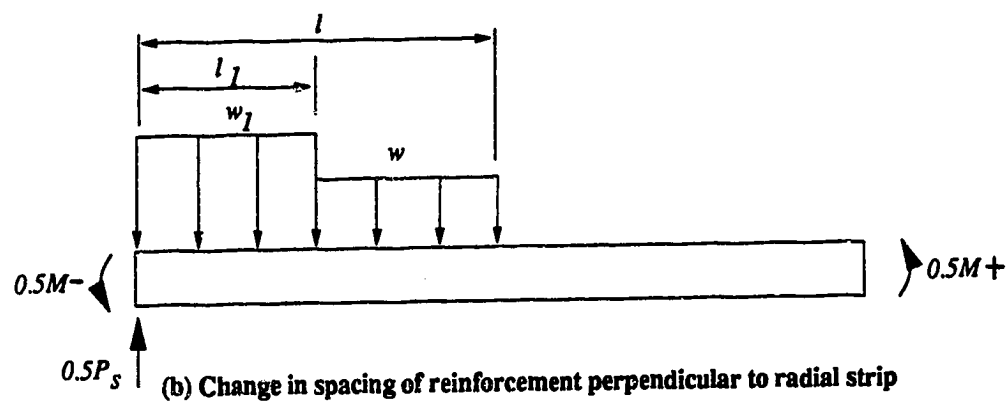
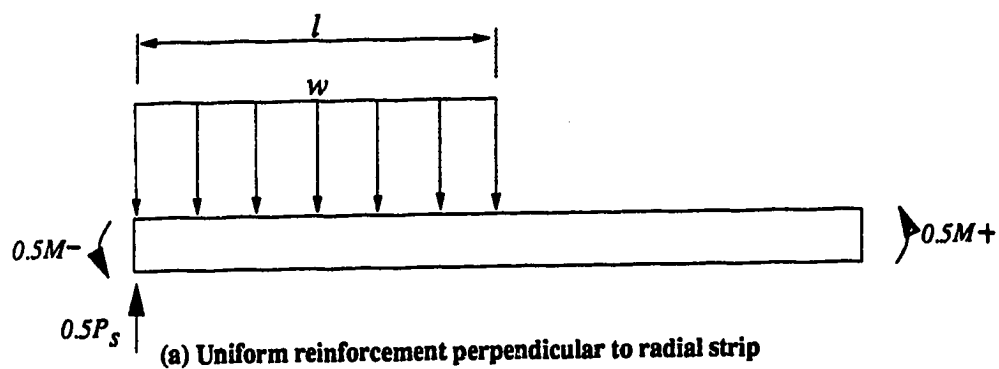


Figure 5.8 Practical Loading of Radial Half-Strip

Chapter 6

Application of Bond Model

6.1 Assessment of Bond Model Mechanism

The bond model describes a slab-column connection as a rectangular grillage of radial strips that cantilever from the column. Each strip is loaded by the adjacent quadrants of two-way plate. According to the bond model, there should be a correlation between the punching load, P_{ult} , of a slab-column connection and the maximum force gradient, $F_b'_{max}$, in the flexural reinforcement perpendicular to the radial strips.

In order to apply the bond model to a test, the loading term, w , and the flexural capacity of the radial strip, M_r , must be determined. These quantities are then related to the failure load, P_{calc} , of each specimen by Equations 5.32 and 5.30 or 5.31. The flexural capacity of each radial strip, M_r , is a function of the plate reinforcement and the extent of rotational boundary restraint. If the value of w is based on measured force gradients, then the comparison of P_{calc} and P_{ult} provides some assessment of the accuracy of the bond model mechanism in describing slab-column behavior.

6.1.1 Measured Force Gradients

The bond model requires an estimate of the maximum bar force gradient, $F_b'_{max}$, that can be maintained in the reinforcement perpendicular to a radial strip. In this investigation, however, most force gradients are measured over intervals that are within and parallel to the radial strip. Only the first interval and possibly the second interval of the perimeter bar are in a position to provide information concerning beam action perpendicular to the radial strip, and even these may be influenced by their close proximity to the column and the parallel radial strips.

Since direct measurements of the force gradients perpendicular to the radial strips were not made, values of $F_b'_{\max}$ are based on the available force gradient measurements (presented in Appendix C) at other locations. These estimated values are recorded in Table 6.1. What follows is a detailed discussion on how the values of $F_b'_{\max}$ were chosen.

It is likely that the available force gradient measurements tend to under-estimate the true values of $F_b'_{\max}$ perpendicular to the radial strips. There are three reasons for this.

- (1) All measured force gradients are on bars whose bond is compromised by the flexural behavior of the plates. The folding pattern of the plates, discussed in Chapter 4, caused significant cracking along the length of the bars within the radial strips. The bond model, however, requires the magnitude of force gradients on bars that do not follow the cracking pattern associated with the yield-line mechanism.
- (2) Force gradients are measured in a predominantly radial direction. According to the mechanics of the bond model, arching action is a dominant feature in the radial direction. Therefore, the gradients measured at some of the intervals are limited by the redistribution associated with a shift from radial beam action to radial arching action.
- (3) Many force gradients are measured over intervals that are 300 mm or more in length. A longer length of interval tends to attenuate the measured values of gradient.

Because of the above-mentioned problems, an average value of the peak force gradients measured over all the intervals in any test is not a meaningful result. It is more appropriate to consider only the higher values of peak gradient. The best that can be expected is to show that the magnitude of the force gradients required to satisfy the bond model are not unreasonable. Therefore, values of $F_b'_{\max}$ for each test must satisfy two criteria: (1) the measured force gradients must meet or exceed the value of $F_b'_{\max}$ and (2)

the value of $F_b'_{\max}$ must be sustainable over a range of loading. In the following discussion, the second criterion is assumed satisfied if the gradient is maintained through at least 5 mm of deflection.

It should be noted that, barring any non-functioning strain gauges, at least four separate strain gauges contribute each average value of bar force reported in Appendix C. Each reported value of bar force gradient is based on the average response of at least four gauges at both the upper and lower gauge locations. As a result, even a single value reported in Appendix C may be considered reproducible.

Force gradient diagrams for the first and third interval of the column bar and the second interval of the perimeter bar for specimen P11F0 (Figures C-13 and C-15) show fairly good agreement on a maximum value of 100 N/mm. Moreover, the results of the second interval of the perimeter bar show that this is a sustainable level of bond.

For specimens P11F31 and P11F66, the maximum gradient over the second interval of the column bar (Figures C-17 and C-21) is about 125 N/mm. Although this gradient has a peak value of about 140 N/mm for specimen P11F31, the sustainable maximum is only about 110 N/mm. The peak value of gradient over the second interval of the column bar for specimen P11F66 is about 125 N/mm. However, because of yielding at the upper gauge location at a deflection of about 20 mm, this value is not sustainable. For both of these specimens, the maximum gradient over the second interval of the perimeter bar (Figures C-19 and C-23) is essentially the same as that measured in specimen P11F0. Therefore, a more modest value for $F_b'_{\max}$ of 110 N/mm is considered reasonable.

For specimen P38F0, a value for $F_b'_{\max}$ of 130 N/mm is based on the results of the third interval of the column bar and the second interval of the perimeter bar (Figures C-25 and C-27). Force gradient diagrams for specimens P38F34 and P38F69 (Figures C-29, C-31, C-33 and C-35) do not appear to be very reliable. The poor per-

formance of the strain gauges in these two tests is discussed in Chapter 4. Although gradients as large as 150 N/mm and 200 N/mm are recorded along the column bars of these tests, the maximum gradient on perimeter bar is only about 100 N/mm. This is less than is recorded for the perimeter bar of specimen P38F0. As a result, there is no convincing evidence for assuming a higher value of $F_b'_{\max}$ for specimens P38F34 and P38F69 than is estimated for specimen P38F0.

The second interval of the column bar of specimen P19S150 (Figure C-33) reaches a peak value of about 120 N/mm. However, the first and second intervals of the perimeter bar have maximum values between 80 N/mm and 90 N/mm. An average value for $F_b'_{\max}$ of 100 N/mm is considered reasonable.

The perimeter bars of both specimens P19S75 and P19S50 mark a change in the spacing of the reinforcement. The spacings of the column bars are 75 mm and 50 mm for specimens P19S75 and P19S50, respectively. However, for specimen P19S75, the distance from the perimeter bar to the first adjacent bar on the column side is 75 mm whereas the distance to the first bar on the other side is 150 mm. Similarly, for specimen P19S50, the spaces on either side of the perimeter bar are 50 mm and 150 mm wide respectively. For Table 6.1, average spacings of 112.5 mm and 100 mm are assigned to the perimeter bars of specimens P19S75 and P19S50, respectively.

From Figure C-41, a reasonable value of $F_b'_{\max}$ for the column bar of specimen P19S75 is about 65 N/mm. For Figure C-43, the average maximum gradient for the perimeter bar is about 80 N/mm. The force gradient results for specimen P19S50 are shown in Figures C-45 and C-47. Maximum gradients for the column and perimeter bars are 45 N/mm and 65 N/mm, respectively.

As the three specimens of the restraint series, P19RE, P19RC and P19RB, were cast from the same batch of concrete and had the same layout of reinforcement, it is considered that these specimens should have a common value of $F_b'_{\max}$. The first and second intervals of the column bar of specimen P19RE (Figure C-49), the first interval of the perimeter bar of specimen P19RC (Figure C-55) and the second interval of the column bar of specimen P19RB (Figure C-57) all reach a maximum value of about 125 N/mm. The fact that the second intervals of the perimeter bars for specimens P19RE and P19RB (Figures C-51 and C-59) reach a maximum value of only about 90 N/mm is somewhat offset by the peak gradient of about 160 N/mm over the second interval of the column bar of specimen P19RC (Figure C-53). A mean value for $F_b'_{\max}$ of about 125 N/mm is considered justified for these specimens.

6.1.2 Boundary Effects

Variations in the rotational restraint at the slab edges have an effect on the flexural capacity of the radial strip. The quantity M_r is the sum of the negative moment capacity of the radial at the column end, M^- , and the effective positive moment capacity of the radial strip at the remote end, $k_r \times M^+$. Assuming adequate anchorage and under-reinforced section, M^- is calculated taking the top mat steel passing through the column at yield. The value of M^+ is calculated in the same way as is the negative moment capacity. The magnitude of the restraint factor, k_r , varies between zero and one, depending upon the amount of rotational restraint provided at the remote end of the radial strip. Prototype slabs and most test specimens in the literature have displacement boundary conditions that make k_r easy to estimate. An isolated, simply supported column-slab specimen has no rotational restraint at the remote end of its radial strips; k_r is zero. A fully continuous plate has full restraint at the remote end of its radial strips; k_r is one.

The specimens of the present investigation were provided with force rather than displacement controlled boundary conditions. The boundary conditions for most of the test specimens are somewhere between simply supported and fully restrained. Taking the bottom reinforcement at yield, the value of M^+ , given by Equations 5.15 and 5.17, is about 4.16 kN·m for all specimens in the present investigation. The magnitude of k , is somewhere between zero and one and must be estimated for each test on the basis of measured boundary loads.

All plates were reinforced with the same bottom mat, shown in Figure A-3. It is assumed that only the full-length bottom bars were effective in distributing the positive edge moments applied by the boundary restraints. Therefore, in any one direction, the bottom mat reinforcement consists of ten #10M reinforcing bars with an average depth of 125 mm. The total moment capacity of these bars is approximately 52.0 kN·m.

Axis A-A in Figure 6.1 shows the location of the maximum positive moment across the full width of plate resulting from the edge restraint. It is assumed that, in the absence of corner restraint, the effect of the edge restraint is spread uniformly across the width of the plate. The restraint factor, k_r , at any point during a test is taken as the fraction of total available positive moment that is engaged by the edge restraint, as follows.

$$ER_{\max} = \frac{52.0 \text{ kN} \cdot \text{m}}{0.88 \text{ m}} = 59.1 \text{ kN} \quad [6.1]$$

$$k_r = \frac{ER}{ER_{\max}} \leq 1.0 \quad [6.2]$$

The corner restraint of specimens P19RC and P19RB tended to fold the plate along axis B-B, shown in Figure 6.1. Because of this, the corner restraint directly engaged only the outer three reinforcing bars of the bottom mat. Therefore, the primary shear load for specimen P19RC is calculated with only top reinforcement contributing to M_r . The magnitude of k_r is taken as zero.

For specimen P19RB it is necessary to account for the combined effects of the edge and corner restraints. Assuming that each corner restraint engages three bottom bars each way, the magnitude of CR required to form a plastic hinge along axis B-B (CR_{max}) is approximately 50.4 kN. The total number of bottom bars engaged by the corner restraint in one direction, N_{CR} , and the corresponding value of k_r , are calculated as follows.

$$N_{CR} = 6 \times \frac{CR}{CR_{max}} \quad [6.3]$$

$$k_r = \frac{ER}{ER_{max} \times \left(1 - \frac{N_{CR}}{10}\right)} \leq 1.0 \quad [6.4]$$

The total moment capacity of each radial strip at failure load is recorded in Table 6.2.

6.1.3 Correlation of Ultimate Load and Measured Force Gradient

Based on the values of $F_b'_{max}$ listed in Table 6.1, the bond model loading term, w , for each specimen is calculated according to Equation 5.13 and recorded in Table 6.2. For all specimens except P19S75 and P19S50, the maximum load for each radial strip is given by Equation 5.30.

For specimens P19S75 and P19S50, there is a change in the spacing of reinforcement at a distance, l_j , of 125 mm from the face of the column. This is accounted for by having a step in the loading diagram and requires two values of w (w and w_j). The

loading term w , applies to the region within l_c of the column face and is based on the force gradient estimates of the column bars. The value of w applies to the more widely spaced reinforcement farther away from the column. In both specimens P19S75 and P19S50, this wider spacing is 150 mm. Therefore, the value of w for both specimens is assumed equal to that obtained for specimen P19S150. For specimens P19S75 and P19S50, the maximum load for each radial strip is given by Equation 5.31.

The total load, P_{calc} , is obtained by summing the contributions from each radial strip. For interior square or circular column-slab connections with the same reinforcement in each direction, this amounts to multiplying the contribution of a single radial strip by four.

6.1.3.1 Specimens Without Fiber Reinforcement

Only specimens P19S75 and P19S50 failed at smaller loads than would be predicted by the bond model using measured values of force gradient. Anchorage failure of some of the reinforcement passing through the column, first discussed in Chapter 4, is considered to be the main reason for the comparatively poor performance of these specimens. There are, however, two other possible contributing factors. First, although additional steel through the column increases the flexural capacity of the radial strip, M_n , it does not add to the torsional strength of the plate at some distance away from the column. It follows that, with concentrated reinforcement through the column, the percentage of total load that is carried by primary shear must increase, reducing the apparent significance of torsional shear. Second, for any particular boundary condition, the value of torsional shear should depend greatly on deflection. Concentrating reinforcement through the column increases the flexural stiffness of the plate, so that development of the torsional shear mechanism is impaired.

Results similar to those obtained for specimens P19S75 and P19S50 are available in the literature. For example, Moe (1961) reports a series of tests in which the total amount of reinforcement was held constant while its distribution across the width of the plate was varied. These specimens were approximately 1800 mm square in plan and 150 mm thick, reinforced with eleven #5 bars (equivalent to #15-M bars) each way. When uniformly spaced across the width of the plate, the bars were 165 mm apart. The spacings of the central bars for the tests with concentrated reinforcement were 115 mm, 75 mm and 50 mm. The specimens with higher concentrations of reinforcement through the column failed at lower loads than did the specimens with uniformly distributed reinforcement. Similar results are reported by Elstner and Hognestad (1956) for specimens the same size as those of Moe but reinforced with #8 bars (#25-M bars). The spacing of the central reinforcement for the tests by Elstner and Hognestad was approximately 65 mm.

As is the case for specimens P19S75 and P19S50, anchorage failure is believed to be responsible for the poorer performance of the specimens with concentrated reinforcement reported by Moe and by Elstner and Hognestad. In the present investigation, anchorage proved to be critical for 100 mm² bars spaced at 50 mm and 75 mm with embedment lengths measured from the center-line of the plate between 1000 mm and 1360 mm. In the tests reported by Moe and by Elstner and Hognestad, the embedment length is reduced to approximately 900 mm and the bar area is increased to either 200 mm² or 500 mm². The reinforcement spacing, however, is similar to that used in the present investigation. It is reasonable to conclude that if anchorage was critical in specimens P19S75 and P19S50, it must surely have been critical in the tests reported by Moe and Elstner and Hognestad.

For all the remaining specimens without fiber reinforcement, the failure load exceeds the calculated load based on measured force gradients. The mechanics of the

bond model suggest that this additional load is mainly the effect of torsional shear. As discussed in Chapter 5, the effect of torsional shear is to redistribute primary shear so that the net loading of each radial strip is applied closer to the column, thereby increasing the total load that may be carried by each radial strip. The existence of torsional shear is an undeniable consequence of the plate equations of equilibrium. In Chapter 5, however, no method is proposed either to measure directly or to predict the magnitude of the torsional shear contribution to punching strength. Instead, the magnitude of the torsional shear contribution must be estimated experimentally, on the basis of the how much the ultimate loads exceed the bond model predictions.

There is a temptation to base an estimate of the torsional shear contribution on the average ratio of P_{ult} to P_{calc} for specimens P19RB, P19RC, P19RE, P19S150, P38F0 and P11F0. However, most of these specimens underwent large deflections prior to punching failure. Large deflections were accompanied by extensive yielding of the reinforcement in the vicinity of the column. Although large deflections may favour the development of torsional shear, extensive yielding reduces primary shear. This means that for most of the test specimens in this investigation, the effects of torsional shear and primary shear may not be entirely additive. Comparing the ultimate test loads with the predictions of the bond model may be misleading since neither the magnitude of the loss of primary shear nor the effect of torsional shear can be determined.

In order to estimate the torsional shear contribution, it is necessary to first determine which specimens, if any, are most likely to have developed torsional shear while maintaining the primary shear close to the column. It is assumed that this condition is satisfied if, for any test specimen, the value of force gradient over the second interval of the perimeter bar is maintained at or near its maximum value through to failure. It can be seen in Figure C-59 that specimen P19RB satisfies this criterion convincingly. The mag-

nitude of the force gradient ranges between 80 N/mm and 100 N/mm from a deflection of about 15 mm through to failure. The gradient over the second interval of the perimeter bar of specimen P38F0, shown in Figure C-27, is well maintained up to a deflection of about 50 mm. Beyond this point, the gradient begins to increase because of a decreasing bar force at the lower gauge location. Figure C-55 shows that the value of the gradient over the second interval of the perimeter bar of specimen P19RC is also relatively constant from a deflection of about 10 mm up to a deflection of about 40 mm. Although in this case, the magnitude of the gradient is not large, its constancy suggests that force gradients perpendicular to the radial strips in the vicinity of the column may have been stable.

If it is assumed that the effects of primary and torsional shear were fully additive in specimens P19RB, P38F0 and P19RC, then the average ratio for these tests of the measured ultimate test load, P_{ult} , to the calculated punching load, P_{calc} , using measured force gradients, is an experimental measure of the ratio of the combined effects of primary shear and torsional shear to primary shear alone. By this reasoning, the contribution of torsional shear is estimated at approximately 29 per cent of the bond model load based on primary shear alone.

For specimens P11F0, P19S150 and P19RE, the ratio of P_{ult} to P_{calc} , although greater than one, is less than would be expected if primary and torsional shear contributions were fully additive. Each of these specimens shows a significant drop in the magnitude of the force gradient over the second interval of the perimeter bar. This loss of gradient is caused by the spread of yielding in the reinforcement close to the column in the later stages of each test. Declining force gradients close to the column must reduce the primary shear contribution to punching strength.

The apparent decrease of shear strength with increased yielding of the reinforcement is an effect that is mentioned elsewhere. Moeble et al. (1988) present data from Hawkins and Mitchell (1979) that shows a decrease in the shear strength of a slab-column connection with increasing yielding of the reinforcement. Hawkins and Mitchell consider the loss of membrane restraint around the column to be the main reason for this effect. The bond model, however, shows that extensive yielding of reinforcement directly attacks one of the mechanisms of shear transfer, namely beam action.

6.1.3.2 Specimens With Fiber Reinforcement

As shown in Table 6.1, the addition of steel fibers to the concrete mix had surprisingly little effect on the magnitude of force gradient. Nevertheless, the fiber reinforced specimens displayed greater strength, stiffness and ductility than the companion specimens without fibers.

It is considered that fiber reinforcement increases punching strength by reducing the effects of cracking on the cross-sectional properties. Prior to cracking, it is reasonable to assume elastic behavior of the gross cross-section, with compatible strains in concrete and reinforcement. For a beam of width, b , and depth, d , shear is approximately related to strain gradient according to equation 6.6., obtained by differentiating Equation 6.5.

$$M \approx \left[E_c \times \frac{bd^2}{6} \right] \times \varepsilon = K_d \times \varepsilon \quad [6.5]$$

$$V \approx \left[E_c \times \frac{bd^2}{6} \right] \times \varepsilon' = K_d \times \varepsilon' \quad [6.6]$$

The term ε' is the strain gradient at the level of the reinforcement. For a fully cracked section under beam action, as is assumed in the bond model, the relationship between shear and strain gradient is given by:

$$V = F'_b \times jd = [E_s \times \rho bd \times jd] \times \epsilon' = K_{cr} \times \epsilon' \quad [6.7]$$

$$K_{ef}/K_{cr} = \frac{E_c}{E_s \times 6j\rho} \quad [6.8]$$

For the fiber reinforced specimens in this investigation, the ratio of K_{ef} to K_{cr} is in excess of four. This means that for any particular strain gradient in the reinforcement, the corresponding shear is over four times greater if uncracked rather than cracked behavior prevails. The effect of fiber reinforcement is to bridge cracks within the concrete, so that the fully cracked behavior assumed in the development of the bond model is never reached. The appropriate relationship between shear and strain gradient for a fiber reinforced section is somewhere between the fully cracked and the uncracked extremes.

Much of the additional strength of the fiber reinforced plates was realized after very large deformations. Because fibers improve the toughness and the post-cracking strength of the concrete, the loss of primary shear as a result of bond failure may have been less of a factor for these specimens. In addition to this, it is likely that the fiber reinforcement improves the torsional strength and torsional stiffness of the plate. This should lead to a higher torsional shear contribution to punching capacity for the fiber reinforced specimens.

6.2 Ultimate Strength Predictions Based on the Bond Model

In Section 6.1, it is shown that the bond model describes a relationship between measured force gradients in the reinforcement and the punching failure load of a slab-column connection. However, in order to use the bond model to predict the punching capacity of a slab-column connection, it is necessary to estimate the loading term, w , without benefit of measured force gradients in the reinforcement.

In Chapter 5, three methods for predicting the loading term, w , are proposed. One, $w_{M\&F}$, is based on the procedure for estimating splitting bond strength proposed by Morita and Fujii (1982). The other two, w_{ACI} and w_{BRIT} , are derived from code estimates of the one-way shear strength of beams. Each of these methods assumes that failure precedes widespread yielding. Ideally, these predictions of w could be assessed by direct comparison to the values based on measured force gradients. Unfortunately, many of the punching failures in the present investigation occurred after extensive yielding of the reinforcement. As a result, the measured force gradients and the corresponding values of w are influenced by yielding. The methods for estimating w proposed in Chapter 5 do not apply to the type of ductile punching failure observed in the present investigation.

In the following sub-sections, the different methods of predicting w are evaluated by comparing measured failure loads for 116 tests from the literature to failure loads predicted by the bond model. These results form the basis of a discussion on the relationships between two-way shear, one-way shear and bond.

6.2.1 Test Results from the Literature

Appendix E gives details of 116 test specimens from the literature. All specimens were orthogonally reinforced with uniformly spaced reinforcement, though not necessarily equally in each direction. All tests had either square or round columns. The scale of the tests varied widely, with flexural depths ranging from 35 mm to 200 mm.

The tests of Lunt (1988) and Ford and Vanderbilt (1970) had significant rotational restraint at the slab boundaries. In calculating the term M_r , these tests were assumed to have fully engaged bottom reinforcement ($k_r = 1.0$). Tests by Moe (1961), Elstner and Hognestad (1956), Regan et al. (1979), Rankin and Long (1987), Gardner (1990) and

Kinnunen and Nylander (1960) had no rotational restraint applied to plate boundaries. Only the term M^- contributes to M_x in these plates, whether or not bottom reinforcement was provided ($k_y = 0$).

Values of failure load, P_{calc} , are calculated according to the bond model using the three different estimates of the loading term, w_{ACI} , w_{BRIT} and $w_{M&F}$. The strength predictions of the bond model are shown in Figures 6.3, 6.4 and 6.5. Each figure shows the effect on the ratio of measured test strength to predicted strength as a function of the top mat reinforcing density of the radial strip, ρ^- , concrete strength, f_c' , and the ratio of column dimension to flexural depth of slab, c/d . For reference, Figures 6.6 and 6.7 show the trends of the strength predictions for the ACI and BS 8110 code procedures for the same body of test data. The results of these calculations are presented in detail in Appendix E and summarized in Table 6.3.

The most consistent result is achieved with the simplest method of estimating w , namely the ACI code value for one-way beam shear. On this body of test data, the bond model combined with w_{ACI} produces the most reliable estimates of punching strength of all the proposed methods, with a coefficient of variation of 12.3 per cent. In addition, Figure 6.3 reveals no consistent trends for the bond model using w_{ACI} .

Using w_{BRIT} , there is a strong relationship between predicted strength and reinforcing density, shown in Figure 6.4(a). As the reinforcing density increases, the ratio of test to predicted strength decreases. This indicates that using w_{BRIT} places too much emphasis on the flexural reinforcement of the slab.

Basing w on a direct estimate of bond strength resulted in the most scattered predictions of punching strength by the bond model. In Figure 6.5(a), it can be seen that there is considerable scatter for lightly reinforced specimens. However, most of the results with ratios of test to predicted failure loading excess of 1.5 are from the tests of Rankin

and Long (1987), raising the possibility that these tests have some feature that causes the Morita and Fujii procedure to be overly conservative in estimating the critical splitting bond stress. In fact, if the specimens of Rankin and Long are not included, then the average test to predicted ratio for the remaining 89 tests is 1.06 with a coefficient of variation of 14.61 per cent. One reason for the higher strengths of these tests may be their unusually small values of clear cover. This will be discussed further in Section 6.2.3.

Part (c) of Figures 6.3, 6.4 and 6.5 shows the trends of bond model predictions with the ratio of column dimension to slab depth. The results show no distinct trend toward more conservative predictions of failure load with increased values of c/d , as predicted in Chapter 5. This is not too surprising, however, since the largest value of c/d for the simply supported test specimens is less than 3.5. By the criteria developed in Chapter 5, the mechanism of the bond model should be fully applicable to all of these tests. All of the specimens shown in Figure 6.5 with values of c/d in excess of 3.5 are from the tests by Shilling and Vanderbilt (1970). These specimens were rotationally restrained on the edges. The largest value of c/d is about 10 (for specimen 8C1-13) and by the criteria developed in Chapter 5, the corresponding critical value of c/d would be in the order of 7. This means that the radial strips of this specimen should be divided between beam and arching action. Approximately 70 per cent of the radial strip carries load by the bond model mechanism; the remaining 30 per cent carries one-way beam shear. The portion of radial strip acting in one-way shear is not large enough to produce a noticeable effect.

6.2.2 One-Way Shear and Two-Way Shear

Two observations make the results obtained with the bond model using w_{ACI} and w_{BRIT} surprising: (1) the relationship between reinforcing density and critical shear stress is not a significant factor in two-way plates and (2) the magnitude of the critical shear

stress is smaller for the punching failure of a slab-column connection than it is for the shear failure of a beam. The purpose of this section is to provide an explanation for these two observations.

In Figure 6.2 from MacGregor (1988), it can be seen that for beams there is a very noticeable trend in the magnitude of the critical shear stress with changes in reinforcing density. The code value of $2\sqrt{f'_c}$ (U.S. customary units) tends to be an unconservative estimate of shear strength for lightly reinforced sections. With increasing reinforcing densities, the code value becomes a lower bound of the test data. However, using the loading term w_{ACI} , which is based on the ACI one-way critical shear stress, the bond model shows no trend in the ratio of test to predicted load with changing reinforcing densities, as shown in Figure 6.3(a). Figure 6.2 supports the approach used in the BS 8110 code, in which the critical nominal shear stress in a beam is partly a function of reinforcing density. Comparing Figures 6.3(a) and 6.4(a), however, suggests that for the bond model, accounting for reinforcing density in the loading term is not required.

The concept of a limiting nominal shear stress is often considered an essentially empirical approach to shear analysis. In two-way plates, where the nominal shear stress is combined with an assumed fixed critical section, this is certainly true. However, in a slender beam, the nominal shear stress is a good measure of the average force gradient in the plane of the reinforcement. In a beam, there is no problem in defining a critical section, and the relationship between moment and shear is fixed by gross geometry. As long as beam action is dominant, the force gradient in the reinforcement can be calculated from measured loads and known geometry. The shear stresses on any horizontal section between the reinforcement and the flexural compression block must approximately equal the nominal shear stress. Whereas nominal shear stress in a plate is usually regarded as merely an index of the severity of loading, nominal shear stress in a beam is a reasonably

accurate estimate of the actual stresses that are required by statics.

In the bond model, the flexural capacity of the radial strips accounts for the effect of variations in reinforcing density. With increasing levels of reinforcement, the flexural capacity increases and consequently, the loaded length of the radial strip increases. This is equivalent to having a critical section for punching that is a function of flexural capacity. Furthermore, it appears from the results presented in the preceding section that for two-way plates no further adjustment is required. For beams, however, the critical section is not a function of reinforcing density and yet there is ample evidence to suggest a dependency of critical shear stress on reinforcing density. Assuming that the mechanism of the bond model is correct, this implies that the factor or factors causing the relationship between critical nominal shear stress and reinforcing density in beams are not present in two-way plates. A contributing factor is that in Equation 5.30, w , which is linearly related to critical shear stress, is raised to the $1/2$ power. Therefore, the predicted punching capacity is not overly sensitive to this parameter. In itself, however, this reduced sensitivity is not enough to compensate for the the variations shown in Figure 6.2.

The bond model assumes that bond failure and shear failure are essentially synonymous. This was the central thesis of Kani (1979) in his work on deep beams. He noted that for beams, distributed bonding of the reinforcement, as distinct from remote anchorage, was a necessary prerequisite of shear failure. The explanation for any difference between one-way and two-way shear should be based on an understanding of how bond failure in a two-way plate may differ from bond failure in a beam.

For beams, the relationship between critical shear stress and reinforcing density may be the result of gradual changes in the mode of failure with changing density of reinforcement. A bond failure in a lightly reinforced beam may result from a reinforcing bar

near the corner breaking away from the rest of the beam, with either a diagonal split across the corner or an L-shaped rupture surface. At higher densities of reinforcement in a single layer, the beam tends to split horizontally at the plane of the reinforcement. Heavily reinforced beams often have multiple layers of reinforcement. With multiple layers of reinforcement, there may be less tendency for the beam to split at any one layer.

There are three reasons why there may be less variability in the critical shear stress of a two-way plate than in a beam.

- (1) In a beam, the maximum bond stress and hence, maximum shear stress, may be controlled by splitting across the corner, splitting in the plane of the reinforcement, or splitting through multiple layers of reinforcement. Such variety is not a feature of bond failure in two-way plates. Bond failures in two-way plates tend to be the result of horizontal splitting in the plane of the reinforcement. Since there is typically only one layer of reinforcement in each of two orthogonal directions, there is no effect from multiple layers of reinforcement. The corner splitting failure of beams has no counterpart in two-way plates. The kinematics of such a failure requires displacements perpendicular to the rupture surface. The horizontal components of these displacements must overcome the in-plane restraint provided by the surrounding slab.
- (2) Cracking along the length of a bar is a significant factor in the bond of that bar (CEB Bulletin d'Information #151, 1982). In a beam, this cracking results from mechanical bond of the deformed reinforcement and is highly unpredictable. In a plate, cracking along the length of each bar is formed and controlled by the two-way flexural behavior. This makes the longitudinal cracking in a plate less erratic than it is in a beam.

- (3) The typical range of slab reinforcing densities is smaller than the range given in Figure 6.2. Heavy reinforcement in the negative moment region of a slab would be in the order of 2 per cent while light reinforcement would be about 0.5 per cent. From Figure 6.2, it appears that the ACI one-way shear estimate is reasonably good for reinforcing densities between about 0.75 and 2.0.

It is concluded that the relationship between critical shear stress and reinforcing density in beams may be the result of changes in the mode of bond failure. Additional scatter in beam test may be due to the unpredictability of longitudinal cracking and variations in the detailing of the beams. In a plate, one mode of bond failure dominates. In addition, longitudinal cracking is controlled by transverse bending. As a result, there is no apparent dependency of critical shear stress on reinforcing density for two-way plates.

The ACI code value for one-way shear is $2\sqrt{f'_c}$ (U.S. customary units) or $0.166\sqrt{f'_c}$ (SI units). In Figure 6.2, for values of reinforcing density greater than about 0.75, this appears to be a lower bound value on shear strength. Therefore, one would expect conservative estimates of punching strength using the loading term w_{ACI} . However, the average ratio of test to predicted load for the bond model using w_{ACI} given in Table 6.3 is 1.29 which, from the discussion in Section 6.1.3.1, is exactly the effect that might be expected from torsional shear. This suggests that the ACI one-way shear stress is very close to the average value of beam action shear that can be sustained in a two-way plate.

The actual nominal shear stress at failure for beams with reinforcing densities between 0.75 per cent and 2.0 per cent is on average about 25 per cent higher than the code value. This means that the critical value of shear stress in a two-way flexural member is estimated at about 80 per cent of the comparable value for a one-way member. This is not a result that is in agreement with building code approaches to shear. The

BS 8110 code uses the same value for one-way shear and two-way shear. The ACI code doubles its one-way shear for application to punching failure, on the assumption that the confinement of the surrounding plate will improve its shear strength.

The underlying assumption in the code approaches is that shear is limited by stresses on a vertical surface, through the thickness of the member. However, if shear failure is the result of bond failure of the reinforcement, then it is not surprising that the critical shear stress in one-way flexure should exceed that of two-way flexure. In either a one-way or two-way flexural member, a horizontal surface between the steel and the reinforcement must supply adequate shear strength to handle the bonding requirements of the reinforcement. Failure occurs when the resultant shear stress on this surface reaches a critical value. In two-way behavior, the resultant shear stress is a vector sum of shears in two directions. This would suggest that the two-way critical shear stress should actually be only about 71 per cent of the one-way critical shear stress. This theoretical value compares reasonably well to the estimated value of 80 per cent.

Both the BS 8110 code shear provisions and the Morita and Fujii procedure for estimating bond attempt to give accurate estimates of failure in one-way members. As a result, these procedures should consistently over-estimate the critical shear in a two-way plate. On the other hand, the ACI code uses what amounts to a lower bound of the beam shear results, if one ignores values of reinforcing density less than about 0.75. By coincidence, this happens to be a good estimate of the actual critical shear stress in a two-way plate.

For completeness, the quantities w_{ACI} , w_{BRIT} and $w_{M\&F}$ are compared to the value of w based on measured force gradients from the present investigation in Table 6.4. All methods of predicting force w overestimate the values based on measured gradients. The value w_{ACI} over-estimates measured values by an average of 26 per cent. The degree of

over-estimate for both w_{BRIT} and $w_{M\&F}$ is also higher than would be expected. The reason why the various methods of estimating w do not work for the tests of the present investigation is the fact that there was extensive yielding in most of these tests. Only in specimens P19S75 and P19S50 are the force gradients controlled entirely by the splitting bond strength of the reinforcement. For the column bars of specimens P19S75 and P19S50, w_{test} agrees quite well with w_{ACI} .

6.2.3 Beam Action Shear and Bond

In applying the bond model to punching tests reported in the literature, using direct estimate of bond strength appears to be the least consistent method of estimating the loading term, w . This does not, however, disprove the hypothesis that bond failure and shear failure are synonymous. In his discussion of cracking in reinforced concrete, Base (1982) points out that some of the factors that control the average force gradient of a reinforcing bar are not directly related to bond.

In particular, Base cites the primary crack pattern, which causes strain incompatibilities between the steel and the concrete, as being a major factor affecting the average bond strength of a reinforcing bar. The primary crack pattern, however, is controlled by the overall flexural behavior of the specimen rather than by bond. In addition to this, in a two-way flexural member, the longitudinal cracking along any particular bar is controlled by the transverse bending. This may explain why code estimates for beam shear, which are based on the gross performance of complete specimens, can be more successful at predicting average bond behavior than attempts to predict the bonding behavior of a single reinforcing bar on the basis of factors such as cover and spacing which intuitively would seem to be most important.

A unique feature of the BS 8110 code is that it accounts for scale effects with the factor $(400/d)^{0.25}$. The importance of bond may help to explain why there appears to a scale effect in punching shear strengths. Descriptions of bond-slip behavior based on non-linear fracture mechanics appear to give good results (Gerstle et al. 1982). One of the implications of the fracture mechanics approach is the existence of a scale effect.

The procedure proposed by Morita and Fujii (1982) is an empirical estimate of the splitting bond failure of a one-way member. It is therefore appropriate as a basis for estimating w . However, the possible effect of a primary crack pattern on bond strength is not considered, nor is there any parameter which accounts for scale effect. The importance of scale effect may in part explain some of the scatter in the predictions of the bond model with $w_{M\&F}$. In Section 6.2.1 it was pointed out that most of this scatter could be attributed to the tests by Rankin and Long (1987). A notable feature of these tests is that the clear cover of the reinforcement is only about 5 mm, which is slightly less than the diameter of the reinforcement. If there is a scale effect and it is not accounted for, then test strengths of specimens with very small values of clear cover should be higher than those with larger values. To some extent and in spite of extensive yielding, this trend to improved performance for small values of cover is illustrated in Table 6.4.

If $w_{M\&F}$ is an accurate estimate of the loading term, then, in order to account for the effect of torsional shear, the average ratio of test strength to predicted strength should be about 1.29. The actual value is 1.16 which is only about 90 per cent of 1.29. This means that primary shear is overestimated by about 11 per cent. According to Equation 5.30, in order to over-estimate primary shear by a factor of 1.11, the loading term, w must be over-estimated by a factor of 1.24. This means that the Morita and Fujii procedure over-estimates the critical shear stress for splitting bond failure in two-way members by a factor of about 1.24. However, the Morita and Fujii procedure was developed for one-way

members. This ratio of one-way to two-way critical shear of 1.24 compares very well with the previous estimate, based on the ACI critical shear stress and Figure 6.2, of 1.25. It follows that both the Morita and Fujii procedure and the ACI critical shear stress are estimates of the same phenomenon.

6.3 Comparison of Bond Model with Code Methods

6.3.1 Critical Sections

Code approaches to estimating the punching strength of slab-column connections assume that there is a limiting nominal shear stress on some critical section, as shown in Figure 6.8. The British code uses a critical section which is $1.5d$ away from the column face and limits the nominal shear to the same value as is used for beams. The ACI code places the critical section at $0.5d$ from the column face but uses double the beam shear value as the limiting nominal stress. The equivalent to a critical section in the bond model would be the loaded length, l , along the side faces of the radial strips, as shown in Figure 6.9.

In fact, if the same value of one-way shear is used then the only difference between the bond model and the code approaches for estimating punching strength is in the definition of the critical section. The bond model assumes that for the length l , the radial strip is loaded on two sides by the maximum one-way shear. Therefore, for any radial strip of an interior column-slab connection, the total length that is loaded by one-way shear is $2l$. The length $2l$ is the equivalent of one face of the BS 8110 critical section, since both are loaded by one-way shear. Alternatively, it may be said that the radial strip is loaded by twice the one-way shear over a length of l . Therefore, the loaded length, l , of a radial strip also compares directly with one face of the ACI critical section, since both are

loaded by twice the critical one-way shear value.

In building codes, the critical section is fixed by the gross geometry of the plate and column. The side length of the critical section for the ACI code is $c + d$ while the corresponding length for the BS 8110 code is $c + 3d$. For the bond model, the length l is calculated from Equation 5.29 and is a function of the flexural strength of the radial strip and the ability of the plate to transmit a one-way shear.

The quantities $(c + d)/l$ and $(c + 3d)/2l$ are shear perimeter ratios that describe the variation between the code and bond model estimates of punching strength, assuming the same value for one-way shear is used in each case. If the shear perimeter ratio is greater than one, then the code is less conservative than the bond model. Figures 6.10 and 6.11 show the predicted effects resulting from variations in reinforcing density, concrete strength and column size.

For average levels of reinforcement and concrete strength, both the ACI and BS 8110 code procedures are in reasonably close agreement with the bond model. The bond model predicts that both code procedures become less conservative decreasing reinforcing ratio or increasing concrete strengths.

The bond model predicts opposite trends for the two codes regarding column size. With increasing column size, the ACI code becomes slightly less conservative while the BS 8110 code becomes marginally more conservative. For column sizes much larger than those shown in Figures 6.10 and 6.11, the ratio of the BS 8110 to bond model shear perimeters will eventually start to rise. It should be noted that ACI 318-89 (11.12.2.1) addresses this problem by reducing the allowable shear stress for columns with larger perimeters.

6.3.2 Effect of Aspect Ratio

For rectangular columns, with column dimensions of c_1 and c_2 , the bond model predicts decreasing strengths as the aspect ratio of the column deviates from one. The relative strength of a rectangular column is the ratio between its predicted strength and the strength of a square column having the same total perimeter.

The primary shear load for a square column with column dimension, c , is given by:

$$P_{square} = \Sigma\{2\sqrt{M \times w}\} = 8 \times \sqrt{\rho \times c \times jd^2 \times \tau_{max}d} \quad [6.9]$$

For a rectangular column, the primary shear capacity is written as follows:

$$c_2 = \beta \times c_1 \quad [6.10]$$

$$P_{rect} = \Sigma\{2\sqrt{M \times w}\} \quad [6.11]$$

$$= 4 \times \sqrt{\rho \times c_1 \times jd^2 \times \tau_{max}d} + 4 \times \sqrt{\rho \times \beta c_1 \times jd^2 \times \tau_{max}d}$$

The relative strength of a rectangular column to a square column is found by calculating the ratio between P_{rect} and P_{square} with the condition that the average side length of the columns be equal.

$$c = \frac{c_1 + c_2}{2} = \frac{c_1(1 + \beta)}{2} \quad [6.12]$$

$$\frac{P_{rect}}{P_{square}} = \text{relative strength} = \frac{\sqrt{c_1} + \sqrt{\beta c_1}}{2\sqrt{c}} = \frac{1 + \sqrt{\beta}}{\sqrt{2(1 + \beta)}} \quad [6.13]$$

The relative strength factor is plotted against aspect ratio in Figure 6.12. For comparison, the aspect ratio factor used in the ACI code is also shown as well as test results from Hawkins et al. (1971). The test results were non-dimensionalized by dividing the failure load by the area of the ACI code critical section times the critical two-way shear stress. Although the test data suggest that the ACI code reduction factor overestimates the effect of column rectangularity, it appears that the bond model slightly underestimates this effect. In the limit, the bond model value for relative strength

approaches $1/\sqrt{2}$. The relative strength factor, however, accounts only for the effects of aspect ratio on primary shear. It is anticipated that there will be an effect on torsional shear as well.

Extreme aspect ratios have a pronounced effect on the curvatures of the surrounding plate. In reporting tests on a nine panel, continuous flat plate specimen with an interior column aspect ratio of nearly 10, Simmonds (1970) states that there was "substantial one-way behavior" spanning parallel to the short face of the column. With true one-way behavior, torsional moments parallel to the reinforcement would be zero and hence, the torsional shear load would be zero. In Section 6.1.3.1, torsional shear is estimated to be about 30 per cent of the primary shear load for a square, concentrically loaded column. The loss of torsional shear would result in a strength reduction of 23 per cent. Combining the loss of torsional shear and the maximum reduction in primary shear, the effect of an extreme aspect ratio would be approximately a 45 per cent reduction in punching load.

6.4 Further Discussion of Bond Model

6.4.1 Causes of Punching Failure

According to the bond model, the punching capacity of a slab-column connection is limited by two independent quantities, namely the flexural capacity of the radial strip and the capacity of the plate to generate force gradient in the reinforcement. Anything that reduces or limits either of these quantities will affect the punching capacity of the connection.

The flexural capacity of the strip is calculated in the same way as any one-way beam. Additional flexural reinforcement in the radial strip should improve the punching strength of a slab-column connection, but only if there is adequate anchorage of this rein-

forcement. Based on the results of strain measurements on the reinforcement, anchorage failure of steel in the radial strip is cited as a likely contributing factor to the failures of specimens P19S75 and P19S50. For these two specimens, however, there were no outward indications of anchorage failure; both plates appeared to undergo typical punching failures. Factors that might contribute to anchorage failures are bar cut-offs, close spacing of steel through the column and flexural cracking which follows the reinforcement.

Heavily concentrated reinforcement through the column may locally over-reinforce the slab. As a result, assuming adequate anchorage, there would be a failure of the cantilever beam sub-structure prior to yielding of steel through the column. While this type of failure is not typical of solid slab-column connections, it may become a factor if there are significant holes in the slab near the column faces.

The loading term, w , is the product of a horizontal shear stress times the flexural depth of the plate. The magnitude of the horizontal shear is limited by the bond strength of the reinforcement. As a result, the horizontal shear is primarily a function of concrete strength. However, there may also be scale effects, owing to the brittle nature of splitting bond failure. In addition, other factors which reduce bond strength may be expected to reduce punching strength. For example, epoxy coating of reinforcement is reported to have detrimental effects on bond. Treece and Jirsa (1989) report that for splitting failures, the bond strength of epoxy coated reinforcement is about 65 per cent of the bond strength for uncoated reinforcement. From Equation 5.30, this would imply that slab-column connections with epoxy coated reinforcement will have about 81 per cent of the capacity of similar connections with uncoated reinforcement.

6.4.2 Edge Column-Slab Connections

While it is beyond the scope of this thesis to include a complete treatment of connections under combined shear and unbalanced moment, it is possible to give some indication as to how the bond model may be used for edge column-slab connections.

At maximum capacity, the only differences between interior, edge and corner column connections are the number of radial strips and the loading of these strips. An interior column has four radial strips. The total load on each strip is $2w$ since each strip has two adjacent quadrants of two-way plate. An edge column-slab connection has three radial strips. Two of these are parallel to a free edge of the plate. The loading of these two strips is limited to w since there is adjacent two-way plate on only one side. The remaining strip is loaded by $2w$ since there are sections of two-way plate on both sides. A corner column has only two radial strips, and each of these is loaded by w .

Based on the discussion above, it may be said that the bond model already handles one point on the shear-moment interaction diagrams of both edge and corner columns. The extension of the bond model to handle the complete interactions of edge and corner columns would be based on the procedure developed for the truss model. The truss model was shown to handle the interaction of shear and moment at an edge column-slab connection very well (Simmonds and Alexander, 1987). The essential feature of this model, allowing the development of a complete shear-moment interaction, is that it ties the flexural capacity of the plate in the immediate vicinity of the column to the shear length of the connection.

The link between flexural capacity and punching strength is also a feature of the bond model. As a result, no great adjustment to the shear-moment interaction procedure of the truss model is required in order to incorporate the bond model mechanism for vertical load transfer.

6.4.3 Relationship Between Other Models and the Bond Model

The bond model is a modification of the truss model. Many of the features of the truss model are retained, such as the presence of radial arching action and the link between flexural capacity and shear strength. However, the mechanism of punching failure proposed in the bond model suggests that the concept of a critical shear stress on a critical section, an approach favoured by most building codes, is not unrealistic. The bond model may be viewed as a bridge between two radically different models of behavior, namely the strut and tie model and the critical shear stress model.

The most important distinction between the bond model and most other models is that the bond model approaches a lower bound estimate for punching shear. There are three requirements for a lower bound solution: (1) equilibrium must be satisfied at every point, (2) no element may be loaded beyond its relevant capacity and (3) there must be sufficient ductility to allow redistribution of load. The development of the bond model in Chapter 5 is based on the equilibrium of a radial strip. The flexural strength of this strip is estimated according to accepted procedures for reinforced concrete. All loads that can enter this strip are limited by the shear capacity of the adjacent quadrants of two-way plate. Equilibrium of the strip is satisfied. Whether or not the bond model constitutes a lower bound solution for punching depends upon the ductility of the bond mechanisms that generate moment gradient and hence, the loading term w . If bond is sufficiently ductile, then the procedure for optimizing the loading of the radial strip satisfies the requirements of a lower bound solution.

6.4.4 Future Work

It is tempting to suggest a design procedure based on the bond model in its present state. In fact, for concentrically loaded columns, Equation 5.30 combined with w_{ACI} is

suitable for design without modification. As shown in Table 6.3, it is more reliable as a predictor of brittle punching failure than either the ACI or BS 8110 codes. This, however, does not constitute a complete design procedure. There are many effects that must be better understood before a general design procedure is developed.

In particular, the factors affecting torsional shear need to be investigated. It is suggested previously that both column aspect ratio and concentration of reinforcement through the column may reduce the effect of torsional shear. Eccentric loading is also likely to affect torsional shear.

Openings in the slab are expected to have several effects. If an opening is located on the side face of the radial strip, then it prevents loading of the strip at this point by the adjacent plate. An opening within the radial strip near the column may result in an over-reinforced condition for the radial strip. Finally, the bond strength of reinforcement passing near an opening may be reduced.

The effects on slab-column behavior from factors such as eccentric loading, aspect ratio, concentration of reinforcement and slab openings can only be understood if tests provide some insight into the internal workings of the connection. There is a considerable body of test data in the literature but these test results focus primarily on the gross load-deflection behavior of the specimens. If it is to extend our understanding of the behavior of slab-column connections, future testing must place more emphasis on strain measurements and, in particular, measurements of strain gradient. The bond model provides a tool for relating internal strain measurements on reinforcement to the punching load of the overall specimen.

Table 6.1 Measured Force Gradients

Test	spacing (mm)	d (mm)	d' (mm)	f'_c (MPa)	$F'_b \text{ max}$ (N/mm)
P11F0	150	133	24	33.2	100
P11F31	150	135	23	35.8	110
P11F66	150	134	23	35.0	110
P38F0	150	107	49	35.6	130
P38F34	150	108	48	38.4	130
P38F69	150	108	47	38.5	130
P19S150	150	127	30	26.0	100
P19S75 (col.bar)	75	124	31	26.0	65
P19S50 (col.bar)	50	126	31	26.0	45
P19S75 (per.bar)	112.5	124	31	26.0	80
P19S50 (per.bar)	100	126	31	26.0	65
R series	150	127	31	35.3	125

Table 6.2 Primary Shear Loads Based on Measured Gradients

Test	M_s (kN·m)	w (N/mm)	w_1 (N/mm)	P_{calc} (kN)	P_{ult} (kN)	$\frac{P_{ult}}{P_{calc}}$
P11F0	9.2	85.2	N/A	224	256	1.14
P11F31	10.8	95.5	N/A	259	324	1.25
P11F66	10.6	94.7	N/A	255	345	1.35
P38F0	7.9	88.6	N/A	212	364	1.24
P38F34	9.1	89.7	N/A	230	308	1.34
P38F66	9.8	89.7	N/A	239	329	1.38
P19S150	9.3	80.3	N/A	218	258	1.18
P19S75	14.5	80.3	96.0	287	258	0.90
P19S50	20.8	80.3	95.6	339	318	0.94
P19RE	9.5	100.1	N/A	247	304	1.23
P19RC	7.0	100.1	N/A	212	282	1.33
P19RB	11.2	100.1	N/A	268	343	1.28

Table 6.3 Summary of Bond Model Results for Tests in Literature (116 Tests)

basis for w	Bond Model			Code Estimates	
	ACI	BS 8110	Morita & Fujii	ACI	BS 8110
Average Test/Predicted	1.29	1.05	1.16	1.59	1.06
Standard Deviation	0.16	0.17	0.25	0.42	0.16
Coeff. of Variation (%)	12.33	16.29	21.66	26.47	15.08

Table 6.4 Measured and Predicted Values of w

Test	w_{TEST}	w_{ACI}	$\frac{w_{TEST}}{w_{ACI}}$	w_{BRIT}	$\frac{w_{TEST}}{w_{BRIT}}$	$w_{M\&F}$	$\frac{w_{TEST}}{w_{M\&F}}$
P11F0	85.2	127.2	0.670	129.6	0.658	146.6	0.581
P11F31	95.5	134.1	0.712	133.7	0.714	149.6	0.638
P11F66	94.7	131.6	0.719	132.3	0.716	146.7	0.645
P38F0	88.6	106.0	0.836	121.1	0.731	189.5	0.467
P38F34	89.7	111.1	0.808	124.7	0.720	199.5	0.450
P38F66	89.7	111.2	0.807	124.8	0.719	199.7	0.449
P19S150	80.3	107.5	0.747	117.2	0.685	147.9	0.543
P19S75(col.)	96.0	105.0	0.915	146.1	0.657	180.7	0.531
P19S50(col.)	95.6	106.7	0.896	168.3	0.568	178.0	0.537
R-Series	100.1	123.3	0.812	128.9	0.777	176.9	0.566
	average		0.792		0.694		0.541
	st.dev.		0.080		0.057		0.071
	C.O.V.		10.073		8.194		13.055

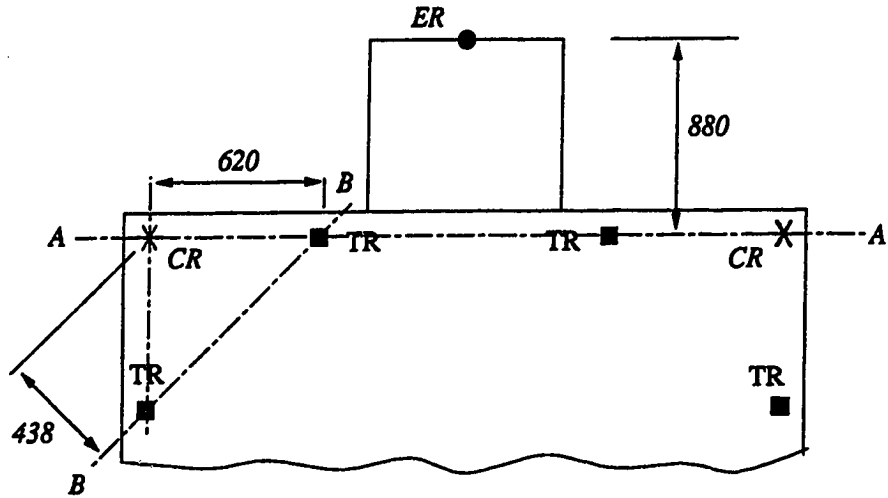


Figure 6.1 Geometry for Determining Effectiveness of Bottom Reinforcement

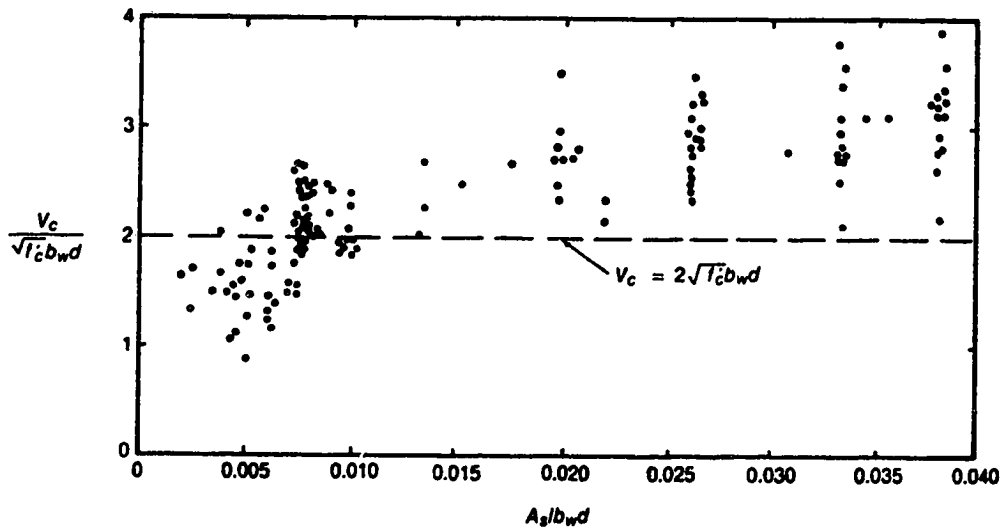


Figure 6.2 Effect of Reinforcement Ratio on One-Way Shear Strength (from MacGregor, 1988)

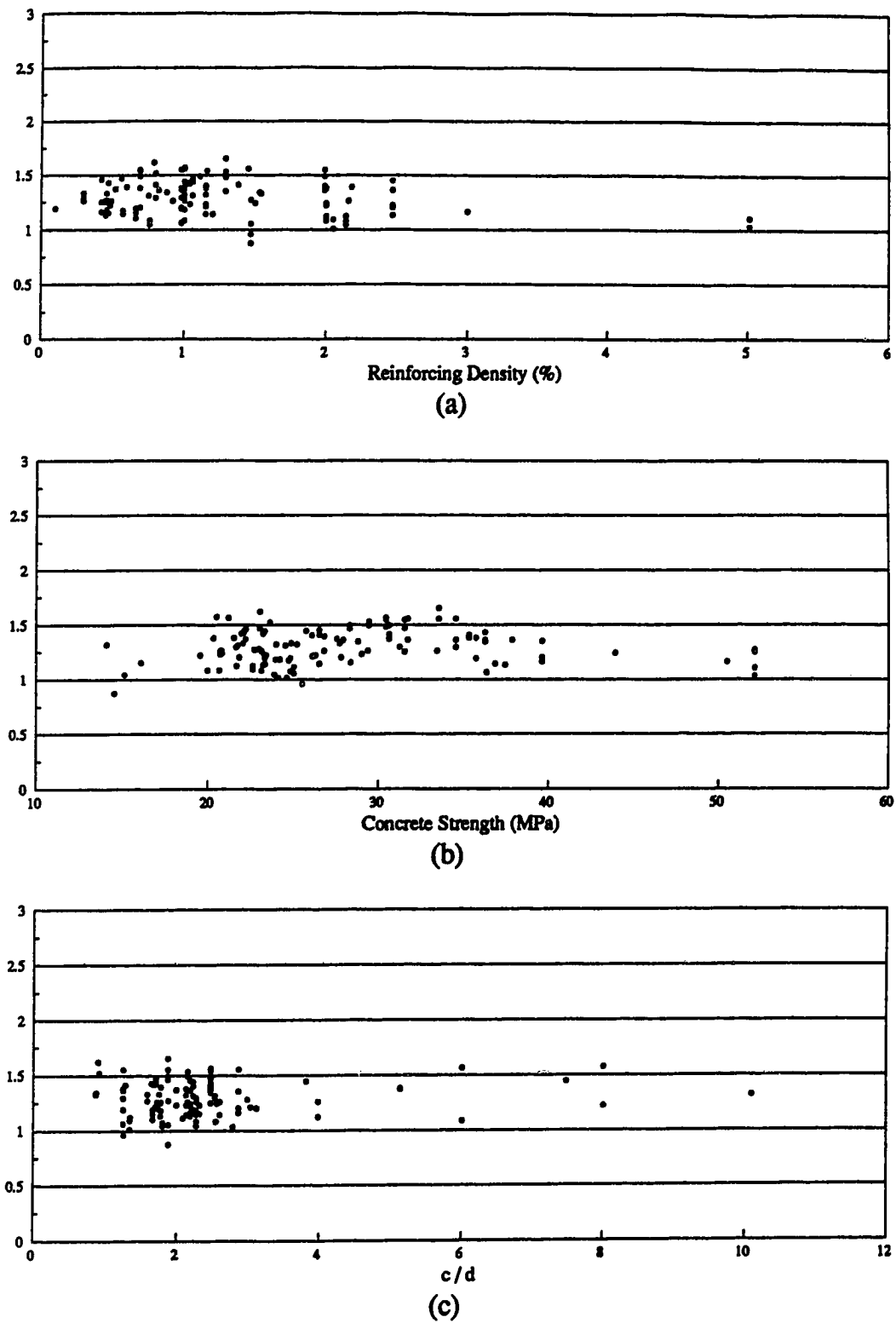


Figure 6.3 Bond Model Predictions Using ACI Code One-Way Shear Stress

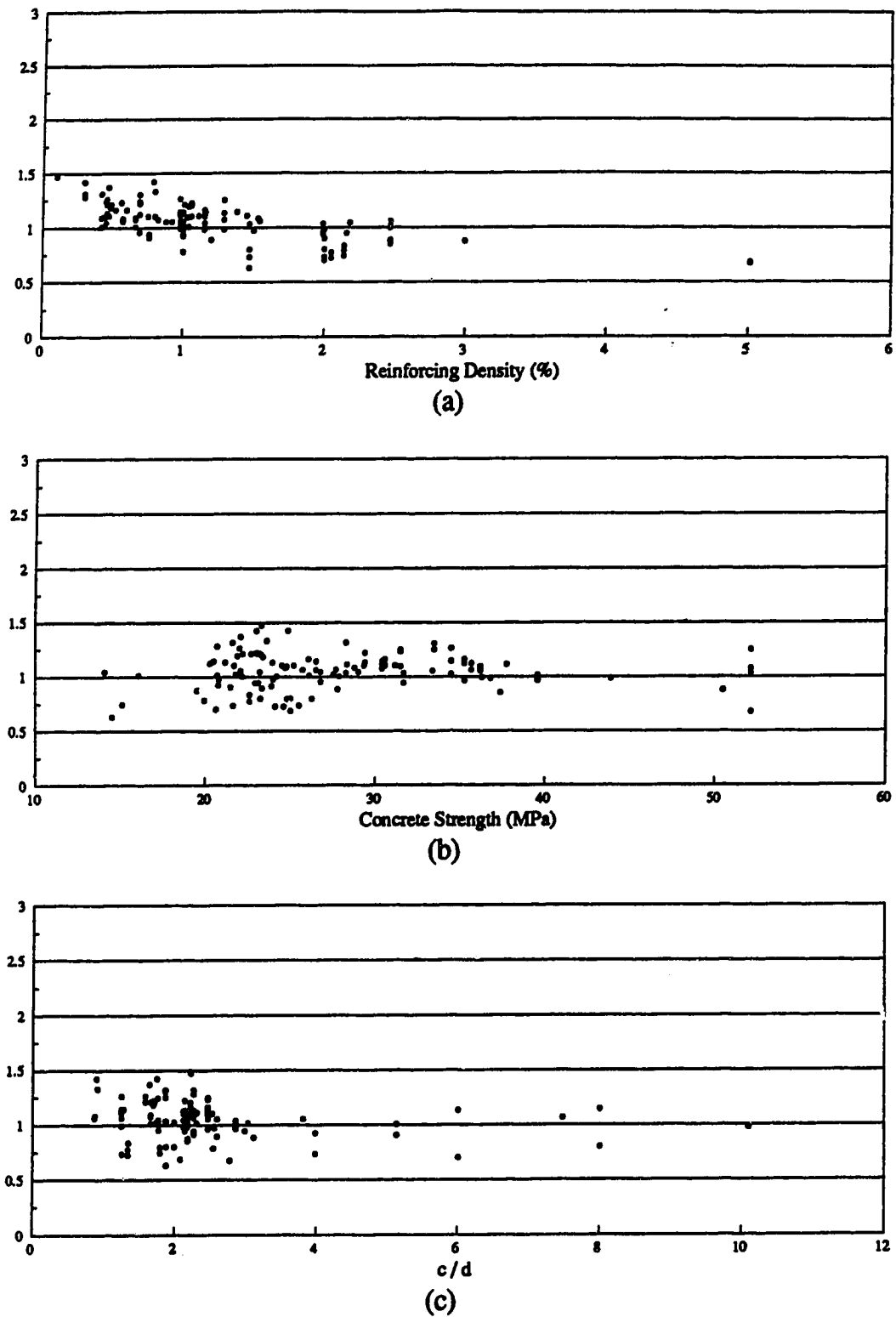


Figure 6.4 Bond Model Predictions Using BS 8110 Code One-Way Shear Stress

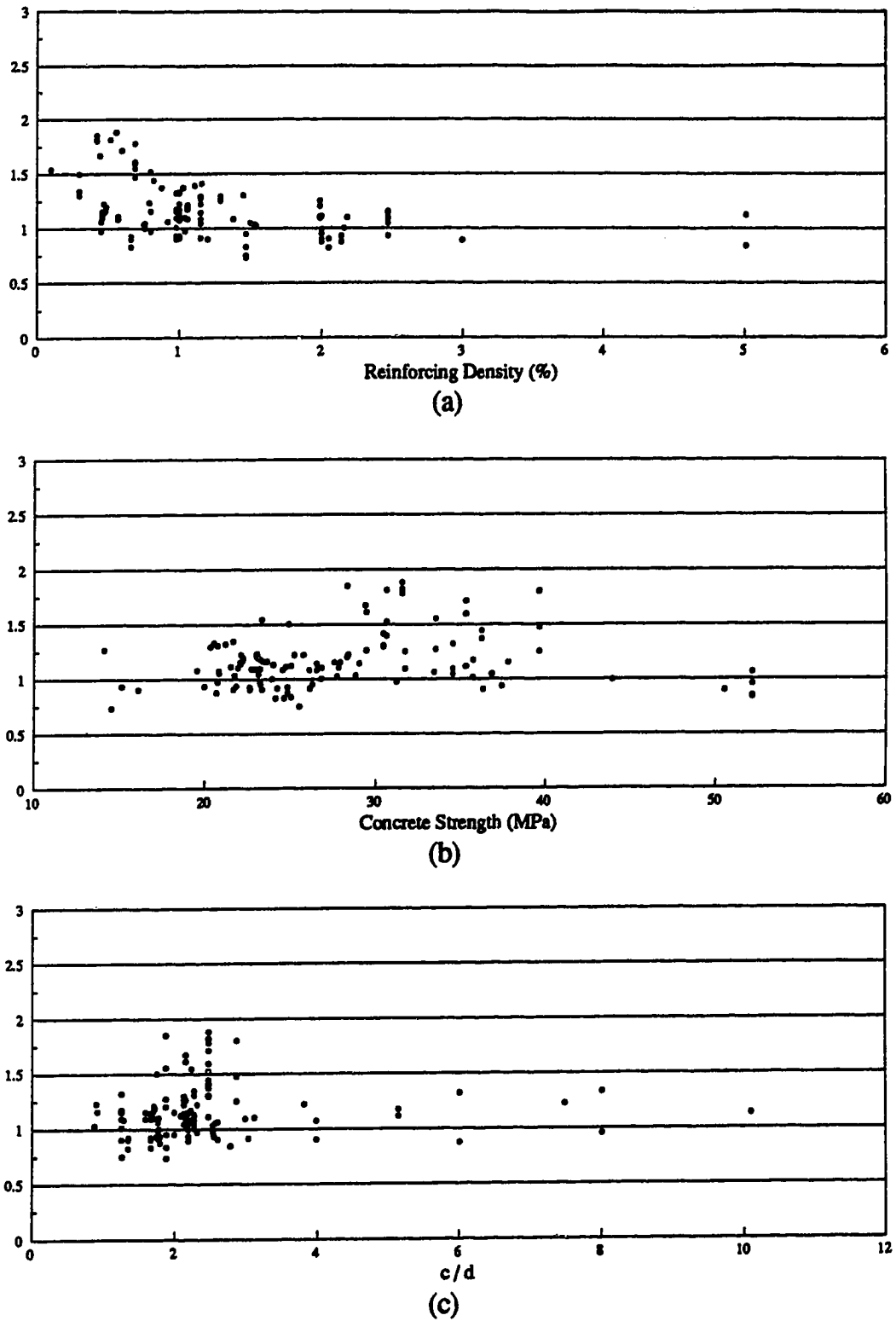


Figure 6.5 Bond Model Predictions Using Morita and Fujii Estimate of Bond Strength

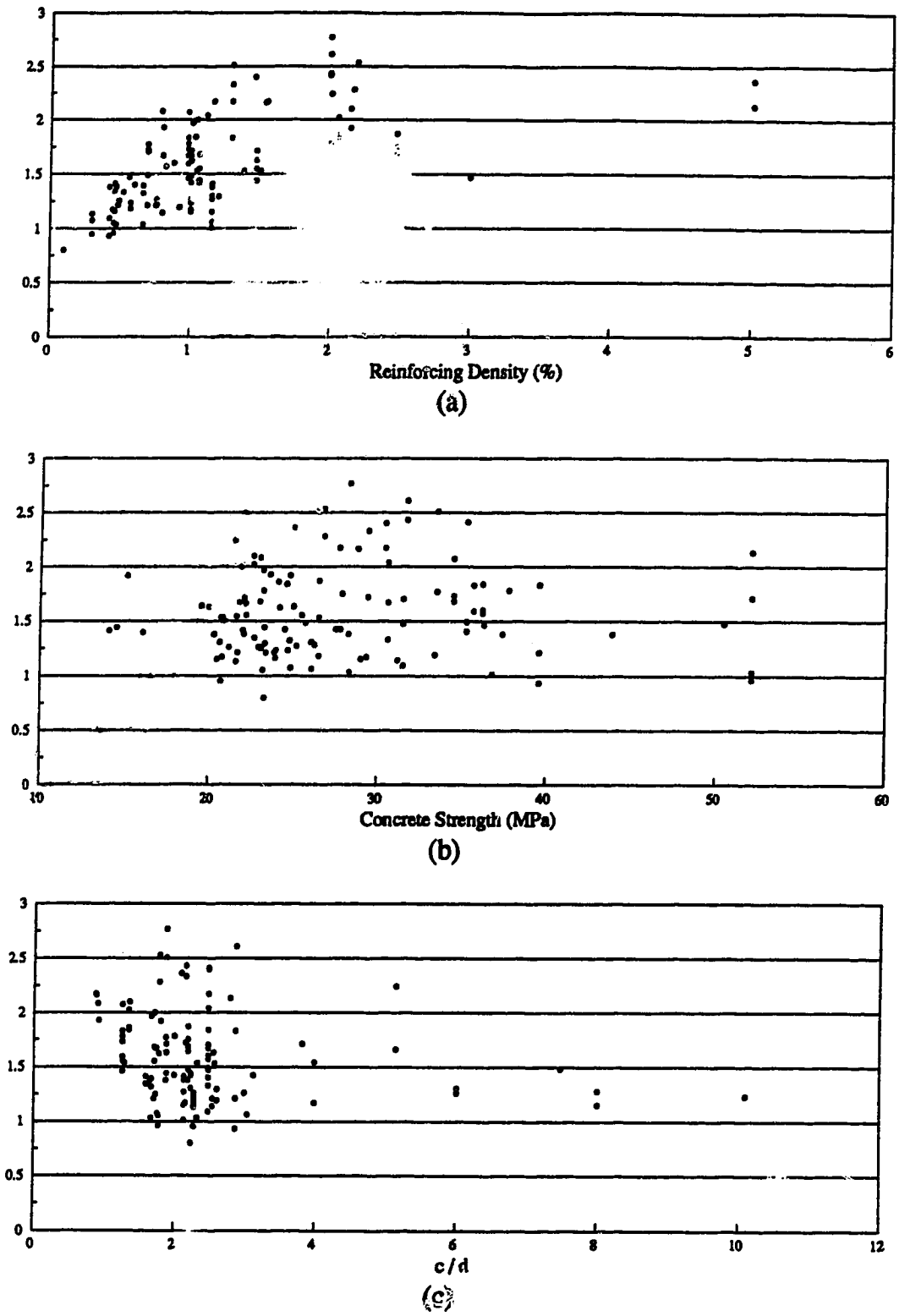


Figure 6.6 ACI Code Predictions

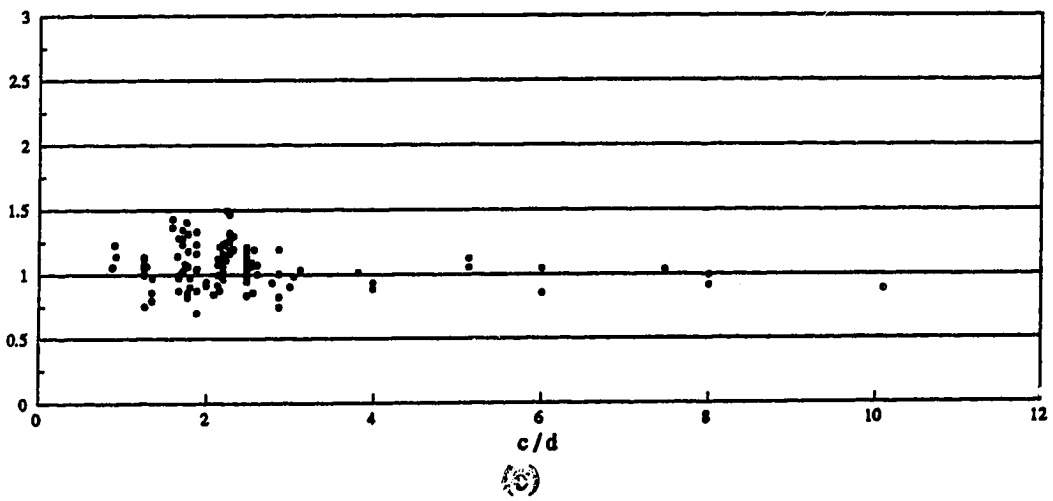
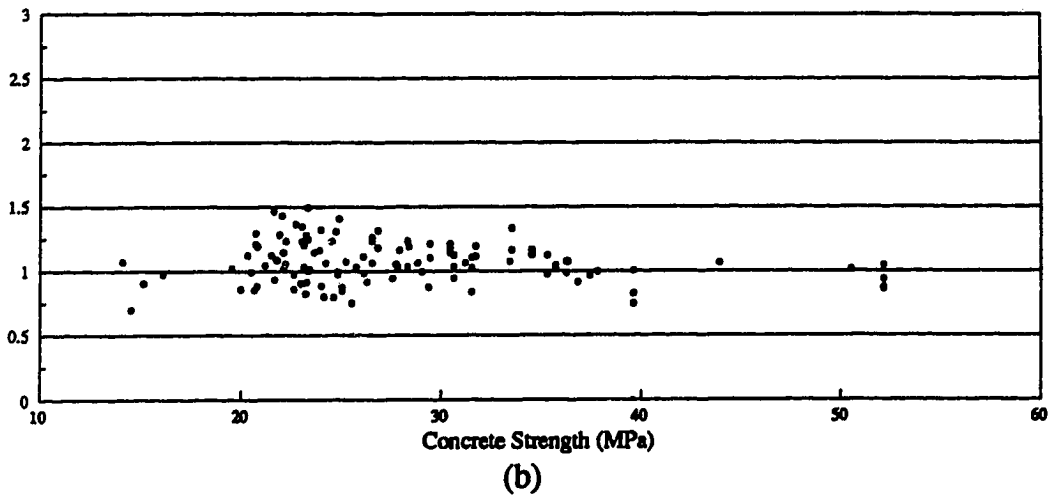
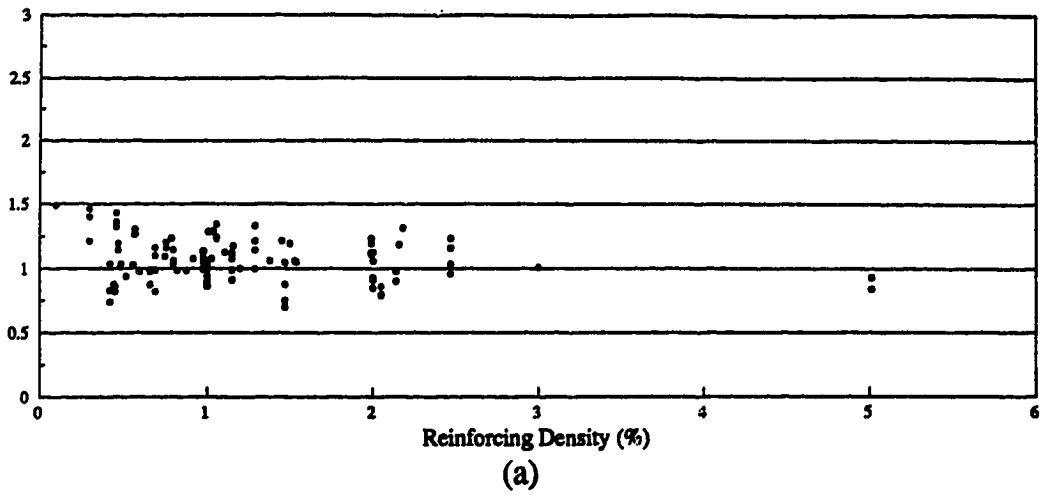


Figure 6.7 BS 8110 Code Predictions

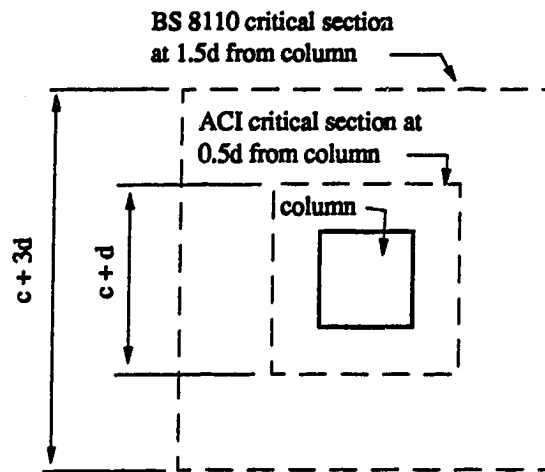


Figure 6.8 Critical Sections Defined by Codes

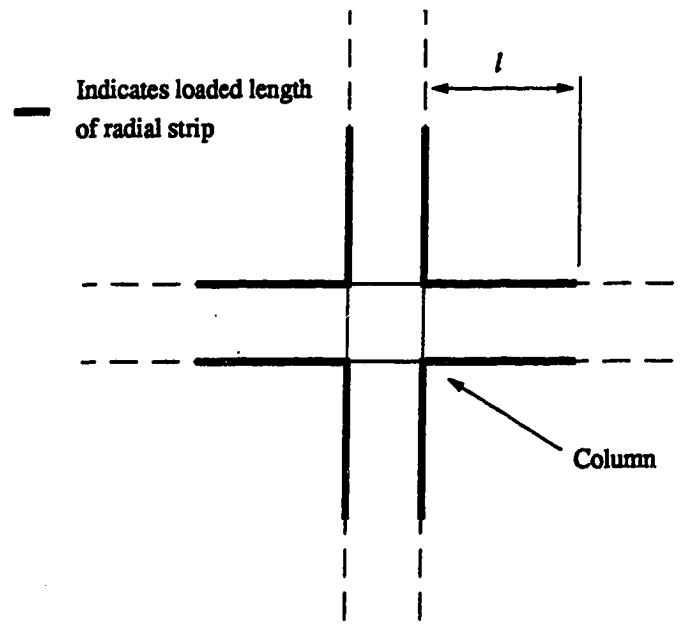
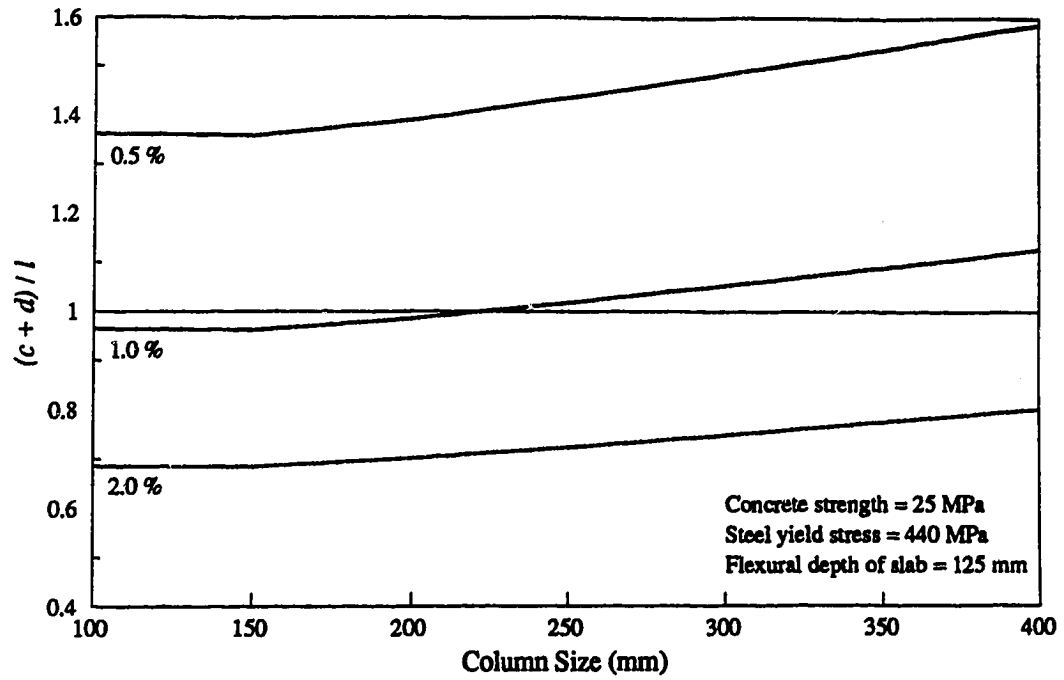
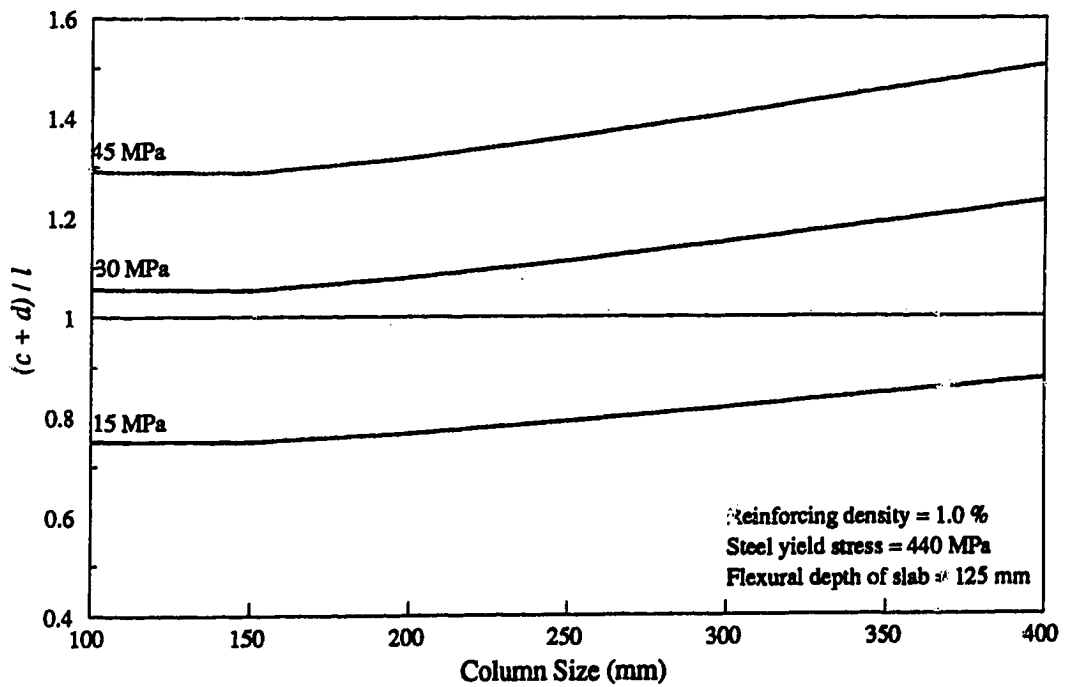


Figure 6.9 Equivalent of Critical Section for Bond Model

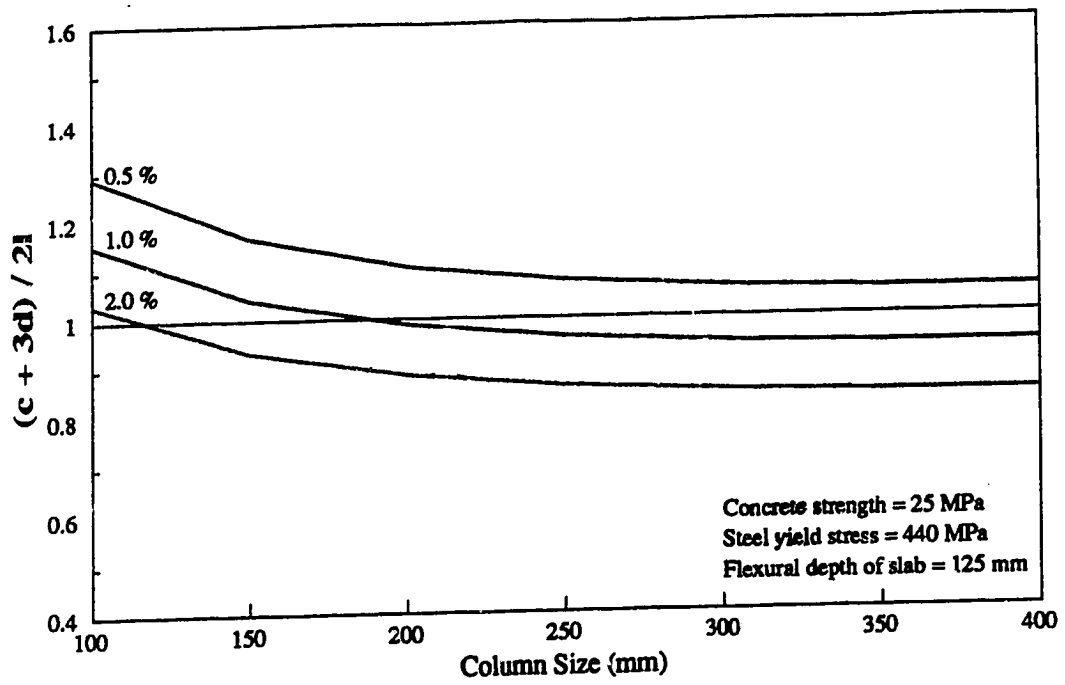


(a) Variation in reinforcing density

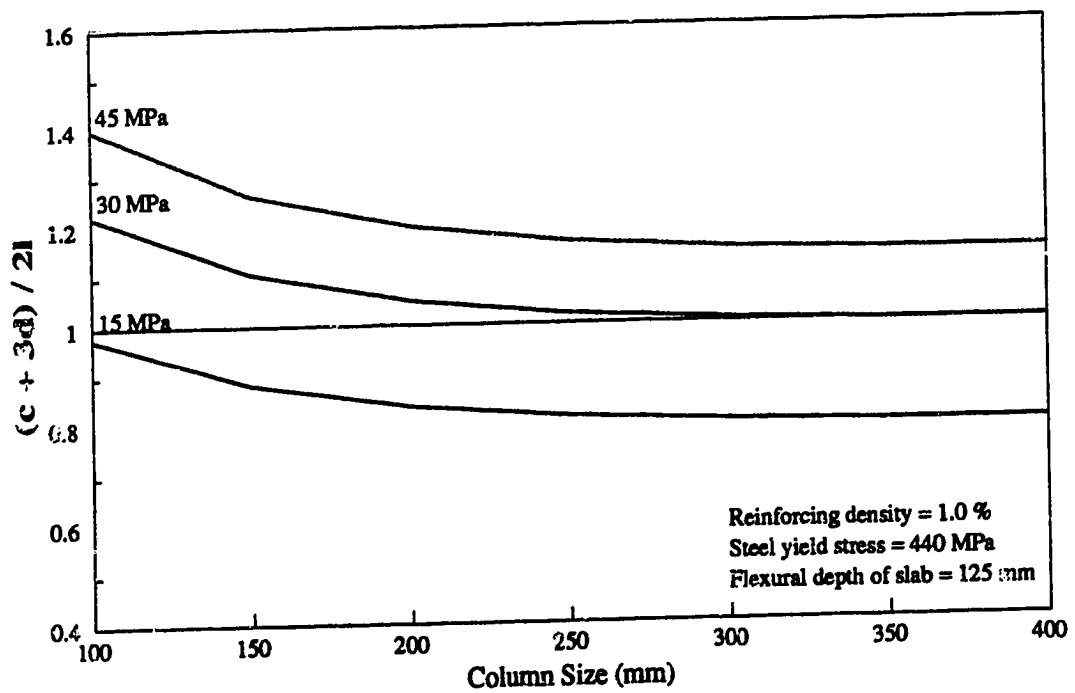


(b) Variation in concrete strength

Figure 6.10 Comparison of Bond Model and ACI Code



(a) Variation in reinforcing density



(b) Variation in concrete strength

Figure 6.11 Comparison of Bond Model and BS 8110 Code

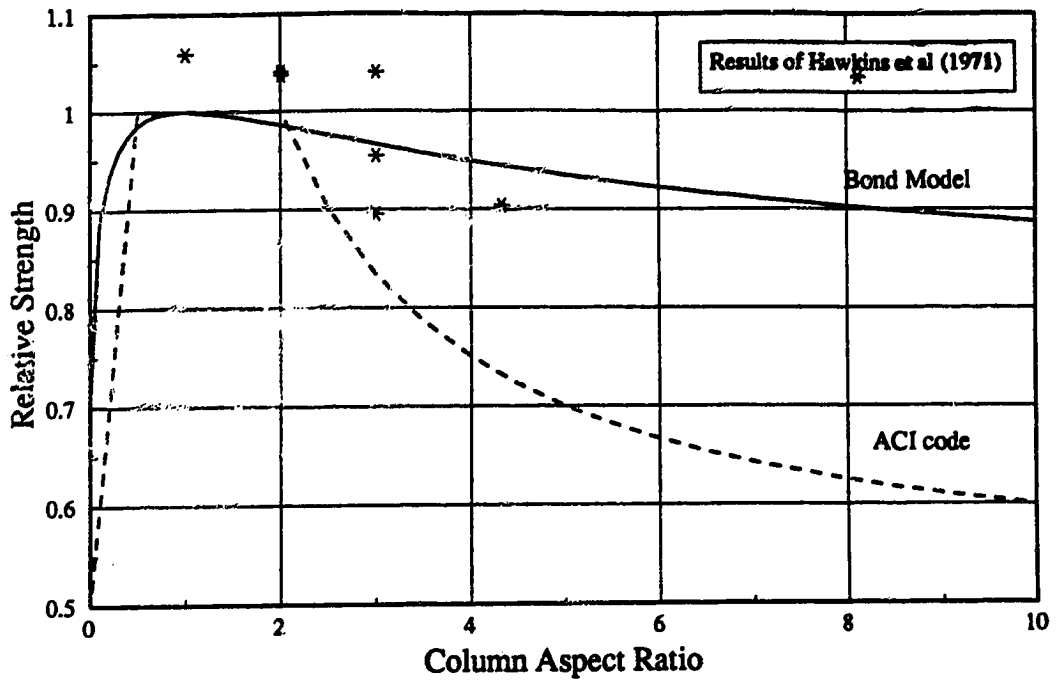


Figure 6.12 Effect of Column Rectangularity

Chapter 7

Conclusions

The major conclusions of this thesis are summarized as follows.

- (1) The truss model does not adequately explain the behavior of slab-column connections.
- (2) A modification of the truss model, called the bond model, addresses the inadequacies of the truss model retaining its advantages.
- (3) Punching failure results from a loss of force gradient in the slab reinforcement close to the column. A loss of force gradient in the reinforcement reduces the ability of the slab to carry shear by beam action.
- (4) Force gradient in slab reinforcement, and hence, beam action shear capacity, may be lost either through yielding of the reinforcement, which leads to a ductile punching failure, or by bond failure, which leads to a brittle punching failure. The ACI code value for critical one-way shear stress is an accurate estimate of beam action shear strength in a two-way plate.
- (5) Anchorage failure of slab reinforcement that passes through the column is not distinguishable from punching failure on the basis of external appearances. Detection of anchorage failure requires strain measurements at intervals along the reinforcement.
- (6) Steel fiber reinforcement improves the strength and ductility of slab-column connections by reducing the effects of cracking and not by increasing the magnitude of force gradient in the reinforcement.
- (7) If future testing is to contribute to the understanding of slab-column connection behavior, it must incorporate strain measurements, and in particular, strain gradient measurements, of the reinforcement.

- (8) The bond model approaches a lower bound solution for punching strength.**
- (9) The bond model provides an explanation as to why the assumption of a critical shear stress on a critical section is not unreasonable. It provides some theoretical justification for the critical shear stress models employed by most building codes.**

References

- ACI Committee 318-83: 1983. Building code requirements for reinforced concrete. American Concrete Institute, Detroit, MI.
- ACI Committee 318-89: 1989 Building code requirements for reinforced concrete. American Concrete Institute, Detroit, MI.
- ACI Committee 584, 1988. Design considerations for steel fiber reinforced concrete. American Concrete Institute Structural Journal, Vol.85, No.5, pp. 563-580.
- Alexander, S.D.B. and Simmonds, S.H. 1986. Shear-Moment Transfer in Slab-Column Connections. Structural Engineering Report No. 141, Department of Civil Engineering, University of Alberta, Edmonton, Alberta.
- Alexander, S.D.B., and Simmonds, S.H. 1987. Ultimate strength of slab-column connections. American Concrete Institute Structural Journal, Vol.84, No.3, pp. 255-261.
- Alexander, S.D.B., and Simmonds, S.H. 1988. Shear-moment interaction of slab-column connections. Canadian Journal of Civil Engineering, Vol.15, No.5, pp. 828-833.
- Bartolotti, L. 1990. Punching shear strength in concrete slabs. American Concrete Institute Structural Journal, Vol.87, No.2, pp. 208-219.
- Base, G.D. 1982. Bond, and control of cracking in reinforced concrete. Bond in Concrete, edited by P. Bartos, Applied Science Publishers, London, pp. 446-457.
- British Standards Institution, 1985. The structural use of concrete: Part 1, Code of practice for design and construction (BS 8110:Part 1). British Standards Institution, London.
- Broms, C.E. 1990. Punching of flat plates- a question of concrete properties in biaxial compression and size effect. American Concrete Institute Structural Journal, Vol.87, No.3, pp. 292-304.
- CAN3-A23.3-M84: 1984. Design of concrete structures for buildings. Canadian Standards Association, Rexdale, Ontario, Canada.
- CEB Bulletin d'Information No. 151 1982. Bond action and bond behavior of reinforcement. Comité Euro-International du Béton. Bulletin No. 151.
- Clyde, D.H., and Carmichael, D. 1974. Lower bound flexural fields and slab shear. Shear in Reinforced Concrete, SP-42, American Concrete Institute, Detroit, MI, pp. 769-783.
- Criswell, M.E. 1974. Static and dynamic response of reinforced concrete slab-column connections. Shear in Reinforced Concrete, SP-42, American Concrete Institute, Detroit, MI, pp. 721-746.

- Criswell, M.E. and Hawkins, N.M. 1974. Shear strength of slabs: basic principle and their relation to current methods of analysis. *Shear in Reinforced Concrete, SP-42*, American Concrete Institute, Detroit, MI, pp. 641-676.
- Elstner, R.C., and Hognestad, H. 1956. Shearing strength of reinforced concrete slabs. *Journal of the American Concrete Institute, Proceedings*, Vol.53, No.1, pp. 29-58.
- Ford, R.O. and Vanderbilt, M.D. 1970. Analysis of shear test structure. *Structural Research Report No. 4*, Colorado State University, Fort Collins.
- Gardner, N.J. 1990. Relationship of the punching shear capacity of reinforced concrete slabs with concrete strength. *American Concrete Institute Structural Journal*, Vol.87, No.1, pp. 66-71.
- Gerstle, W.; Ingraffea, A.R.; Gergely, P. 1982. Tension stiffening: a fracture mechanics approach. *Bond in Concrete*, edited by P. Bartos, Applied Science Publishers, London, pp. 97-106.
- Gesund, H. 1975. Punching strength design criteria for flat slabs. Meeting Preprint, ASCE National Structural Engineering Convention, New Orleans, 28 pp.
- Hawkins, N.M.; Fallsen, H.; Hinojosa, R. 1971. Influence of column rectangularity on the behavior of flat plate structures. *Cracking, Deflection and Ultimate Load of Concrete Slab Systems, SP-30*, American Concrete Institute, Detroit, MI, pp. 127-146.
- Hawkins, N.M., and Mitchell, D. 1979. Progressive collapse of flat plate structures. *Journal of the American Concrete Institute, Proceedings*, Vol.76, No.7, pp. 775-808.
- Hillerborg, A. 1975. Strip method of design. Viewpoint Publications, Cement and Concrete Association, Wexham Springs, Slough.
- Hillerborg, A. 1985. Results of three comparative test series for determining the fracture energy G_f of concrete. *Materials and Structures, Research and Testing (RILEM, Paris)*, Vol.18, No.107, pp. 407-413
- Kani, G.N.J. 1979. Kani on shear in reinforced concrete. Edited by M.W. Kani, M.W. Huggins and R.R Wittkopp. Department of Civil Engineering, University of Toronto.
- Kanoh, Y., and Yoshizaki, S. 1979. Strength of slab-column connections transferring shear and moment. *Journal of the American Concrete Institute, Proceedings*, Vol.76, No.3, pp. 461-478
- Kinnunen, S., and Nylander, H. 1960. Punching of concrete slabs without shear reinforcement. *Transactions of the Royal Institute of Technology (Sweden)*, No.158, Stockholm, pp. 1-110.
- Long, A.E., and Masterson, D.M. 1974. Improved experimental procedure for determining the punching strength of reinforced concrete flat slab structures. *Shear in Reinforced Concrete, SP-42*, American Concrete Institute, Detroit, MI, pp 921-935.

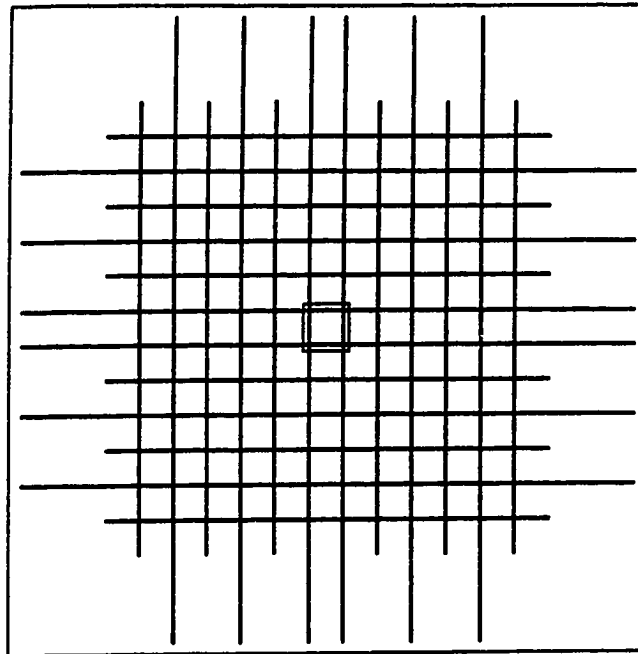
- Long, A.E. 1975. A two-phase approach to the prediction of the punching strength of slabs. *Journal of the American Concrete Institute, Proceedings*, Vol.72, No.2, pp. 37-45.
- Lunt, B.G. 1988. Shear strength of reinforced concrete slabs at column supports. PhD thesis, Faculty of Engineering, University of Witwatersrand, Johannesburg. 292 pp.
- Marti, P., and Kong, K. 1987. Response of reinforced concrete slab elements to torsion. *Journal of Structural Engineering, ASCE*, Vol.113, No.5, pp. 976-993.
- Masterson, D.M., and Long, A.E. 1974. The punching strength of slabs, a flexural approach using finite elements. *Shear in Reinforced Concrete, SP-42, American Concrete Institute, Detroit, MI*, pp. 747-768
- MacGregor, J.G. 1988. *Reinforced Concrete*. Prentice Hall, Englewood Cliffs, New Jersey.
- MacGregor, J.G. 1989. Free body diagrams, mechanical models, and experimental evidence. *Concrete International*, Vol.11, No.6, pp. 72-78.
- Moe, J. 1961. Shearing strength of reinforced concrete slabs and footings under concentrated loads. *Development Department Bulletin No. D47, Portland Cement Association, Skokie*.
- Moehle, J.P.; Kreger, M.E.; Leon, L. 1988. Background to recommendations for design of reinforced concrete slab-column connections. *American Concrete Institute Structural Journal*, Vol.85, No.6, pp. 636-644.
- Morita, S., and Fujii, S. 1982. Bond capacity of deformed bars due to splitting of surrounding concrete. *Bond in Concrete*, edited by P. Bartos, Applied Science Publishers, London, pp. 331-341.
- Rankin, G.I.B., and Long, A.E. 1987. Predicting the punching strength of conventional slab-column specimens. *Proceedings of the Institution of Civil Engineers, Part 1*, Vol.82, pp. 327-346.
- Regan, P.E. 1983. Behavior of reinforced concrete flat slabs. CIRIA Report 89, Construction Industry Research and Information Association, London, United Kingdom.
- Regan, P.E.; Walker, P.R.; Zakaria, K.A.A. 1979. Tests of reinforced concrete flat slabs. CIRIA Project No. RP 220, Polytechnic of Central London.
- Regan, P.E., and Braestrup, M.W. 1985. Punching shear in reinforced concrete: a state of the art report. *Bulletin d'Information No. 168, Comité Euro-International du Béton, Lausanne, Switzerland*.
- RILEM, 1985. Determination of the fracture energy of mortar and concrete by means of three-point bend tests on notched beams: draft recommendation. *Materials and Structures, Research and Testing (RILEM, Paris)*. Vol.18, No.106, pp. 285-290.

- Shilling, R.C., and Vanderbilt, M.D. 1970. Behavior of shear test structure. Structural Research Report No. 4, Colorado State University, Fort Collins. 66 pp.
- Simmonds, S.H. 1970. Flat slabs supported on columns elongated in plan. Journal of the American Concrete Institute, Proceedings, Vol.67, No. 12, pp. 967-975.
- Simmonds, S.H., and Alexander, S.D.B. 1987. Truss model for edge column-slab connections. American Concrete Institute Structural Journal, Vol.84, No.4, pp. 296-303.
- Treece, R.A. and Jirsa, J.O. 1989. Bond strength of epoxy-coated reinforcing bars. American Concrete Institute Materials Journal, Vol.86, No.2, pp. 167-174.

Appendix A: Reinforcement Details

Top mat for:

- P11F0
- P11F31
- P11F66
- P38F0
- P38F34
- P38F69
- P19S150

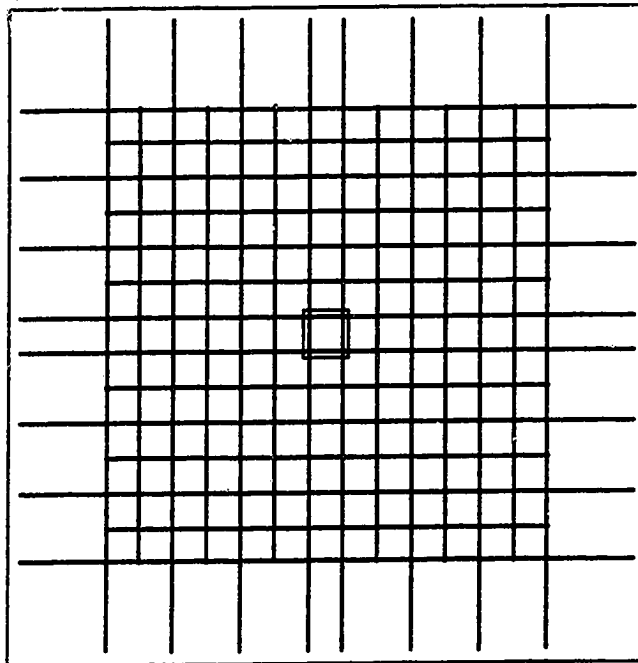


11 @ 150

2000
2720

Top mat for:

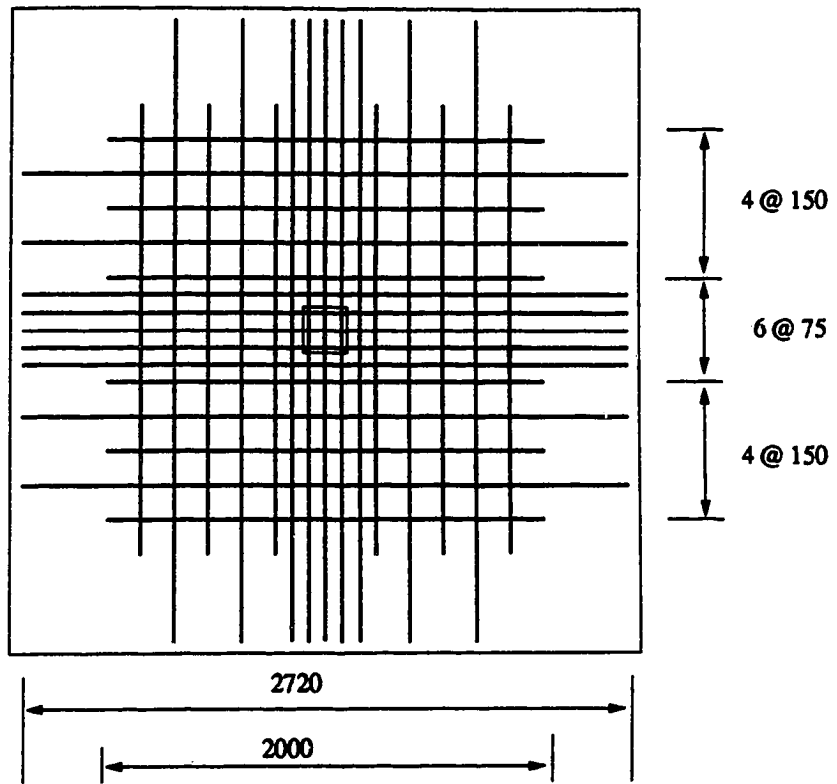
- P19RE
- P19RC
- P19RB



13 @ 150

Figure A-1 Top Mats with Reinforcement Spaced at 150 mm

Top mat: P19S75



Top mat: P19S50

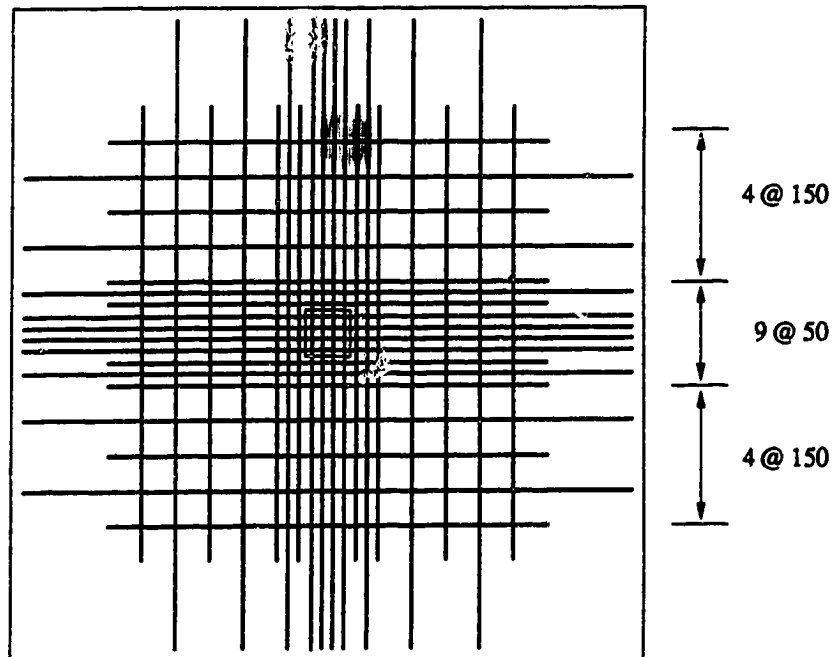


Figure A-2 Top Mats for Specimens P19S75 and P19S50

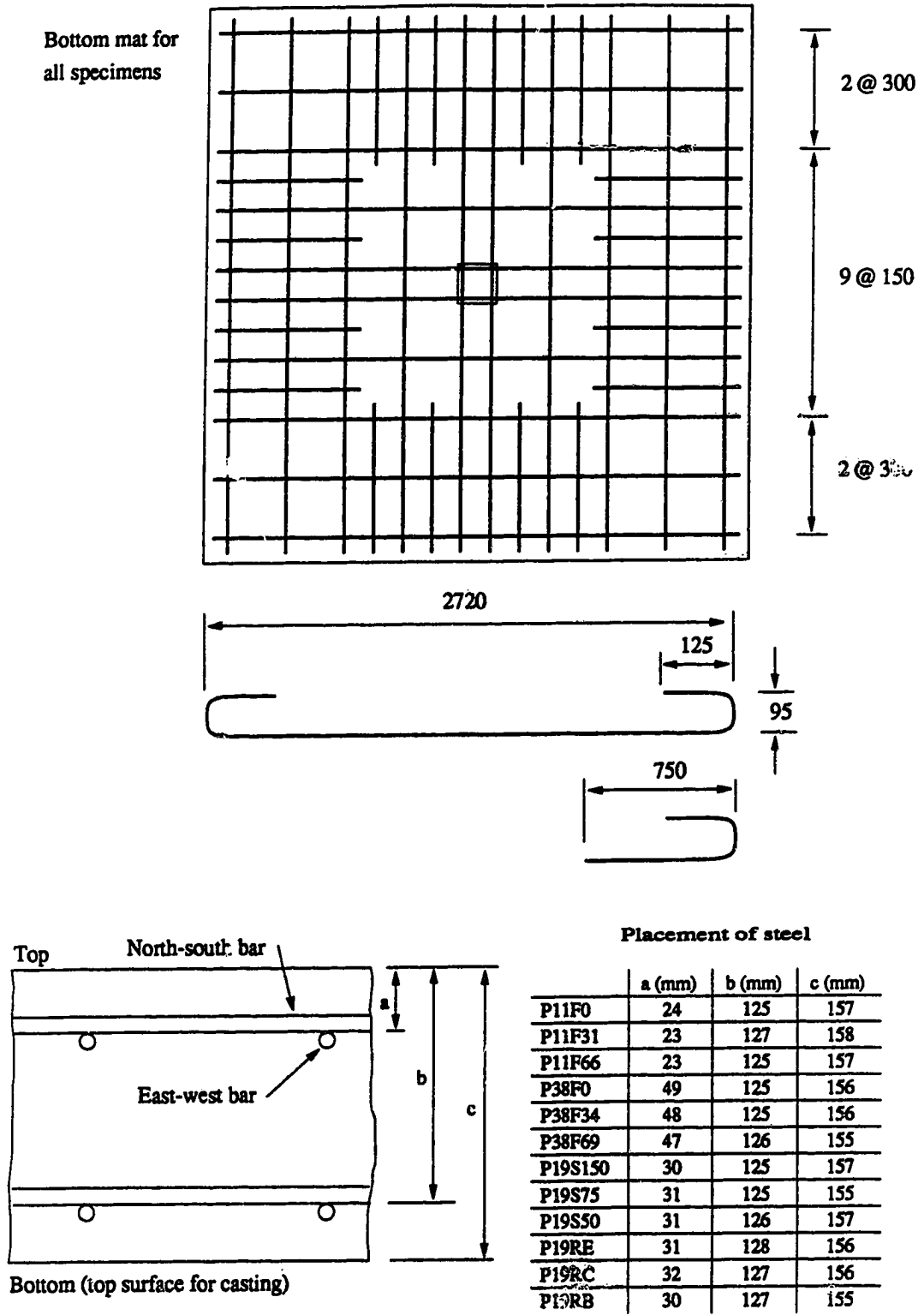


Figure A-3 Bottom Mat and Positions of Reinforcement

Appendix B: Load and Deformation Measurements

Diagrams plotting center deflection against average tie rod load, center load and edge and corner restraint loads are provided for each test. These are complete records in that unloading sequences have not been edited for clarity.

In addition, plots of the ratio of edge restraint and/or corner restraint against *stroke* are given. These ratios are used in the flexural analysis discussed in Chapter 4.

For all tests except P19RE, measurements were made of the *plate* edge movements. The raw LVDT readings and calculated expansions across the center-line of the plate are plotted against *stroke*.

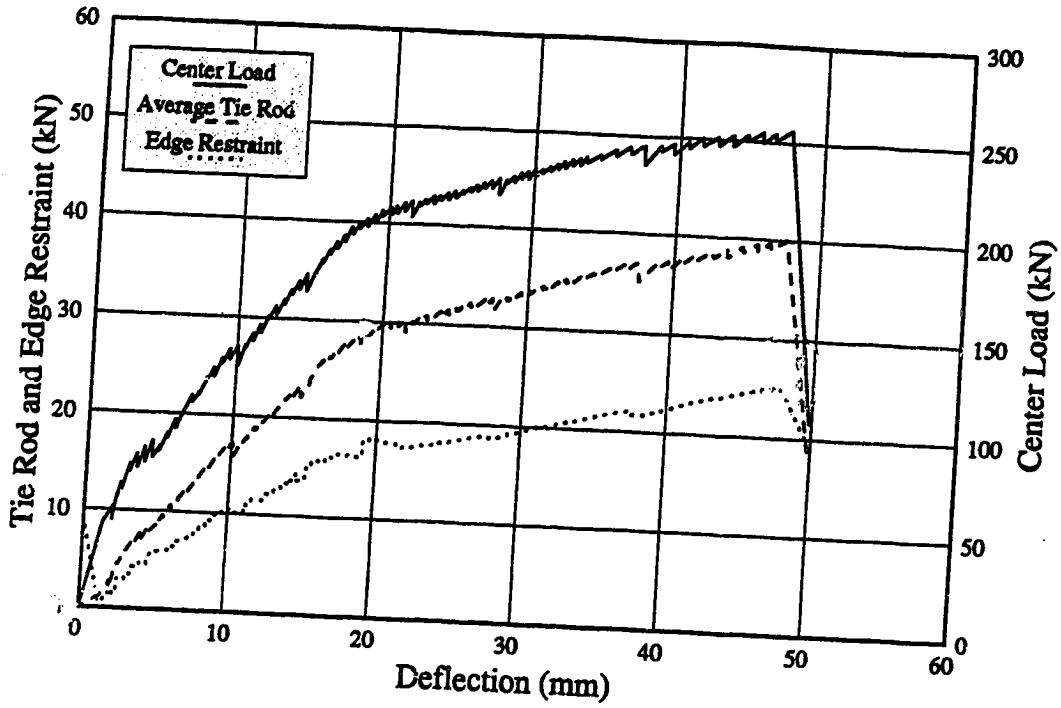


Figure B-1 Load-Deflection Diagrams: P11F0

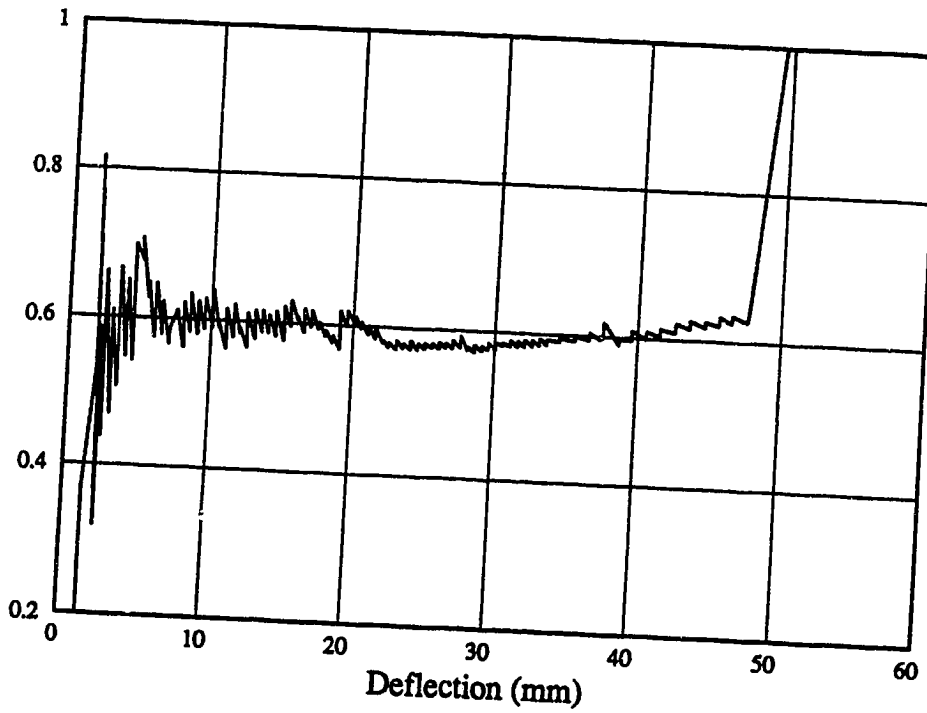


Figure B-2 Ratio of Edge Restraint to Average Load in Tie Rods: P11F0

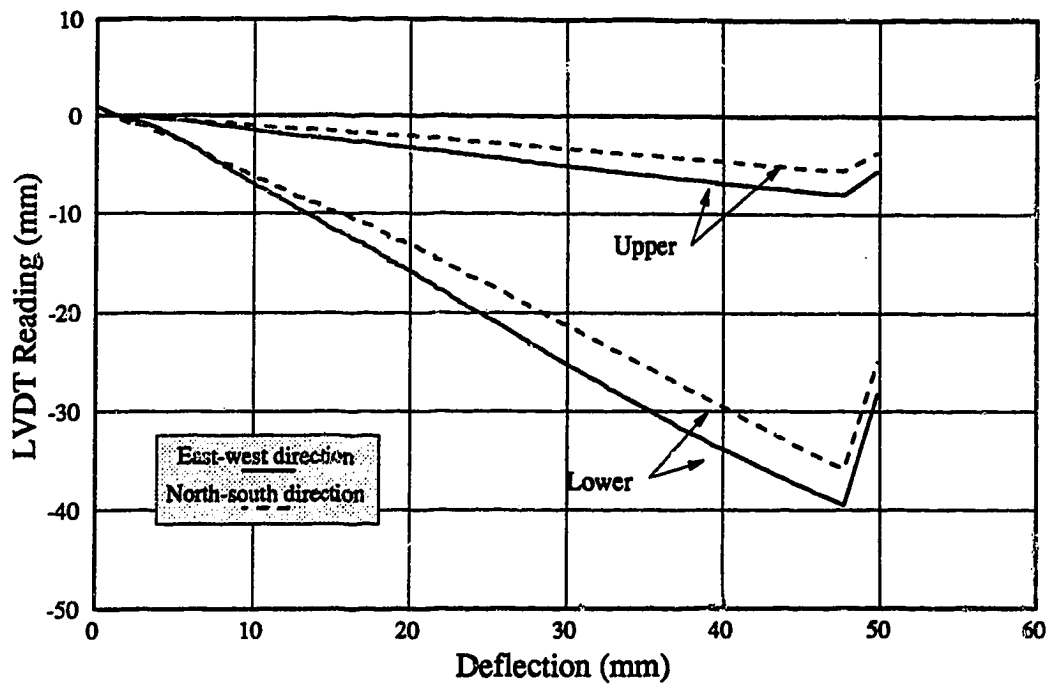


Figure B-3 Data from LVDT's Measuring Plate Expansion: P11F0

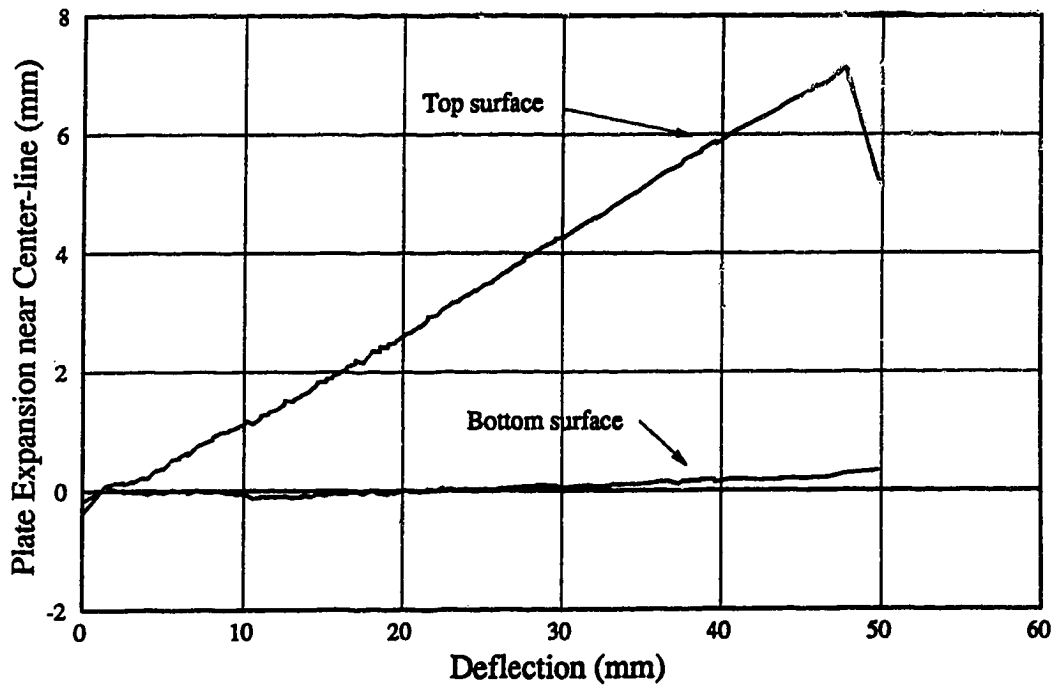


Figure B-4 In-Plane Expansion of Plate Near Center-Line: P11F0

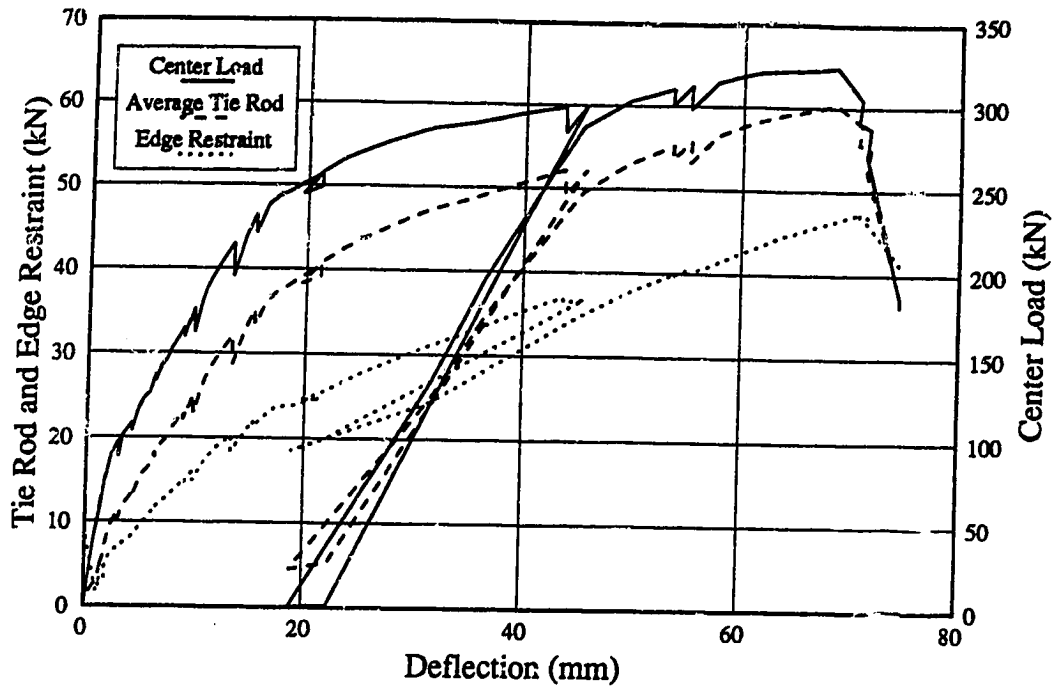


Figure B-5 Load-Deflection Diagrams: P11F31

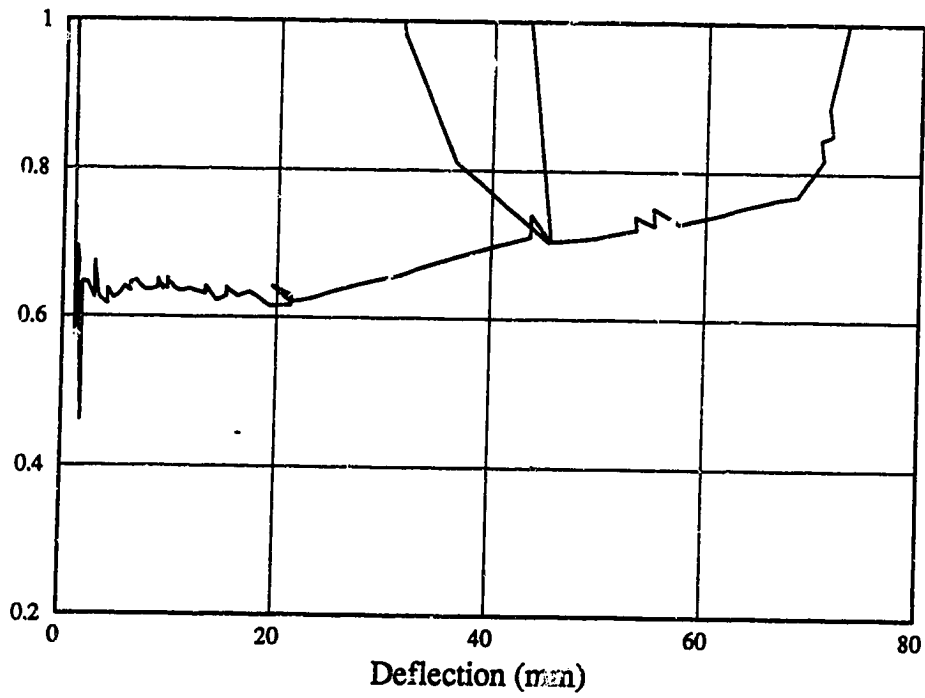


Figure B-6 Ratio of Edge Restraint to Average Load in Tie Rods: P11F31

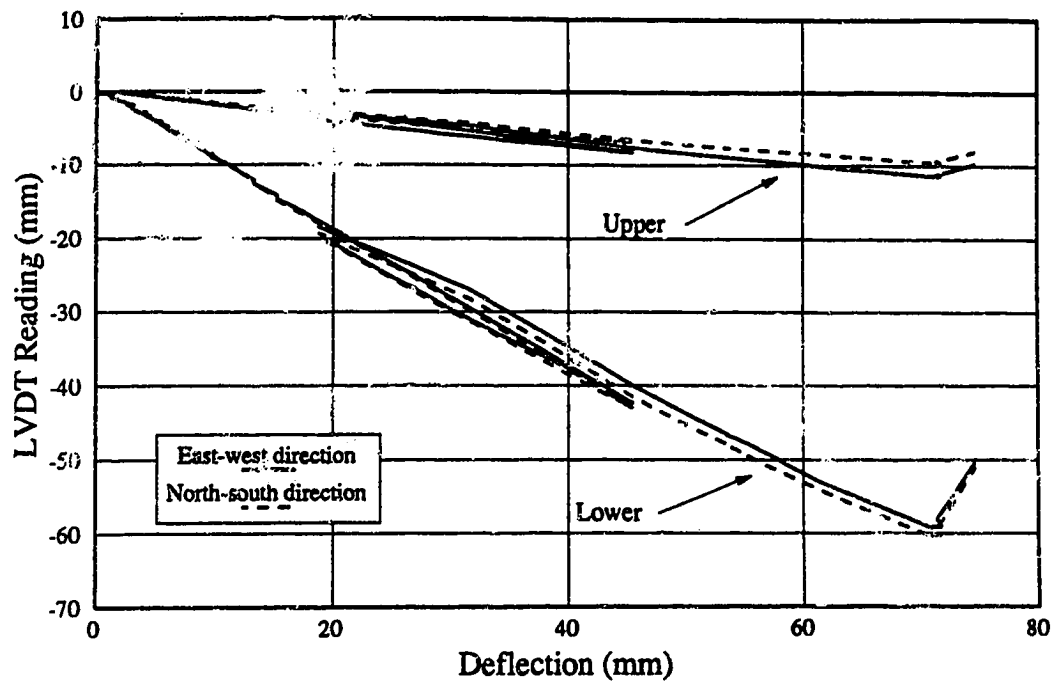


Figure B-7 Data from LVDT's Measuring Plate Expansion: P11F31

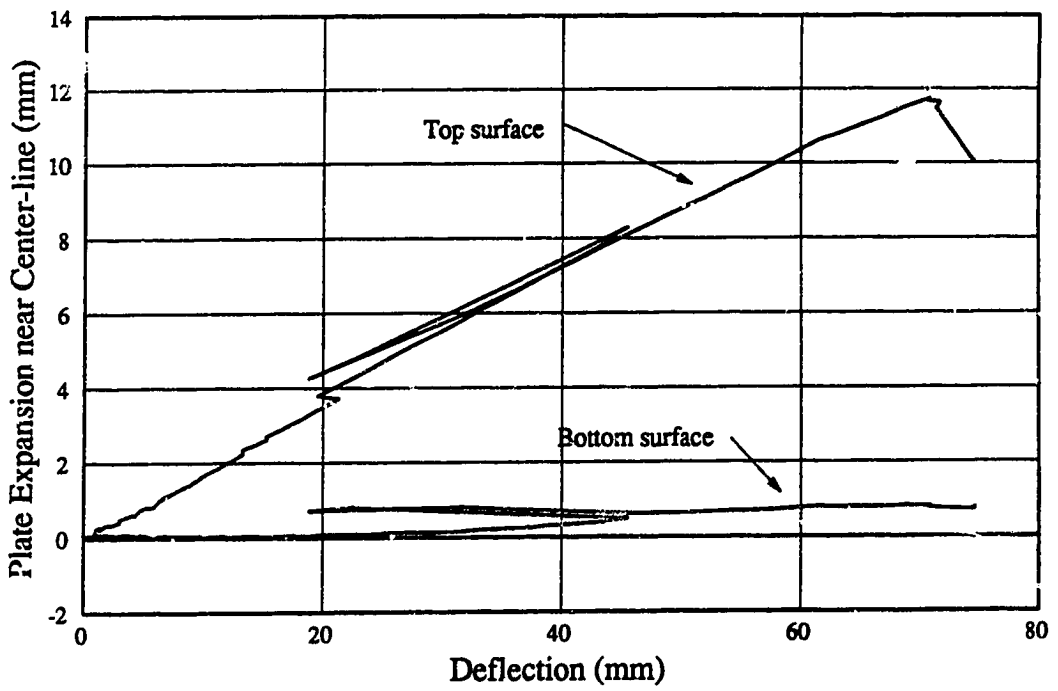


Figure B-8 In-Plane Expansion of Plate Near Center-Line: P11F31

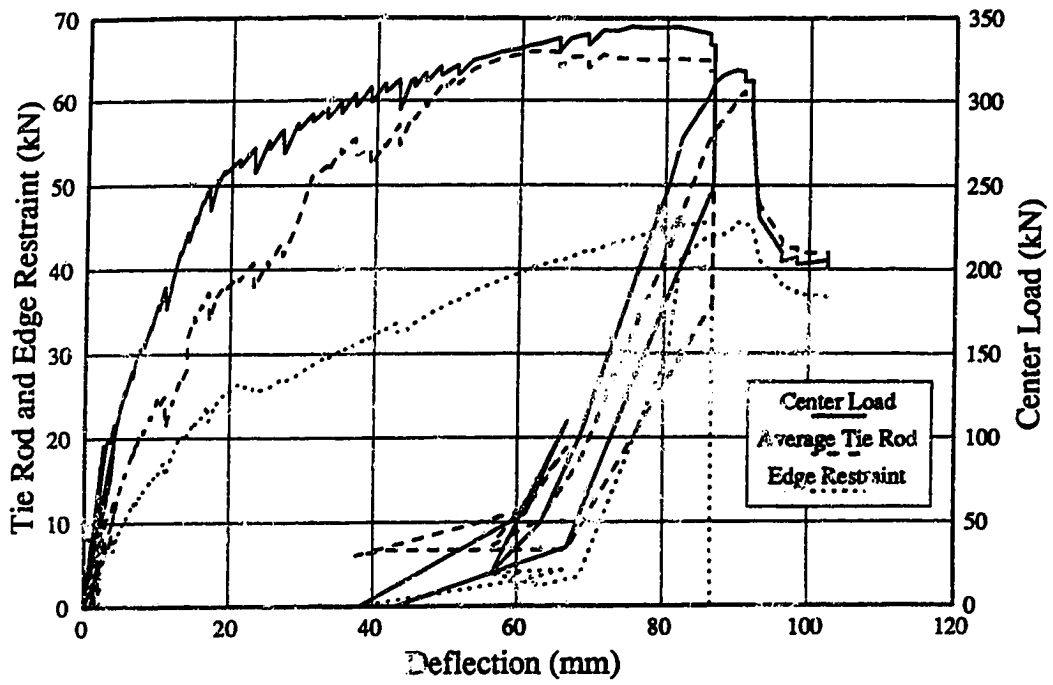


Figure B-9 Load-Deflection Diagrams: P11F66

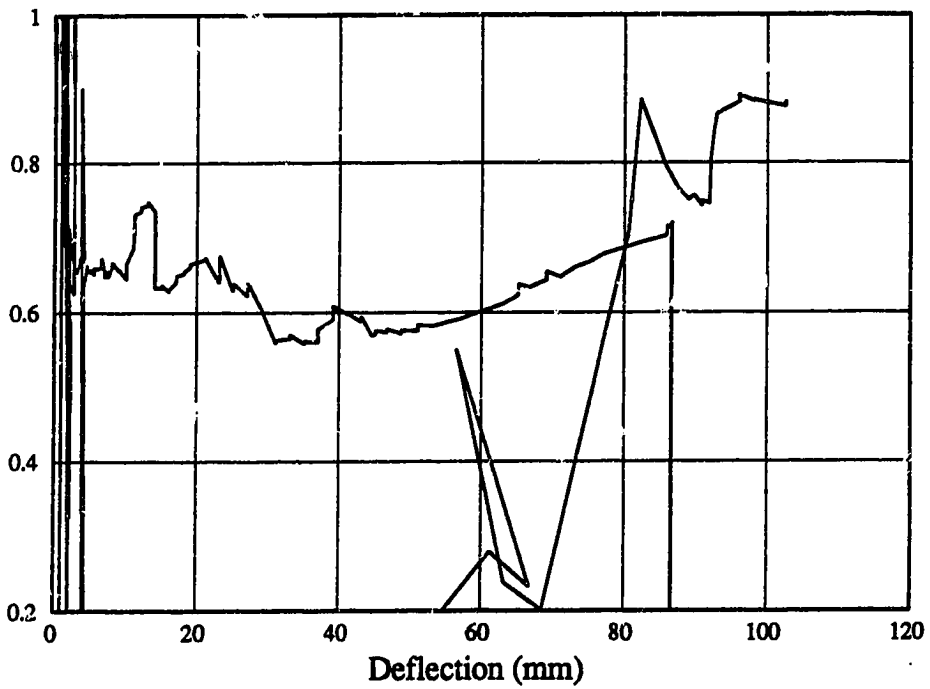


Figure B-10 Ratio of Edge Restraint to Average Load in Tie Rods: P11F66

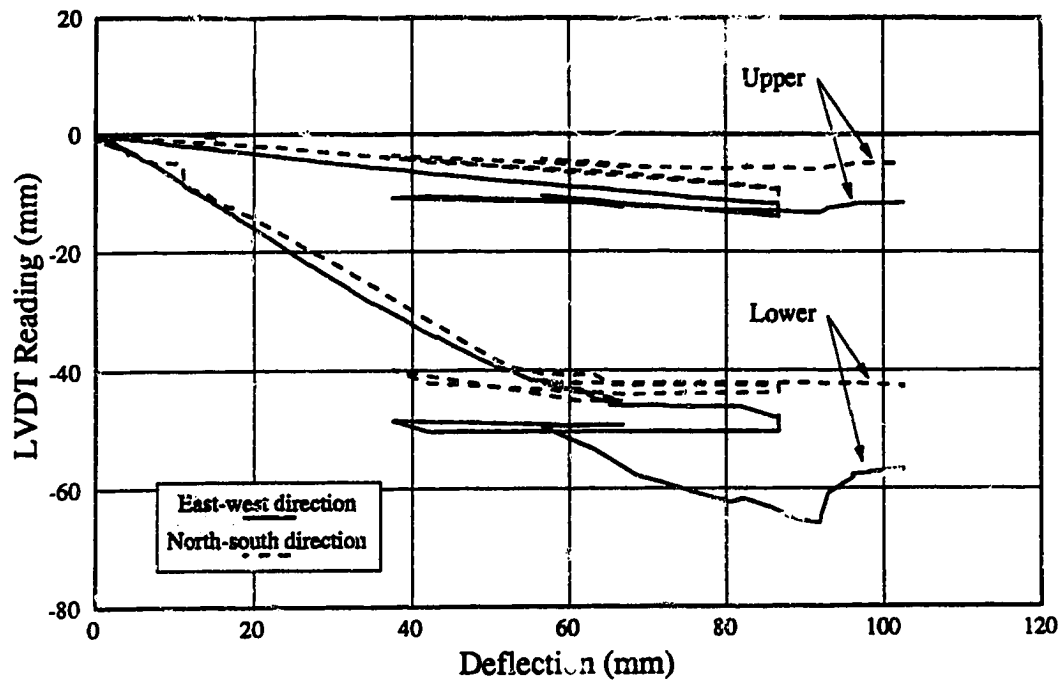


Figure B-11 Data from LVDT's Measuring Plate Expansion: P11F66

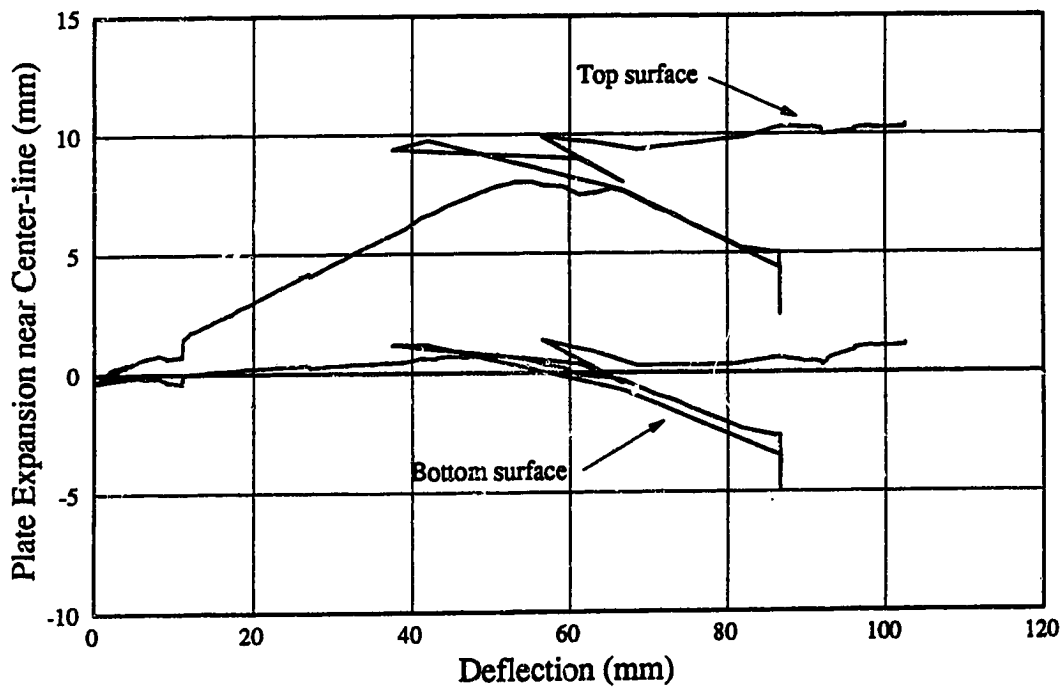


Figure B-12 In-Plane Expansion of Plate Near Center-Line: P11F66

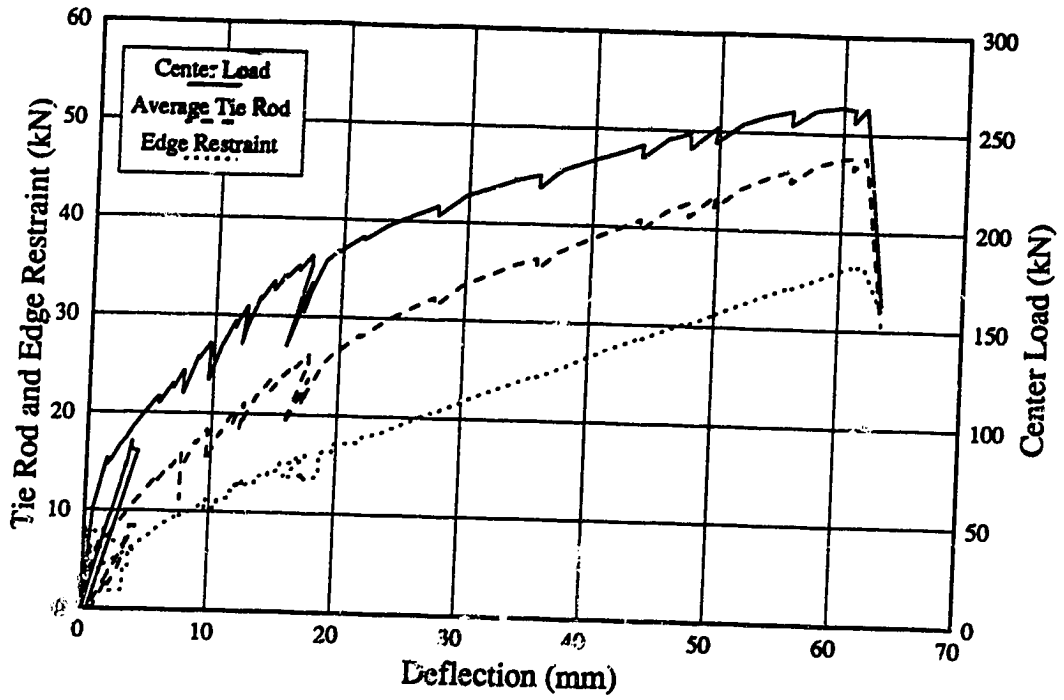


Figure B-13 Load-Deflection Diagrams: P38F0

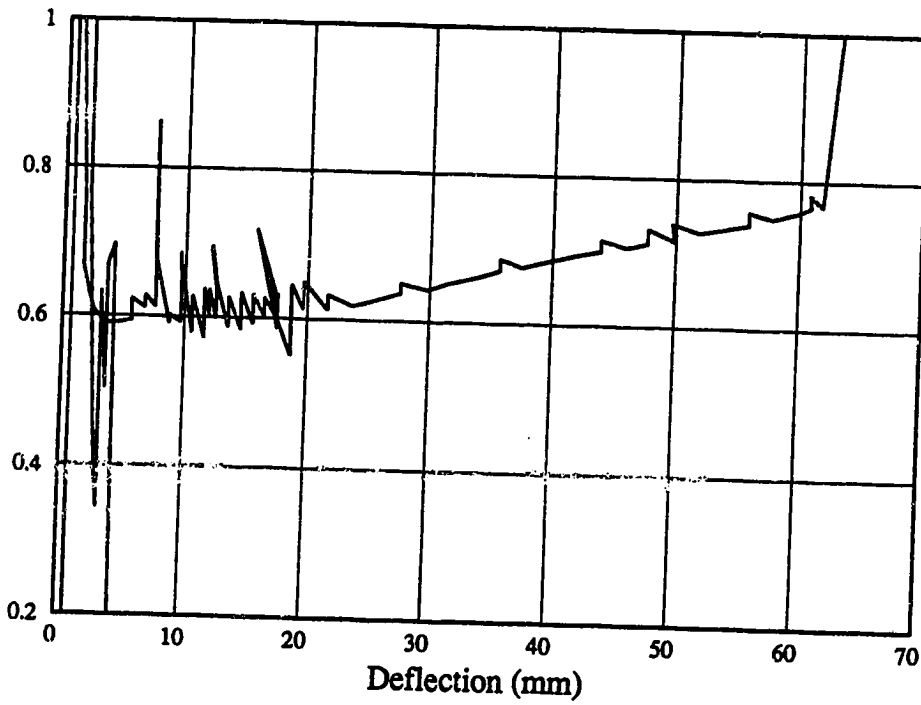


Figure B-14 Ratio of Edge Restraint to Average Load in Tie Rods: P38F0

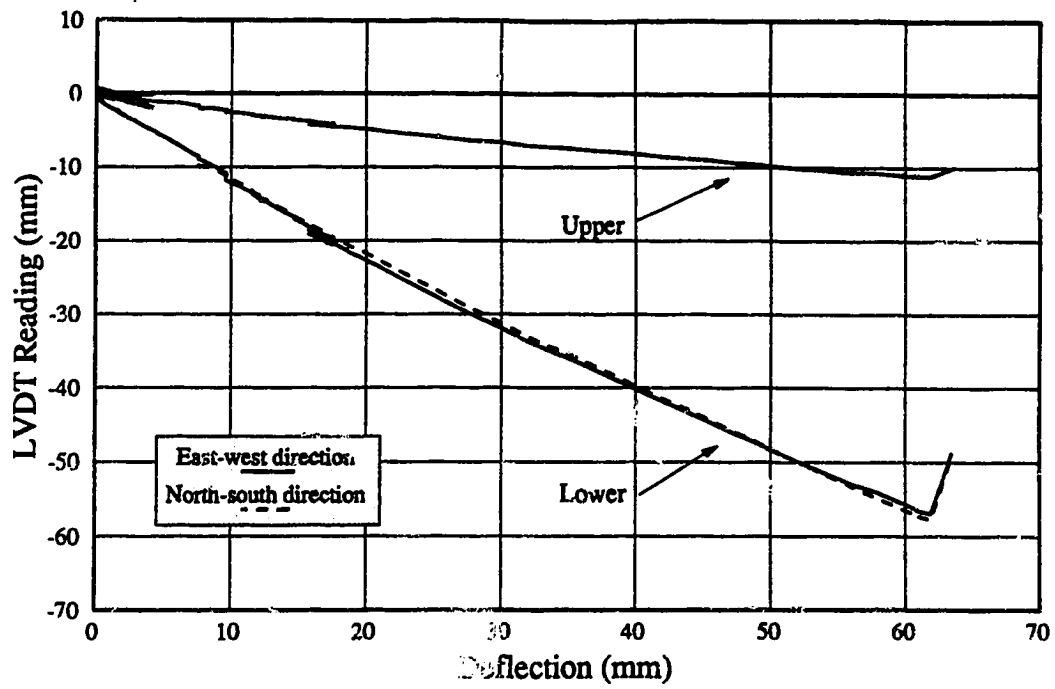


Figure B-15 Data from LVDT's Measuring Plate Expansion: P38F0

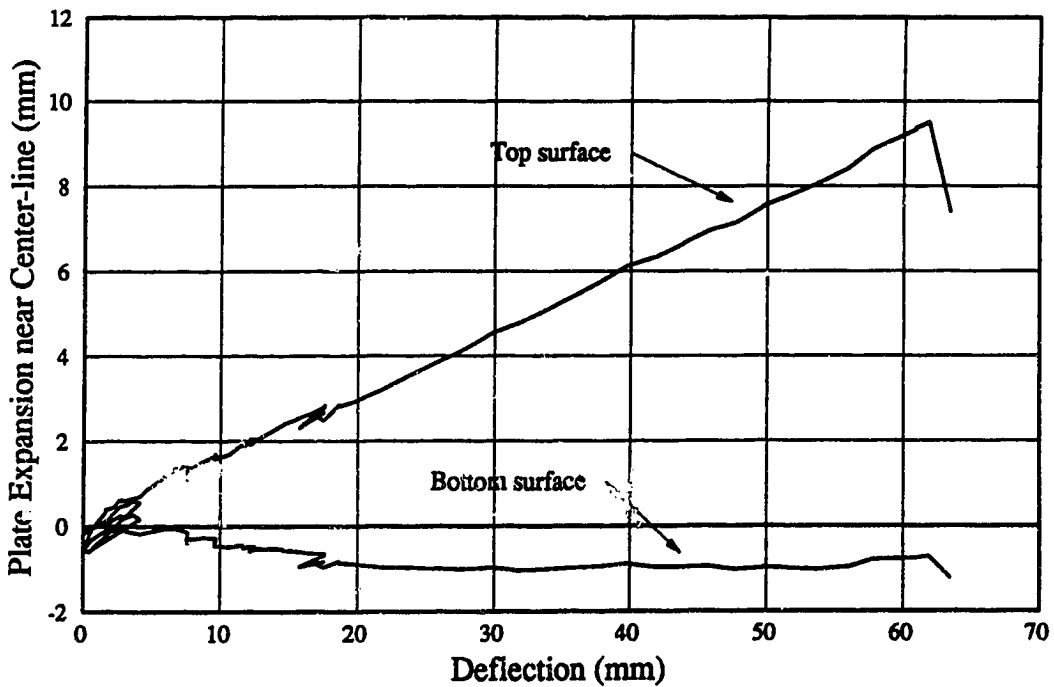


Figure B-16 In-Plane Expansion of Plate Near Center-Line: P38F0

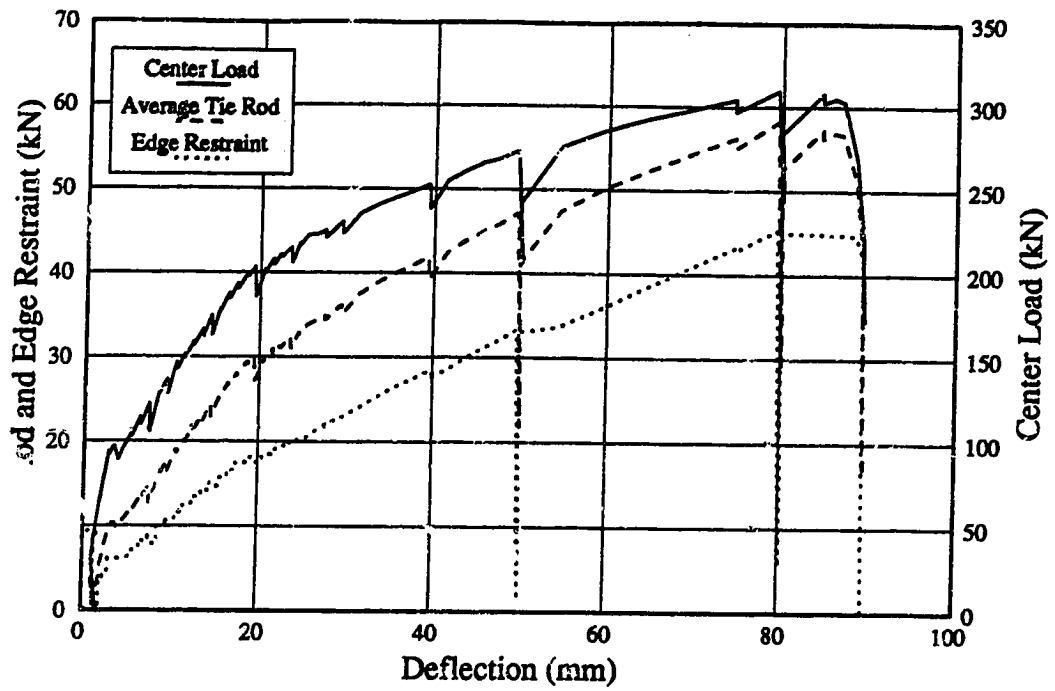


Figure B-17 Load-Deflection Diagrams: P38F34

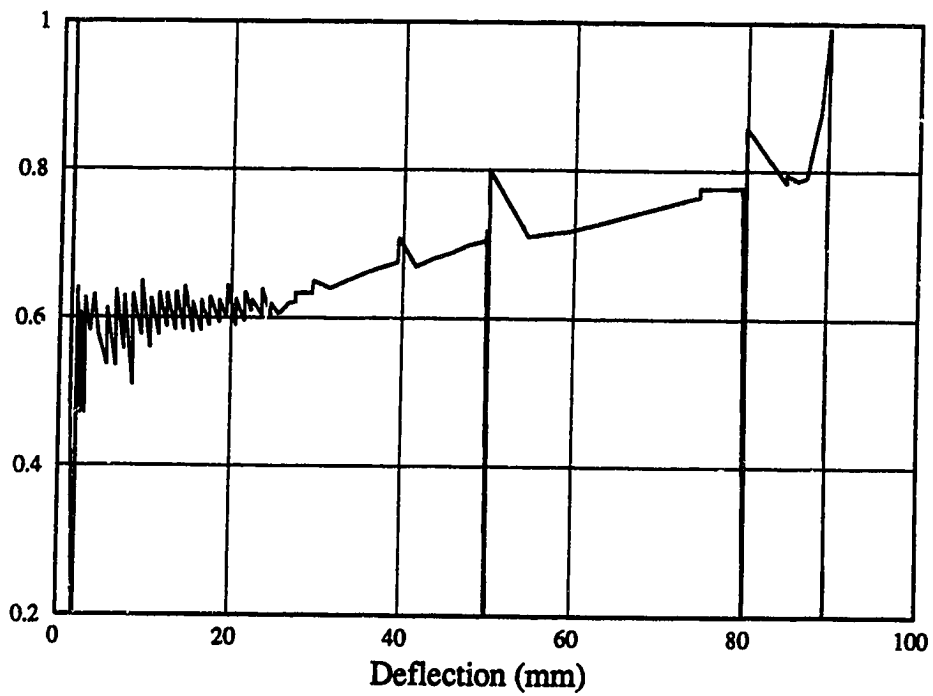


Figure B-18 Ratio of Edge Restraint to Average Load in Tie Rods: P38F34

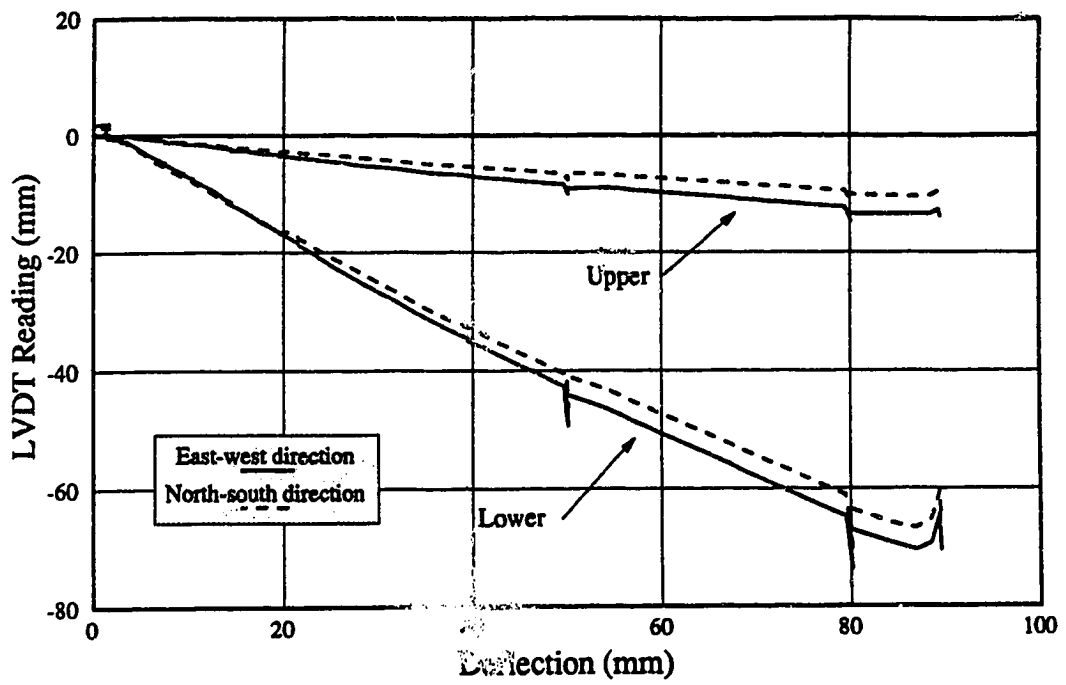


Figure B-19 Data from LVDT's Measuring Plate Expansion: P38F34

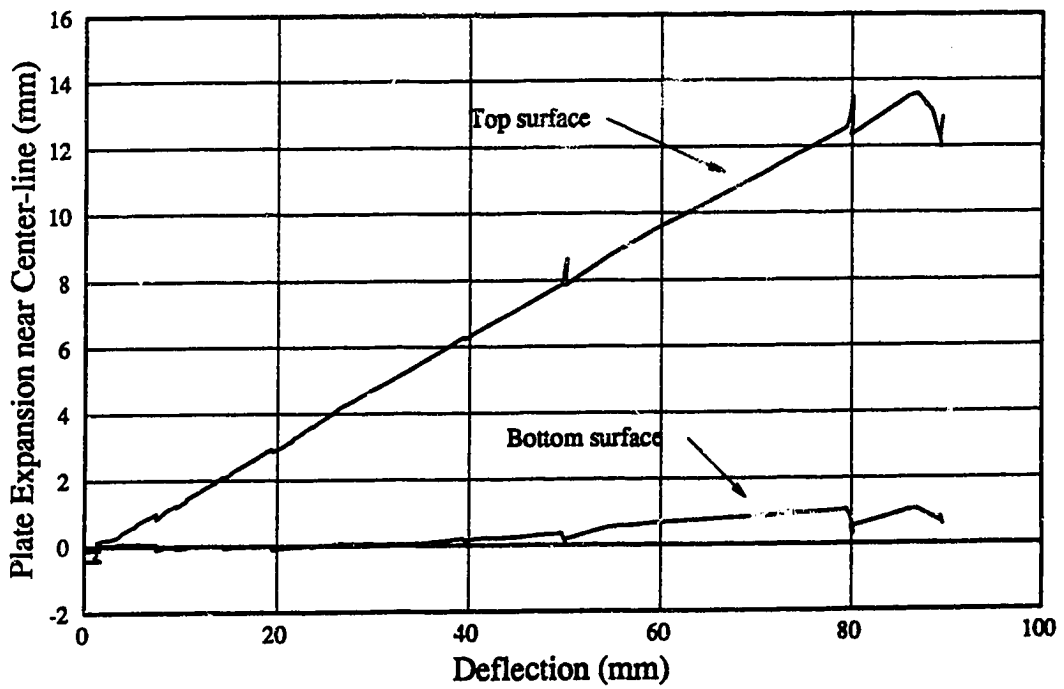


Figure B-20 In-Plane Expansion of Plate Near Center-Line: P38F34

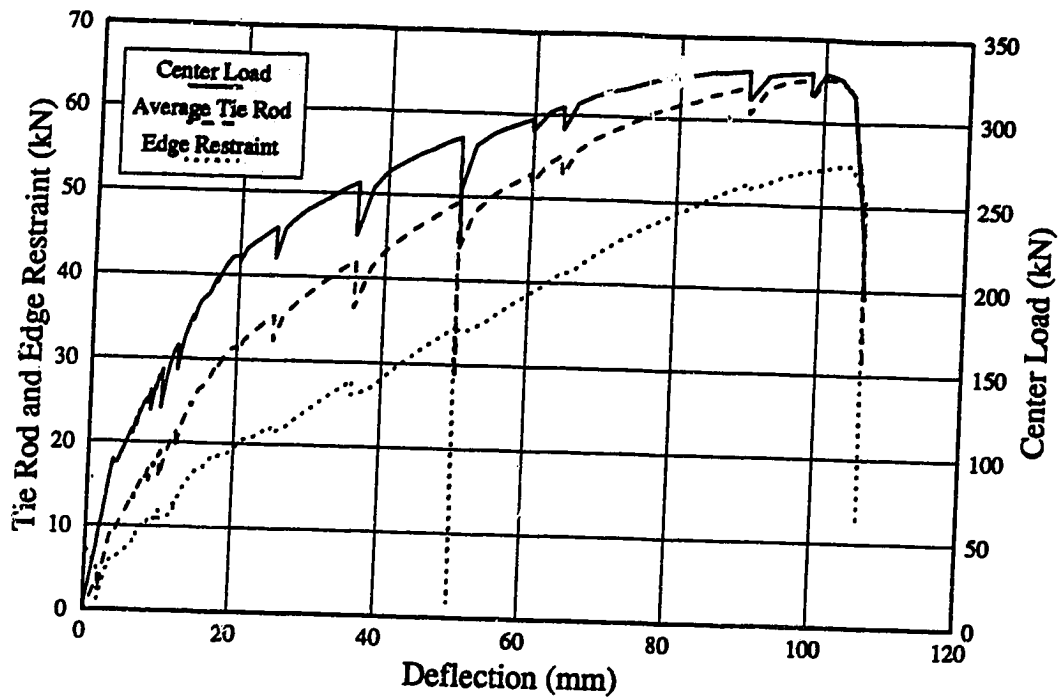


Figure B-21 Load-Deflection Diagrams: P38F69

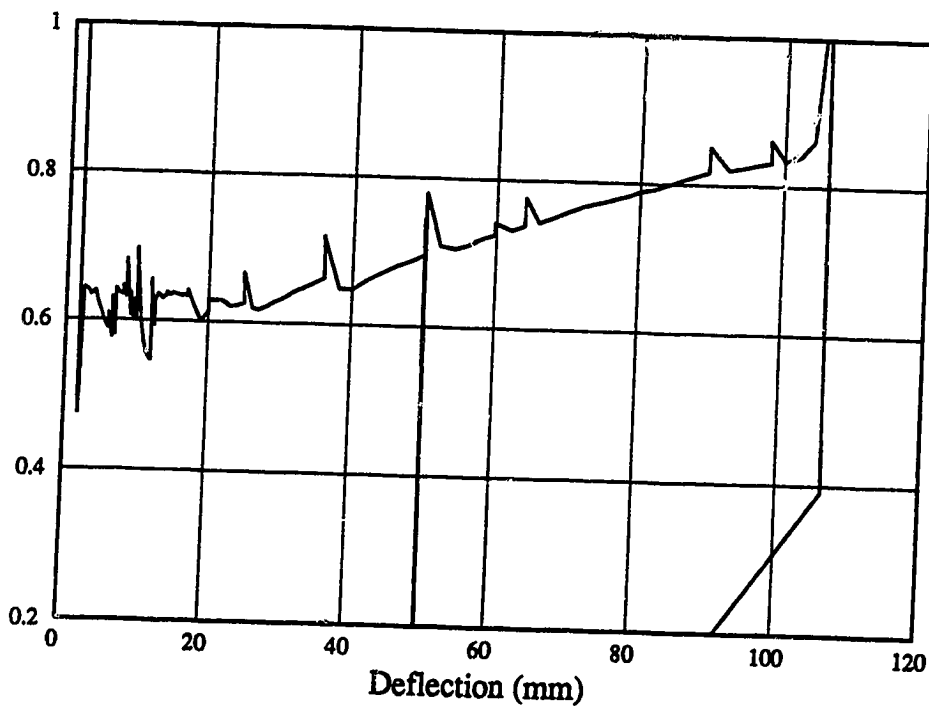


Figure B-22 Ratio of Edge Restraint to Average Load in Tie Rods: P38F69

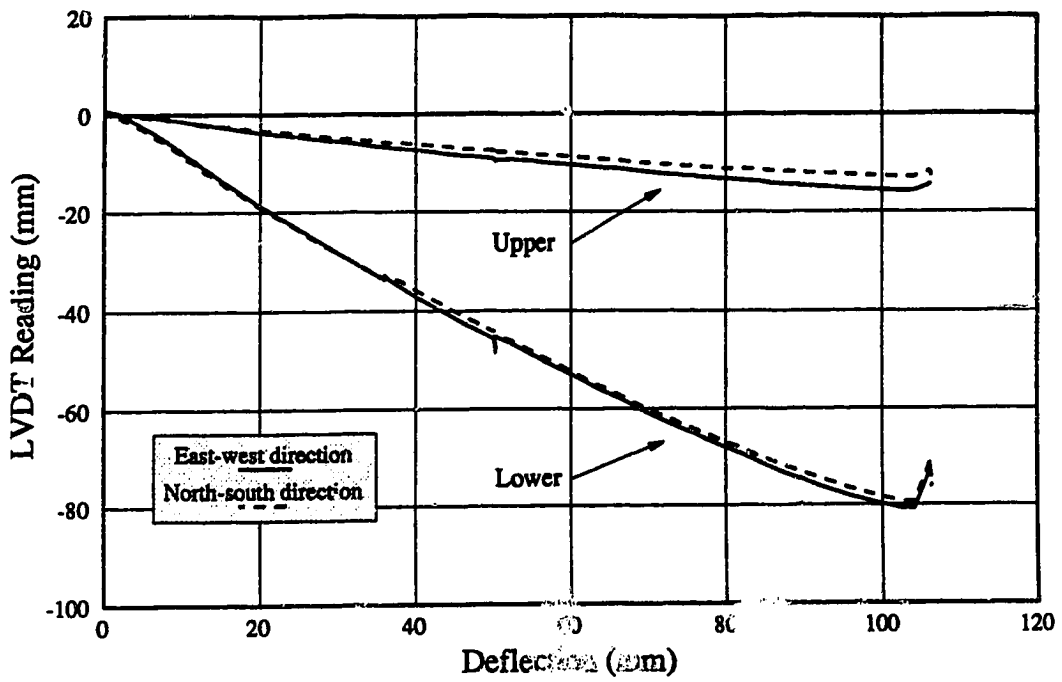


Figure B-23 Data from LVDT's Measuring Plate Expansion: P38F69

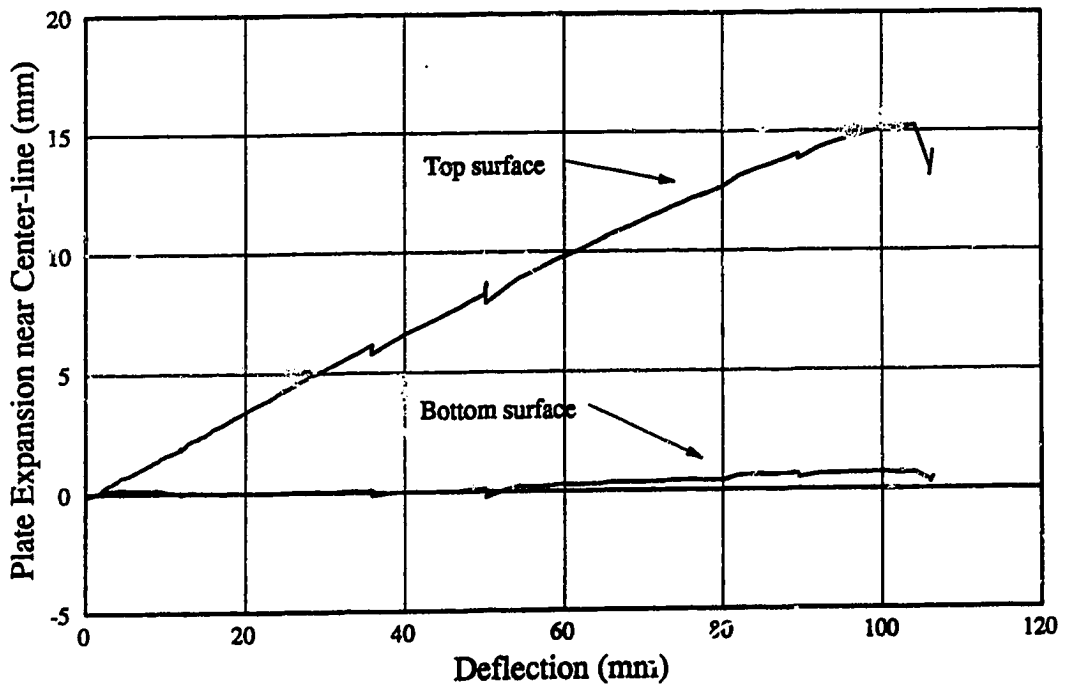


Figure B-24 In-Plane Expansion of Plate Near Center-Line: P38F69

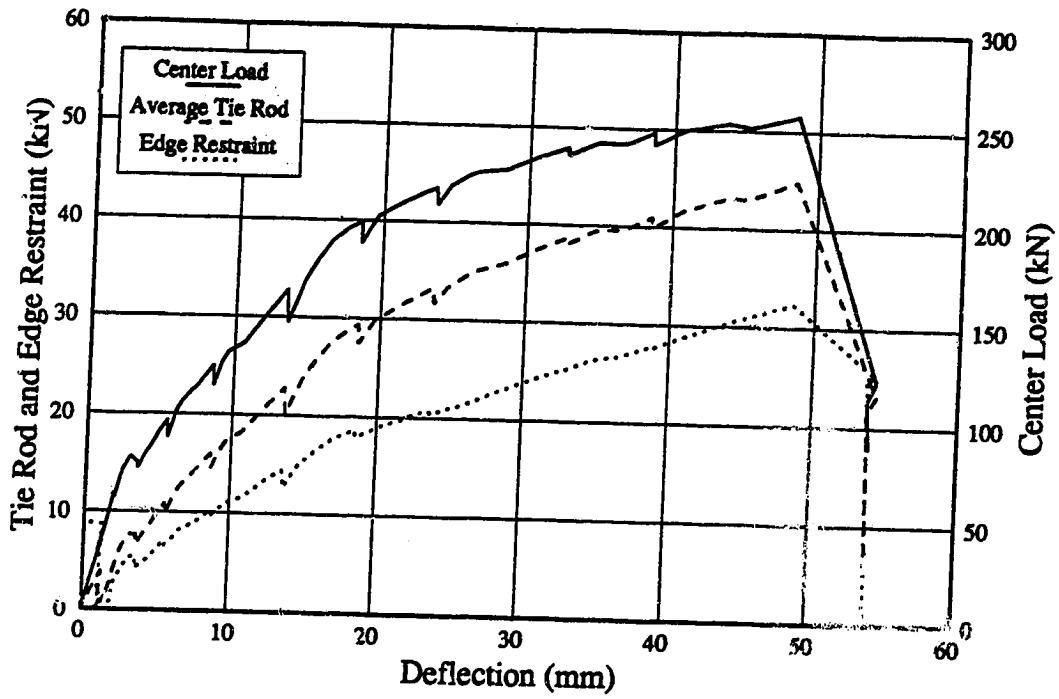


Figure B-25 Load-Deflection Diagrams: P19S150

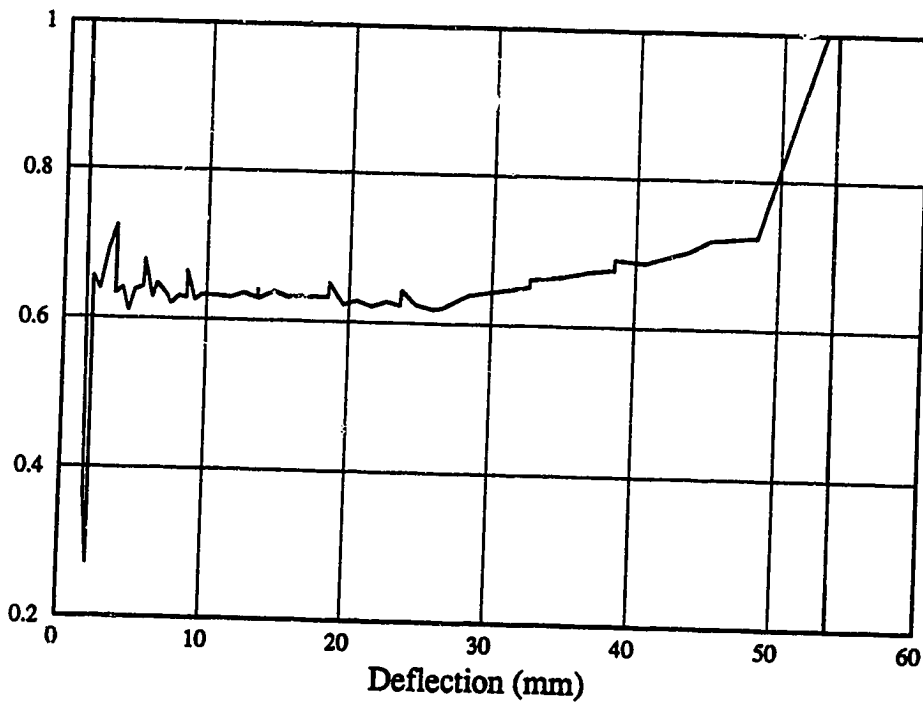


Figure B-26 Ratio of Edge Restraint to Average Load in Tie Rods: P19S150

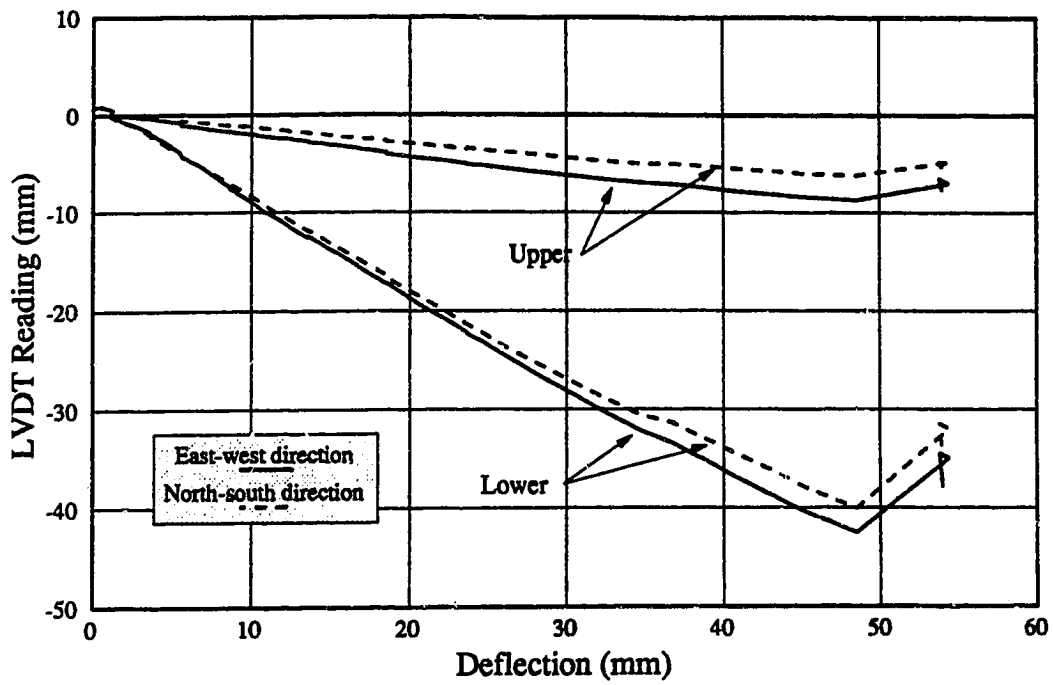


Figure B-27 Data from LVDT's Measuring Plate Expansion: P19S150

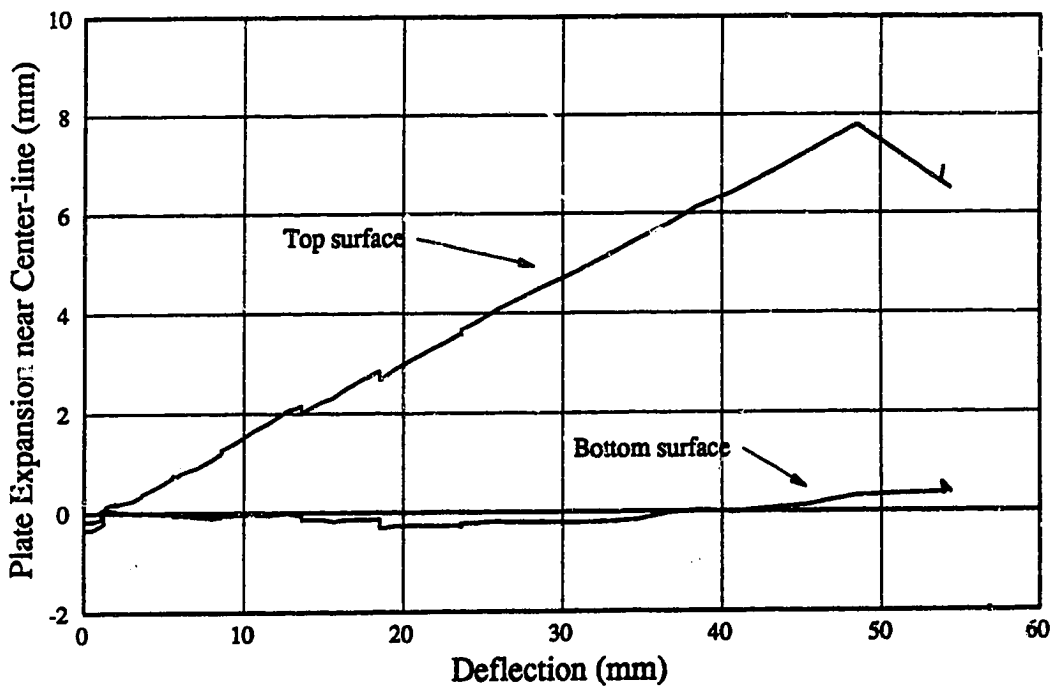


Figure B-28 In-Plane Expansion of Plate Near Center-Line: P19S150

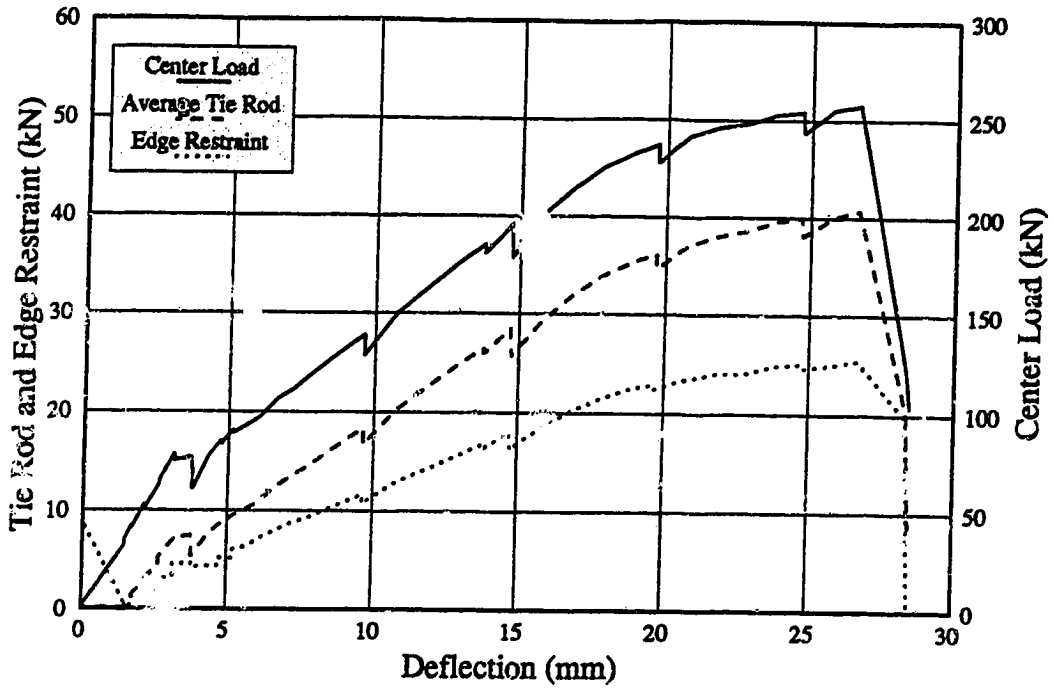


Figure B-29 Load-Deflection Diagrams: P19S75

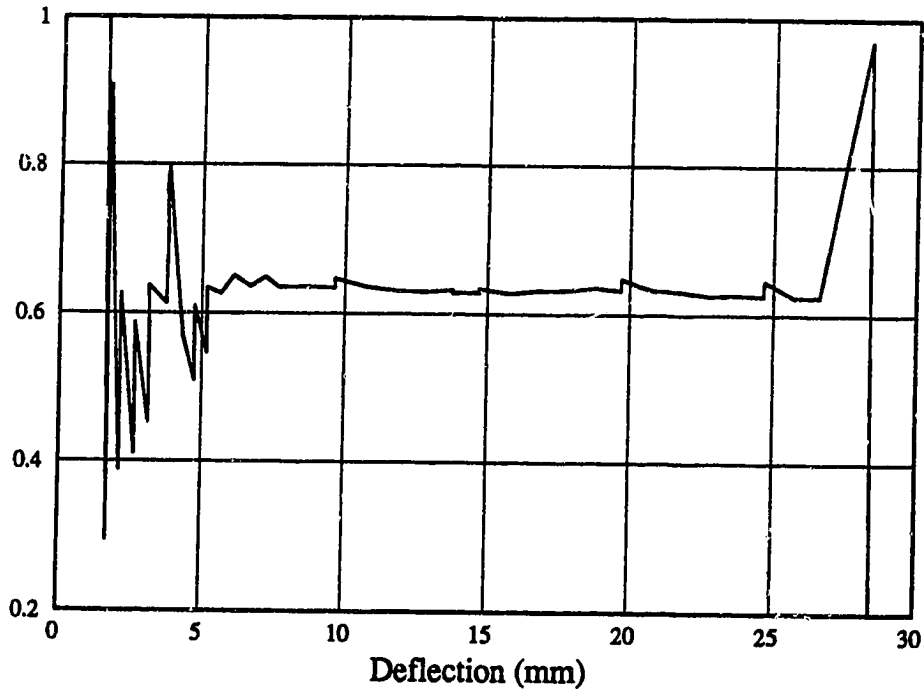


Figure B-30 Ratio of Edge Restraint to Average Load in Tie Rods: P19S75

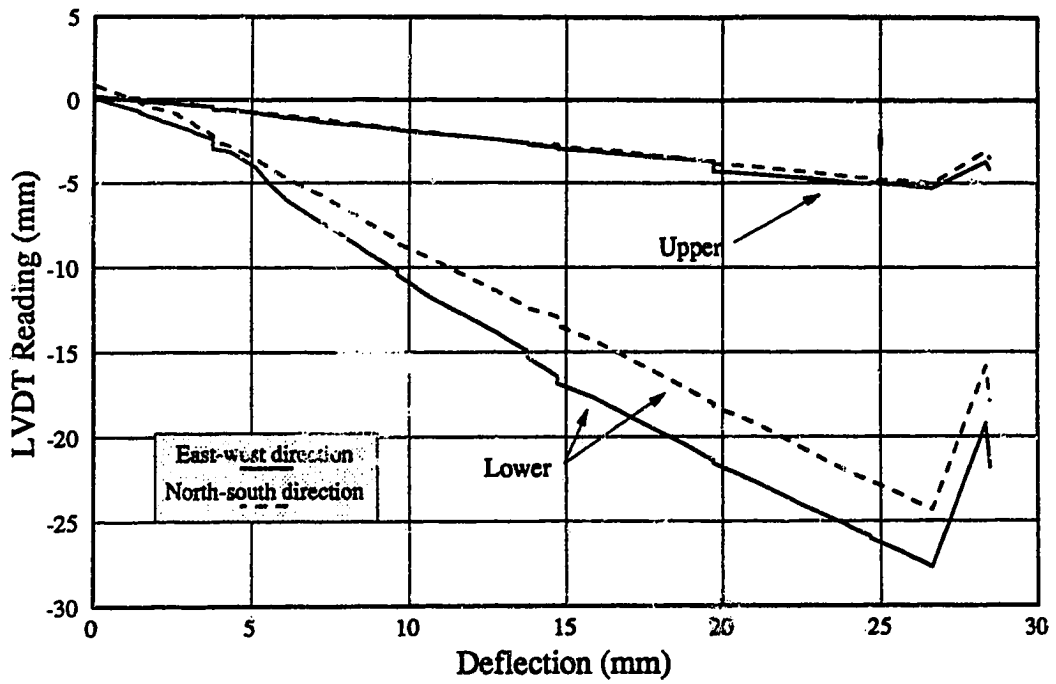


Figure B-31 Data from LVDT's Measuring Plate Expansion: P19S75

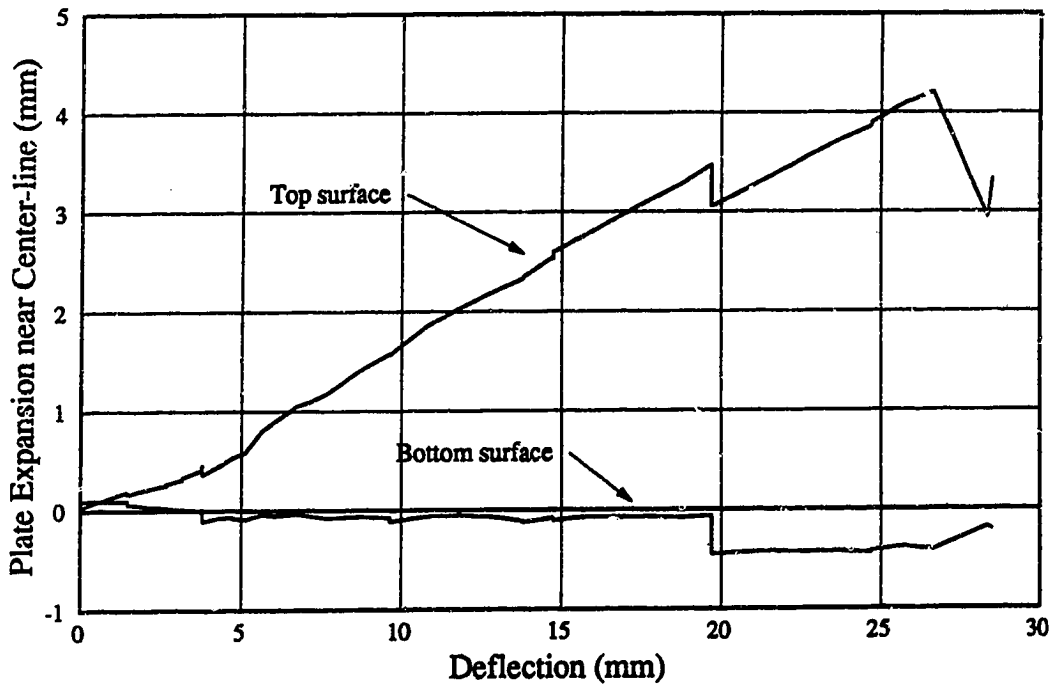


Figure B-32 In-Plane Expansion of Plate Near Center-Line: P19S75

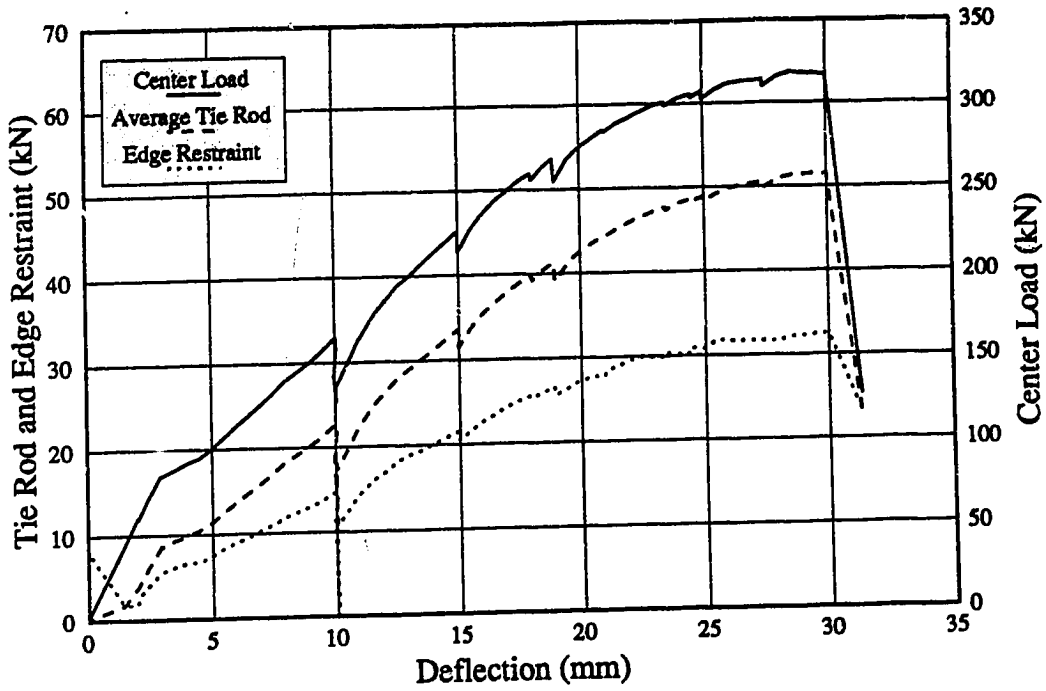


Figure B-33 Load-Deflection Diagrams: P19S50

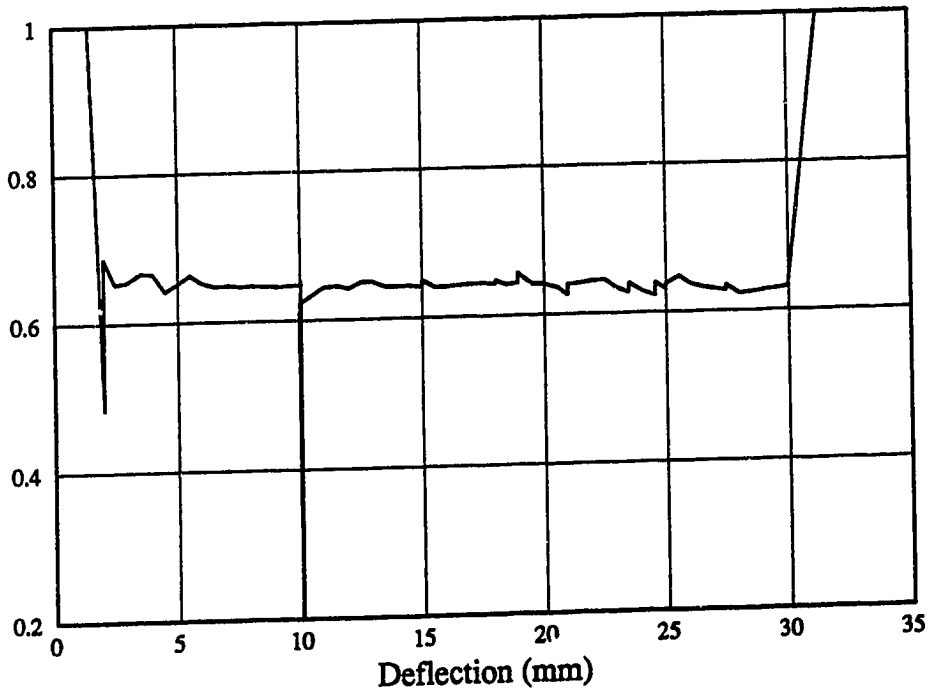


Figure B-34 Ratio of Edge Restraint to Average Load in Tie Rods: P19S50

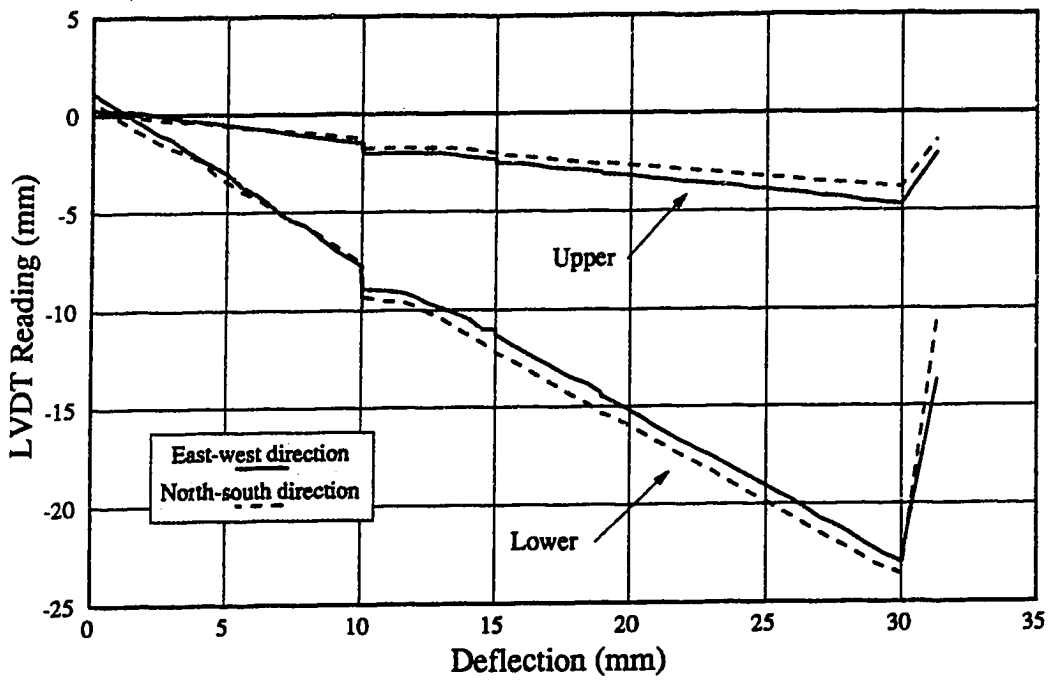


Figure B-35 Data from LVDT's Measuring Plate Expansion: P19S50

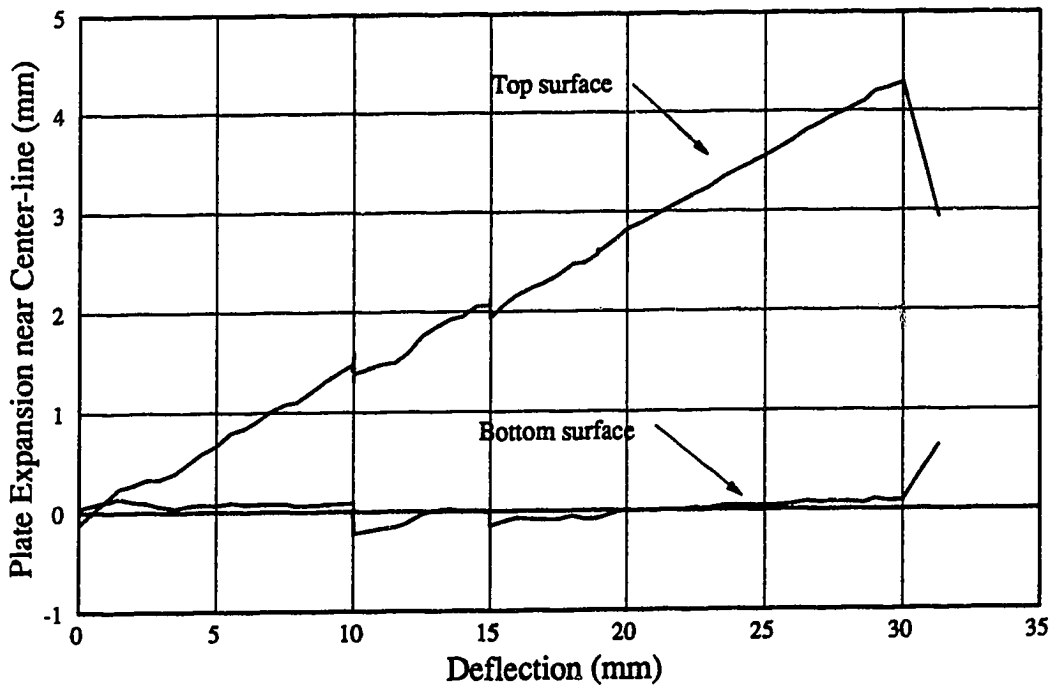


Figure B-36 In-Plane Expansion of Plate Near Center-Line: P19S50

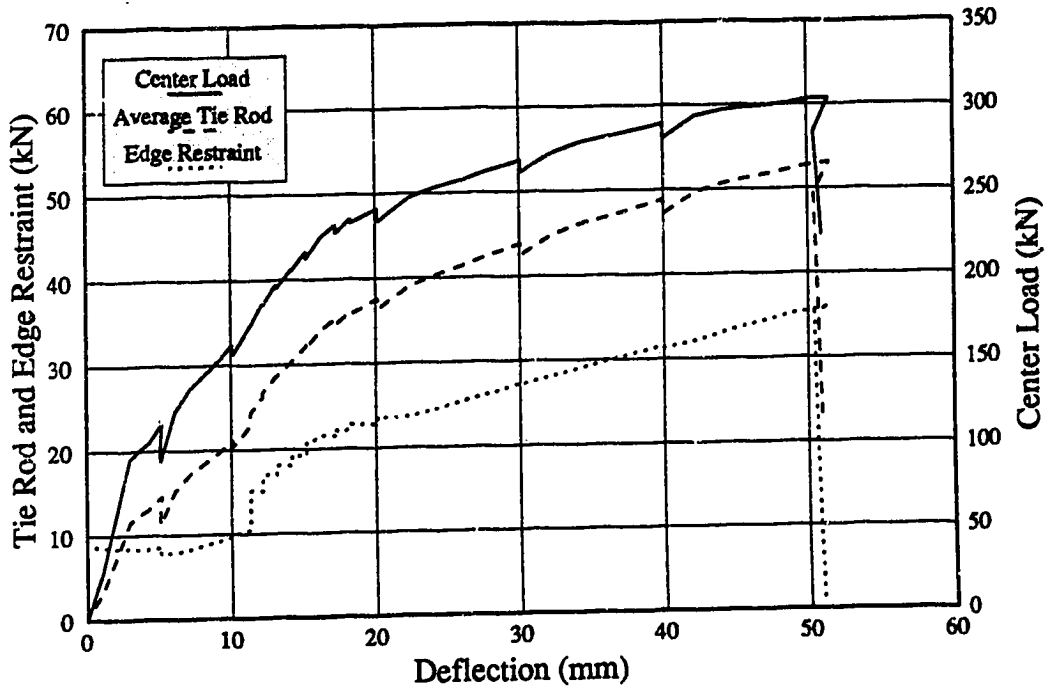


Figure B-37 Load-Deflection Diagrams: P19RE

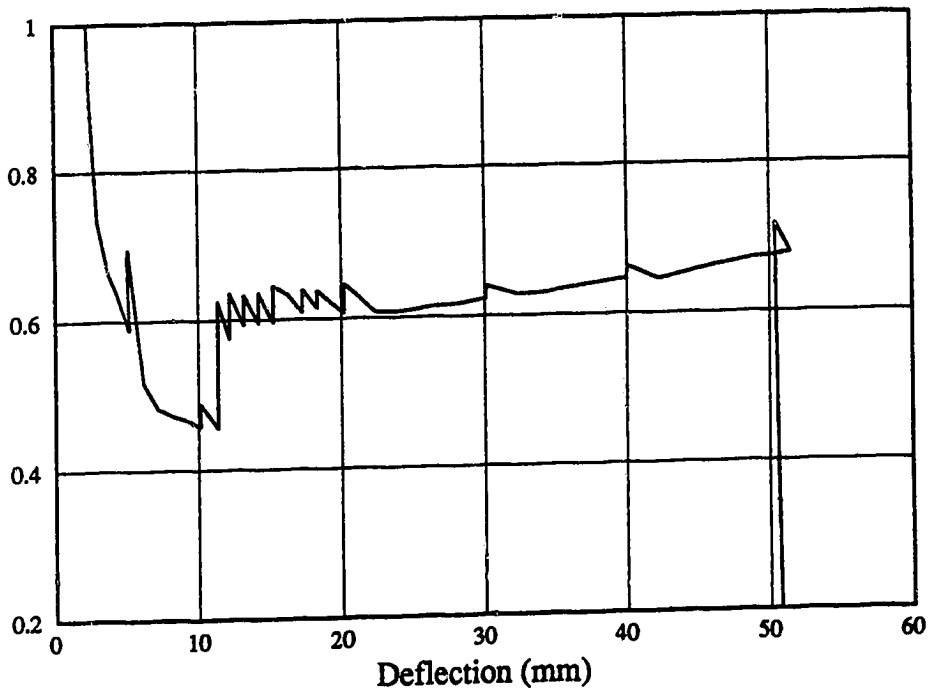


Figure B-38 Ratio of Edge Restraint to Average Load in Tie Rods: P19RE

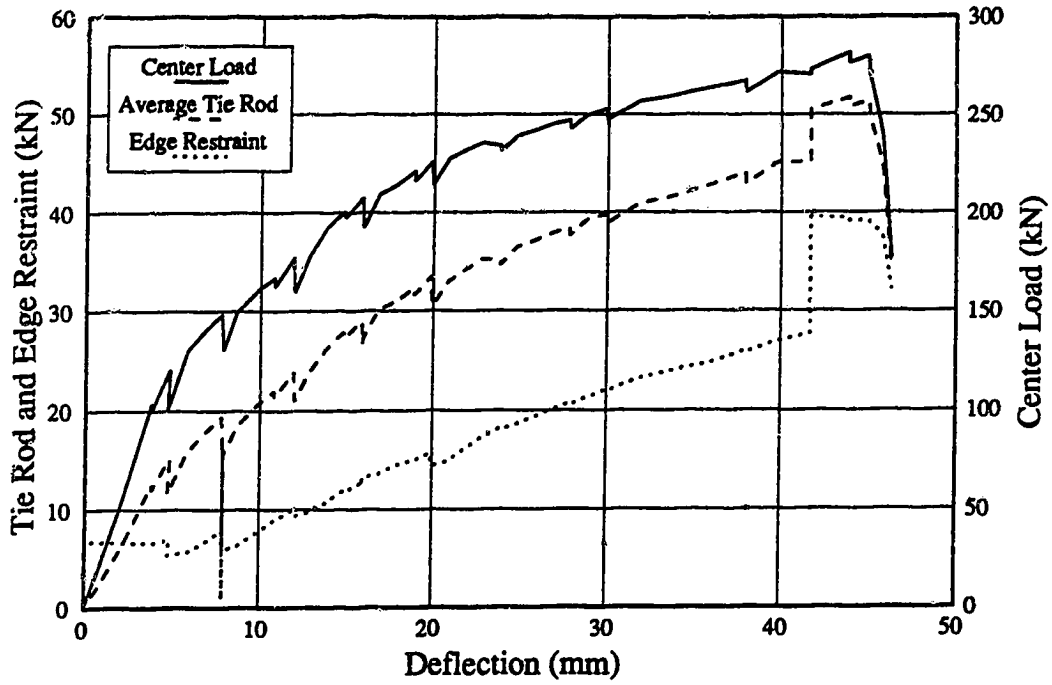


Figure B-39 Load-Deflection Diagrams: P19RC

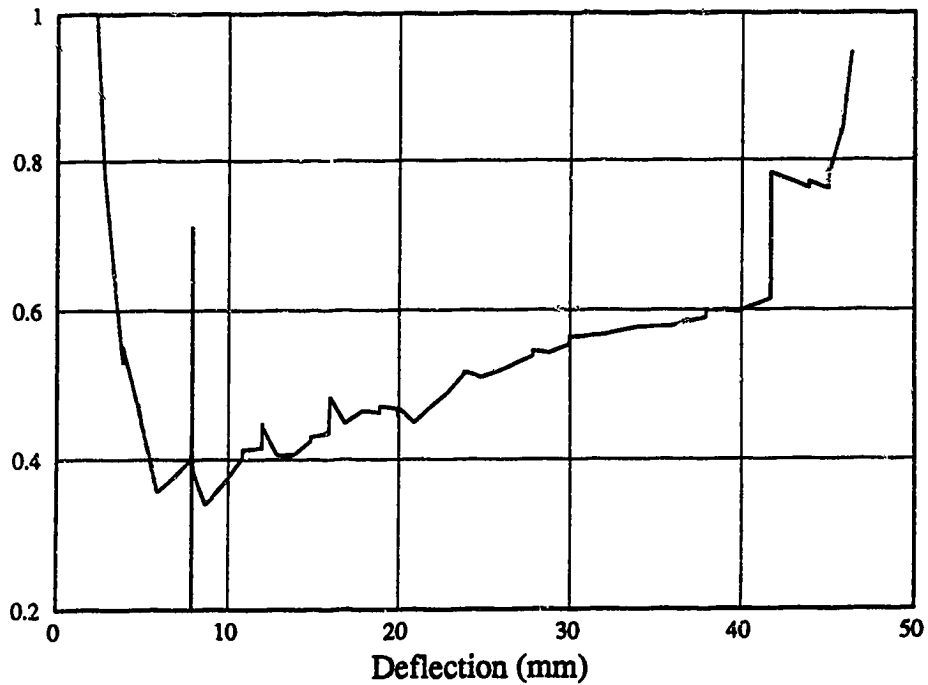


Figure B-40 Ratio of Edge Restraint to Average Load in Tie Rods: P19RC

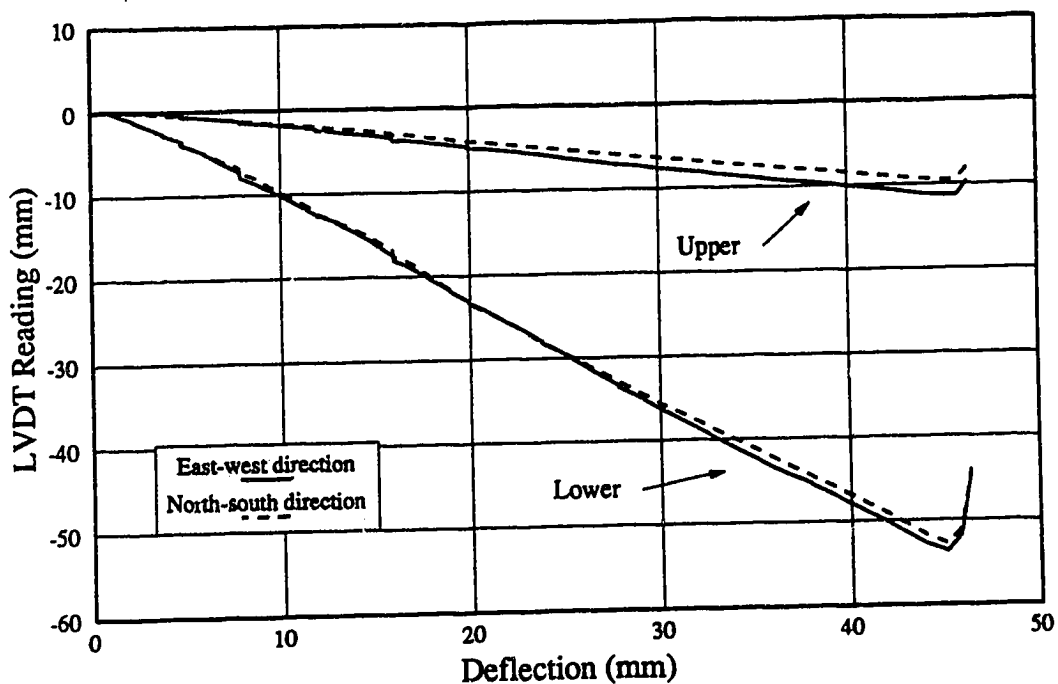


Figure B-41 Data from LVDT's Measuring Plate Expansion: P19RC

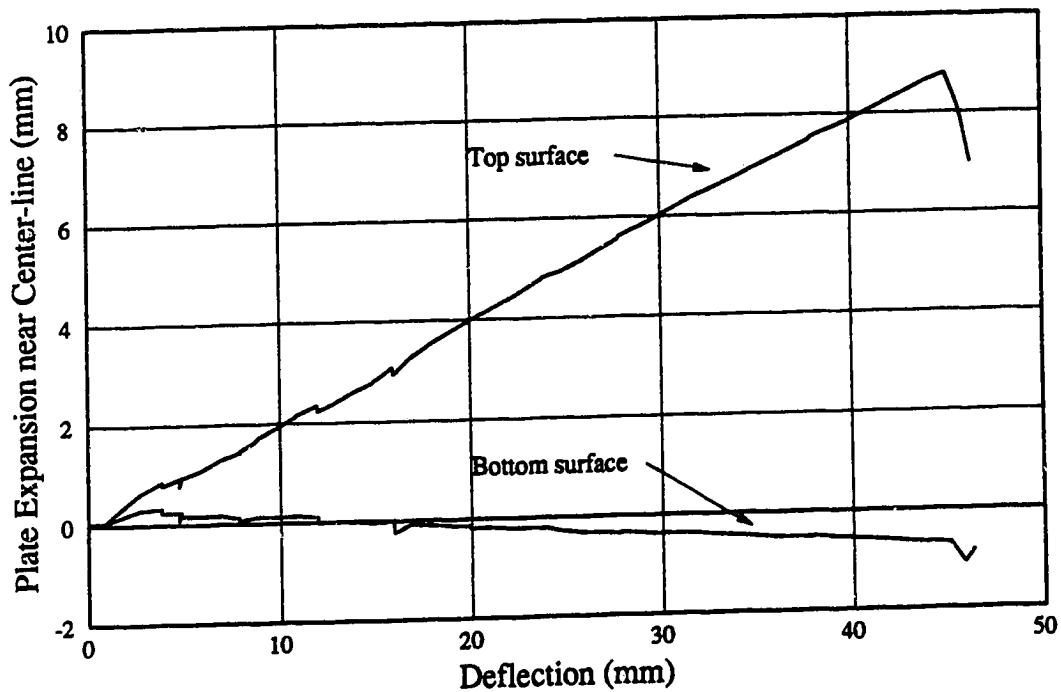


Figure B-42 In-Plane Expansion of Plate Near Center-Line: P19RC

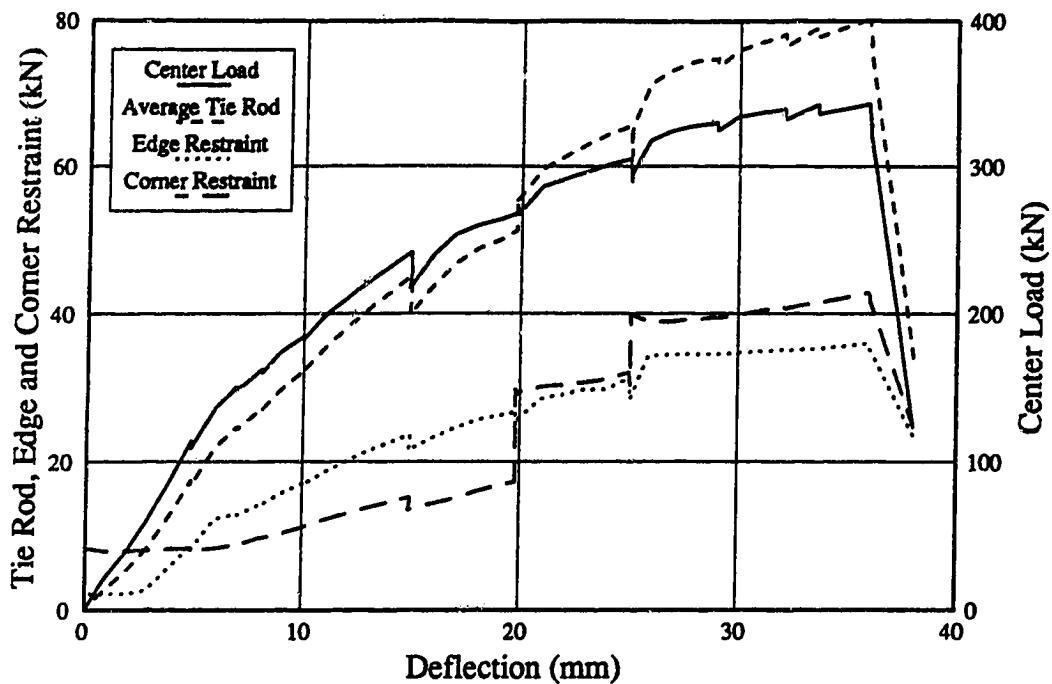


Figure B-43 Load-Deflection Diagrams: P19RB

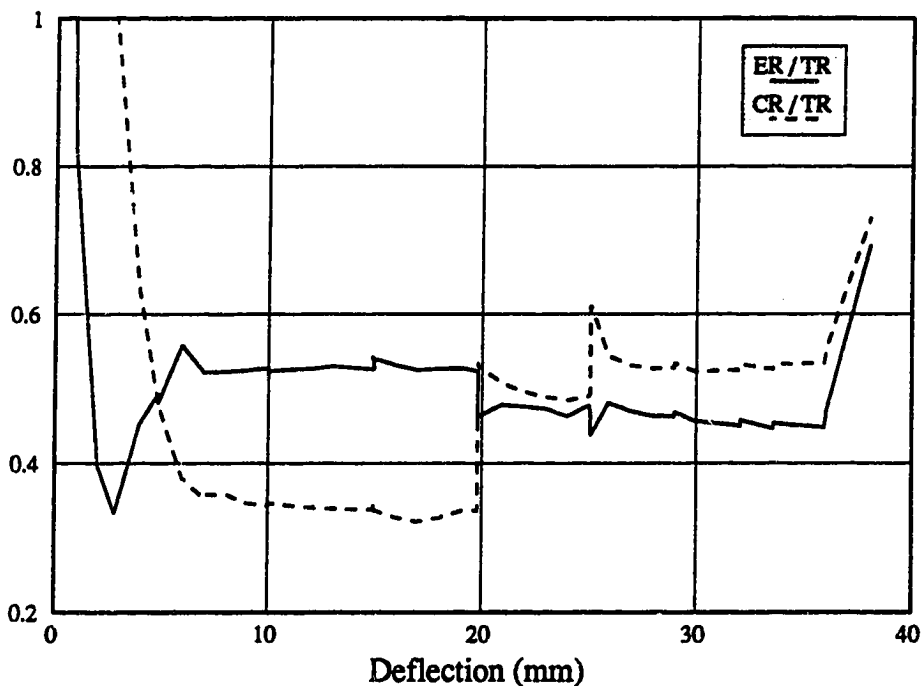


Figure B-44 Ratios of Edge and Corner Restraint to Average Load in Tie Rods: P19RB

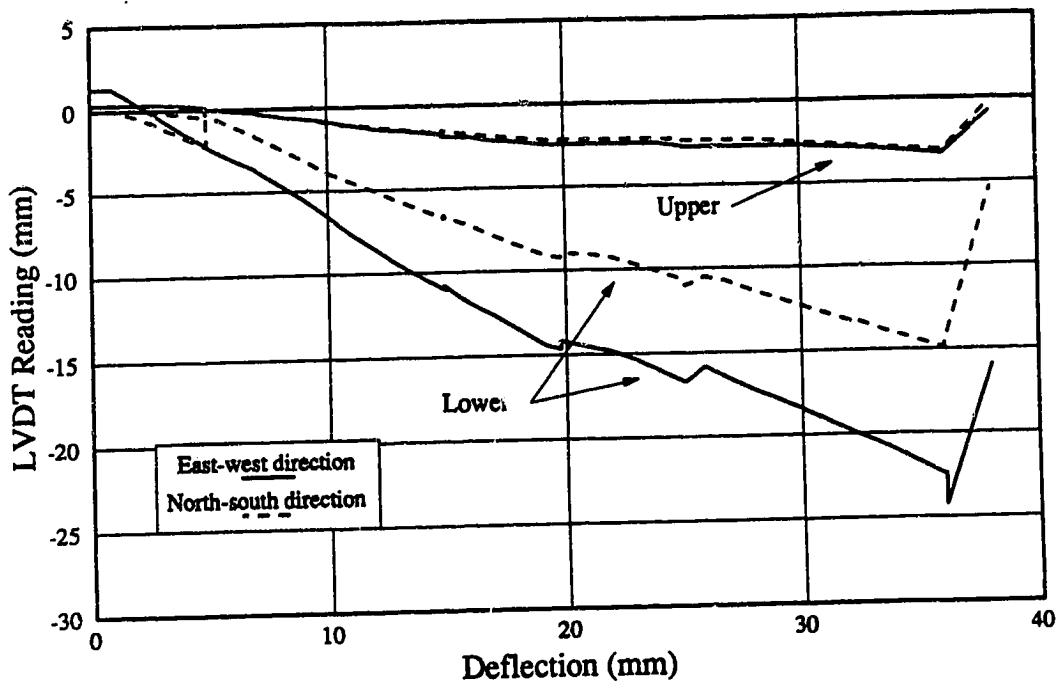


Figure B-45 Data from LVDT's Measuring Plate Expansion: P19RB

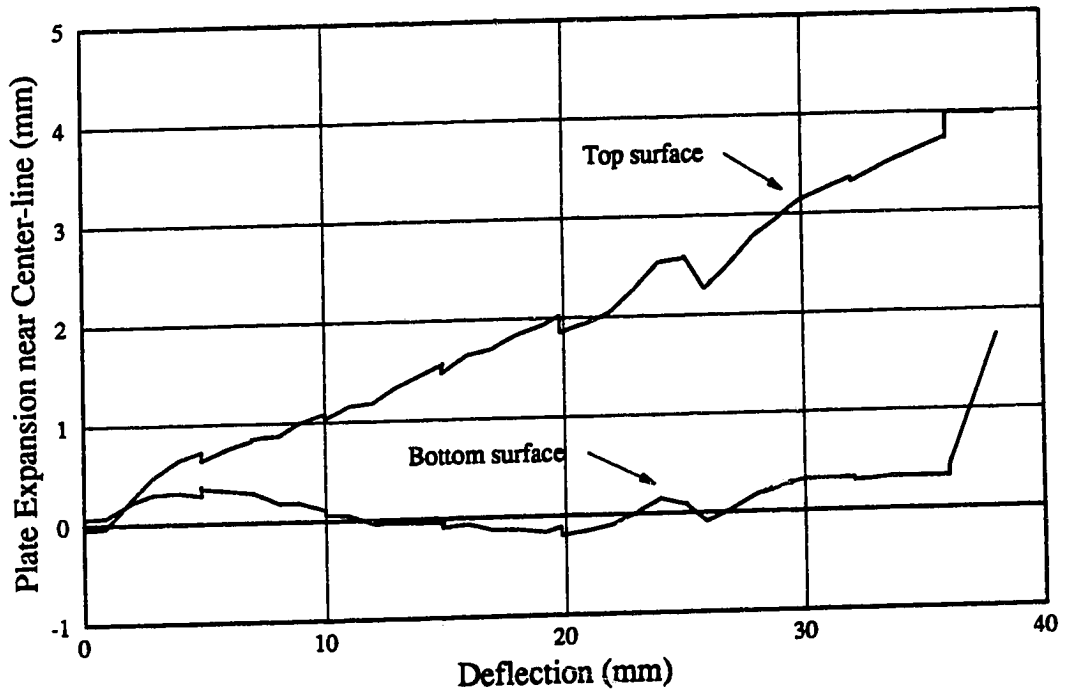


Figure B-46 In-Plane Expansion of Plate Near Center-Line: P19RB

Appendix C: Strain Gauge Data

All strain data were converted to bar forces on the basis of coupon tests. The results from geometrically similar gauge locations were then averaged.

Strain gauge results are presented in two ways. In the first part of Appendix C, bar force profiles at selected load levels for each test are presented. In the second part, diagrams showing values of force gradient and bar force plotted against stroke are presented. For reference, a load deflection curve for the overall specimen is included in each force gradient and bar force plot. Details on how the force gradients were calculated are presented in Chapter 4.

Table C-1 Description of Force Gradient Intervals

Interval	Column Bar				Perimeter Bar		
	1st	2nd	3rd	4th	1st	2nd	3rd
Distance of upper gauge from center-line (mm)	85	225	375	675	75	225	525
Distance of lower gauge from center-line (mm)	225	375	675	end	225	525	end
Length of interval (mm)	140	150	300	685	150	300	475

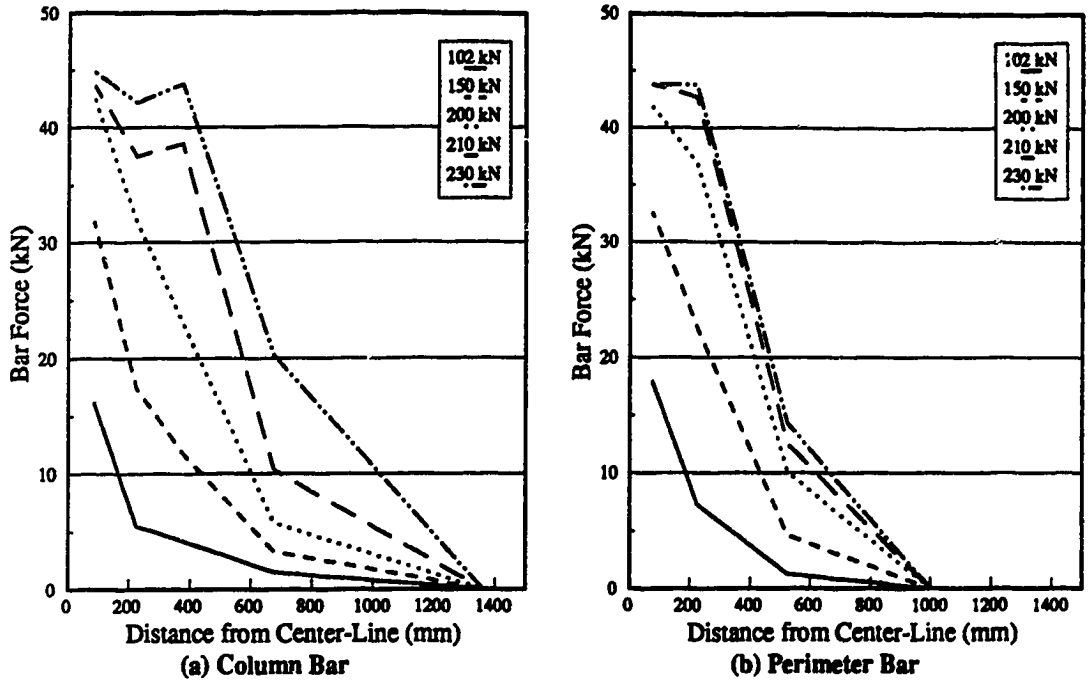


Figure C-1 Bar Force Profiles: P11F0

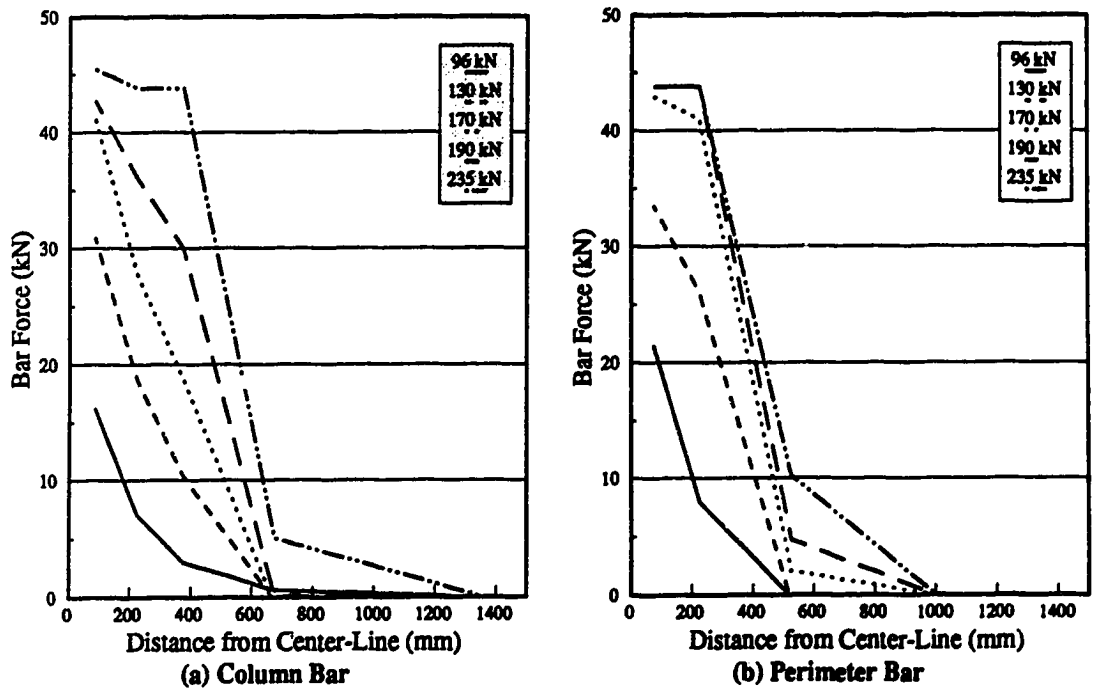


Figure C-2 Bar Force Profiles: P38F0

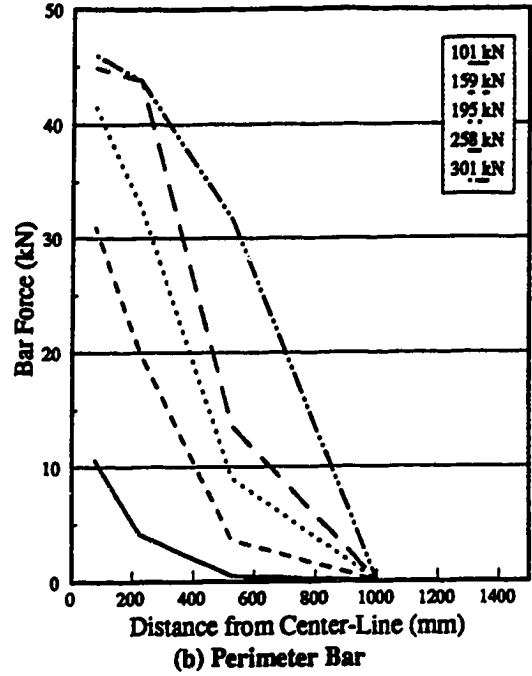
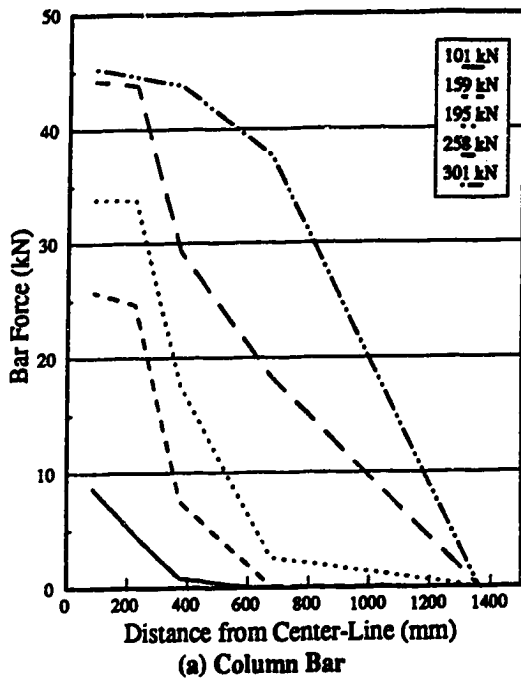


Figure C-3 Bar Force Profiles: P11F31

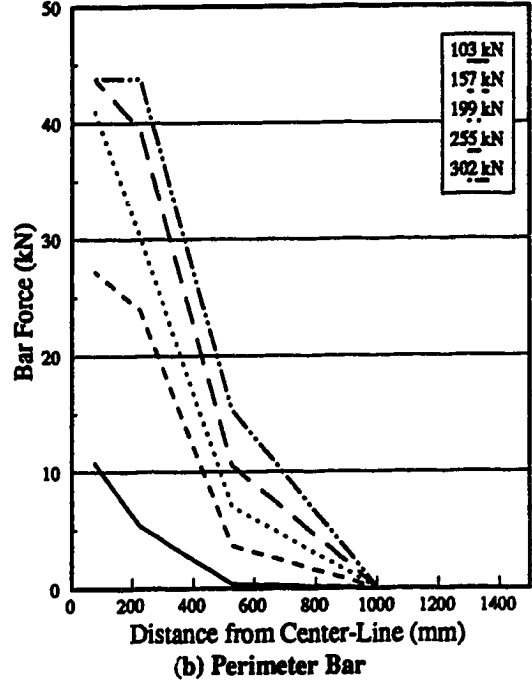
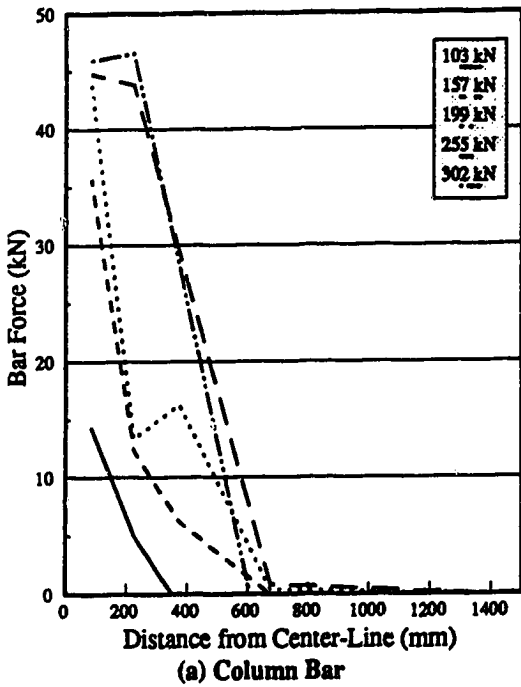


Figure C-4 Bar Force Profiles: P38F34

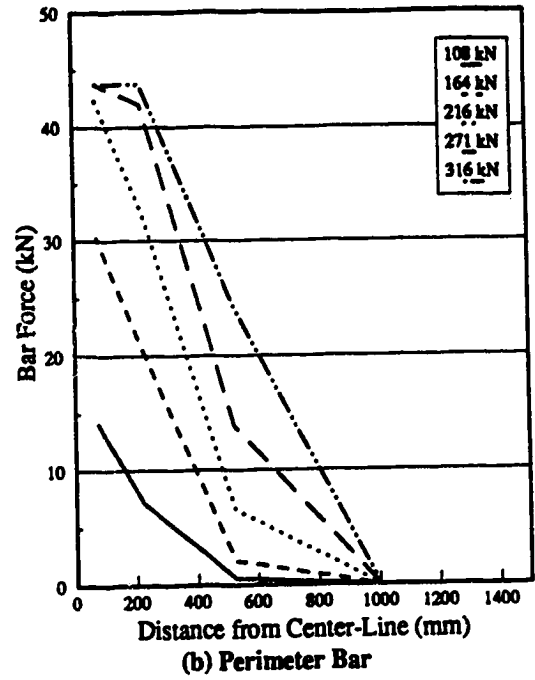
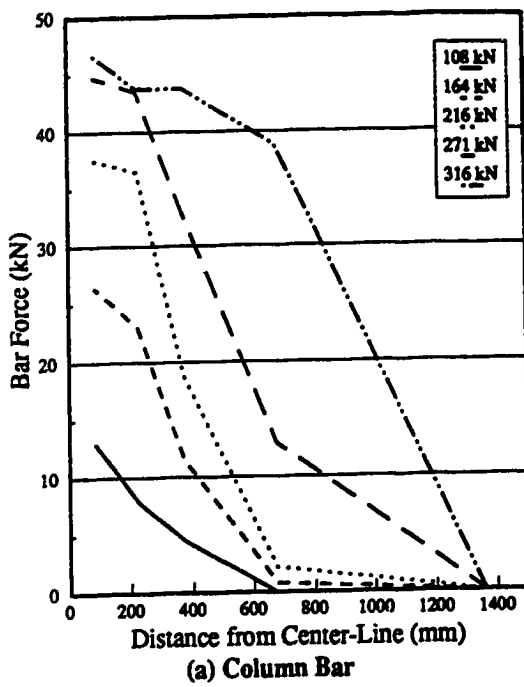


Figure C-5 Bar Force Profiles: P11F66

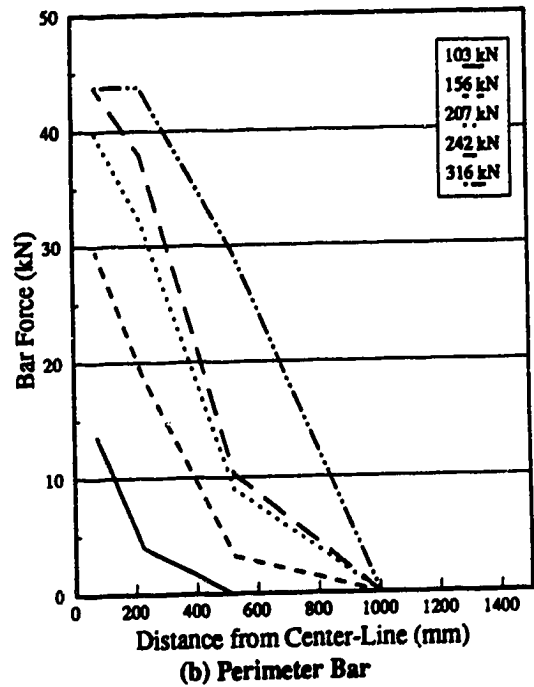
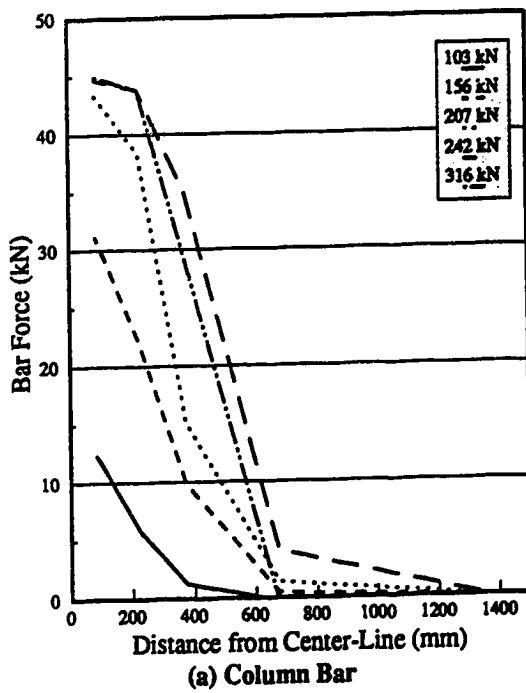


Figure C-6 Bar Force Profiles: P38F69

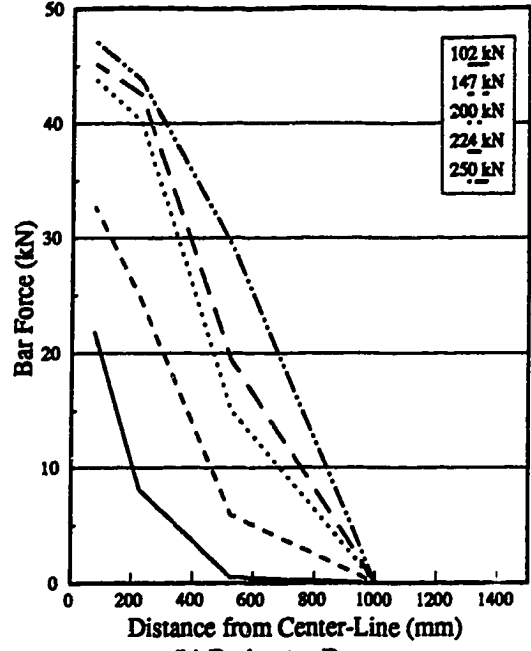
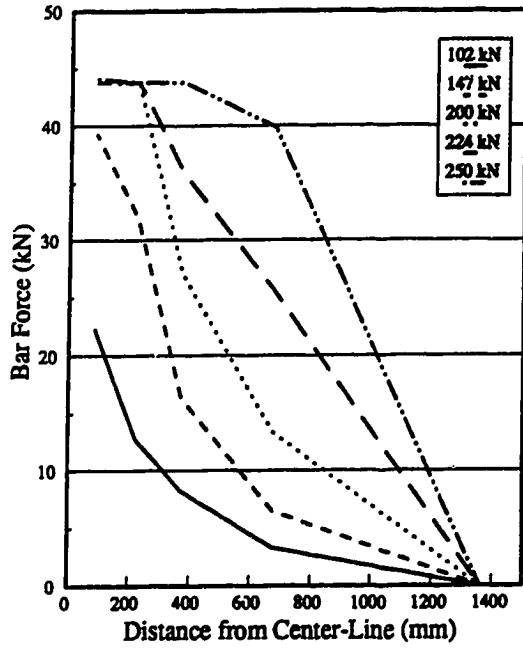


Figure C-7 Bar Force Profiles: P19S150

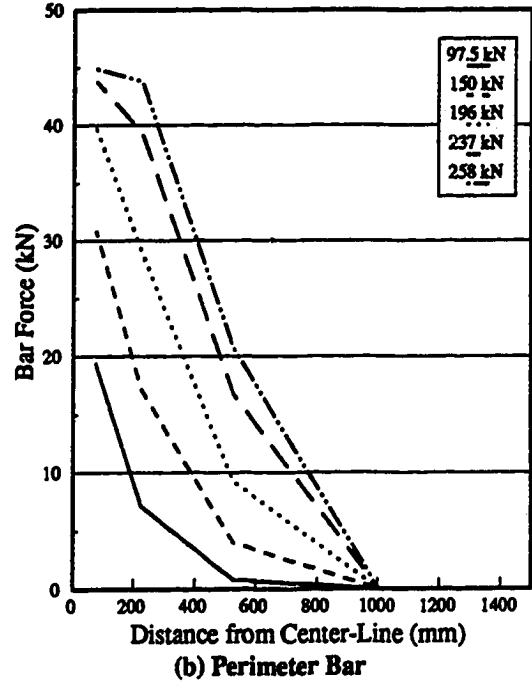
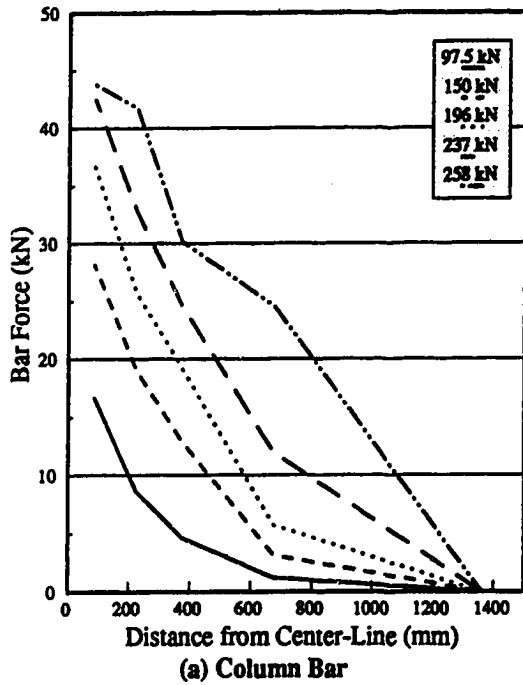
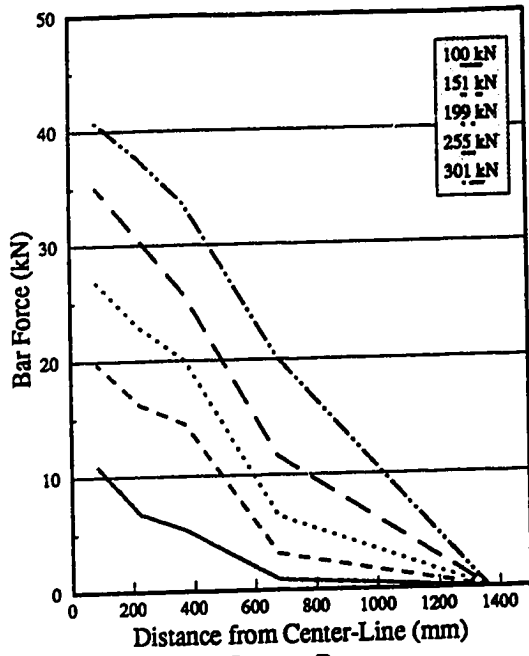
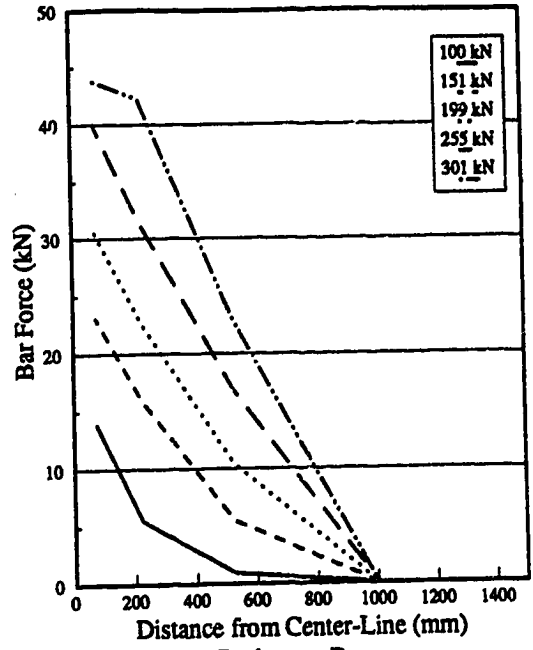


Figure C-8 Bar Force Profiles: P19S75

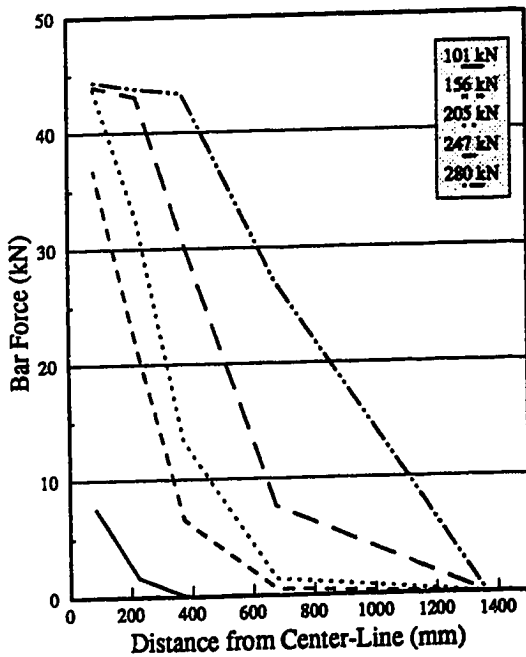


(a) Column Bar

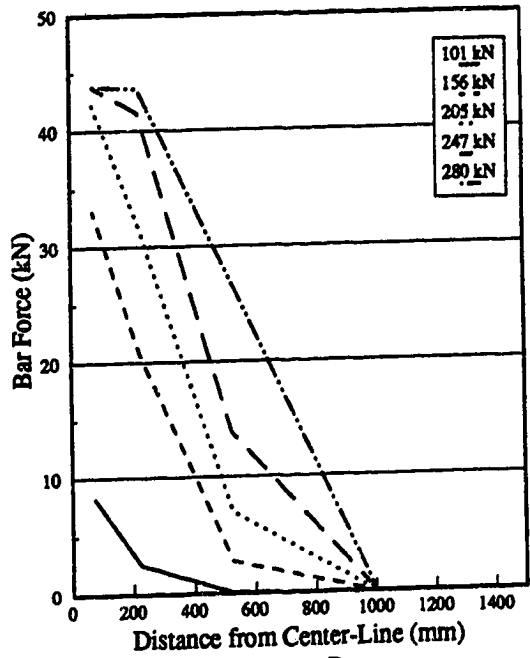


(b) Perimeter Bar

Figure C-9 Bar Force Profiles: P19S50



(a) Column Bar



(b) Perimeter Bar

Figure C-10 Bar Force Profiles: P19RE

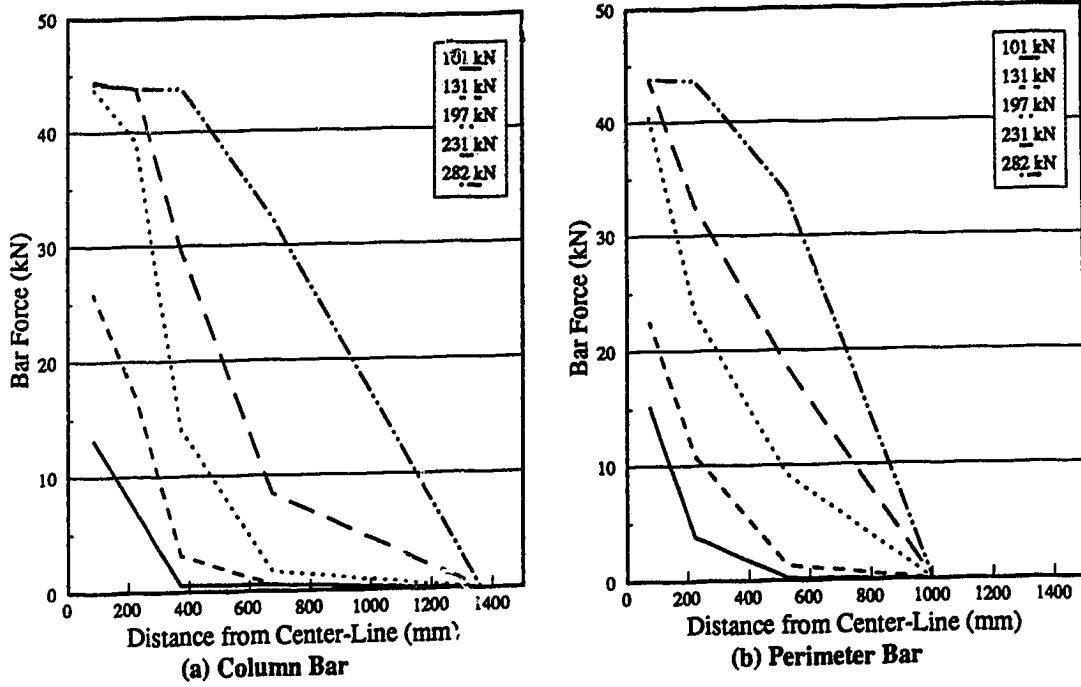


Figure C-11 Bar Force Profiles: P19RC

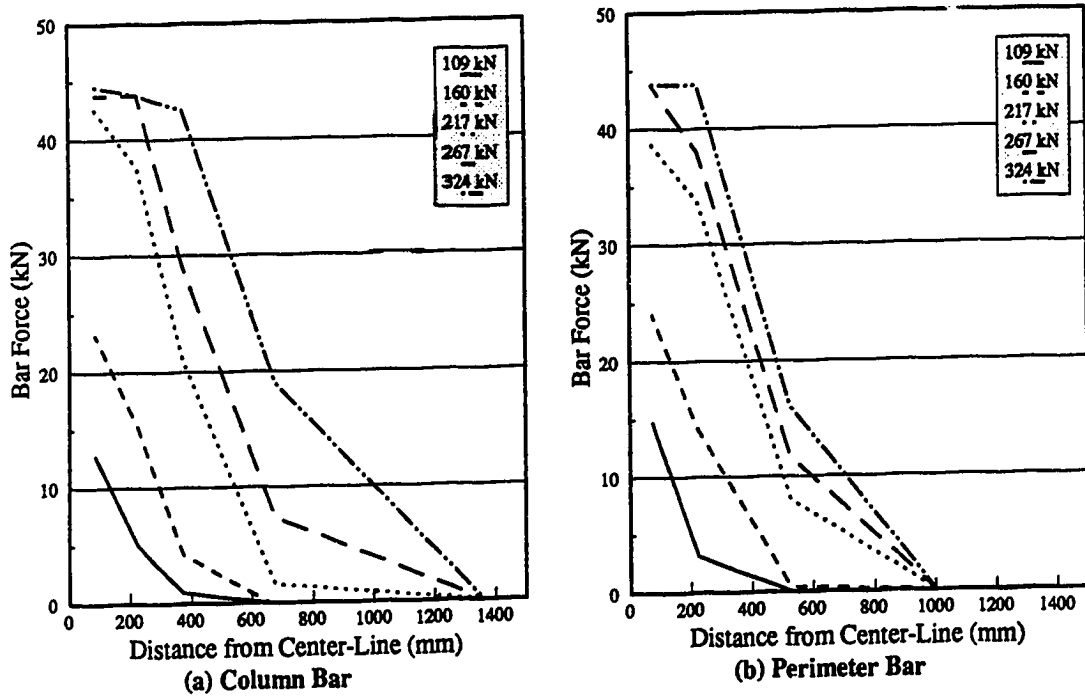


Figure C-12 Bar Force Profiles: P19RB

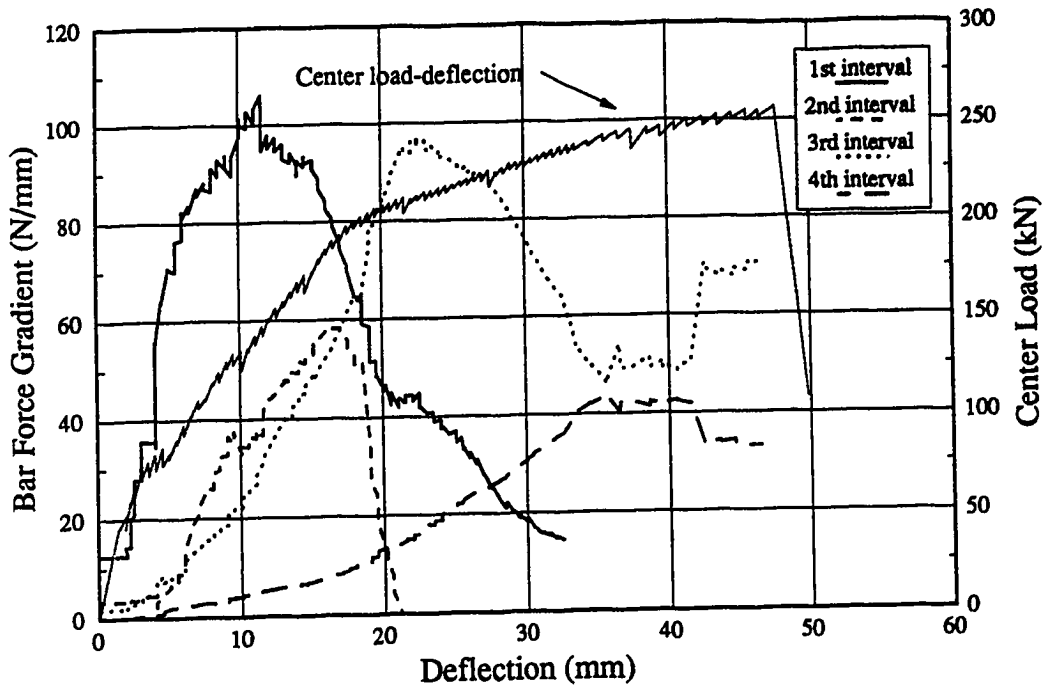


Figure C-13 Column Bar Force Gradients: P11F0

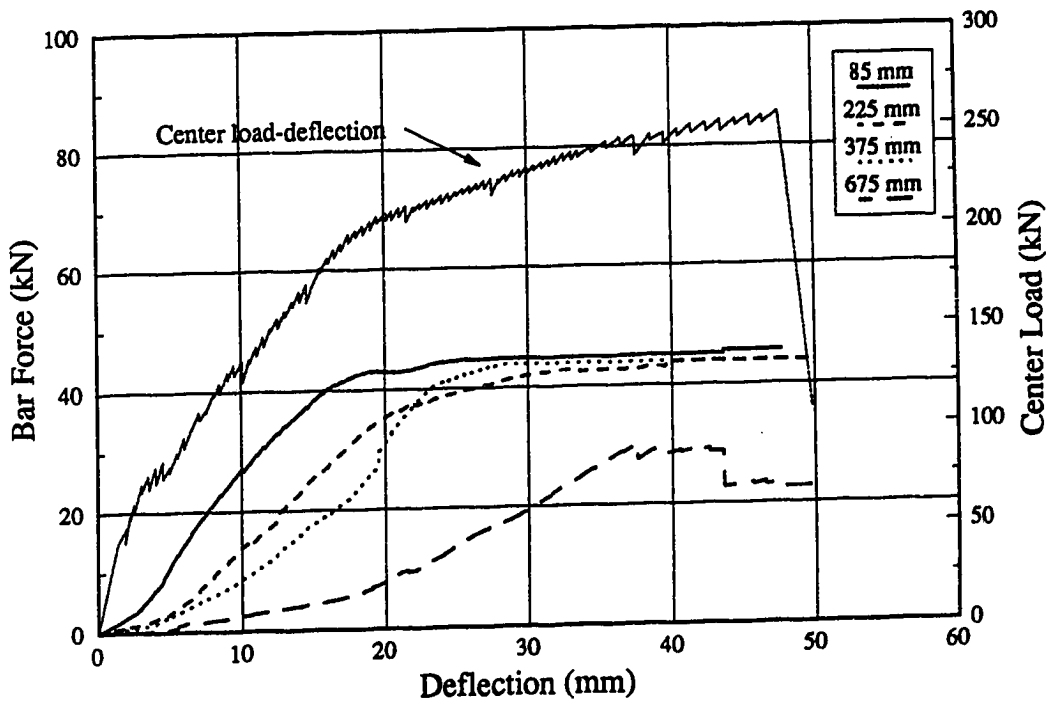


Figure C-14 Column Bar Forces: P11F0

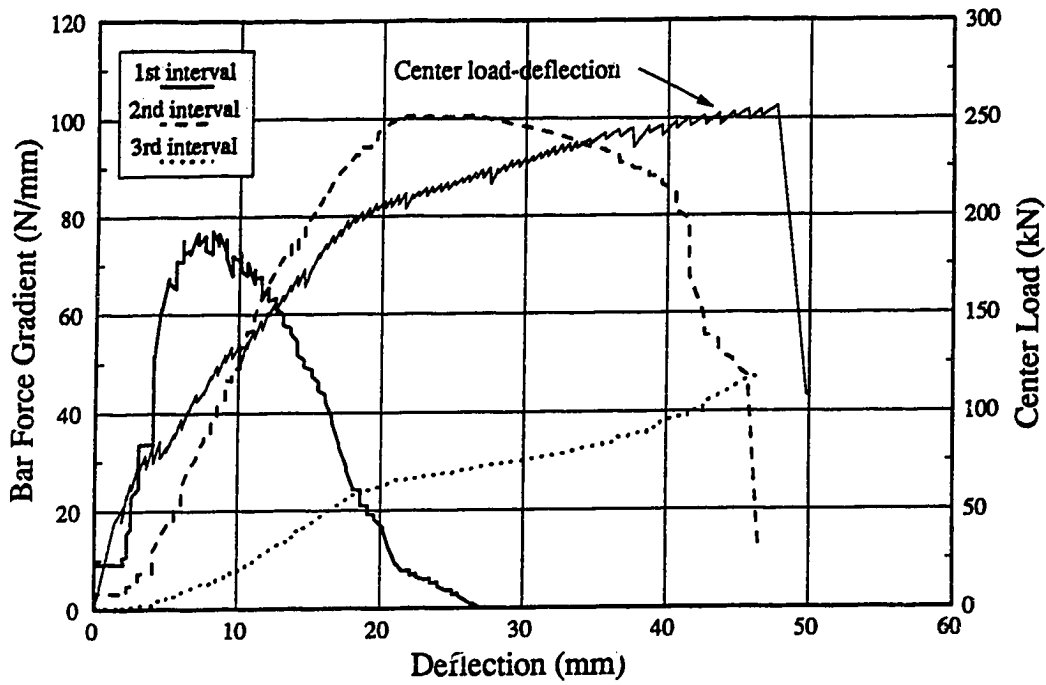


Figure C-15 Perimeter Bar Force Gradients: P11F0

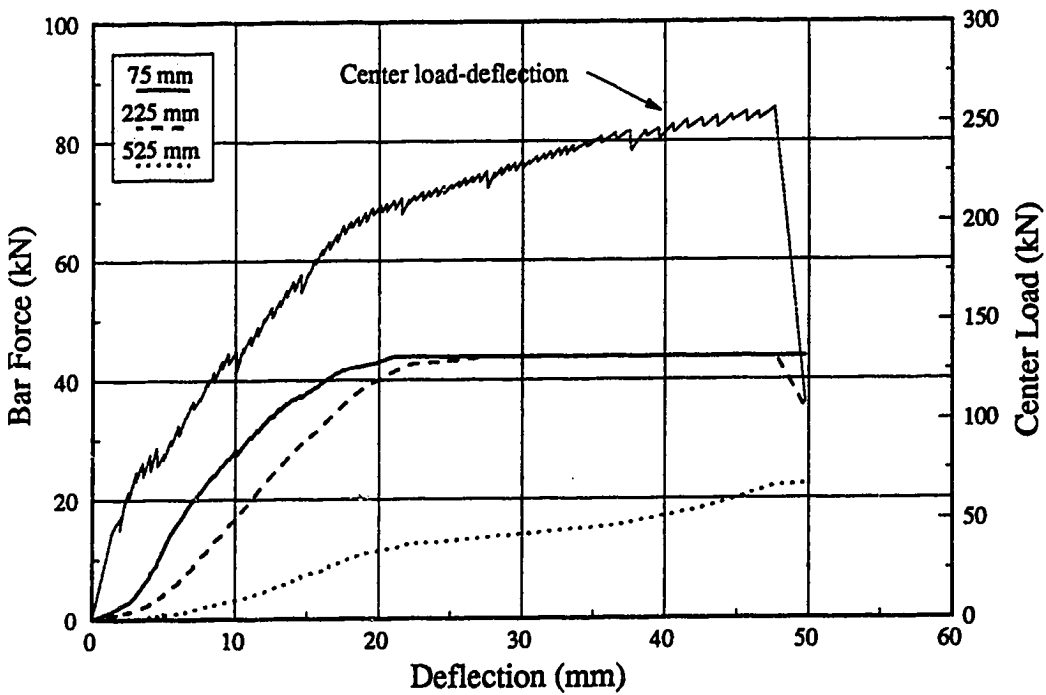


Figure C-16 Perimeter Bar Forces: P11F0

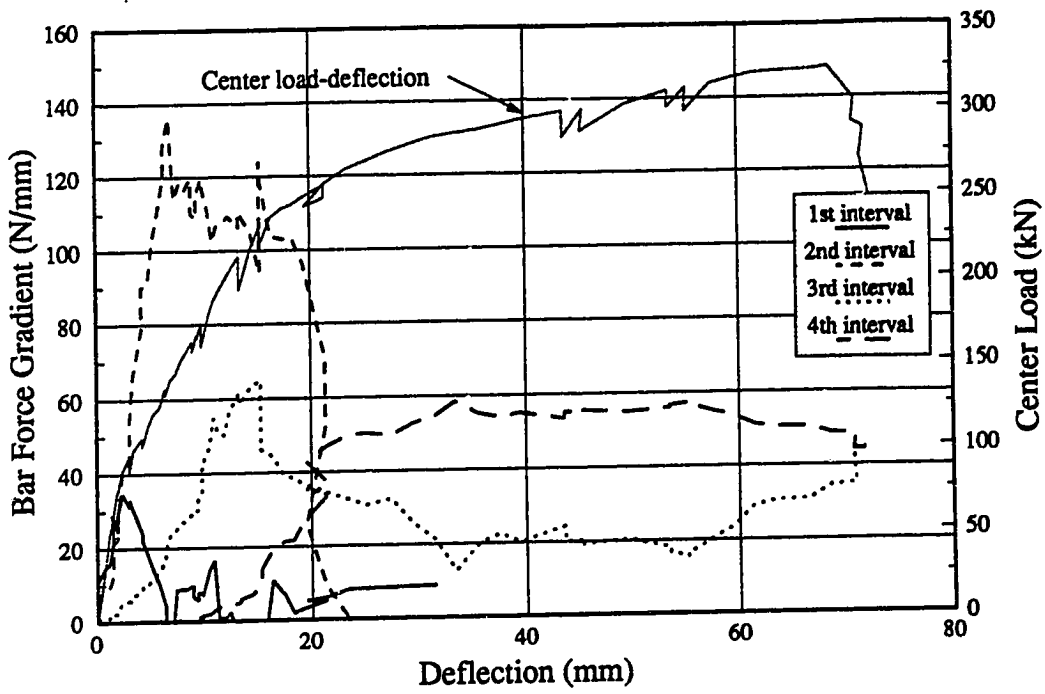


Figure C-17 Column Bar Force Gradients: P11F31

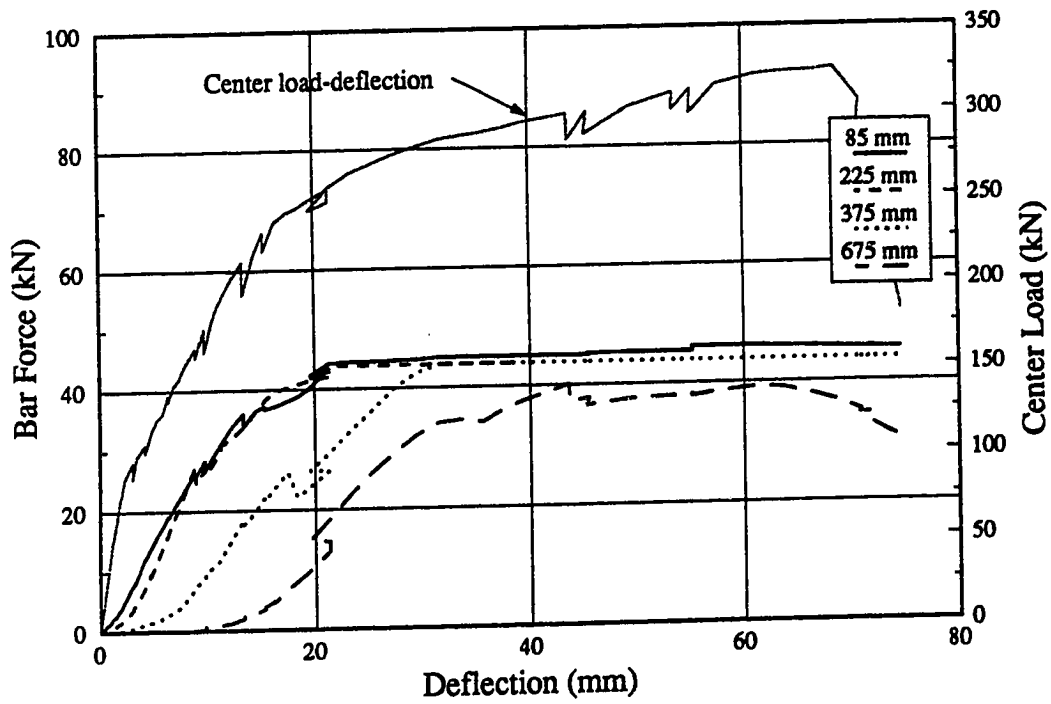


Figure C-18 Column Bar Forces: P11F31

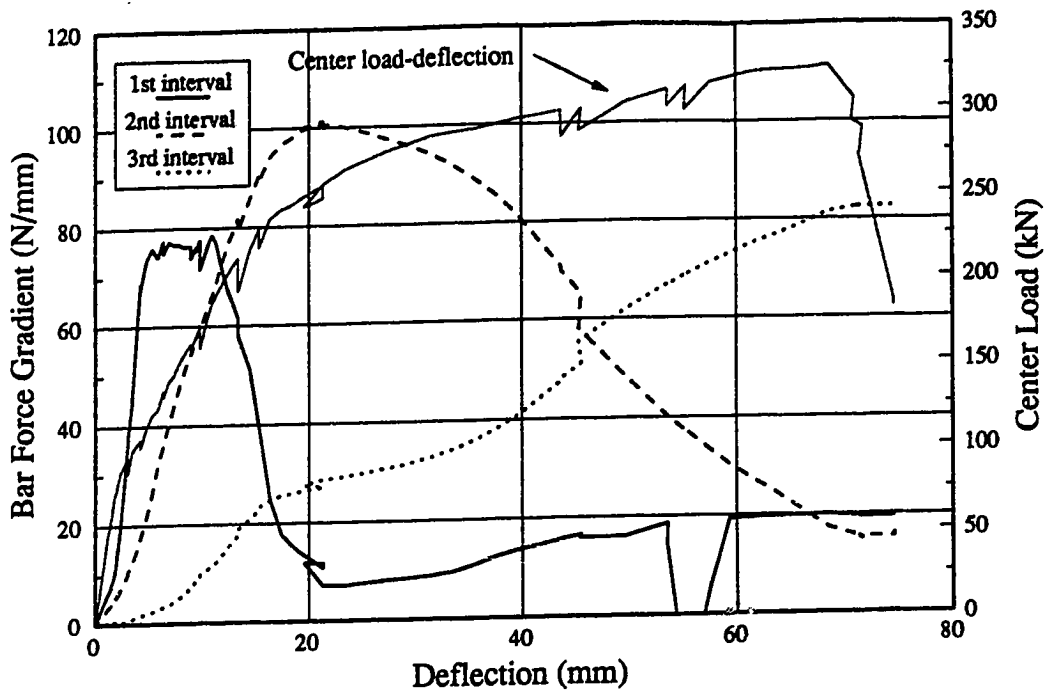


Figure C-19 Perimeter Bar Force Gradients: P11F31

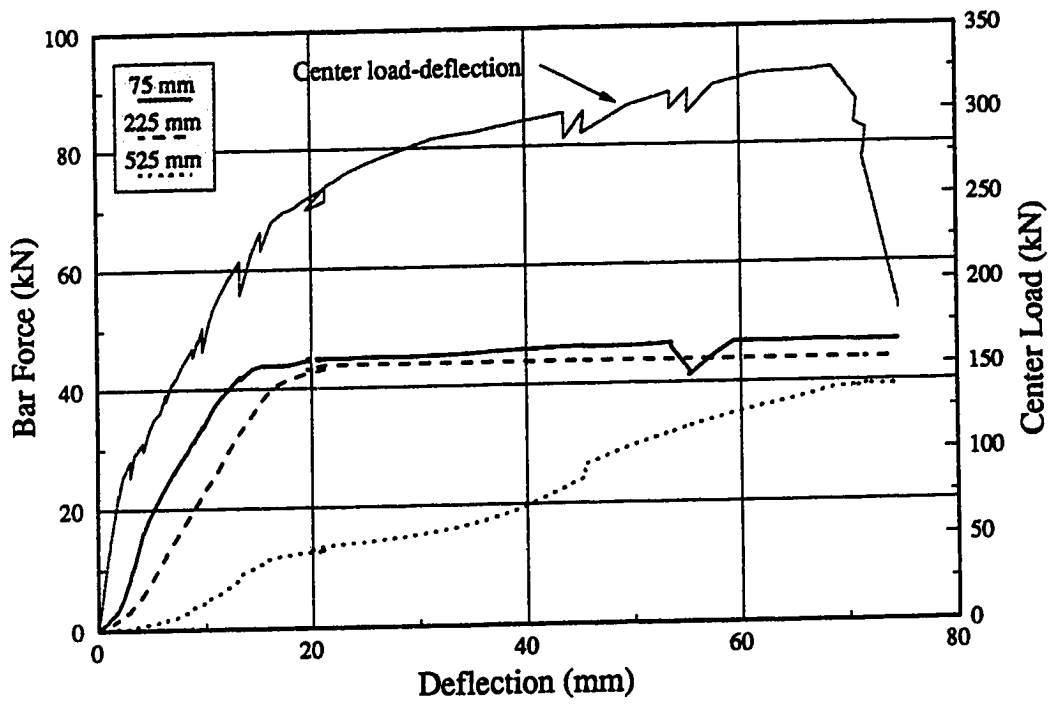


Figure C-20 Perimeter Bar Forces: P11F31

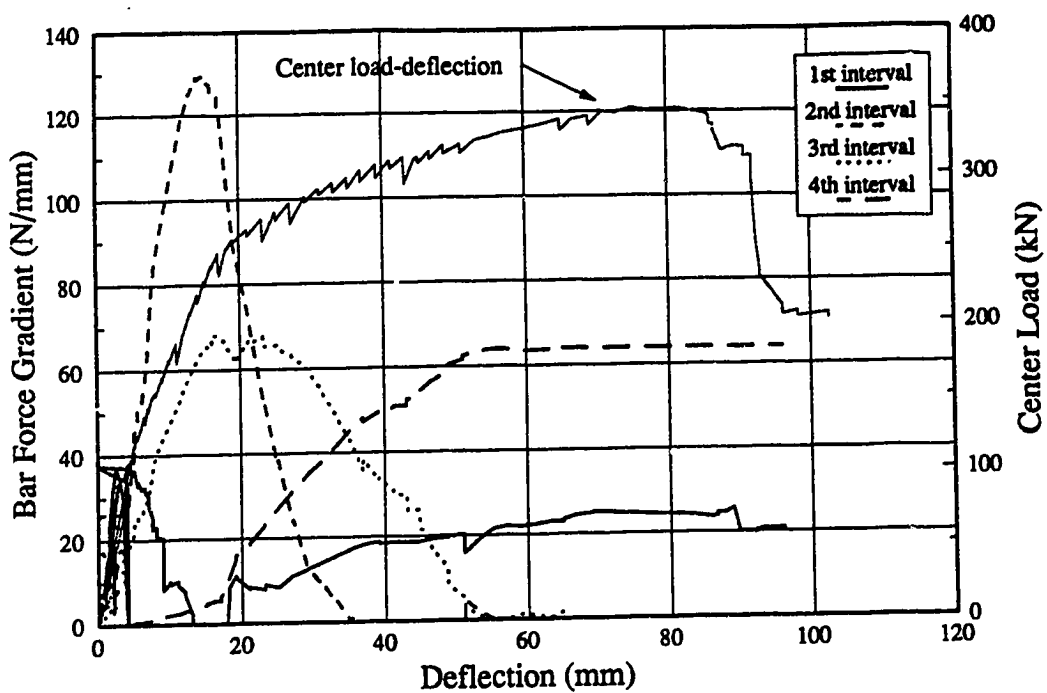


Figure C-21 Column Bar Force Gradients: P11F66

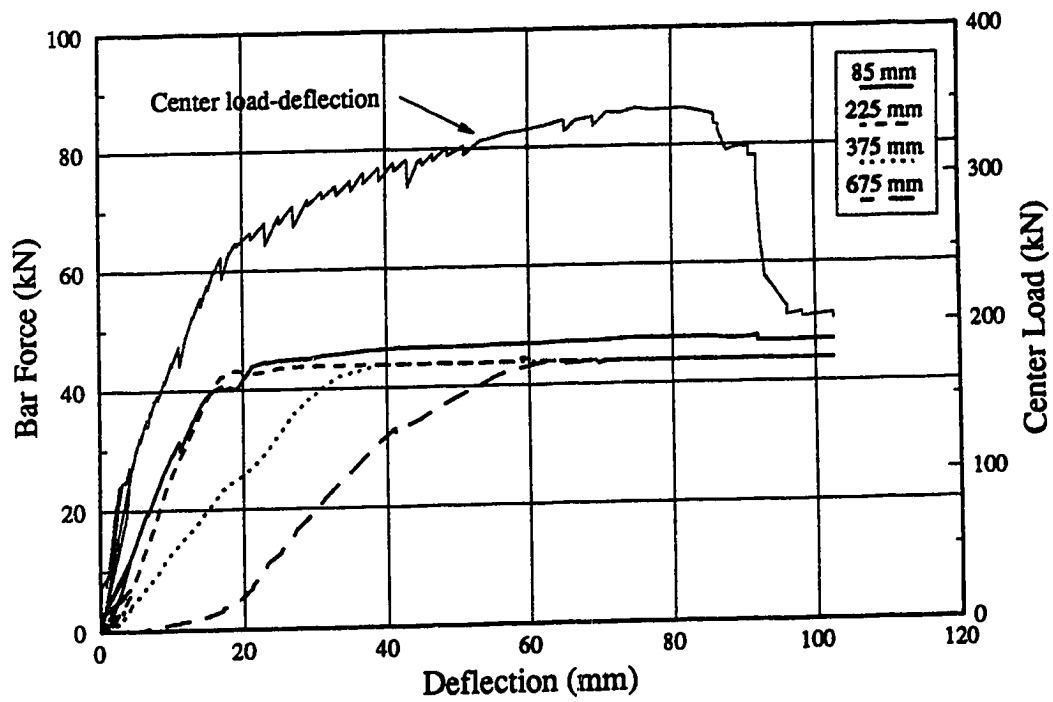


Figure C-22 Column Bar Forces: P11F66

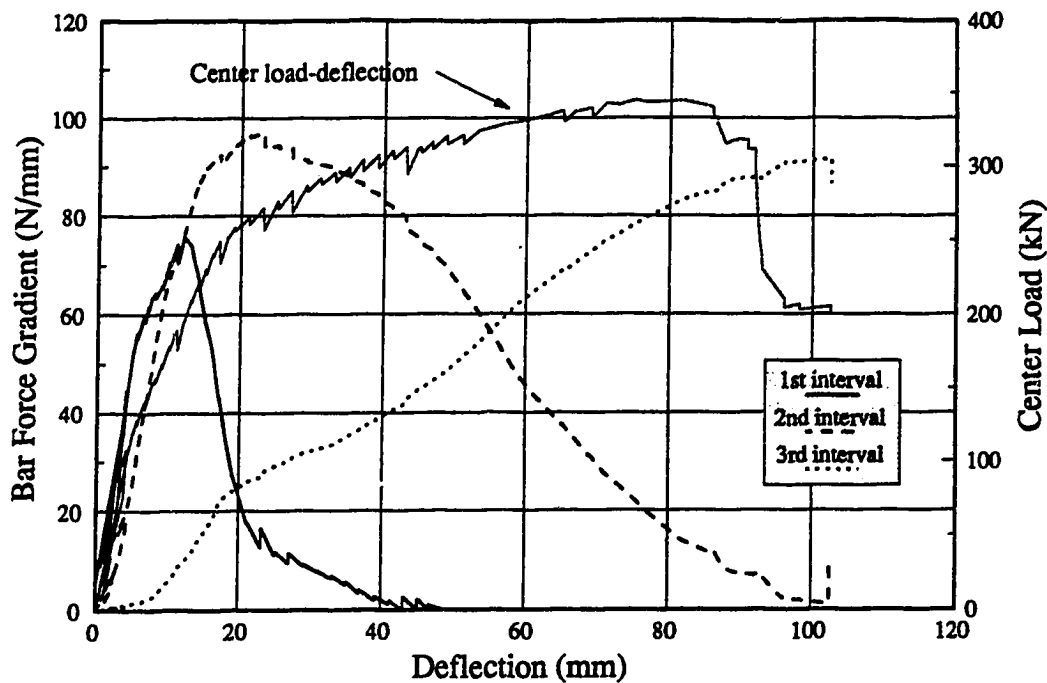


Figure C-23 Perimeter Bar Force Gradients: P11F66

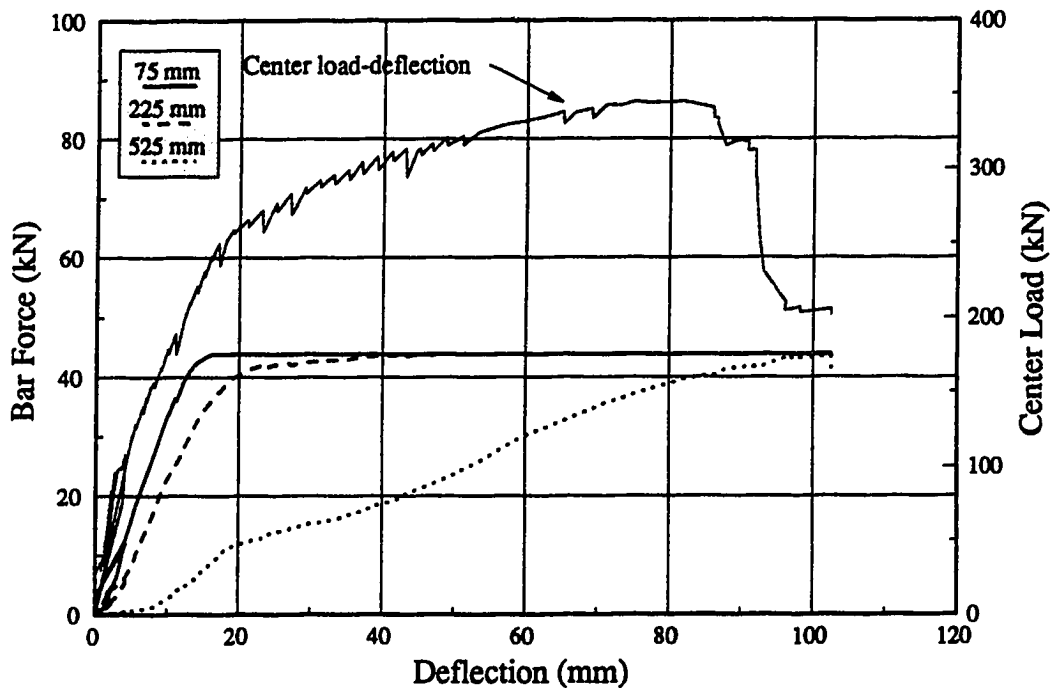


Figure C-24 Perimeter Bar Forces: P11F66

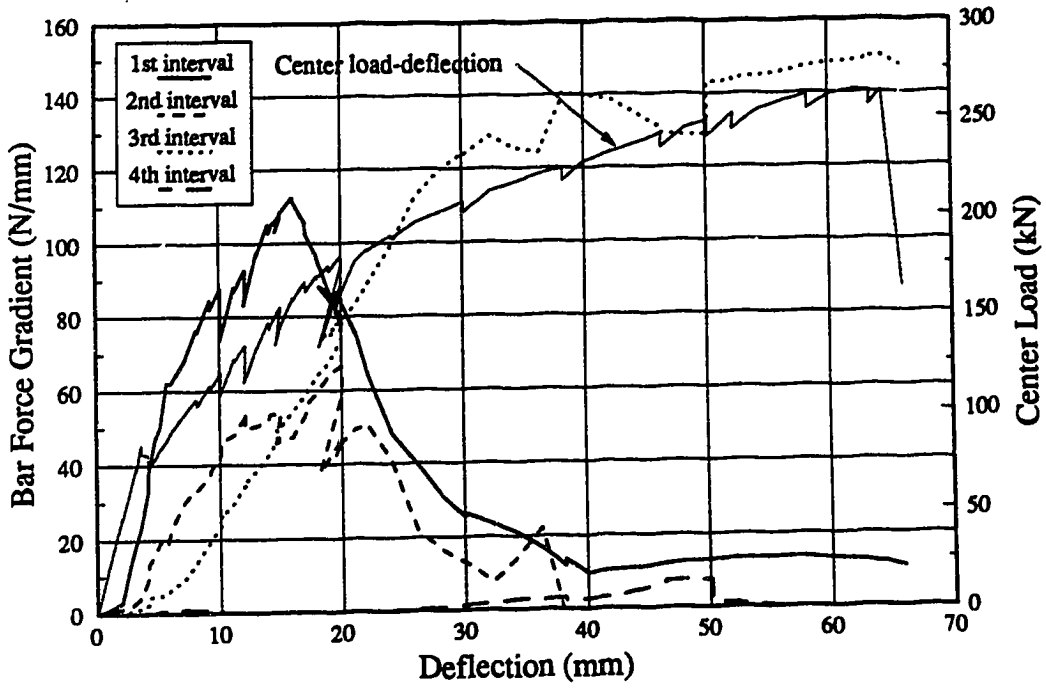


Figure C-25 Column Bar Force Gradients: P38F0

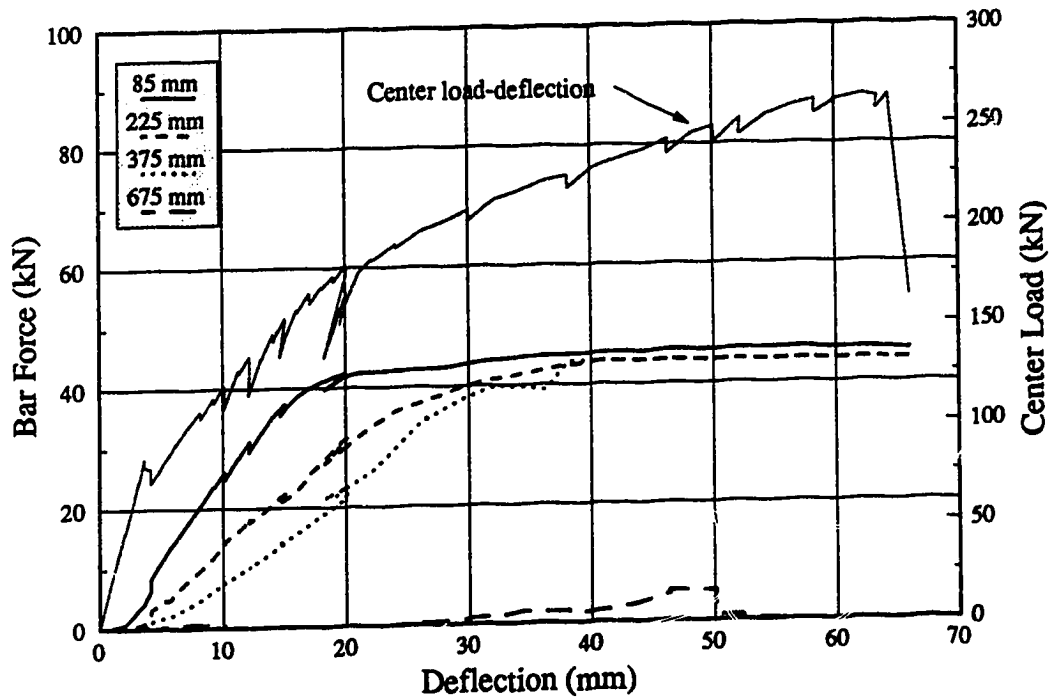


Figure C-26 Column Bar Forces: P38F0

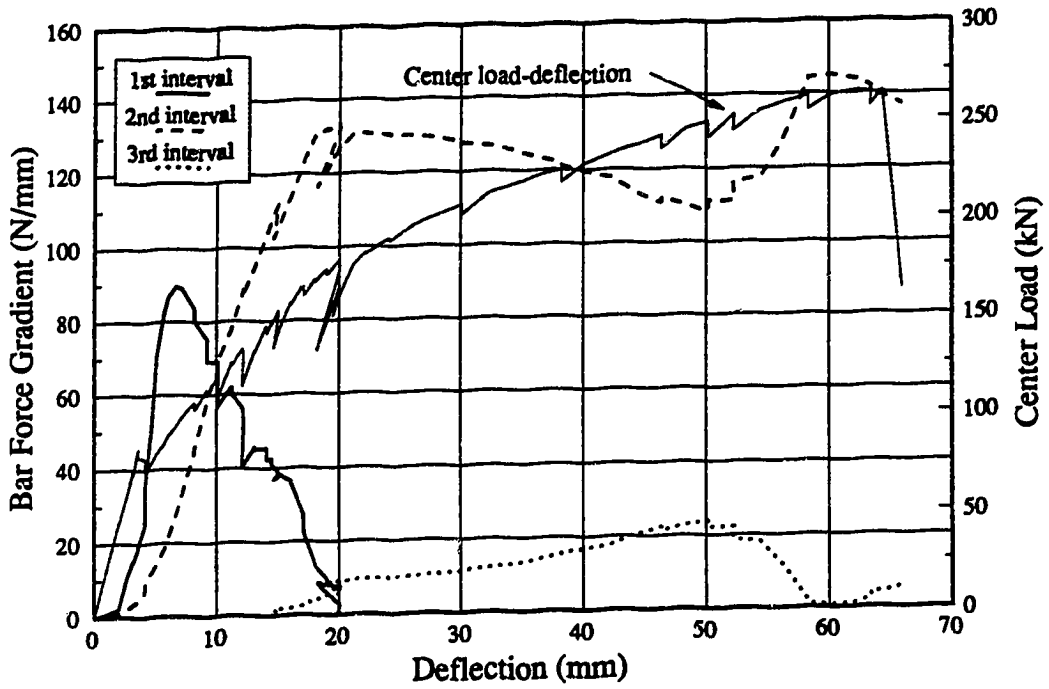


Figure C-27 Perimeter Bar Force Gradients: P38F0

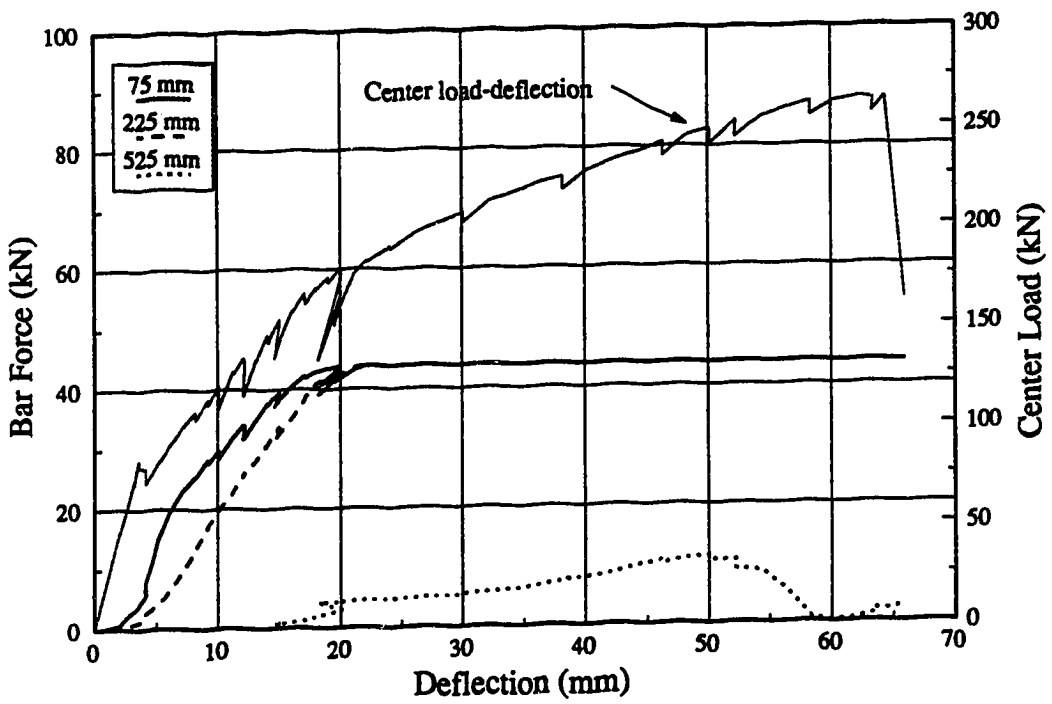


Figure C-28 Perimeter Bar Forces: P38F0

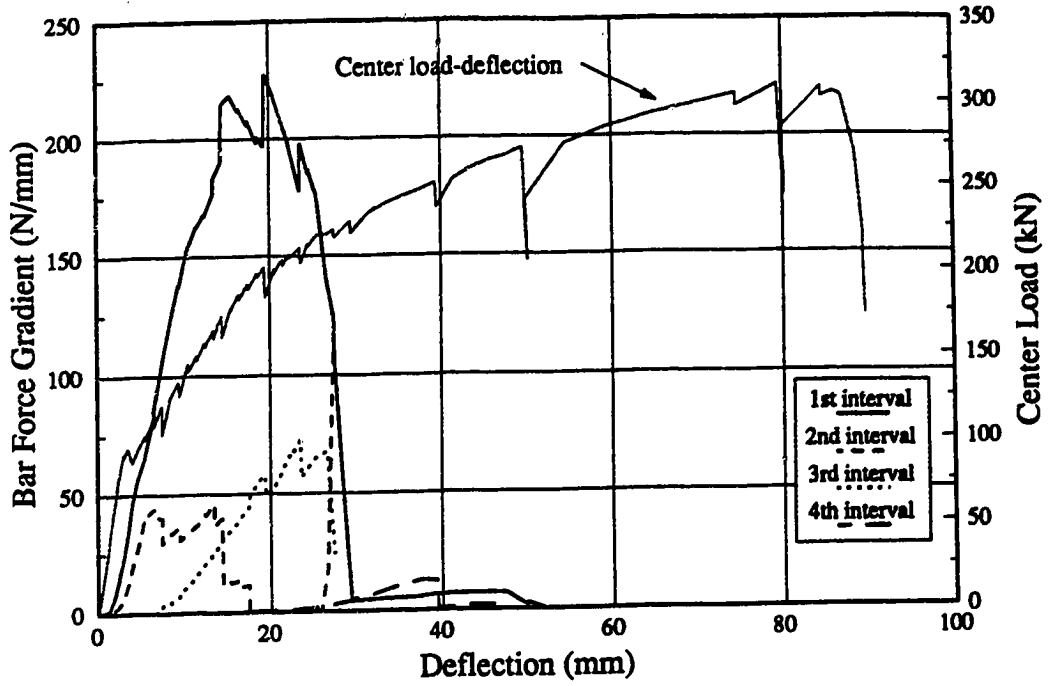


Figure C-29 Column Bar Force Gradients: P38F34

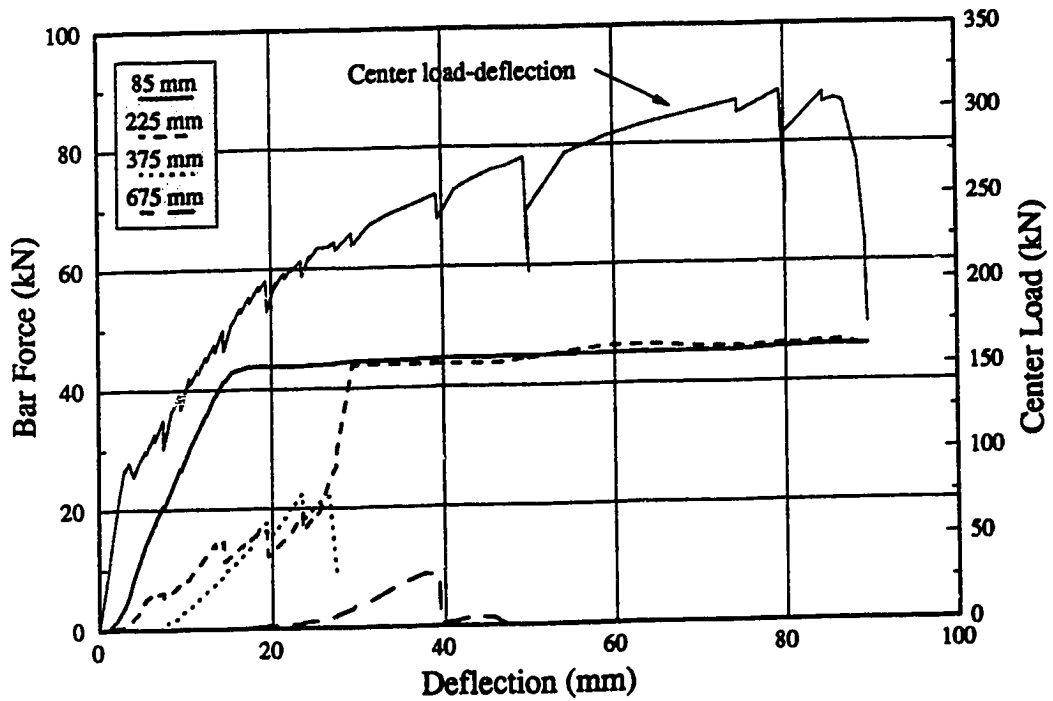


Figure C-30 Column Bar Forces: P38F34

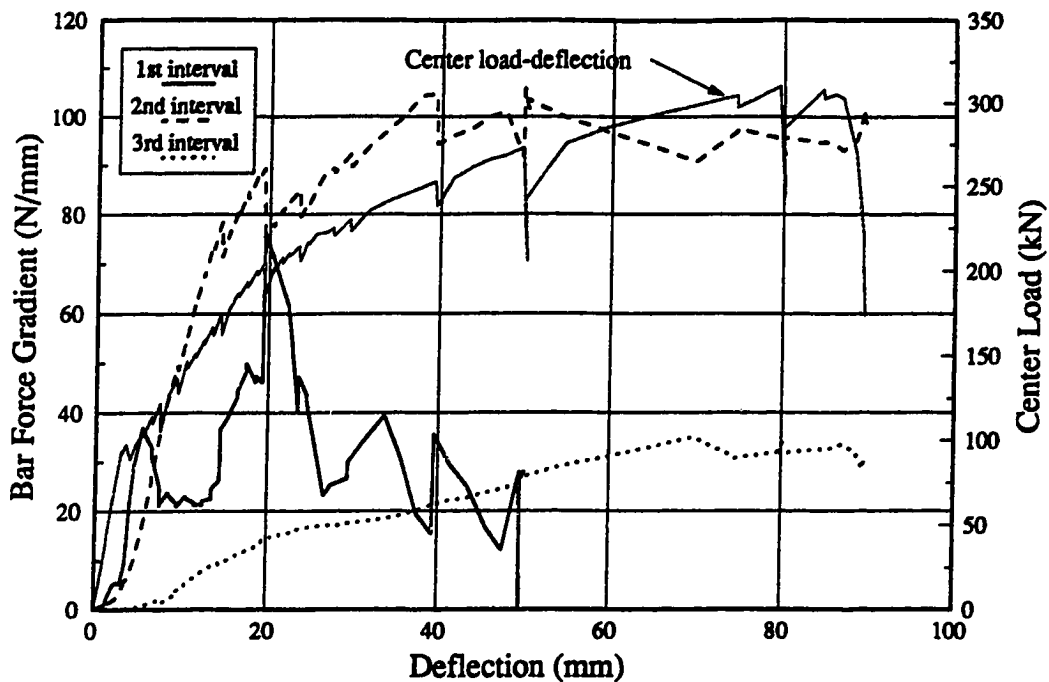


Figure C-31 Perimeter Bar Force Gradients: P38F34

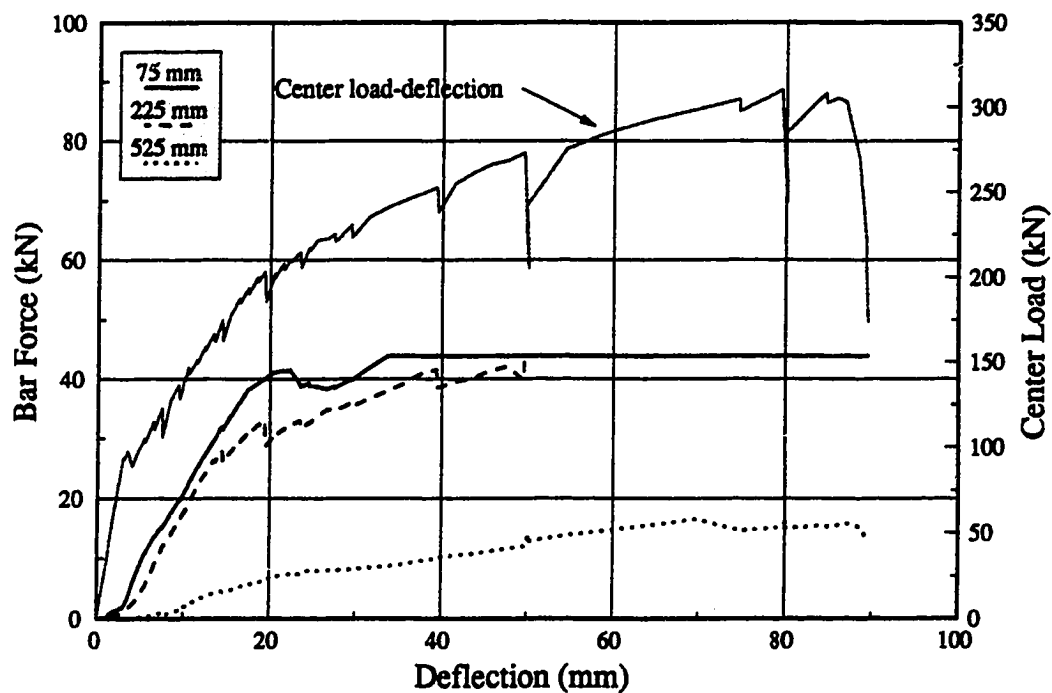


Figure C-32 Perimeter Bar Forces: P38F34

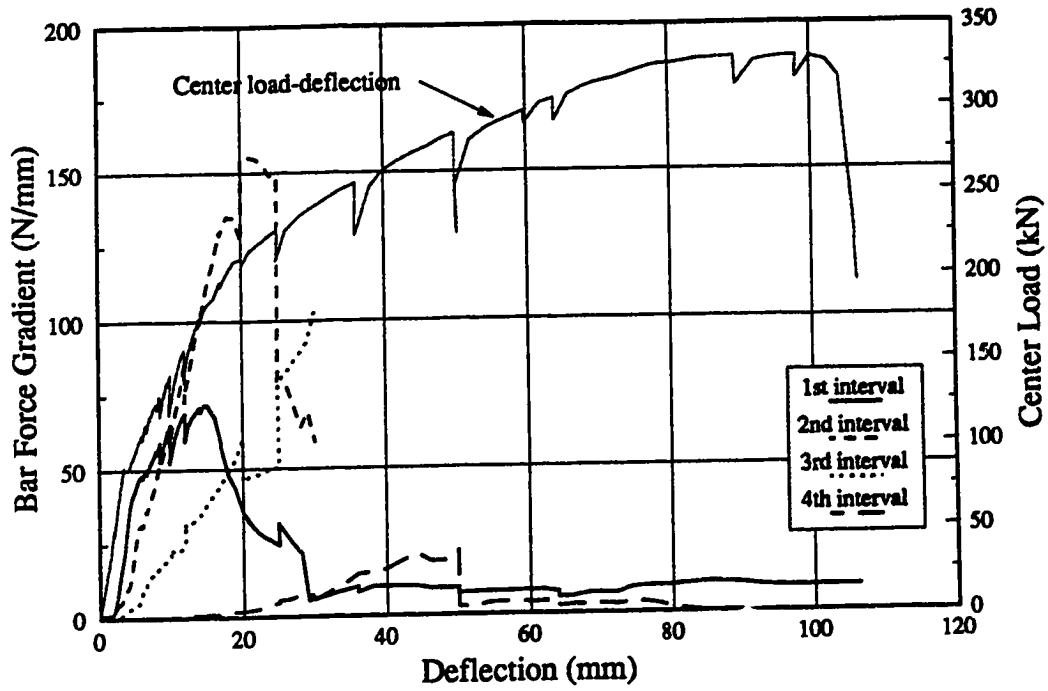


Figure C-33 Column Bar Force Gradients: P38F69

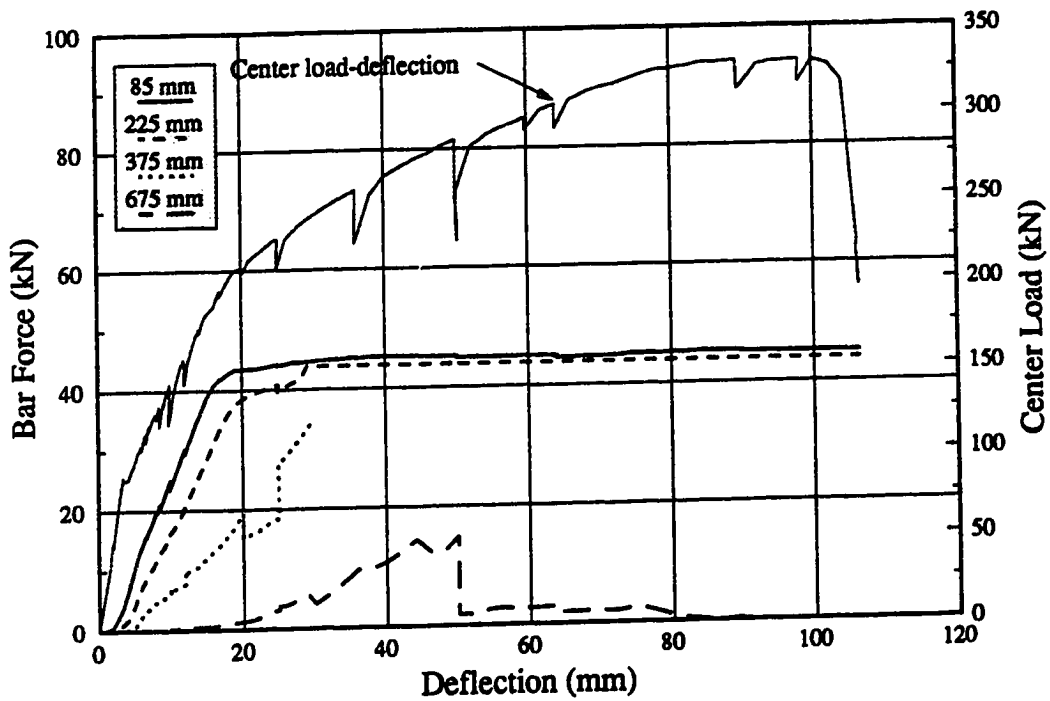


Figure C-34 Column Bar Forces: P38F69

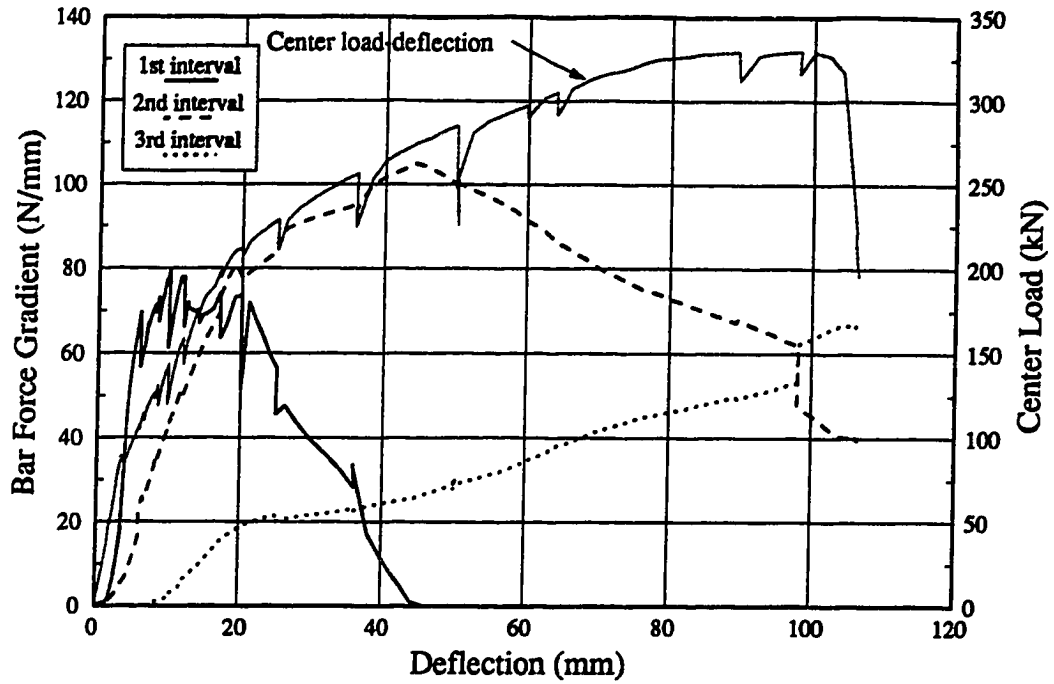


Figure C-35 Perimeter Bar Force Gradients: P38F69

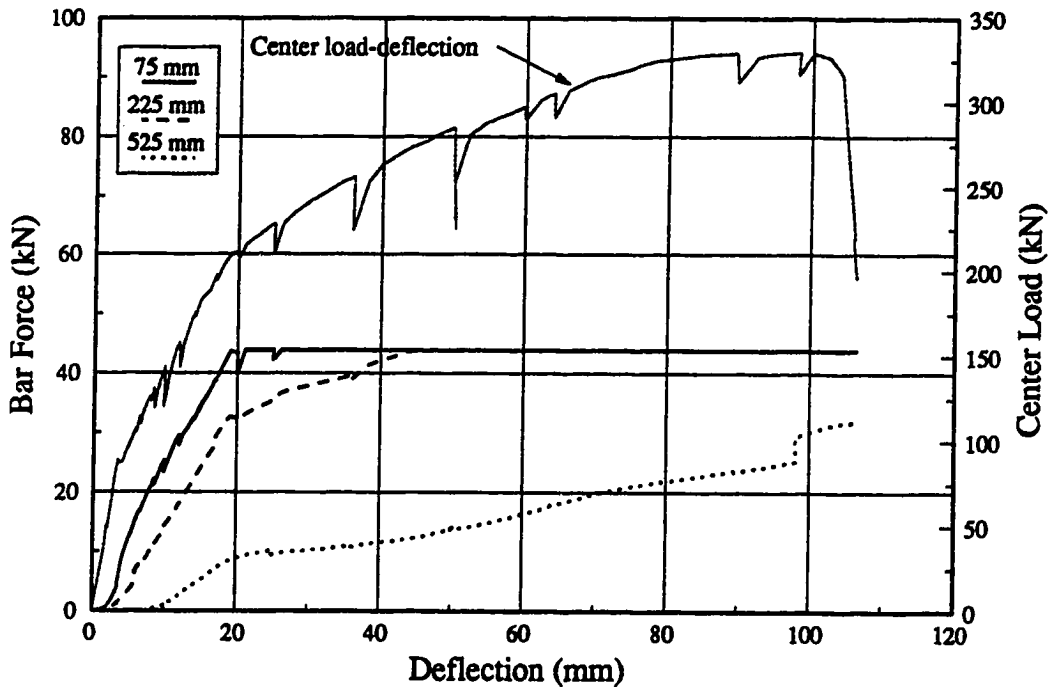


Figure C-36 Perimeter Bar Forces: P38F69

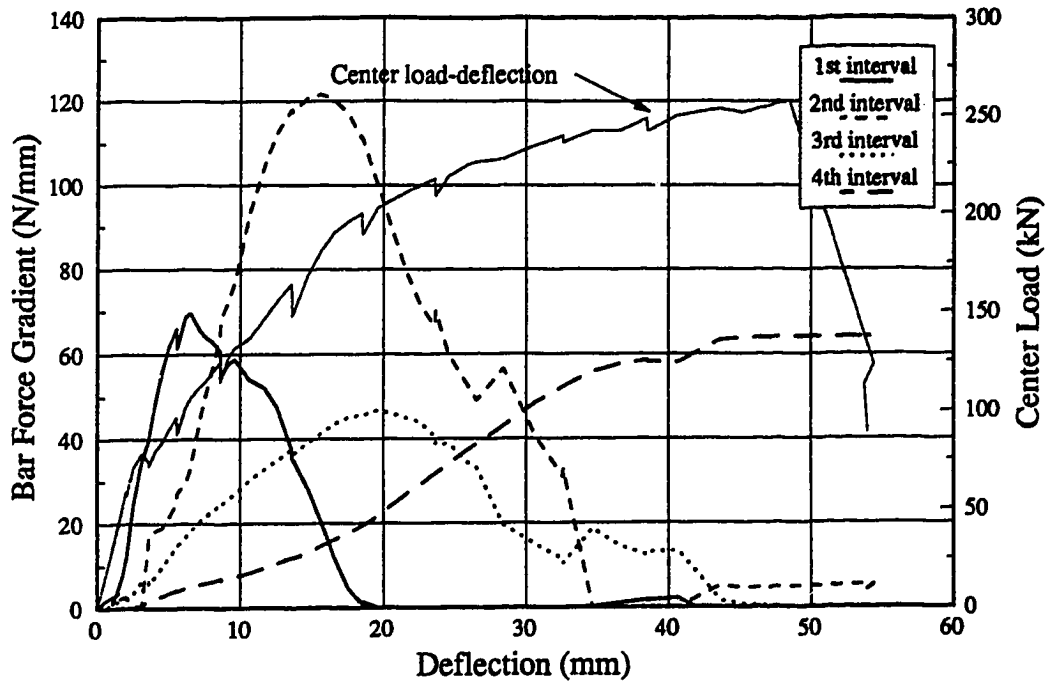


Figure C-37 Column Bar Force Gradients: P19S150

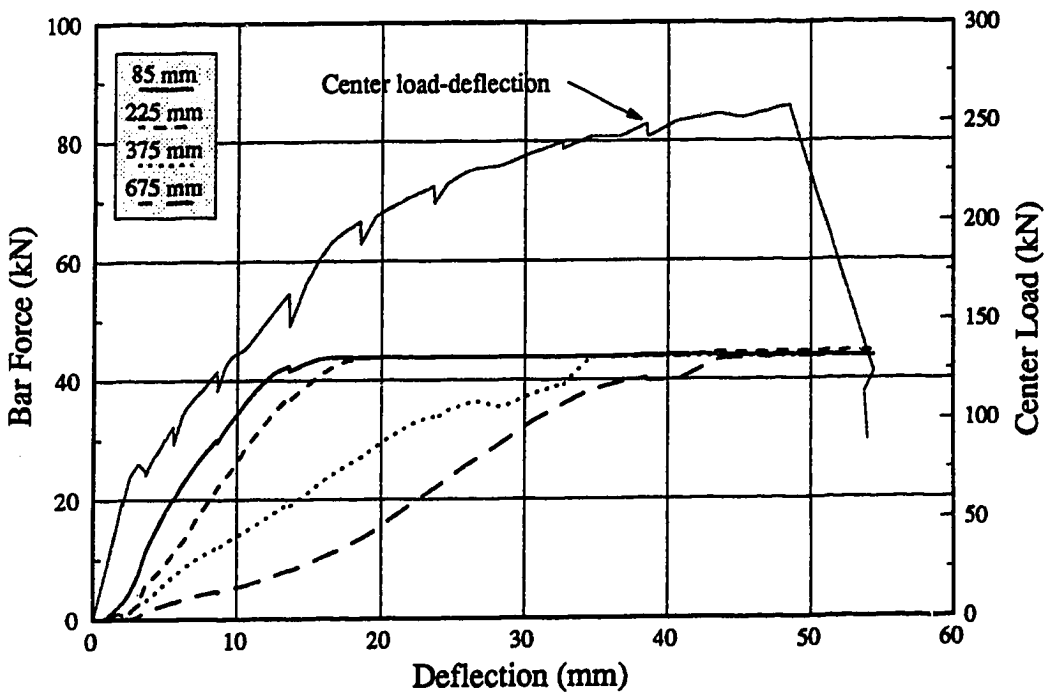


Figure C-38 Column Bar Forces: P19S150

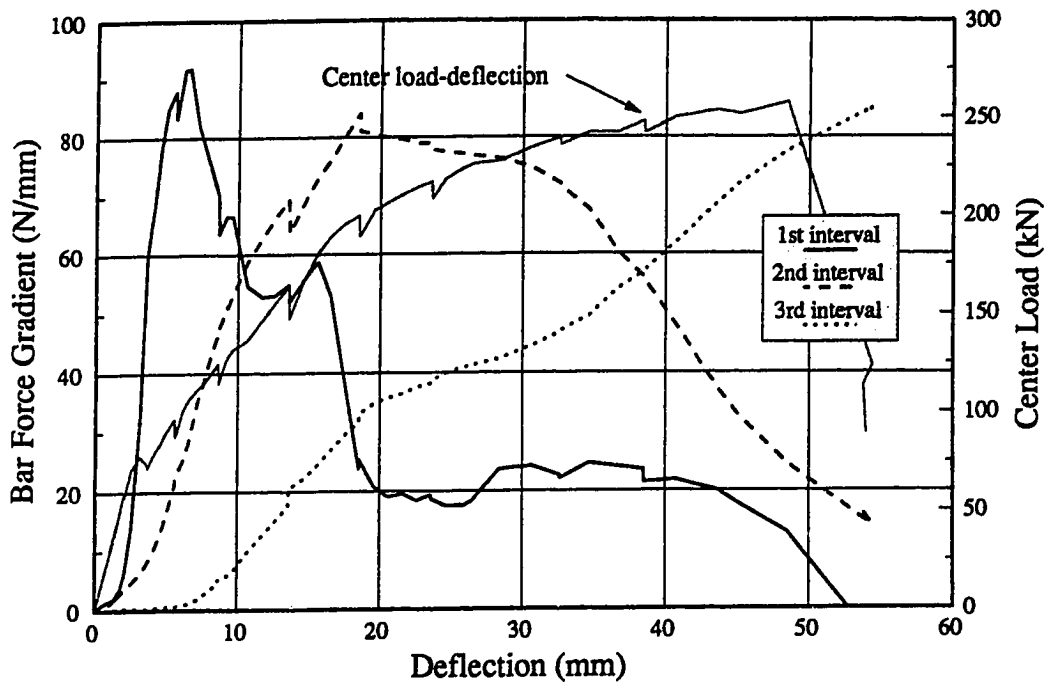


Figure C-39 Perimeter Bar Force Gradients: P19S150

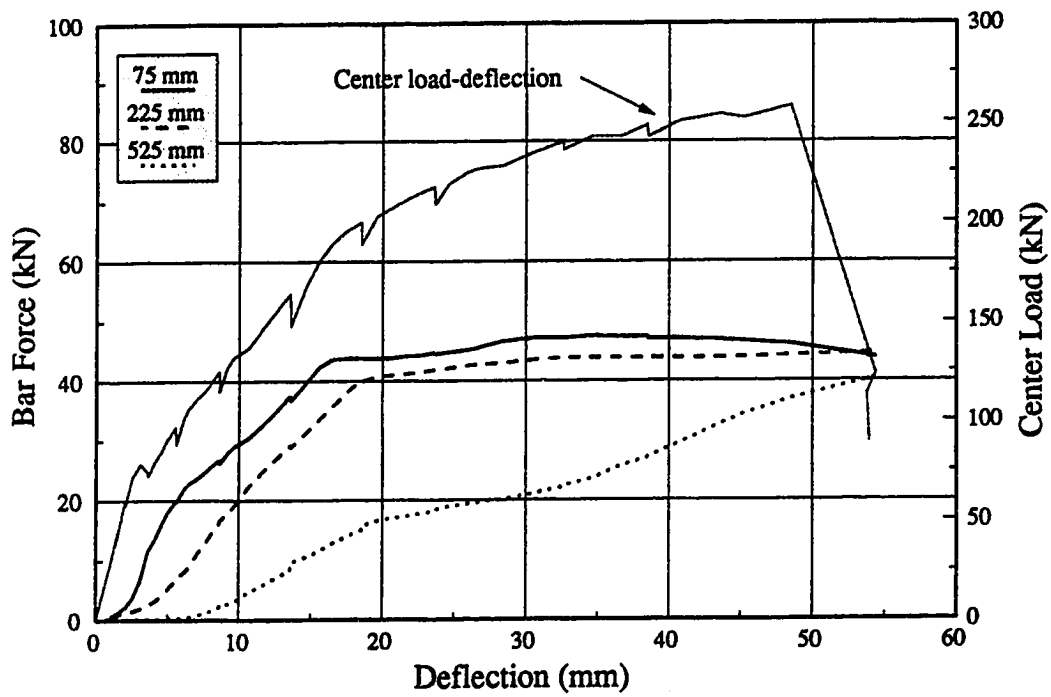


Figure C-40 Perimeter Bar Forces: P19S150

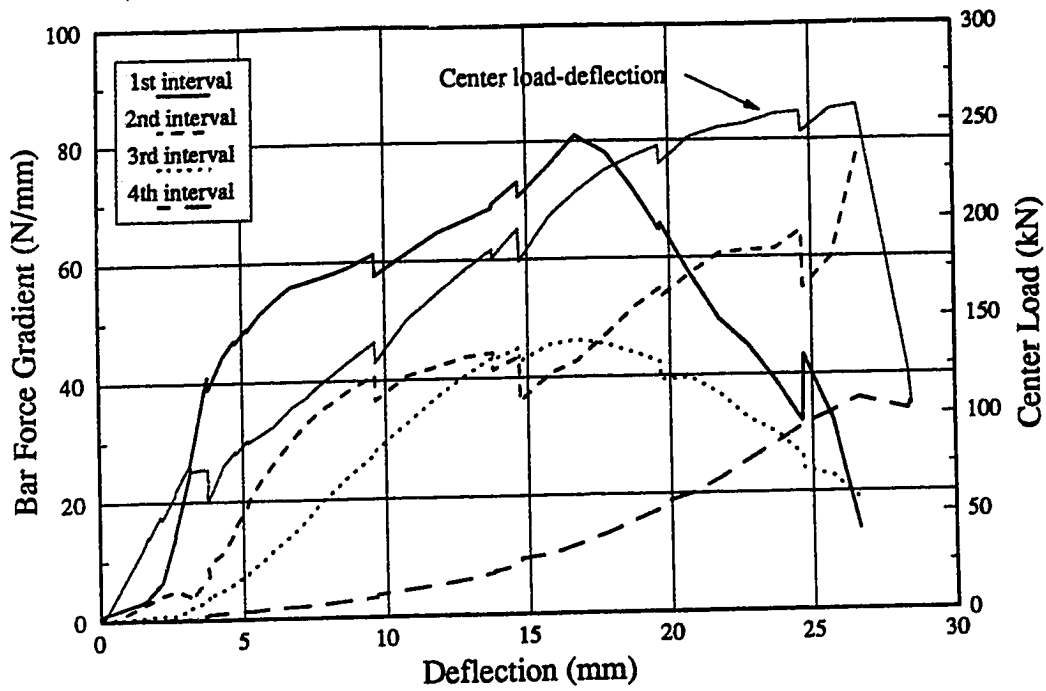


Figure C-41 Column Bar Force Gradients: P19S75

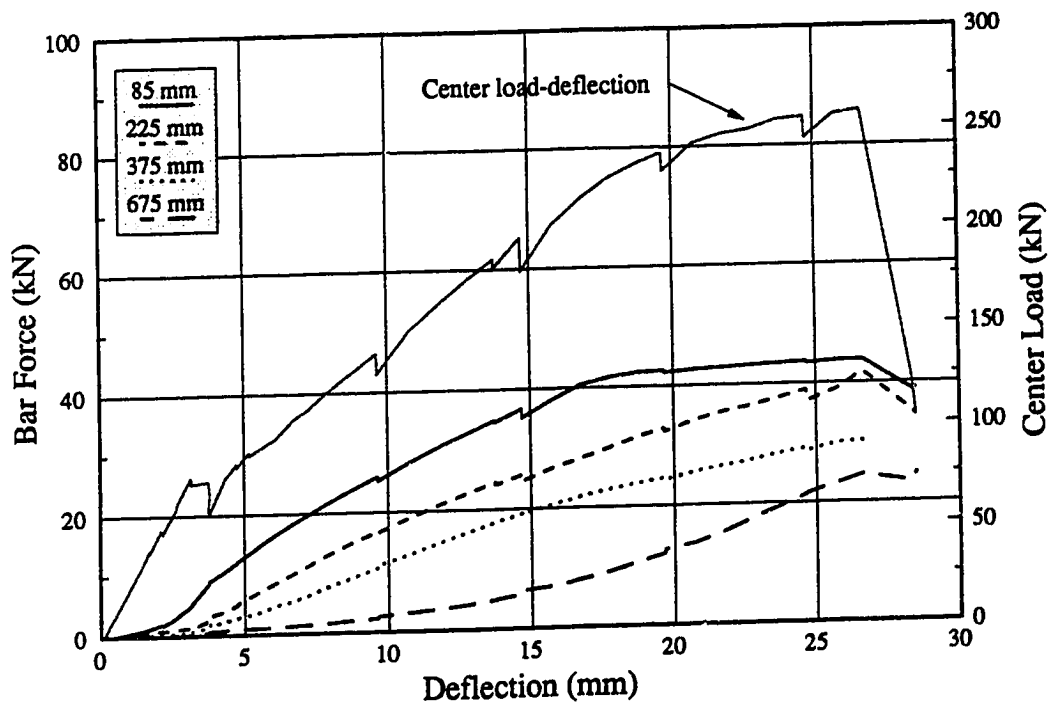


Figure C-42 Column Bar Forces: P19S75

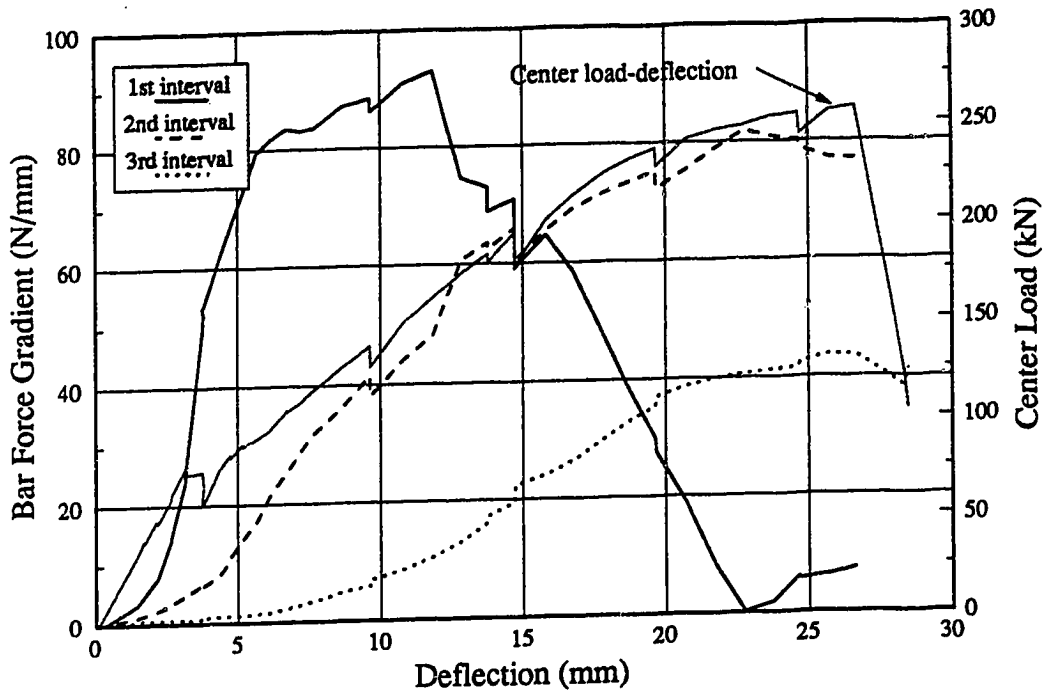


Figure C-43 Perimeter Bar Force Gradients: P19S75

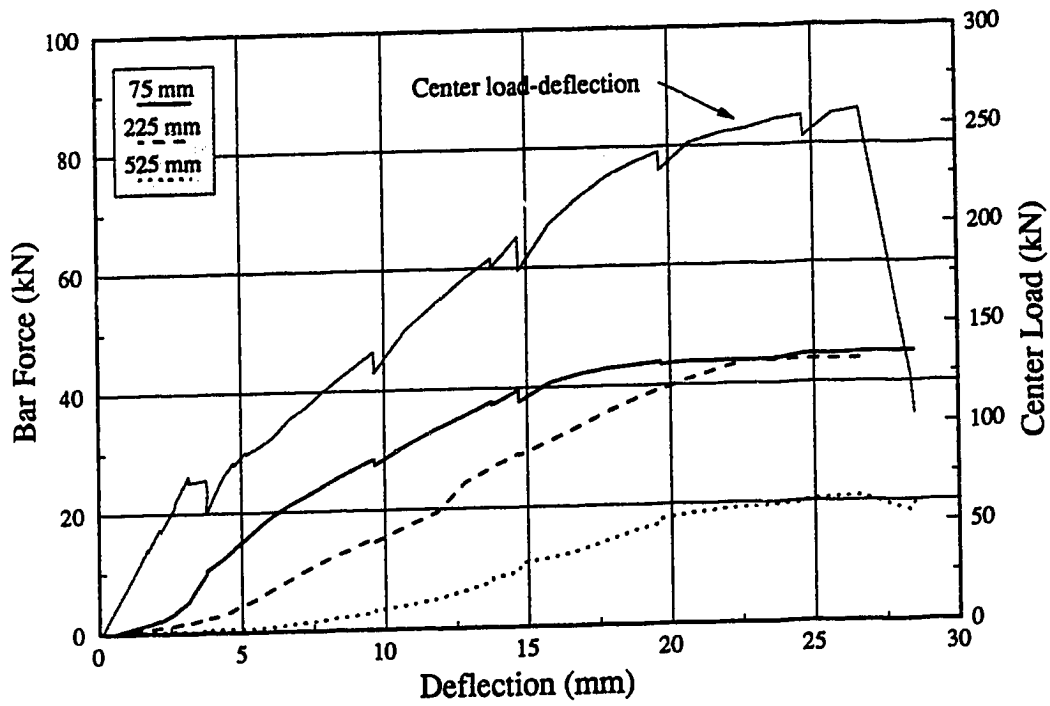


Figure C-44 Perimeter Bar Forces: P19S75

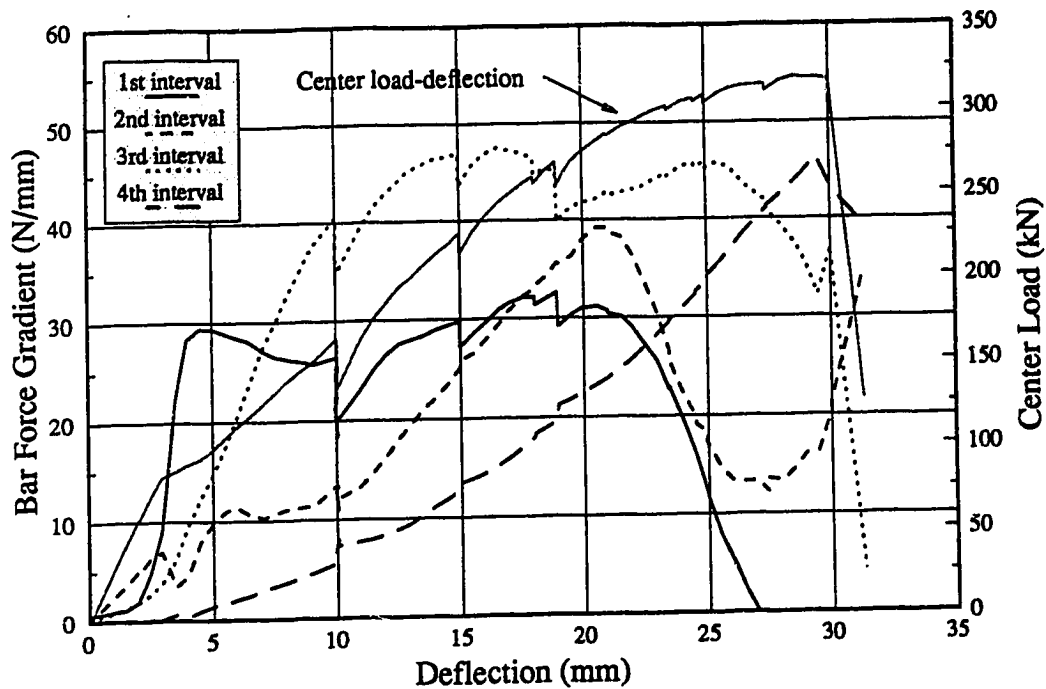


Figure C-45 Column Bar Force Gradients: P19S50

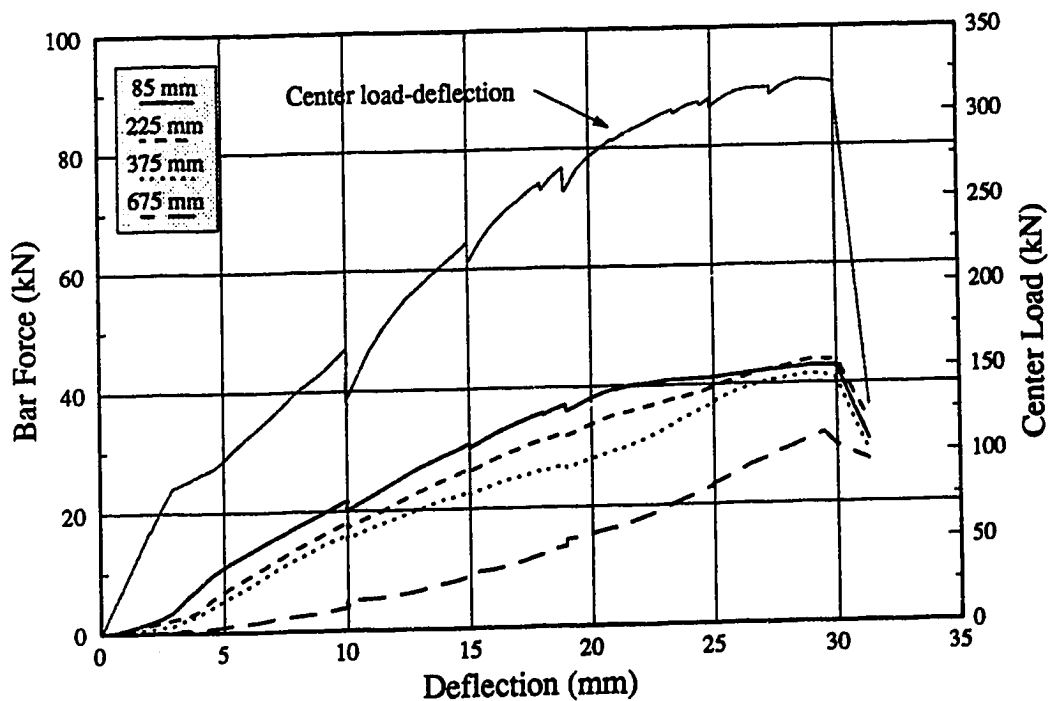


Figure C-46 Column Bar Forces: P19S50

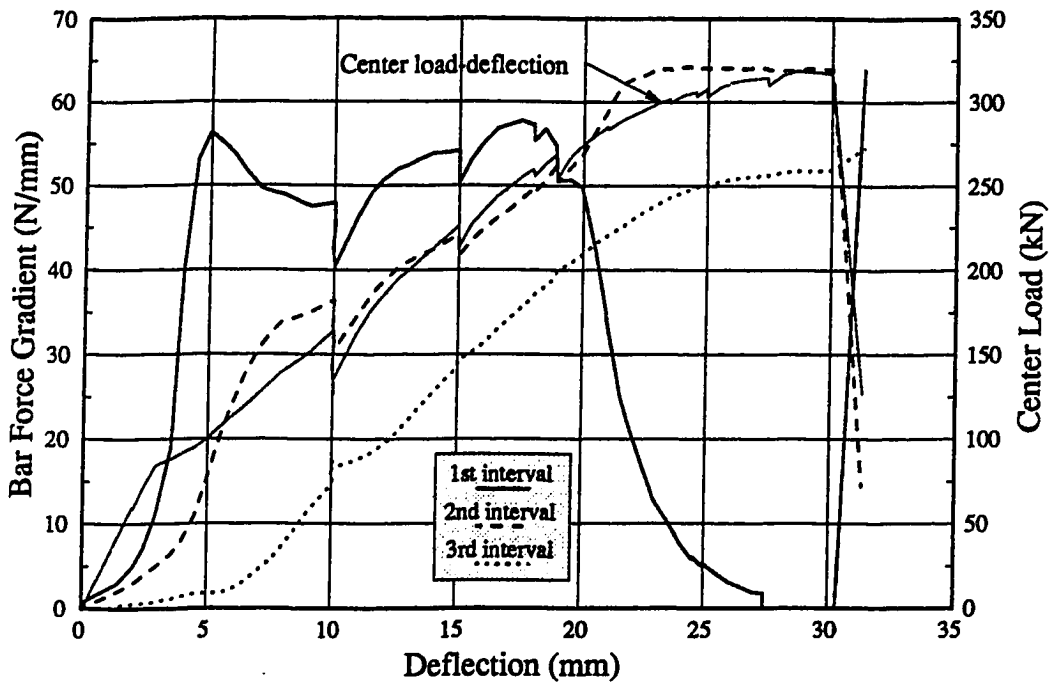


Figure C-47 Perimeter Bar Force Gradients: P19S50

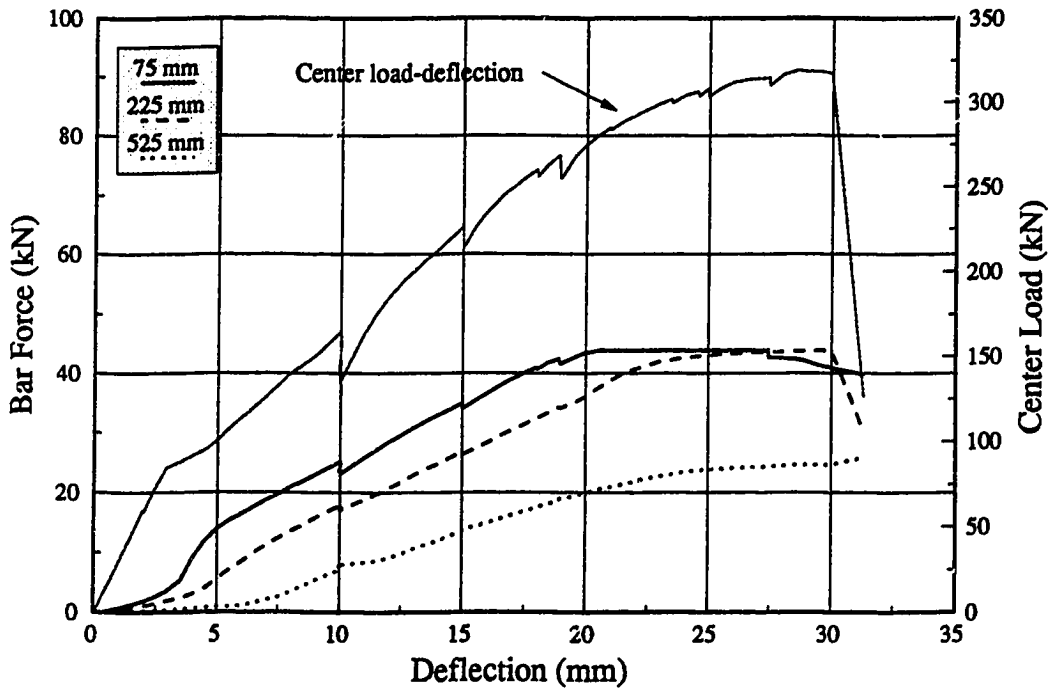


Figure C-48 Perimeter Bar Forces: P19S50

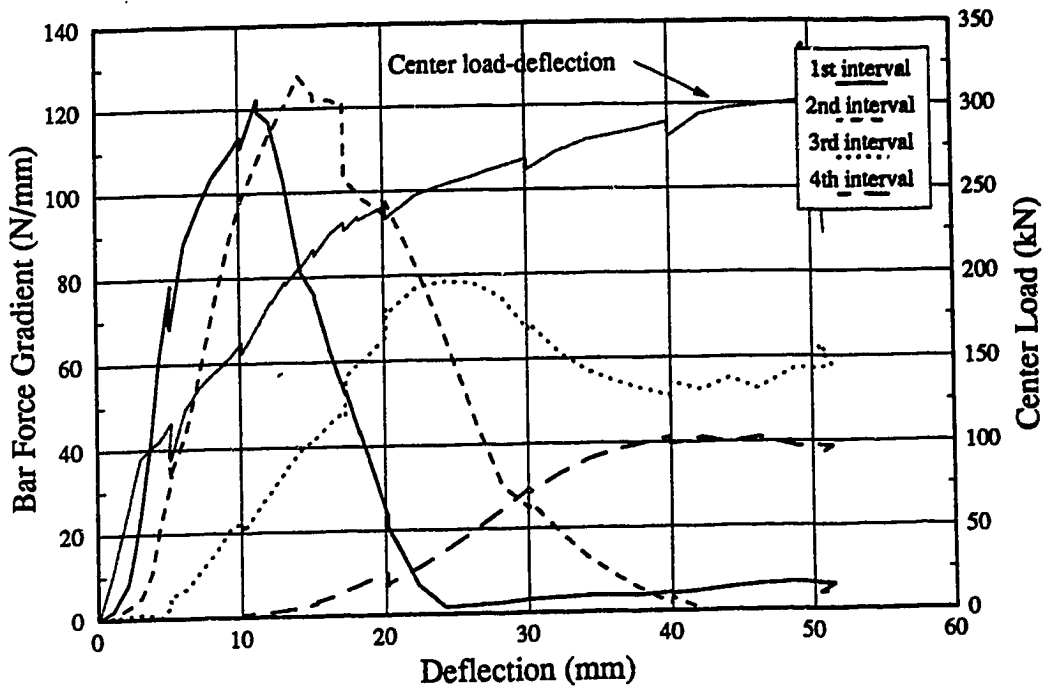


Figure C-49 Column Bar Force Gradients: P19RE

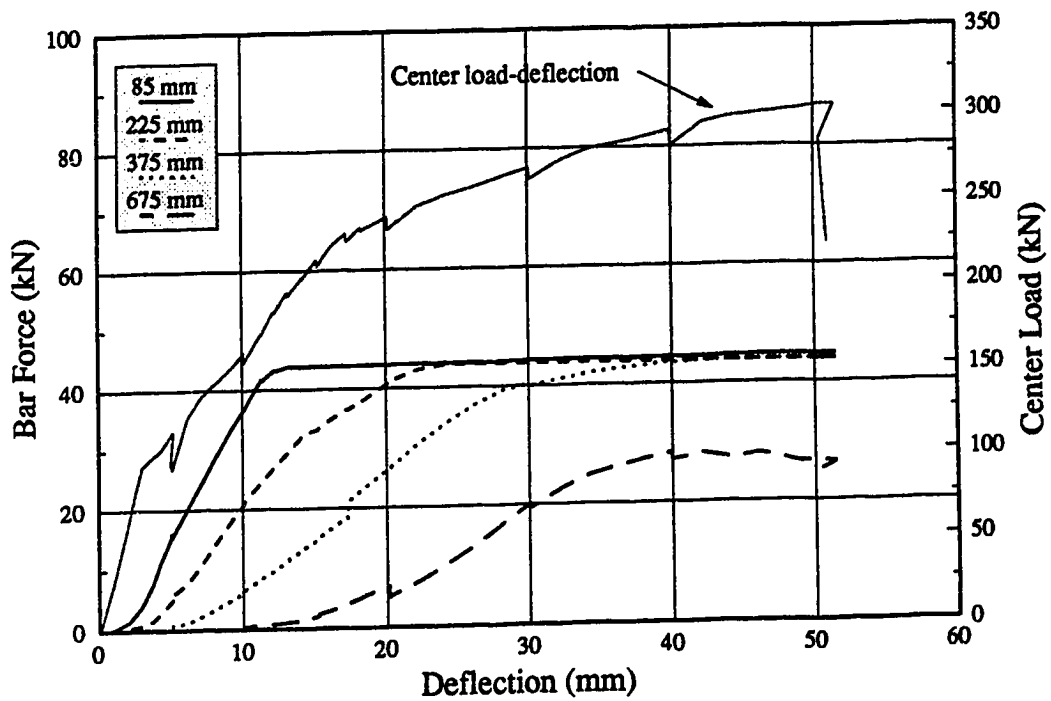


Figure C-50 Column Bar Forces: P19RE

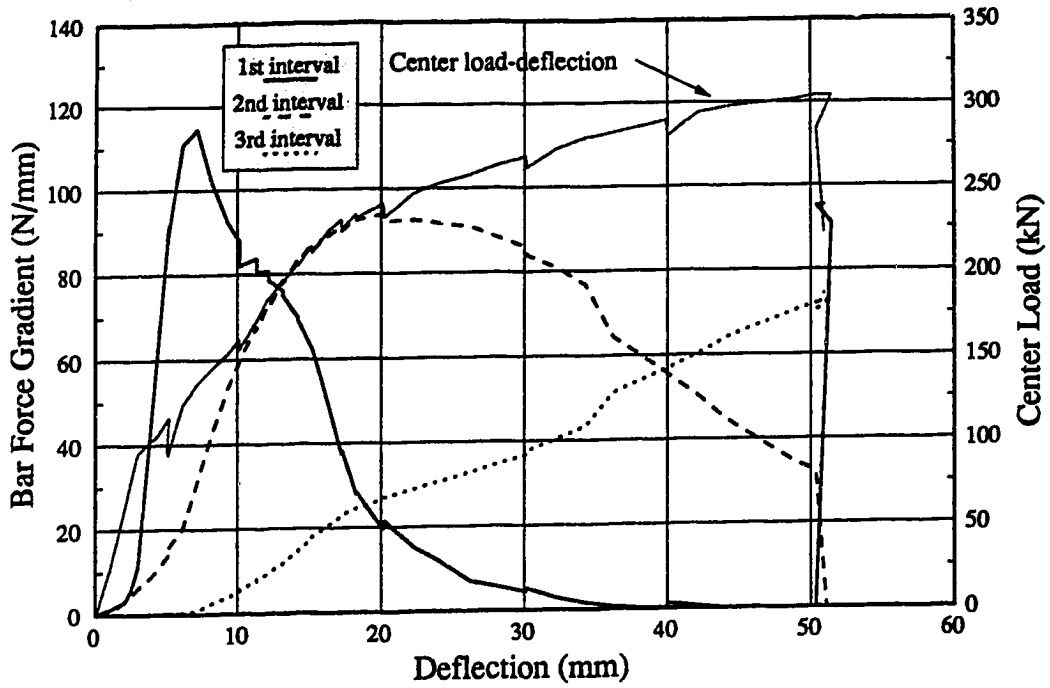


Figure C-51 Perimeter Bar Force Gradients: P19RE

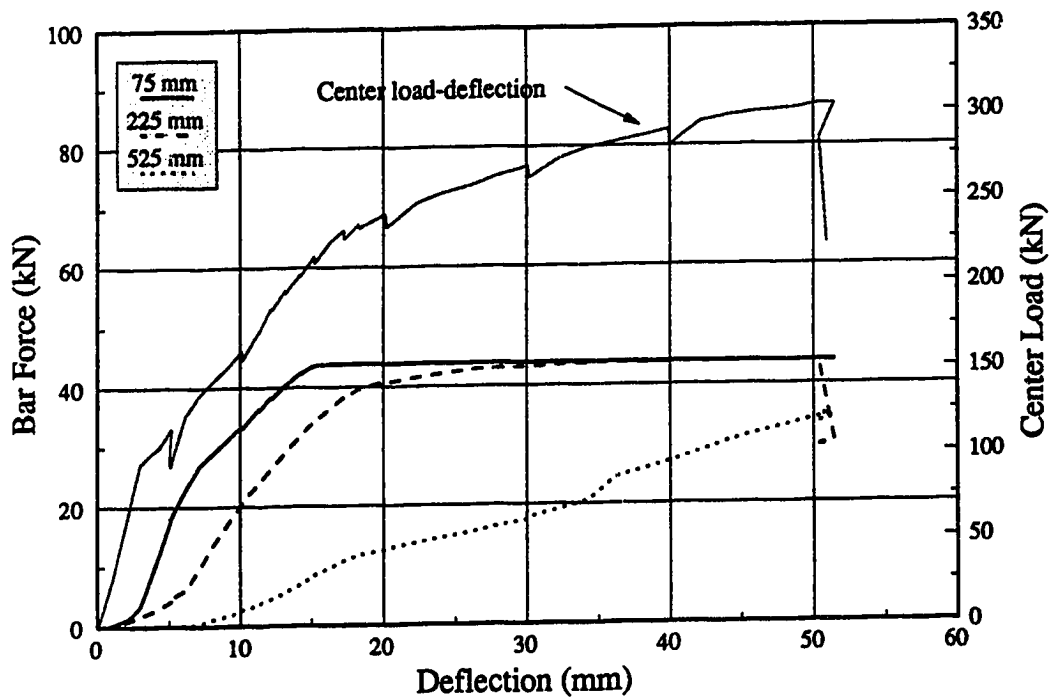


Figure C-52 Perimeter Bar Forces: P19RE

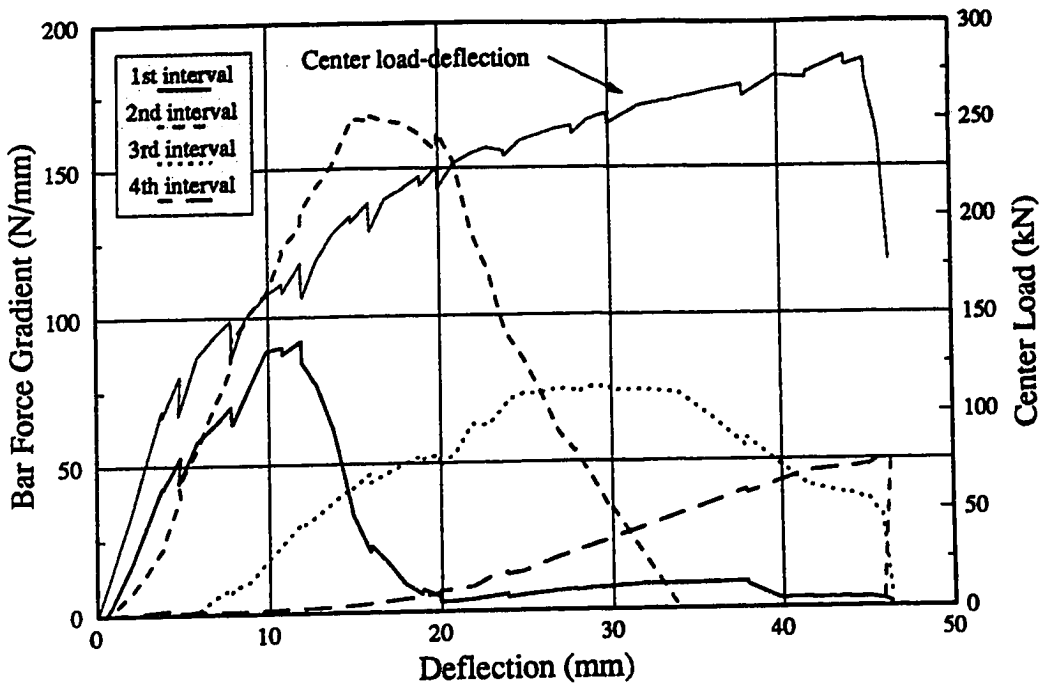


Figure C-53 Column Bar Force Gradients: P19RC

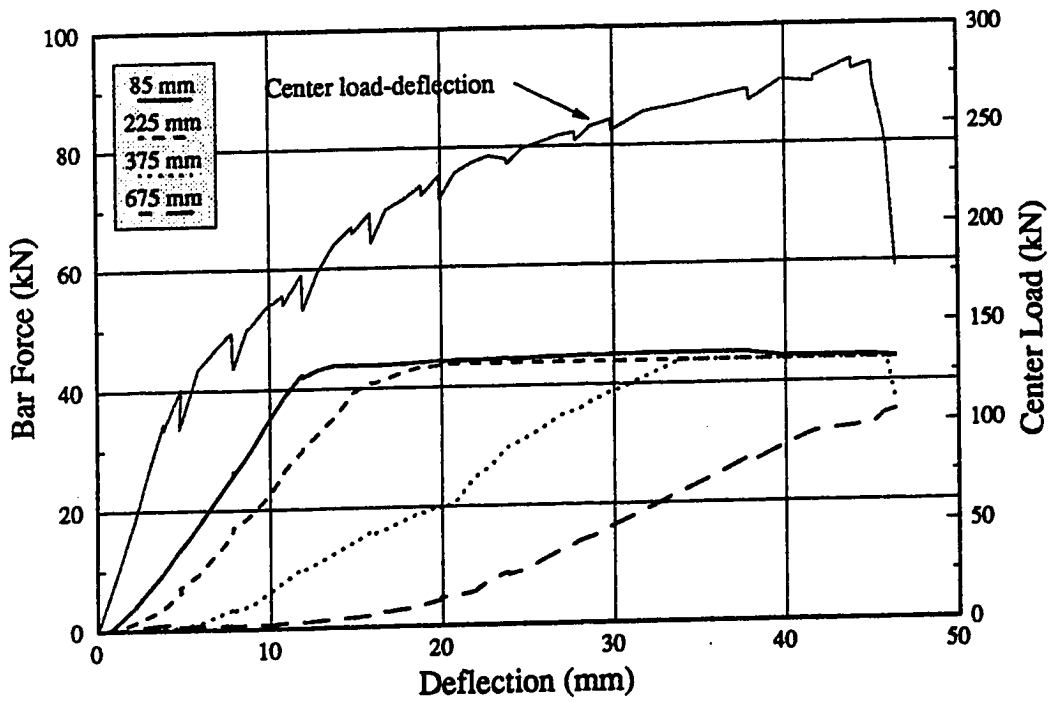


Figure C-54 Column Bar Forces: P19RC

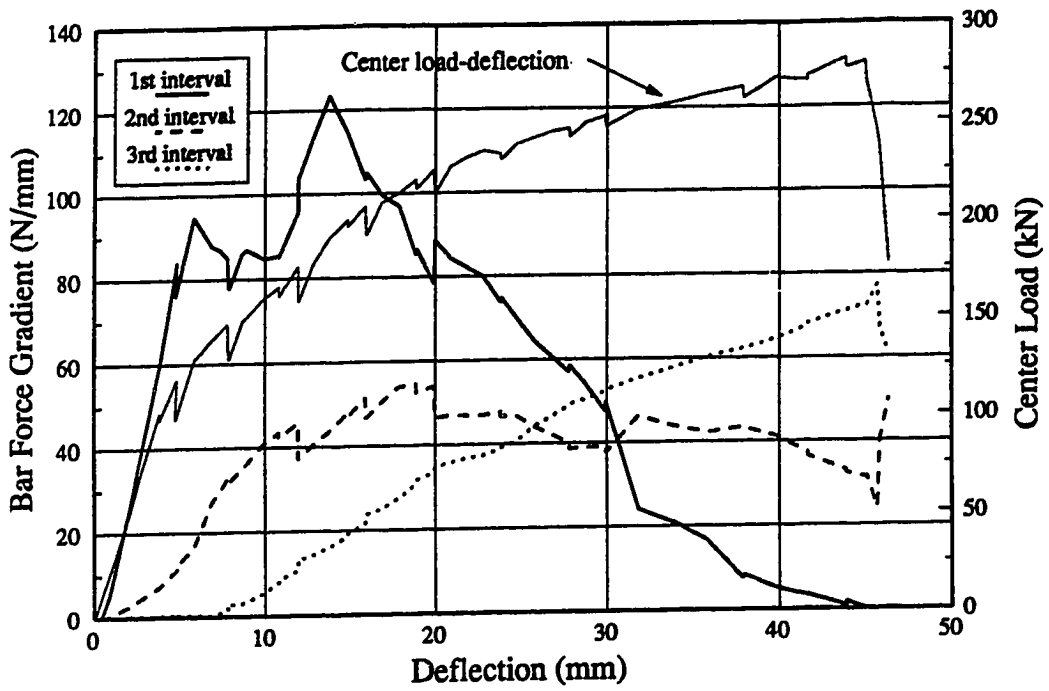


Figure C-55 Perimeter Bar Force Gradients: P19RC

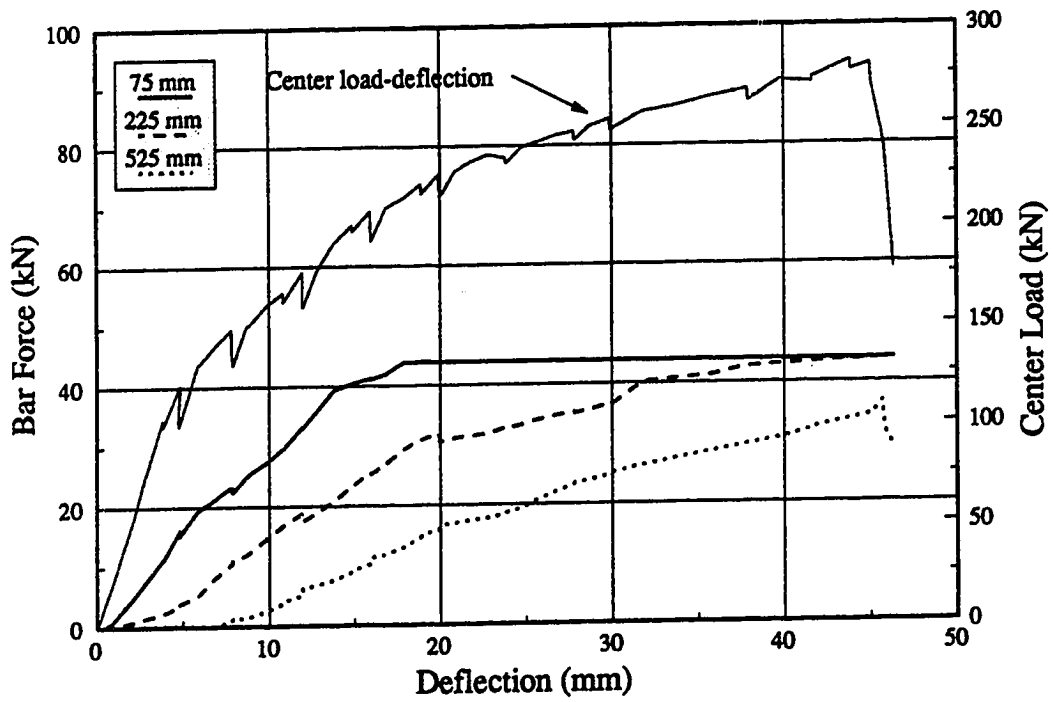


Figure C-56 Perimeter Bar Forces: P19RC

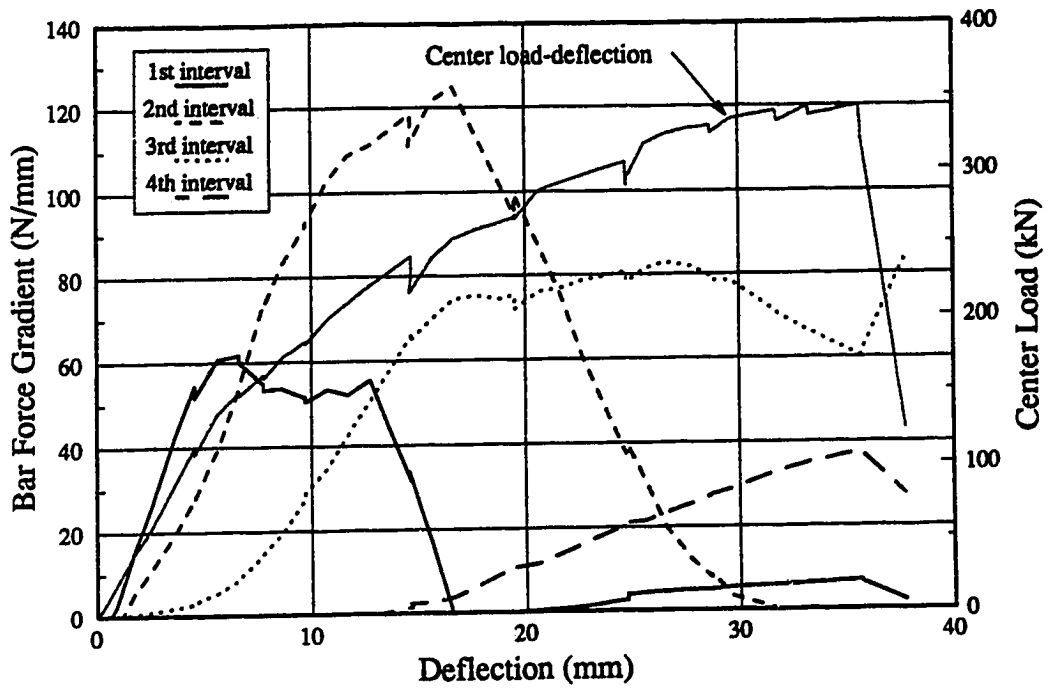


Figure C-57 Column Bar Force Gradients: P19RB

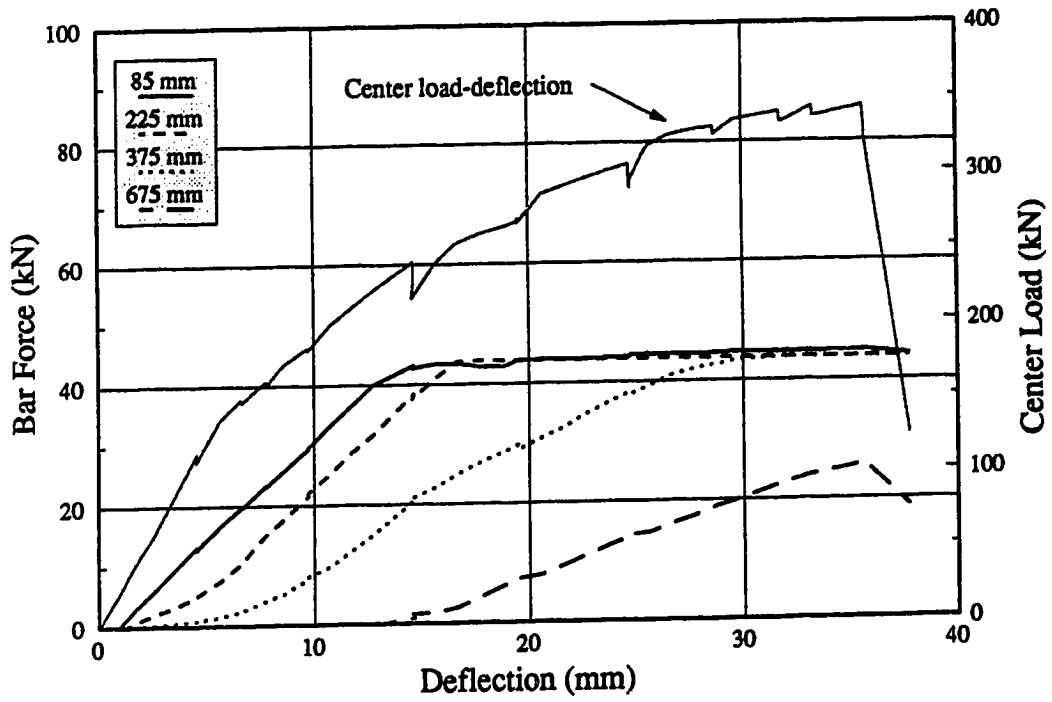


Figure C-58 Column Bar Forces: P19RB

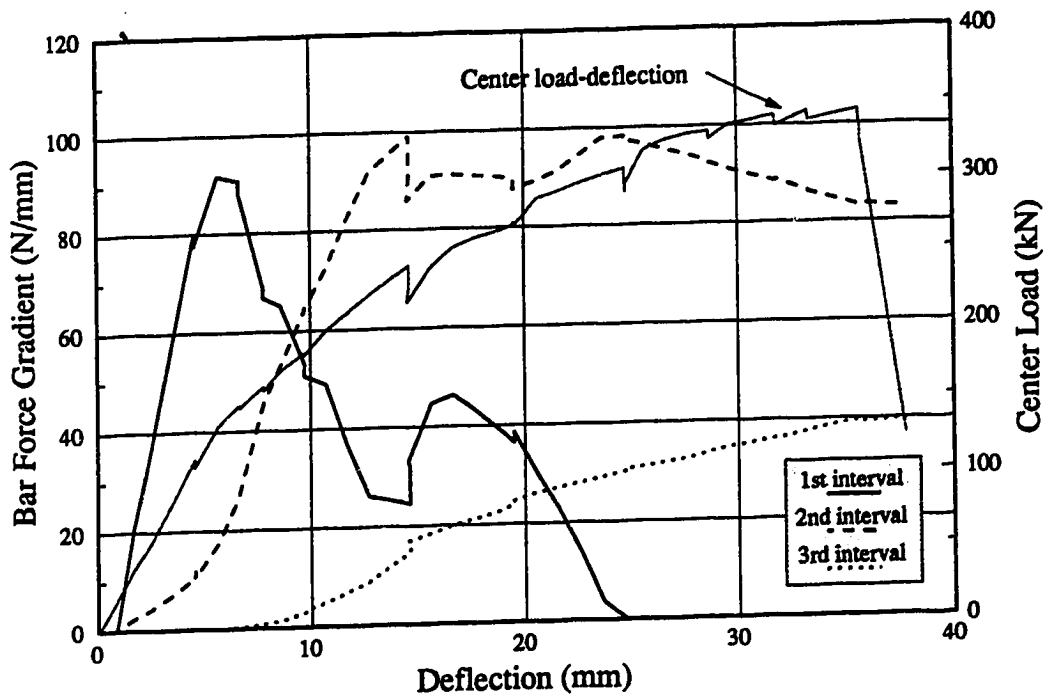


Figure C-59 Perimeter Bar Force Gradients: P19RB

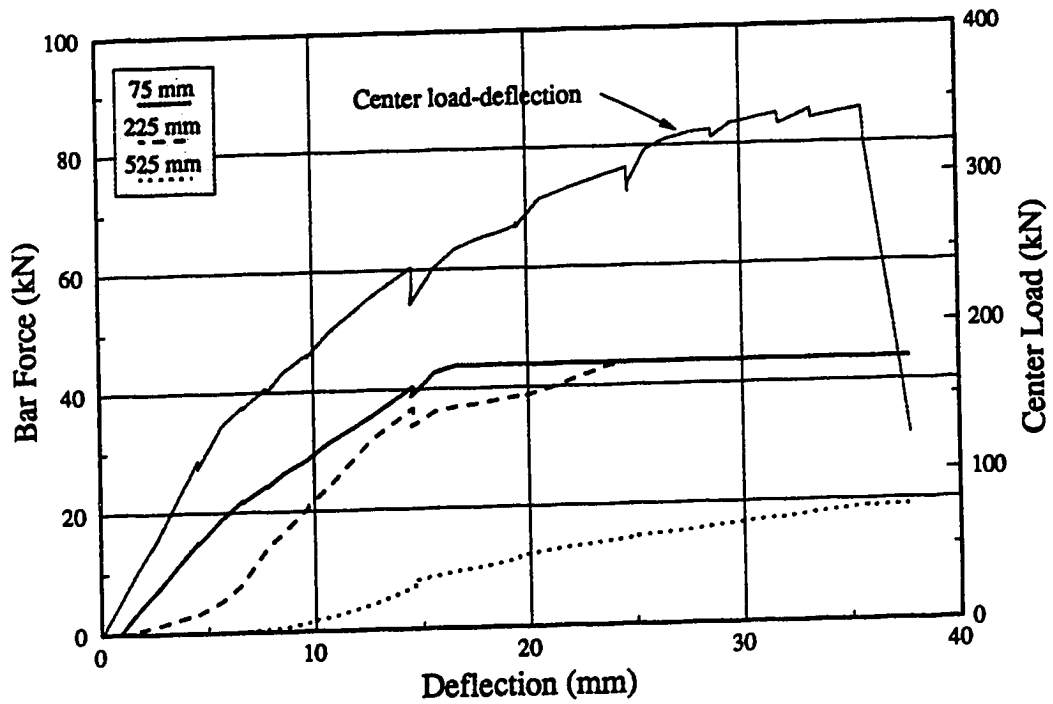


Figure C-60 Perimeter Bar Forces: P19RB

Appendix D: Demec Data

Demec results are presented as bar force profiles at selected load levels. Results are available for all tests except P19RE and P19RB. In these specimens, the quality of brazing that attached the extension lugs to the reinforcing bars was not as good as in the other specimens. As a result, there was too much flexibility in the connection between the lug and the reinforcing bar to permit accurate measurements.

In each diagram, vertical grid-lines indicate the position of transverse reinforcement.

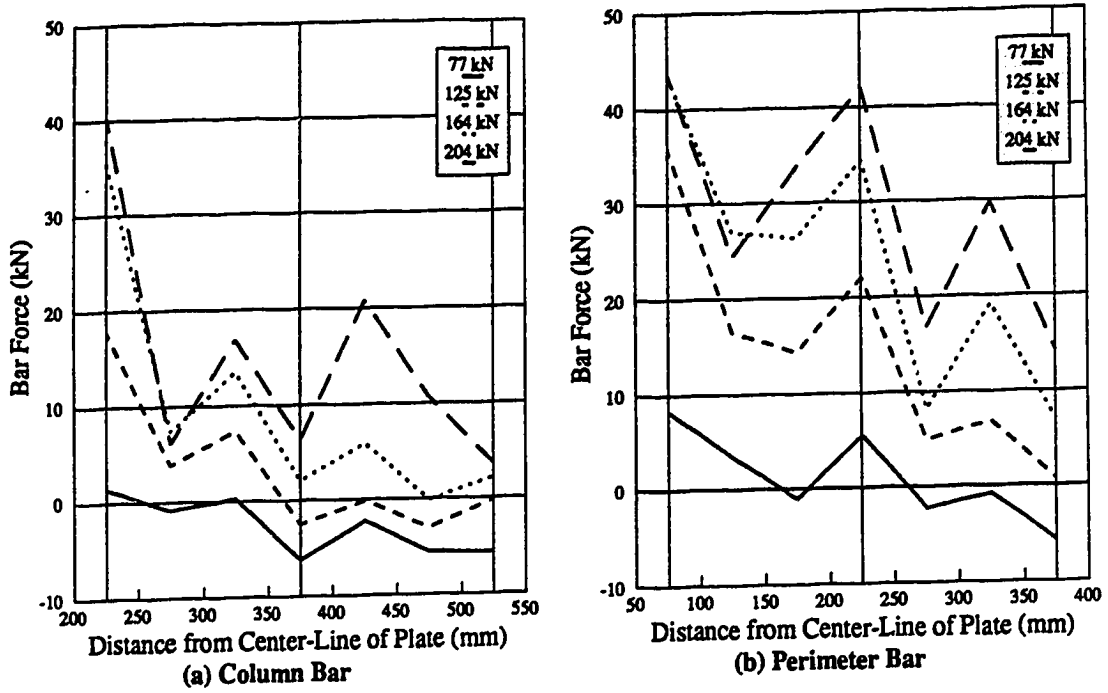


Figure D-1 Bar Force Profiles from Demec Measurements: P11F0

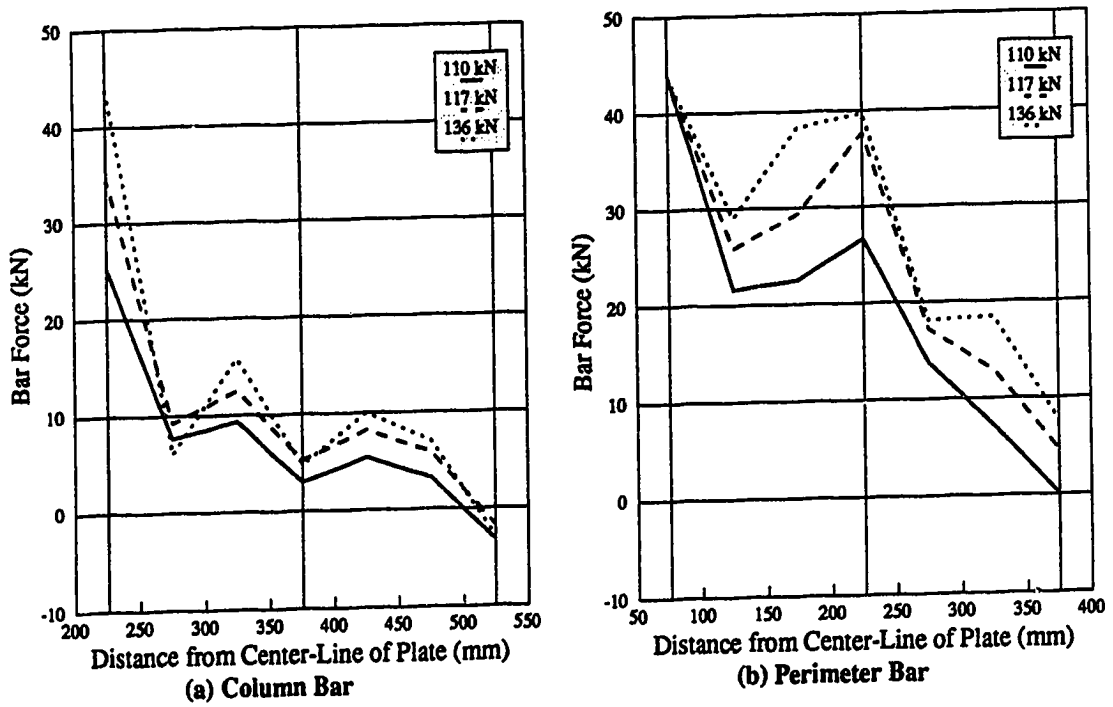


Figure D-2 Bar Force Profiles from Demec Measurements: P38F0

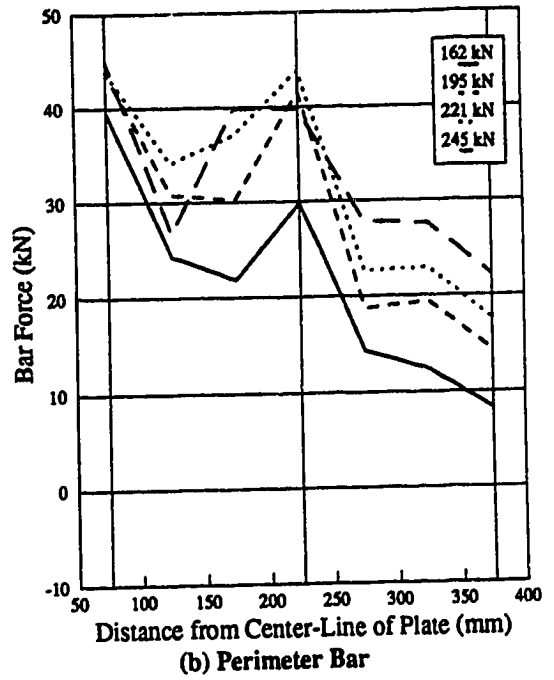
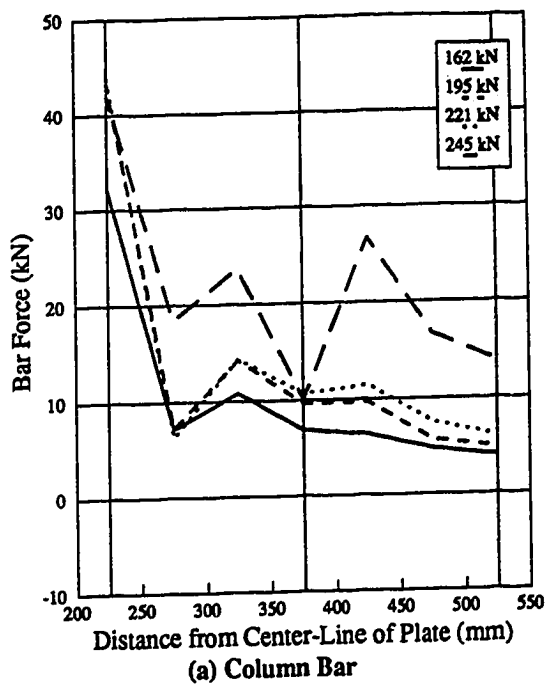


Figure D-3 Bar Force Profiles from Demec Measurements: P11F31

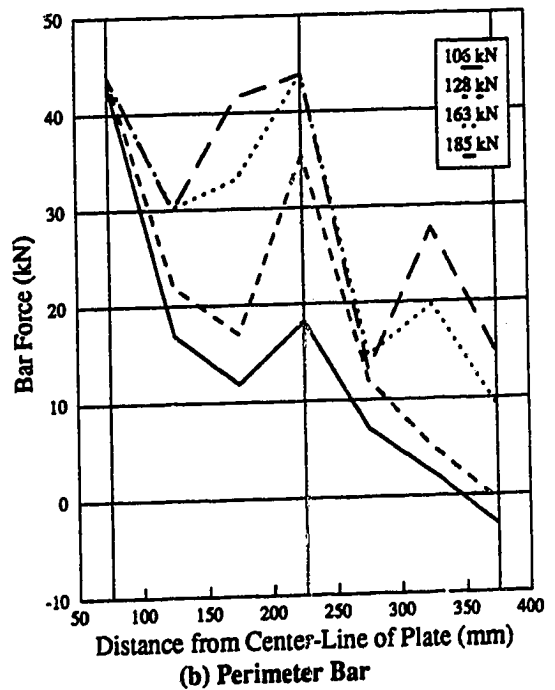
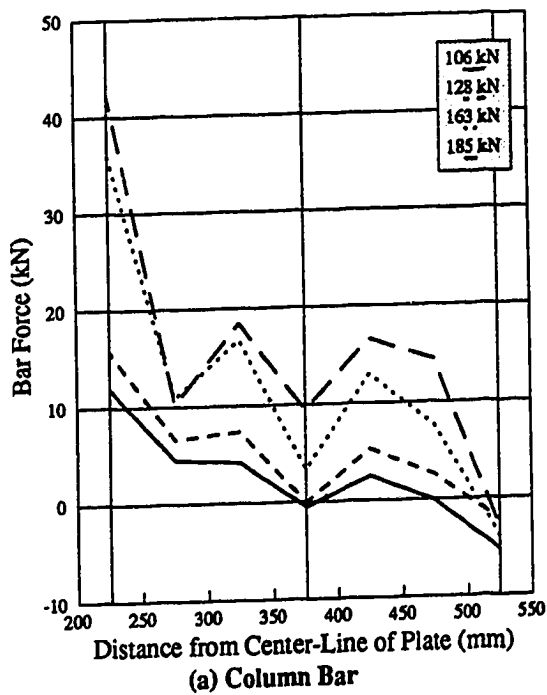


Figure D-4 Bar Force Profiles from Demec Measurements: P38F34

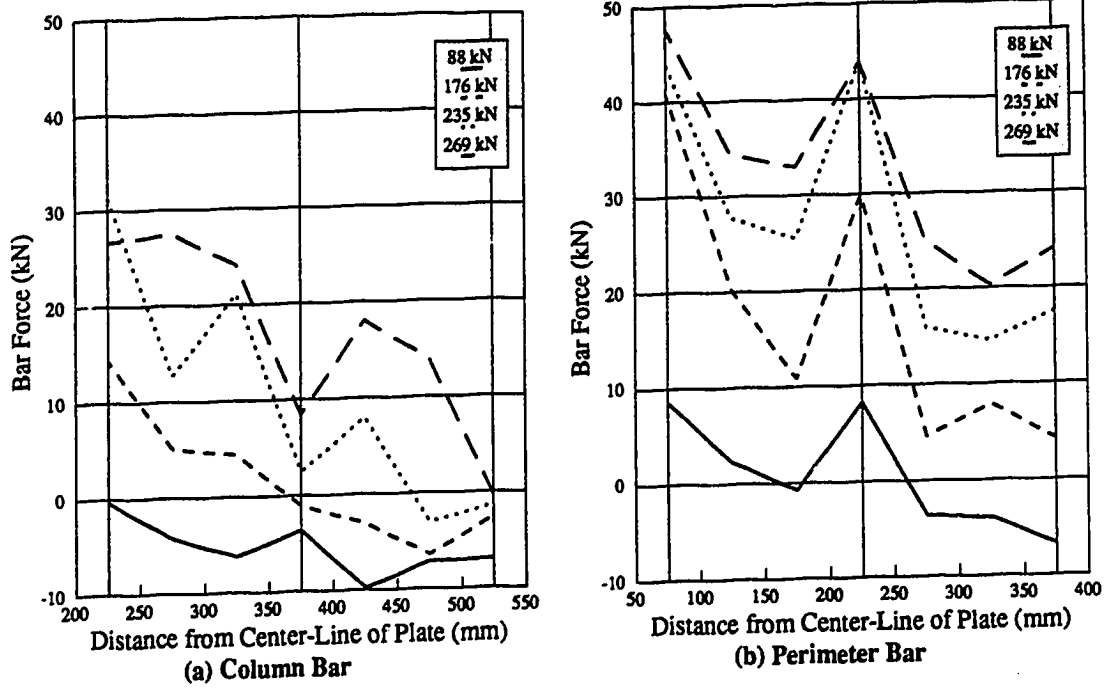


Figure D-5 Bar Force Profiles from Demec Measurements: P11F66

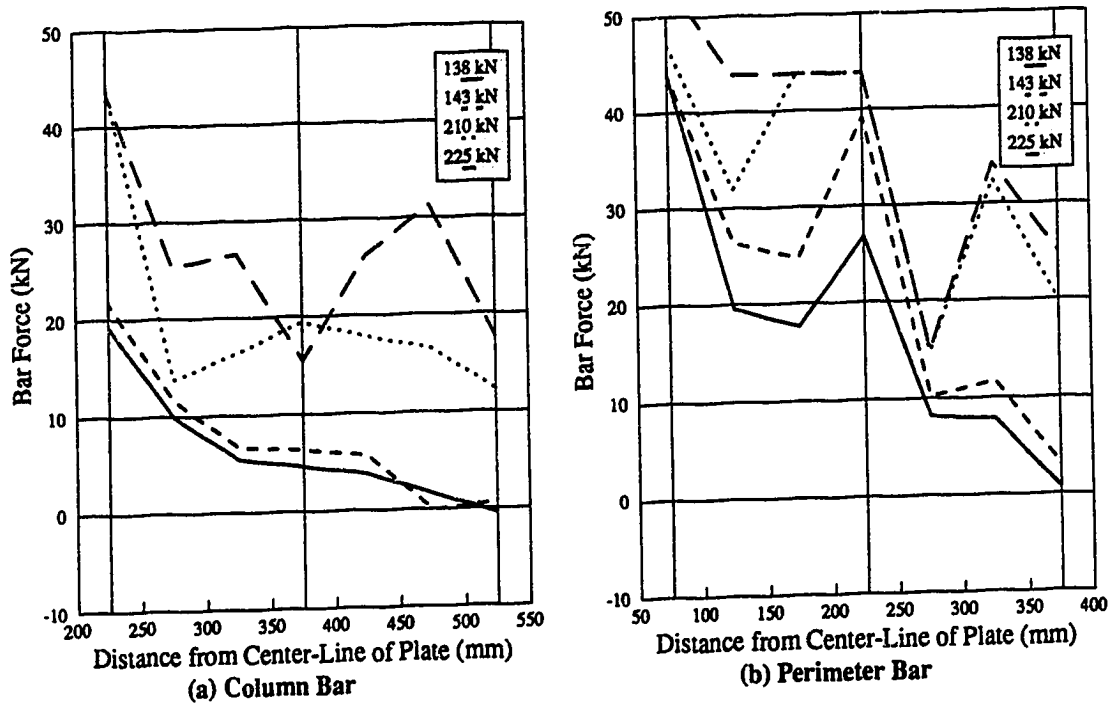


Figure D-6 Bar Force Profiles from Demec Measurements: P38F69

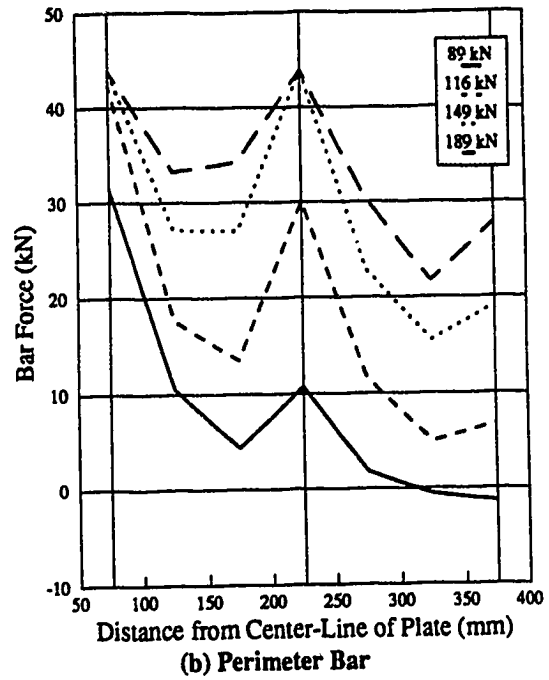
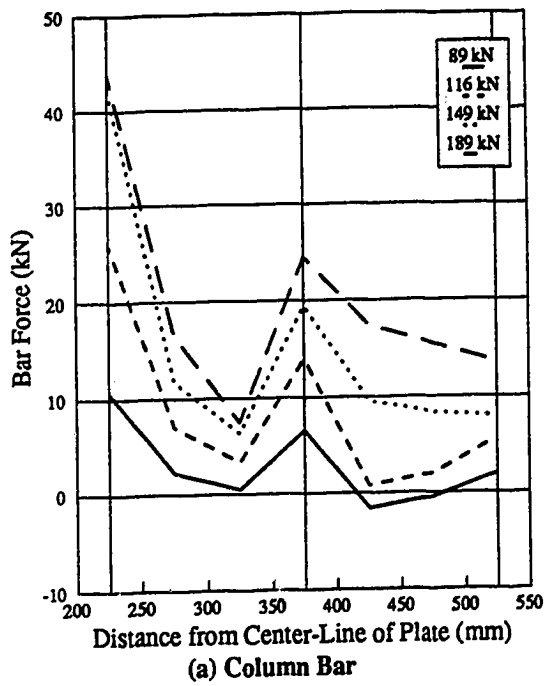


Figure D-7 Bar Force Profiles from Demec Measurements: P19S150

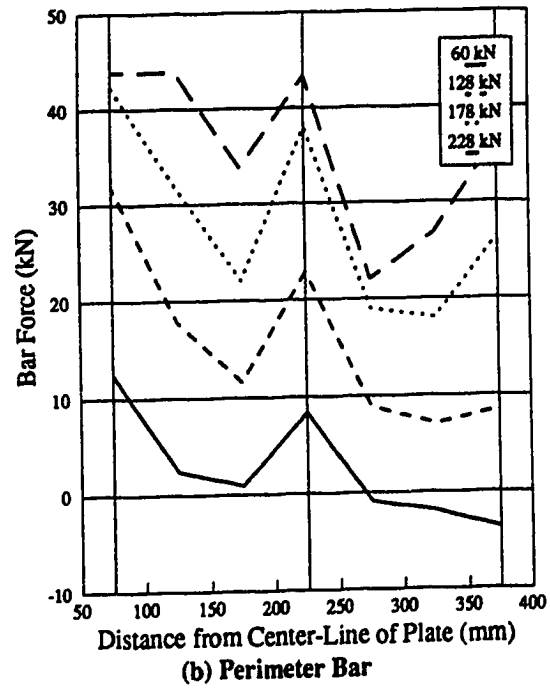
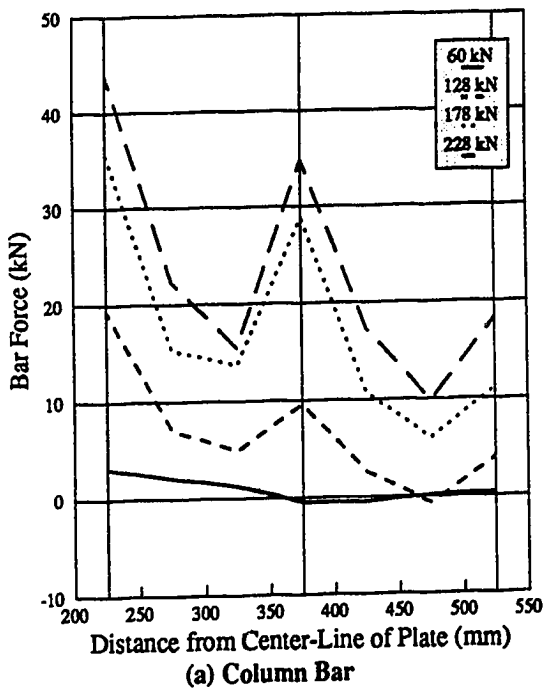


Figure D-8 Bar Force Profiles from Demec Measurements: P19S75

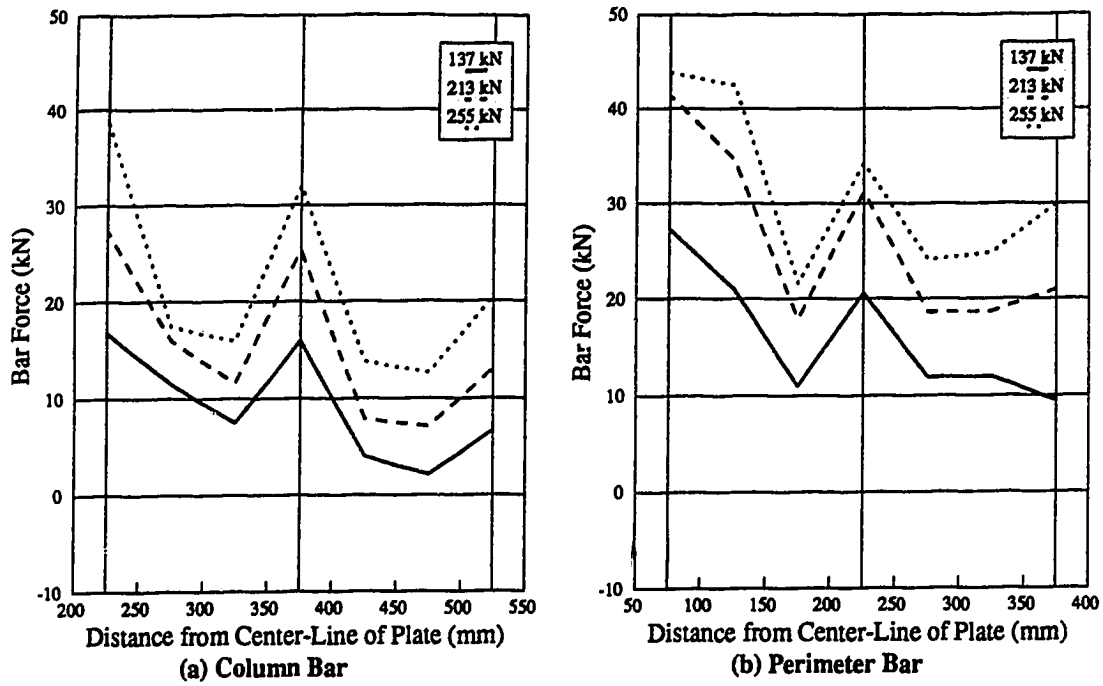


Figure D-9 Bar Force Profiles from Demec Measurements: P19S50

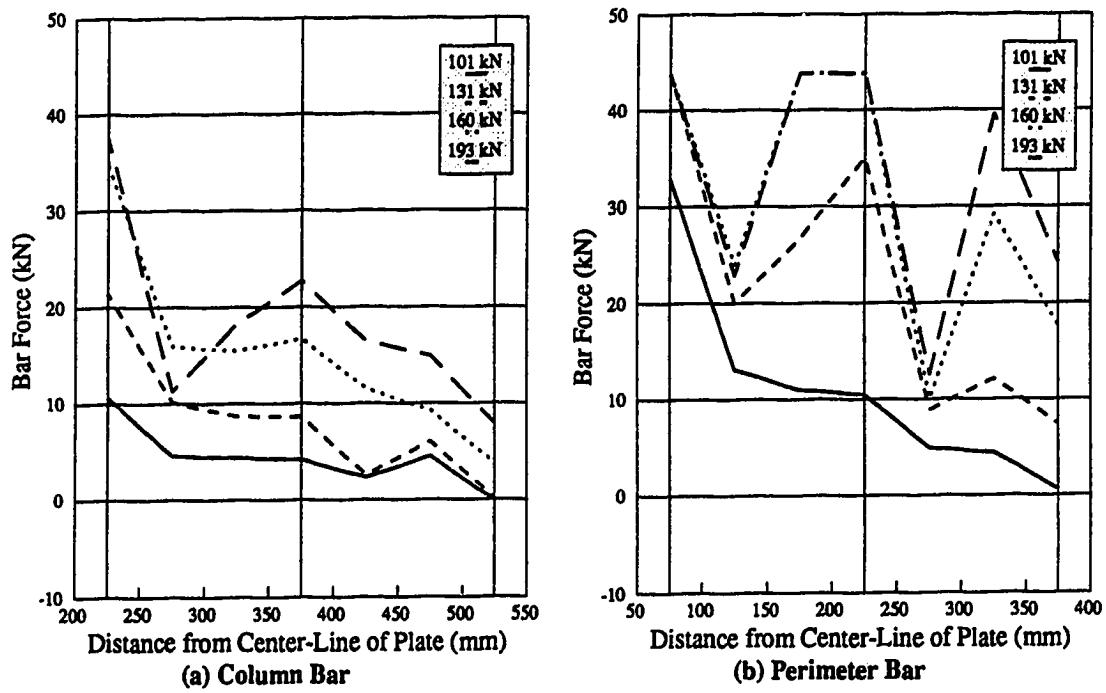


Figure D-10 Bar Force Profiles from Demec Measurements: P19RC

Appendix E: Tests in the Literature

Table E-1 Description of Test Specimens: Moe (1961)

Mark	P_{ult} (kN)	f_c (MPa)	f_y (MPa)	ρ^- (%)	d (mm)	d' (mm)	d_b (mm)	s (av) (mm)	c (mm)
H1	371	26.1	328	1.15	114	38	16	152	254
S1-60	389	23.3	399	1.06	114	38	16	165	254
S1-70	392	24.5	482	1.06	114	38	16	165	254
S5-60	343	22.2	399	1.06	114	38	16	165	195
S5-70	378	23.0	483	1.06	114	38	16	165	195
R2	311	26.5	328	1.38	114	38	16	127	146
M1A	433	20.8	481	1.50	114	38	19	165	293

Table E-2 Description of Test Specimens: Elstner and Hognestad (1956)

Mark	P_{ult} (kN)	f_c (MPa)	f_y (MPa)	ρ^- (%)	d (mm)	d' (mm)	d_b (mm)	s (av) (mm)	c (mm)
A-1a	302	14.1	332	1.15	117	35	19	210	254
A-1b	365	25.2	332	1.15	117	35	19	210	254
A-1c	356	29.0	332	1.15	117	35	19	210	254
A-1d	351	36.8	332	1.15	117	35	19	210	254
A-1e	356	20.3	332	1.15	117	35	19	210	254
A-2b	400	19.5	321	2.47	114	38	25	181	254
A-2c	467	37.4	321	2.47	114	38	25	181	254
A-7b	512	27.9	321	2.47	114	38	25	181	254
A-3c	534	26.5	321	2.47	114	38	25	121	254
A-3d	547	34.5	321	2.47	114	38	25	121	254
A-4	400	26.1	332	1.15	117	35	19	121	356
A-5	534	27.8	321	2.47	114	38	25	210	356
B-9	505	43.9	341	2.00	114	38	22	170	254
B-14	578	50.5	325	3.00	114	38	25	149	254

Table E-3 Description of Test Specimens: Kinnunen and Nylander (1960)

Mark	P_{ult} (kN)	f'_c (MPa)	f_y (MPa)	ρ (%)	d (mm)	d' (mm)	d_b (mm)	s (av) (mm)	c (mm)
IA15a-5	255	23.6	441	0.80	117	32	12	123	106
-6	275	23.0	454	0.79	118	33	12	123	106
IA15c-11	333	28.8	436	1.53	121	32	12	62	106
-12	331	27.7	439	1.54	122	32	12	62	106
IA30a-24	430	23.2	455	1.01	128	30	12	88	212
-25	408	21.9	451	1.04	124	30	12	88	212
IA30c-30	490	26.8	434	2.16	120	31	12	44	212
-31	539	26.8	448	2.18	119	32	12	44	212
IA30d-32	258	23.1	448	0.49	123	32	12	193	212
-33	258	23.4	461	0.48	125	31	12	193	212
IA30e-34	331	24.2	460	1.00	120	30	12	96	212
-35	331	21.8	458	0.98	122	31	12	96	212

Table E-4 Description of Test Specimens: Regan, Walker and Zakaria (1979)

Mark	P_{ult} (kN)	f'_c (MPa)	f_y (MPa)	ρ (%)	d (mm)	d' (mm)	d_b (mm)	s (av) (mm)	c (mm)
SS2	176	23.3	500	1.20	77	23	10	85	200
SS4	194	33.4	500	0.92	77	23	10	110	200
SS6	165	21.7	480	0.75	79	21	8	85	200
SS7	186	31.2	480	0.80	79	21	8	80	200
SS8	825	36.3	530	0.98	200	50	25	250	250
SS9	390	34.5	485	0.98	128	32	16	160	160
SS10	365	35.7	485	0.98	128	32	16	160	160
SS11	117	34.5	480	0.98	64	16	8	80	80
SS12	105	35.7	480	0.98	64	16	8	80	80
SS13	105	37.8	480	0.98	64	16	8	80	80

Table E-5 Description of Test Specimens: Rankin and Long (1987)

Mark	P_{ult} (kN)	f'_c (MPa)	f_y (MPa)	ρ^- (%)	d (mm)	d' (mm)	d_b (mm)	s (av) (mm)	c (mm)
1	36	31.5	530	0.42	41	11	6	165	100
2	49	31.5	530	0.56	41	11	6	125	100
3	57	31.5	530	0.69	41	11	6	101	100
4	56	36.2	530	0.82	41	11	6	85	100
5	57	36.2	530	0.88	41	11	6	79	100
6	66	36.2	530	1.03	41	11	6	68	100
7	71	30.4	530	1.16	41	11	6	60	100
8	71	30.4	530	1.29	41	11	6	54	100
9	79	30.4	530	1.45	41	11	6	48	100
10	44	30.6	530	0.52	41	11	6	135	100
11	55	30.6	530	0.80	41	11	6	87	100
12	67	30.6	530	1.11	41	11	6	63	100
13	49	35.3	530	0.60	41	11	6	116	100
14	52	35.3	530	0.69	41	11	6	101	100
15	85	35.3	530	1.99	41	11	6	35	100
1A	45	29.4	530	0.44	47	11	6	138	100
2A	66	29.4	530	0.69	47	11	6	88	100
3A	90	29.4	530	1.29	47	11	6	47	100
4A	97	31.7	530	1.99	47	11	6	31	100
1B	29	39.6	530	0.42	35	11	6	191	100
2B	38	39.6	530	0.69	35	11	6	117	100
3B	57	39.6	530	1.29	35	11	6	63	100
4B	73	31.7	530	1.99	35	11	6	41	100
1C	63	28.3	530	0.42	54	11	6	125	100
2C	88	33.5	530	0.69	54	11	6	77	100
3C	124	33.5	530	1.29	54	11	6	41	100
4C	126	28.3	530	1.99	54	11	6	27	100

Table E-6 Description of Test Specimens: Gardner (1990)

Mark	P_{ult} (kN)	f_c (MPa)	f_y (MPa)	ρ^- (%)	d (mm)	d' (mm)	d_b (mm)	s (av) (mm)	c (mm)
8	129	24.1	430	2.05	76	25	13	83	102
9	136	22.6	430	2.05	76	25	13	83	102
10	129	24.6	430	2.05	76	25	13	83	102
11	311	22.6	430	2.14	113	39	20	124	152
12	357	24.8	430	2.14	113	39	20	124	203
13	271	24.8	430	0.66	122	31	11	124	203
14	202	25.0	430	5.01	73	29	20	83	152
15	160	25.0	430	1.47	81	21	11	83	152
16	107	23.2	430	0.45	86	16	6	83	152
17	121	25.5	430	1.47	81	21	11	83	102
19	271	22.1	430	0.47	123	29	10	124	203
20	278	15.1	430	2.14	113	39	20	124	203
21	230	16.1	430	0.66	122	31	11	124	203
23	108	14.5	430	1.47	81	21	11	83	152
25	306	52.1	430	0.66	122	31	11	124	203
26	323	52.1	430	5.01	73	29	20	83	203
27	243	52.1	430	1.47	81	21	11	83	152
28	148	52.1	430	0.45	86	16	6	83	152

Table E-7 Description of Test Specimens: Shilling and Vanderbilt (1970)

Mark	P_{ult} (kN)	f_c (MPa)	f_y (MPa)	ρ^r (%)	d (mm)	d' (mm)	d_b (mm)	s (av) (mm)	c (mm)	$\frac{M^+}{M^-}$
2S1-1	43	27.6	296	1.00	38	13	6	64	76	0.50
3S1-2	47	23.0	296	1.00	38	13	6	64	114	0.50
4S1-3	51	20.8	296	1.00	38	13	6	64	152	0.50
3C1-4	58	22.1	296	1.00	38	13	6	64	145	0.50
6S1-5	78	21.2	296	1.00	38	13	6	64	229	0.50
8S1-6	90	20.5	296	1.00	38	13	6	64	305	0.50
2S2-7	50	23.2	296	2.00	38	13	6	32	76	0.50
4S2-8	69	21.6	386	2.00	38	13	6	32	152	0.50
6C1-9	96	25.7	386	1.00	38	13	6	64	285	0.50
8S2-10	114	26.3	386	2.00	38	13	6	32	305	0.50
2C1-11	39	20.0	386	1.00	38	13	6	64	97	0.50
4C1-12	73	22.2	386	1.00	38	13	6	64	196	0.50
8C1-13	101	24.0	386	1.00	38	13	6	64	385	0.50
6S2-14	80	20.6	386	2.00	38	13	6	32	229	0.50
4C2-15	97	21.5	386	2.00	38	13	6	32	196	0.50

Table E-8 Description of Test Specimens: Lunt (1988)

Mark	P_{ult} (kN)	f_c (MPa)	f_y (MPa)	ρ_r (%)	d (mm)	d' (mm)	d_b (mm)	s (av) (mm)	c (mm)	$\frac{M'}{M''}$
A1	398	24.9	532	0.30	143	22	10	200	250	0.50
B1	282	28.4	532	0.47	108	22	10	175	250	0.42
B2	299	24.0	637	0.46	110	25	8	150	250	0.36
B3	321	24.7	637	0.57	110	20	8	120	250	0.29
B4	311	23.9	637	0.76	110	20	8	120	250	0.22
B5	319	26.5	637	0.57	110	20	8	120	250	0.29
B6	319	23.1	637	0.76	110	20	8	120	250	0.22
B10	277	21.6	637	0.30	110	20	8	150	250	0.55
B11	358	20.7	532	1.04	108	22	10	70	250	0.19
B12	207	23.3	656	0.10	112	18	6	210	250	1.60
M1	228	20.7	346	0.30	110	20	8	150	250	1.01
C1	265	22.7	637	0.46	110	20	8	100	175	0.36
C2	275	22.0	637	0.46	110	20	8	100	175	0.36

Table E-9 Calculated Results: Moe (1961)

Mark	Bond model using w_{ACI}			Bond model using w_{BARR}			Bond model using w_{MAF}			Code Predictions			
	w_{ACI} (N/mm)	P_{calc} (kN)	P_{ul}/P_{calc}	w_{BARR} (N/mm)	P_{calc} (kN)	P_{ul}/P_{calc}	w_{MAF} (N/mm)	P_{calc} (kN)	P_{ul}/P_{calc}	ACI (kN)	P_{ul}/P_{calc}	BS 8110 (kN)	P_{ul}/P_{calc}
H1	97	266	1.40	141	321	1.16	163	345	1.08	285	1.30	336	1.11
S1-60	92	271	1.44	132	325	1.20	139	334	1.17	270	1.44	315	1.24
S1-70	94	299	1.31	134	357	1.10	140	365	1.08	277	1.42	320	1.23
S5-60	89	234	1.46	130	282	1.21	135	288	1.19	221	1.55	279	1.23
S5-70	91	257	1.47	131	309	1.22	134	312	1.21	225	1.68	283	1.34
R2	98	221	1.41	150	274	1.14	168	289	1.08	204	1.53	294	1.06
M1A	87	349	1.24	143	448	0.97	120	411	1.05	282	1.53	363	1.19

Table E-10 Calculated Results: Elstner and Hognestad (1956)

Mark	Bond model using w_{ACI}			Bond model using w_{BART}			Bond model using w_{MAF}			Code Predictions			
	w_{ACI} (N/mm)	P_{calc} (kN)	P_{ult}/P_{calc}	w_{BART} (N/mm)	P_{calc} (kN)	P_{ult}/P_{calc}	w_{MAF} (N/mm)	P_{calc} (kN)	P_{ult}/P_{calc}	ACI (kN)	P_{ult}/P_{calc}	BS 8110 (kN)	P_{ult}/P_{calc}
A-1a	73	230	1.32	117	290	1.04	79	238	1.27	215	1.41	282	1.07
A-1b	98	277	1.32	142	333	1.10	114	299	1.22	288	1.27	342	1.07
A-1c	105	288	1.23	149	343	1.04	124	313	1.14	309	1.15	359	0.99
A-1d	118	309	1.14	161	360	0.98	142	338	1.04	348	1.01	388	0.91
A-1e	88	259	1.38	132	317	1.12	100	276	1.29	258	1.38	318	1.12
A-2b	84	328	1.22	165	460	0.87	107	371	1.08	244	1.64	391	1.02
A-2c	116	414	1.13	205	550	0.85	171	502	0.93	338	1.38	485	0.96
A-7b	100	375	1.36	186	510	1.00	140	444	1.15	292	1.75	440	1.16
A-3c	98	368	1.45	183	504	1.06	159	469	1.14	285	1.87	433	1.23
A-3d	112	403	1.36	199	539	1.02	190	526	1.04	325	1.68	473	1.16
A-4	100	331	1.21	144	397	1.01	176	440	0.91	378	1.06	407	0.98
A-5	100	443	1.20	185	604	0.88	121	487	1.10	376	1.42	518	1.03
B-9	126	407	1.24	201	515	0.98	199	512	0.99	366	1.38	477	1.06
B-14	135	498	1.16	241	666	0.87	232	653	0.89	393	1.47	572	1.01

Table E-11 Calculated Results: Kinnunen and Nylander (1960)

Mark	Bond model using w_{ACI}			Bond model using w_{BRIT}			Bond model using w_{MAF}			Code Predictions			
	w_{ACI} (N/mm)	P_{calc} (kN)	P_{adj}/P_{calc}	w_{BRIT} (N/mm)	P_{calc} (kN)	P_{adj}/P_{calc}	w_{MAF} (N/mm)	P_{calc} (kN)	P_{adj}/P_{calc}	ACI (kN)	P_{adj}/P_{calc}	BS 8110 (kN)	P_{adj}/P_{calc}
IA15a-5	94	168	1.52	123	192	1.33	162	220	1.16	132	1.93	224	1.14
-6	94	170	1.62	122	194	1.42	161	223	1.23	132	2.08	224	1.23
IA15c-11	108	248	1.34	167	309	1.08	182	323	1.03	154	2.16	313	1.06
-12	107	250	1.33	166	312	1.06	179	323	1.02	153	2.17	314	1.05
IA30a-24	102	304	1.42	141	357	1.21	173	395	1.09	219	1.97	336	1.28
-25	96	287	1.42	137	342	1.19	161	372	1.10	204	2.00	319	1.28
IA30c-30	103	388	1.26	182	514	0.95	165	490	1.00	215	2.28	416	1.18
-31	102	389	1.39	181	517	1.04	162	489	1.10	213	2.53	412	1.31
IA30d-32	98	204	1.26	107	214	1.21	111	218	1.19	207	1.25	250	1.03
-33	100	211	1.22	109	219	1.18	111	222	1.16	213	1.21	255	1.01
IA30e-34	98	280	1.18	136	330	1.00	166	364	0.91	205	1.62	311	1.06
-35	95	275	1.20	132	324	1.02	159	356	0.93	199	1.67	305	1.08

Table E-12 Calculated Results: Regan, Walker and Zakaria (1979)

Mark	Bond model using w_{ACI}			Bond model using w_{BART}			Bond model using w_{MAF}			Code Predictions			
	w_{ACI} (N/mm)	P_{calc} (kN)	P_{adj}/P_{calc}	w_{BART} (N/mm)	P_{calc} (kN)	P_{adj}/P_{calc}	w_{MAF} (N/mm)	P_{calc} (kN)	P_{adj}/P_{calc}	ACI (kN)	P_{adj}/P_{calc}	BS 8110 (kN)	P_{adj}/P_{calc}
SS2	62	154	1.14	102	199	0.89	100	196	0.90	137	1.29	176	1.00
SS4	74	154	1.26	105	184	1.05	105	184	1.06	164	1.19	182	1.07
SS6	61	126	1.31	87	150	1.10	99	160	1.03	136	1.21	152	1.09
SS7	73	144	1.29	100	169	1.10	128	191	0.97	163	1.14	175	1.06
SS8	200	781	1.06	227	832	0.99	277	920	0.90	566	1.46	771	1.07
SS9	125	303	1.29	159	342	1.14	173	357	1.09	226	1.73	347	1.12
SS10	127	306	1.19	161	345	1.06	177	361	1.01	230	1.59	351	1.04
SS11	62	75	1.55	95	93	1.26	87	89	1.32	56	2.07	103	1.13
SS12	63	76	1.38	96	93	1.12	89	90	1.17	57	1.83	104	1.01
SS13	65	77	1.36	98	95	1.11	92	92	1.15	59	1.78	106	0.99

Table E-13 Calculated Results: Rankin and Long (1987)

Mark	Bond model using w_{ACI}			Bond model using w_{BRR}			Bond model using w_{MAF}			Code Predictions			
	w_{ACI} (N/mm)	P_{calc} (kN)	P_{ult}/P_{calc}	w_{BRR} (N/mm)	P_{calc} (kN)	P_{ult}/P_{calc}	w_{MAF} (N/mm)	P_{calc} (kN)	P_{ult}/P_{calc}	ACI (kN)	P_{ult}/P_{calc}	BS 8110 (kN)	P_{ult}/P_{calc}
1	38	29	1.25	49	33	1.09	18	20	1.82	33	1.09	44	0.83
2	38	33	1.47	54	40	1.23	23	26	1.88	33	1.47	48	1.02
3	38	37	1.54	58	46	1.24	28	32	1.78	33	1.70	51	1.10
4	40	41	1.36	64	52	1.07	36	39	1.44	36	1.57	57	0.98
5	40	43	1.34	66	55	1.05	38	42	1.37	36	1.60	58	0.98
6	40	46	1.43	69	60	1.09	44	48	1.37	36	1.84	61	1.07
7	37	46	1.54	68	62	1.14	44	50	1.41	33	2.17	60	1.17
8	37	48	1.48	71	66	1.07	48	55	1.29	33	2.17	63	1.14
9	37	50	1.56	73	71	1.11	53	61	1.30	33	2.40	65	1.21
10	37	32	1.37	52	38	1.16	21	24	1.81	33	1.33	46	0.94
11	37	39	1.41	60	50	1.10	32	36	1.52	33	1.67	54	1.03
12	37	45	1.49	67	61	1.11	43	48	1.39	33	2.04	60	1.12
13	40	36	1.39	58	43	1.16	26	29	1.71	35	1.40	51	0.97
14	40	38	1.38	60	47	1.12	30	33	1.59	35	1.49	53	0.98
15	40	60	1.40	86	89	0.96	64	76	1.11	35	2.41	76	1.12

Table E-13 (cont'd) Calculated Results: Rankin and Long (1987)

Mark	Bond model using w_{ACI}			Bond model using w_{FRIT}			Bond model using w_{MAF}			Code Predictions			
	w_{ACI} (N/mm)	P_{calc} (kN)	P_{ult}/P_{calc}	w_{FRIT} (N/mm)	P_{calc} (kN)	P_{ult}/P_{calc}	w_{MAF} (N/mm)	P_{calc} (kN)	P_{ult}/P_{calc}	ACI (kN)	P_{ult}/P_{calc}	BS 8110 (kN)	P_{ult}/P_{calc}
1A	42	36	1.26	54	41	1.10	24	27	1.67	38	1.17	52	0.87
2A	42	44	1.49	63	54	1.22	36	41	1.61	38	1.72	60	1.10
3A	42	58	1.53	78	80	1.13	62	71	1.26	38	2.33	74	1.21
4A	43	71	1.36	92	104	0.94	69	90	1.09	40	2.43	88	1.11
1B	37	25	1.16	48	28	1.01	15	16	1.80	31	0.93	39	0.74
2B	37	31	1.20	56	39	0.96	24	26	1.47	31	1.21	46	0.82
3B	37	42	1.35	69	58	0.98	43	45	1.25	31	1.83	57	1.00
4B	33	47	1.55	74	70	1.03	51	58	1.25	28	2.61	61	1.19
1C	47	43	1.46	59	48	1.31	29	34	1.85	46	1.38	61	1.03
2C	51	57	1.55	73	68	1.30	51	57	1.55	50	1.77	76	1.16
3C	51	75	1.65	90	99	1.25	87	98	1.27	50	2.51	94	1.33
4C	47	84	1.49	98	122	1.03	73	105	1.20	46	2.77	102	1.23

Table E-14 Calculated Results: Gardner (1990)

Mark	Bond model using w_{ACI}			Bond model using w_{BRIT}			Bond model using w_{MAF}			Code Predictions			
	w_{ACI} (N/mm)	P_{calc} (kN)	P_{calc}/P_{calc}	w_{BRIT} (N/mm)	P_{calc} (kN)	P_{calc}/P_{calc}	w_{MAF} (N/mm)	P_{calc} (kN)	P_{calc}/P_{calc}	ACT (kN)	P_{calc}/P_{calc}	BS 8110 (kN)	P_{calc}/P_{calc}
8	62	127	1.01	122	179	0.72	94	157	0.82	69	1.86	162	0.80
9	60	124	1.09	120	175	0.77	89	151	0.90	67	2.02	158	0.86
10	63	128	1.01	123	180	0.72	95	158	0.82	70	1.84	163	0.79
11	89	278	1.12	164	377	0.83	131	338	0.92	149	2.10	321	0.97
12	93	334	1.07	169	449	0.79	141	411	0.87	186	1.92	366	0.97
13	101	227	1.19	121	249	1.09	170	295	0.92	206	1.32	275	0.99
14	61	183	1.11	162	299	0.68	60	181	1.12	86	2.36	240	0.84
15	67	152	1.05	116	200	0.80	110	194	0.83	98	1.63	184	0.87
16	69	95	1.13	80	103	1.04	93	111	0.97	103	1.05	131	0.82
17	68	125	0.96	117	165	0.73	111	160	0.75	78	1.55	162	0.75
19	96	190	1.43	104	198	1.37	151	239	1.14	196	1.38	239	1.14
20	73	267	1.04	143	374	0.74	90	297	0.93	145	1.92	310	0.90
21	81	200	1.15	105	227	1.01	132	254	0.90	166	1.39	238	0.97
23	51	124	0.87	97	171	0.63	73	148	0.73	75	1.44	153	0.70
25	146	279	1.10	155	287	1.07	256	368	0.83	298	1.03	352	0.87
26	87	314	1.03	207	483	0.67	132	386	0.84	152	2.13	349	0.93
27	97	191	1.27	148	236	1.03	173	254	0.95	142	1.71	235	1.04
28	103	118	1.25	105	119	1.24	143	139	1.06	154	0.96	172	0.86

Table E-15 Calculated Results: Shilling and Vanderbilt (1970)

Mark	Bond model using w_{ACI}			Bond model using w_{BRIT}			Bond model using w_{MAF}			Code Predictions			
	w_{ACI} (N/mm)	P_{calc} (kN)	P_{ult}/P_{calc}	w_{BRIT} (N/mm)	P_{calc} (kN)	P_{ult}/P_{calc}	w_{MAF} (N/mm)	P_{calc} (kN)	P_{ult}/P_{calc}	ACI (kN)	P_{ult}/P_{calc}	BS 8110 (kN)	P_{ult}/P_{calc}
2S1-1	33	31	1.37	60	42	1.02	47	37	1.15	30	1.42	46	0.94
3S1-2	30	36	1.28	56	50	0.94	42	43	1.09	37	1.26	52	0.90
4S1-3	29	41	1.26	55	56	0.92	40	48	1.07	44	1.17	58	0.88
3C1-4	30	40	1.44	56	55	1.05	41	48	1.22	34	1.71	58	1.01
6S1-5	29	50	1.56	55	69	1.13	40	59	1.32	62	1.26	75	1.04
8S1-6	29	57	1.57	54	79	1.14	40	68	1.33	79	1.15	91	0.99
2S2-7	30	40	1.23	71	62	0.80	51	52	0.95	28	1.78	54	0.91
4S2-8	29	62	1.12	70	95	0.73	46	77	0.90	45	1.54	74	0.93
6C1-9	32	67	1.44	59	91	1.06	44	79	1.22	65	1.48	94	1.03
8S2-10	32	94	1.22	74	142	0.80	53	119	0.95	89	1.28	125	0.91
2C1-11	28	36	1.08	54	50	0.78	38	42	0.93	24	1.63	46	0.86
4C1-12	30	53	1.37	56	73	1.00	40	62	1.17	44	1.66	69	1.05
8C1-13	31	76	1.32	57	104	0.97	42	89	1.13	82	1.23	114	0.88
6S2-14	29	74	1.08	69	115	0.70	44	92	0.87	61	1.30	94	0.85
4C2-15	29	70	1.38	70	108	0.90	45	87	1.11	43	2.24	86	1.12

Table E-16 Calculated Results: Lunt (1988)

Mark	Bond model using w_{ACI}			Bond model using w_{BART}			Bond model using w_{MAF}			Code Predictions			
	w_{ACI} (N/mm)	P_{calc} (kN)	P_{ult}/P_{calc}	w_{BART} (N/mm)	P_{calc} (kN)	P_{ult}/P_{calc}	w_{MAF} (N/mm)	P_{calc} (kN)	P_{ult}/P_{calc}	ACI (kN)	P_{ult}/P_{calc}	BS 8110 (kN)	P_{ult}/P_{calc}
A1	118	299	1.33	105	281	1.42	93	265	1.50	372	1.07	284	1.40
B1	95	245	1.15	103	254	1.11	85	231	1.22	273	1.03	236	1.19
B2	89	253	1.18	98	265	1.13	98	265	1.13	257	1.16	227	1.32
B3	91	274	1.17	106	297	1.08	101	289	1.11	261	1.23	246	1.30
B4	89	299	1.04	116	341	0.91	96	310	1.00	257	1.21	268	1.16
B5	94	280	1.14	109	301	1.06	105	296	1.08	271	1.18	252	1.26
B6	88	296	1.08	114	338	0.94	94	306	1.04	253	1.26	265	1.20
B10	85	215	1.29	82	211	1.31	78	206	1.34	244	1.13	190	1.46
B11	82	291	1.23	121	354	1.01	132	370	0.97	234	1.53	277	1.29
B12	90	174	1.19	59	141	1.47	54	134	1.54	260	0.80	139	1.49
M1	83	180	1.26	81	178	1.28	79	176	1.30	239	0.95	188	1.21
C1	87	208	1.27	96	219	1.21	118	242	1.09	198	1.34	194	1.36
C2	86	206	1.33	95	218	1.26	116	240	1.15	195	1.41	192	1.43